U.S. DEPARTMENT OF ENERGY

PNNL-23340
DSGREP-RPT-005, Rev. 0

Prepared for the U.S. Department of Energy
under Contract DE-AC05-76RL01830

Evaluation of Gas Retention in Waste Simulants: Tall Column Experiments

PP Schonewill
PA Gauglitz
RW Shimskey
KM Denslow
MR Powell
GK Boeringa
JR Bontha
NK Karri
LS Fifield
DN Tran
SA Sande
DJ Heldebrant

Pacific Northwest National Laboratory

JE Meacham
DB Smet
WE Bryan
RB Calmus

Washington River Protection Solutions LLC

May 2014

Pacific Northwest NATIONAL LABORATORY

Proudly Operated by Battelle Since 1965

DISCLAIMER

PACIFIC NORTHWEST NATIONAL LABORATORY
operated by
BATTELLE
for the
UNITED STATES DEPARTMENT OF ENERGY
under Contract DE-AC05-76RL01830

Printed in the United States of America

Available to DOE and DOE contractors from the
Office of Scientific and Technical Information,
P.O. Box 62, Oak Ridge, TN 37831-0062;
ph: (865) 576-8401
fax: (865) 576-5728
email: reports@adonis.osti.gov

Available to the public from the National Technical Information Service
5301 Shawnee Rd., Alexandria, VA 22312
ph: (800) 553-NTIS (6847)
email: orders@ntis.gov <http://www.ntis.gov/about/form.aspx>
Online ordering: http://www.ntis.gov


This document was printed on recycled paper.
(8/2010)

PNNL-23340
DSGREP-RPT-005, Rev. 0

Evaluation of Gas Retention in Waste Simulants: Tall Column Experiments

PP Schonewill
PA Gauglitz
RW Shimskey
KM Denslow
MR Powell
GK Boeringa
JR Bontha
NK Karri
LS Fifield
DN Tran
SA Sande
DJ Heldebrant

Pacific Northwest National Laboratory

JE Meacham
DB Smet
WE Bryan
RB Calmus

Washington River Protection Solutions, LLC

May 2014

Prepared for
the U.S. Department of Energy
under Contract DE-AC05-76RL01830

Pacific Northwest National Laboratory
Richland, Washington 99352

Executive Summary

Gas generation in Hanford's underground waste storage tanks may, under certain conditions, lead to gas accumulation within the layer of settled solids (sludge) at the tank bottom. The gas, which typically has hydrogen as the major component together with other flammable species, is formed principally by radiation-driven chemical reactions. Accumulation of these gases within the sludge in a waste tank is undesirable and limits the amount of tank volume for waste storage. Further, accumulation of large amounts of gas in the sludge may potentially result in an unacceptable release of the accumulated gas if the sludge-layer density is reduced to less than that of the overlying sludge or that of the supernatant liquid. Rapid release of large amounts of flammable gases could endanger personnel and equipment near the tank. For this reason, a thorough understanding of the circumstances that can lead to a potentially problematic gas accumulation in sludge layers is needed. To respond to this need, the Deep Sludge Gas Release Event Project (DSGREP) was commissioned to examine gas release behavior in sludges.

Work by van Kessel and van Kesteren (2002)[1] implies that for sludge of sufficient shear strength, there is a sludge depth (denoted as d_{max} and measured from the sludge surface) that marks a transition between two types of gas retention behavior. They suggest that at depths less than d_{max} (the region of the sludge between the surface and d_{max}), connected cracks and channels allow gas to escape the sludge and gas is prevented from accumulating beyond the level needed to establish the connected channels. At depths greater than d_{max}, however, the work of van Kessel and van Kesteren (2002) argues that overburden stress is sufficient to prevent formation of the connected-channel network and any generated gas will tend to accumulate in the sludge until the sludge bulk density is low enough that the layer becomes unstable and the gas is released.

Based on a survey of previous work on gas retention and release, the overall expected behavior in strong (> 500 Pa) sludge materials is for bubbles to grow as slits and cracks, at all depths, and interconnect to form pathways for gas release. A gas release channel may temporarily be blocked, but a local increase in the pressure of a gas bubble will either reopen the previously open channel or will expand by extending a fracture in some other direction and eventually connect with an open channel. While this behavior is expected at all depths because bubbles should be able to expand and interconnect at all depths, the predicted closing of the gas release channels below d_{max} by van Kessel and van Kesteren (2002) is an uncertainty that needs to be evaluated. Based on available information, the d_{max} prediction for a change in bubble retention has not been observed experimentally.

If van Kessel's and van Kesteren's theory is applicable to sludge waste tanks, it prevents waste transfers from continuing in order to avoid unsafe waste configurations. Therefore, it was crucial to evaluate the feasibility of d_{max} for sludge waste at full scale, as this reduces the need to project or extrapolate results to the waste tanks, thereby minimizing the uncertainty in the conclusions. Thus, a set of experiments was conducted using a full-scale column (more commonly referred to as the "tall column"). The principal objective of the tall column tests was to evaluate the accuracy of the d_{max} theory described by van Kessel and van Kesteren (2002) at full-scale waste sludge depth (~310 in), using a

[1] van Kessel T and WGM van Kesteren. 2002. "Gas Production and Transport in Artificial Sludge Depots." *Waste Management* 22(1):19–28.

simulant that had shear strengths (500 to 1000 Pa) representative of the sludge waste (which varies with depth from ~150 to ~4000 Pa). The tall column tests challenged the d_{max} theory directly by determining whether gas retention changes significantly at sludge depths below (deeper than) d_{max}. The tests were designed to observe gas retention behavior directly and to collect data that allowed the gas fraction (or void) in the tall column to be calculated.

The tall column was fabricated using a 3/8-in.-thick steel tube that was 45 ft tall with a 60-in. inside diameter. It was set on load cells and was equipped with a heating system that fed heated air through an annular space around the column. The annulus was created by a framework of insulated panels. The heating system was used to maintain a minimum temperature required for the gas generation reaction to occur and keep the simulant temperature approximately constant. Inside the column was an approximately 12 × 12 in. square tube that housed a series of video cameras (the viewing column). The cameras were orientated toward the column interior, where one side of the viewing column had acrylic windows. The tall column headspace was purged with nitrogen gas during the tests, and the inlet purge gas volume and the exiting gas volume (a combination of nitrogen and the hydrogen gas produced by the in-situ reaction) from the headspace were both measured continuously. Other instrumentation was also installed on the column at multiple elevations, including thermocouples, pressure transducers, sample ports, and ultrasonic sensors.

Tests were performed in the tall column using a kaolin-water simulant laced with small amounts of iron micropowder. The iron corroded to produce hydrogen gas. The simulant was prepared at the tall column test site using industrial equipment, with the mixing occurring in cement trucks. The kaolin slurry from the trucks was loaded into the column using a pumper truck to the target level for the test. After loading, the tall column was monitored using the video cameras to observe the gas generation and retention behavior; as gas was generated and voids formed in the simulant, other data were collected to quantify the gas fractions retained in the simulant.

The equipment and instruments were used to measure the following important quantities during the tall column tests:

- Simulant characteristics, e.g., shear strength and moisture content
- Bulk void fraction (by tracking changes in height)
- Gas retention and morphology (using video and still images from the cameras)
- Local void fraction, using three techniques – ultrasonic sensors, tracking motion of bubble features, and image analysis
- Test characteristics such as temperature of the simulant, pressure (in the column), and mass of the column.

The average (bulk) void fraction was calculated using the rise in simulant level during a test. Measurement of bulk void fraction, though critical data, is not as instructive as the void distribution in the column in evaluating the predicted change in gas retention below d_{max}. To probe the gas retention behavior as a function of elevation (or simulant depth), methods were devised that would permit the void fraction to be estimated in sub-regions of the tall column (and obtain local measurements of void fraction). Of particular interest was to determine if gas was concentrated at the lowest elevations of the column, resulting in higher local void fractions at those locations. At the outset of tall column testing,

three methods were planned: ultrasonic measurements, core sample measurements, and analysis of post-test compression data. Uncertainty regarding the accuracy of these methods led to the development of two other techniques after the tests were conducted, both of which depended on still images extracted from the video files collected during the tests: feature tracking during void growth (used previously in Powell et al. 2014[1]) and image analysis for void fraction.

Three tests were performed; two with a target shear strength of 500 Pa and one with a target shear strength of 1000 Pa. Table S.1 summarizes the major results of each test. The three tests reached peak bulk void fractions between 8% and 12%, despite peak gas generation rates that varied by a factor of more than two. The initial simulant level in all the tests was greater than the 310-in. target level (target level was chosen to represent a full-scale DST sludge depth, specifically that of tank 241-AN-101), resulting in regions of the simulant that were deeper than even the most conservative estimate of d_{max} theory. Sufficient amounts of gas were generated to permit bulk void fractions of ~50% if the simulant had been capable of retaining gas in those amounts. Despite having enough iron present to obtain ~50% hydrogen gas, void fractions achieved in the tests only reached 8 to 12%. More significantly, the void fraction grew to peak values of 8 to 12% over a couple of days, and then decreased for the remainder of the test.

Table S.1. Summary Table of Tall Column Tests

Test No.	Bulk Shear Strength (Pa)	Initial Simulant Level (in.)	Conservative Estimate of d_{max} (in.)	Initial Bulk (average) Void (%)	Peak Bulk (average) Void (%)	Final Bulk (average) Void (%)	Peak Gas Generation Rate (L/min)
1	594	320.25	221.3	2.3	8.3	7.1	4.55
2	627	318.75	226.3	1.3	9.1	7.6	7.12
3	~920[(a)]	353.5	310.8	7.2	11.8	9.4	11.90

(a) Refer to discussion in Section 7.3 for justification of this bulk shear strength.

It was significant that the bulk void fraction peaked and then began to decline, suggesting that no additional retention mechanism was present. This was supported by observations of gas transport in the tall column tests. In all three tests, gas was transported freely from all depths in the column, even before the peak void fraction was achieved, and the void morphology was not a function of the simulant depth, i.e., the voids had a similar appearance (primarily slits and cracks) from the top of the simulant layer to the bottom. In the tests, the gas generation reaction was allowed to proceed until more than 1 L of gas was produced for every liter of slurry. Consequently, the visual evidence collected during each test, namely that gas retention behavior in the simulant did not obey d_{max} predictions, was a significant finding.

The void profile data for all three tests, regardless of the method used, were in agreement that the relative change in void fraction from the top of the column to the bottom was negligible (and thus, no

[1] Powell MR, PA Gauglitz, KM Denslow, CM Fischer, DJ Heldebrant, MS Prowant, SA Sande, JM Davis, and MR Telander. 2014. *Evaluation of Gas Retention in Waste Simulants: Intermediate-Scale Column and Open-Channel Depth Tests*. PNNL-23136, DSGREP-RPT-003, Pacific Northwest National Laboratory, Richland, Washington.

change in retention below d_{max}). If anything, the lowest elevations in the column had lower void fractions than other elevations. Since the accuracy of the void profile calculation methods varied, the void profile of each method was integrated and compared to the bulk void fraction at the same point in time. Based on this comparison and the limitations of some of the other analysis techniques, feature tracking was deemed to provide the best estimate of the void fraction profile in the column. Void profiles obtained by feature tracking all showed reduced void fraction at the lowest elevations (regions where the simulant was below d_{max}).

The sum of evidence collected during the tall column tests substantiates the conclusion that d_{max} theory is not an appropriate predictor of the effect of simulant depth on gas retention and release behavior in the shear strength ranges tested (refer again to Table S.1). By extension, the same can be concluded regarding waste sludge layers of similar shear strength currently stored in double-shell tanks (DSTs). Thus, application of d_{max} theory to the sludge waste tanks would likely result in inaccurate predictions of gas retention behavior. The inaccurate predictions would imply a potential for an instability to occur in the DSTs that is not supported by the tall column testing. Given the data collected in the tall column experiments, the outcome of increasing waste depth in DSTs would be gas fractions at the lowest depths that are either similar to or lower than the current bulk gas fractions in the DSTs. No changes from historical trends in gas retention behavior in the waste sludge tanks due to increases in sludge depth are anticipated.

Acknowledgments

The authors would like to thank all the PNNL staff who assisted in developing test equipment, conducting the tall column tests, performing data analysis, carefully reviewing calculations, and other tasks. The PNNL staff that helped in these ways include:

Paul MacFarlan	Garrett Brown	Don Rinehart	Beric Wells
Jim Davis	Monte Elmore	Renee Russell	Matt Prowant
Chris Fischer	Lanee Snow	Sandy Fiskum	Stan Owsley
Matt Fountain	Matt Edwards	Rich Pires	Derek Hopkins
Lenna Mahoney	Ellen Baer	Bill Buchmiller	Randy Norheim
Kurt Recknagle	Jim Fort	Thomas Yokuda	Richard Carter

Also critical was the support provided by PNNL craftspeople in fabricating and modifying equipment needed for testing; they are too numerous to list by name. The report was improved immensely through the technical editing of Matt Wilburn, the thorough technical review by Richard Daniel, the review by Kirsten Meier, and the consistent support of the project quality engineer, Bill Dey.

The tall column testing could not have been conducted without the willing partnership of WRPS and many of their staff: Terry Sams, Nick Kirch, Chris Watson, Morgan Harding, Robert Frank, Stephanie Harrington, Jordan Follett, Ben Gallaher, Curtis Evans, and Mike Grigsby. The Department of Energy Office of River Protection also provided overall direction for the work, with special thanks to Brian Stickney.

Many other agencies and their staff supported the tall column testing efforts, including:

- Total Site Services (special thanks to field work supervisors Lea Hogue and Tony Nash);
- HiLine Engineering, who fabricated the tall column and supported operations: Troy Stokes, Sean Steven, Lucas White, and Kelly Bright;
- Dade Moeller and their industrial hygiene support (special thanks to Van Fidino and Karlene Dysland);
- American Rock Products and their drivers;
- Ralph's Concrete Pumping Incorporated;
- Harms Pacific Transport Incorporated;
- Intermech Incorporated

The content in this report was also greatly improved by comments and suggestions made by independent experts, such as the subject matter experts convened to review the work: Bill Wilmarth and Charles Nash (Savannah River National Laboratory), Guillermo Terrones (Los Alamos National Laboratory), Mike Epstein (Fauske & Associates), and Robert Holtz (University of Washington).

Acronyms and Abbreviations

AN-101	Hanford DST receiving sludge waste
AN-106	Hanford DST receiving sludge waste
APEL	Applied Process Engineering Laboratory
ASO	Analytical Support Operations
ASTM	ASTM International (formerly the American Society for Testing and Materials)
BNC	Bayonet Neill-Concelman
DAS	data acquisition system
dB	decibel
DC	dry content
d_{max}	maximum depth below which gas-release channels are closed off in a sludge bed
DSGRE	deep-sludge gas release event
DSGREP	DSGRE Project
DST	double-shell tank
Fe	iron
FIO	For Information Only
GRE	gas release event
GVF	gas void fraction
HASQARD	Hanford Analytical Services Quality Assurance Requirements Documents
LRB	Laboratory Record Book
M&TE	measuring and test equipment
MSA	Mission Support Alliance
PNNL	Pacific Northwest National Laboratory
PT	pressure transducer
QA	quality assurance
TP	Test Plan
TS	total solids
UT	ultrasonic transducer
UT-DAS	ultrasonic transducer data acquisition system
VSB	vessel-spanning bubble
vol%	volume percent
WRPS	Washington River Protection Solutions LLC
wt%	weight percent
WWFTP	WRPS Waste Form Testing Program

Nomenclature

A_1	amplitude of ultrasonic signal through gas-free kaolin
A_2	amplitude of ultrasonic signal through gassy kaolin
D	vessel diameter
d_f	average floc size
d_{max}	maximum depth below which gas-release channels are closed off in a sludge bed
d_o	capacity (fractal, Housdorff) dimension
δ	coefficient obtained by fitting
e	void ratio (ρ_p/ρ_w)
E	modulus of elasticity
ϕ	volume fraction
ϕ_A	void fraction computed over an area by image analysis
ϕ_{avg}	average retained gas fraction determined by compression
$\phi_{avg,h}$	average retained gas fraction between column bottom and level h
ϕ_{bulk}	bulk (average) void fraction measured by level change
ϕ_{local}	local average gas fraction between h_1 and h_2
ϕ_o	initial bulk void fraction
$\Delta\phi_{bulk}$	change in bulk void fraction
$\Delta\phi_{bulk}/\Delta t$	rate of change of bulk void fraction with Δt
g	gravitational acceleration
h	level above column bottom
H	sludge height in a vessel
h_1	level 1 above column bottom
h_2	level 2 above column bottom
h_{init}	initial level of a tracer or feature
h_s	simulant depth before compression
$h_{s,o}$	height of simulant, initial
$h_{s,t}$	height of simulant at time t
$h_{w,o}$	height of water, initial
$h_{w,t}$	height of water at time t
$\Delta h(t)$	difference between h and h_{init} as a function of time
Δh_c	measured elevation change of simulant surface upon compression
j	current pixel index
K_o	ratio between horizontal and vertical effective stress
L	floc size (length-scale)
L_p	primary particle size (length-scale)

$M_{s,o}$	initial simulant mass
n	total number of pixels in an analyzed image
n_v	number of pixels indicating void
ν	Poisson's ratio
p_j	binary value of current pixel (0, 1)
P_{atm}	atmospheric pressure
P_{hyd}	hydrostatic head above simulant surface before compression
ΔP	change in pressure at simulant surface upon compression
r_o	radius of an undisturbed channel
ρ_{act}	initial actual density of simulant
ρ_{gf}	gas-free density of the sludge simulant
ρ_o	initial density of simulant implied by mass in column
ρ_p	dry (material) density of sediment particles
ρ_s	sludge or simulant density, bulk
ρ_w	density of water
t	elapsed time
τ_s	undrained shear strength
$\tau_{s,o}$	shear strength target prior to accounting for withheld water
$\tau_{s,bound}$	adjusted shear strength target accounting for withheld water
$V_{s,o}$	initial simulant volume
X	volume of water withheld for iron slurry
x_k	mass fraction of kaolin
ξ	coefficient obtained by fitting
Y_G	gravity yield parameter

Contents

Figures

Tables

1.0 Introduction

Gas generation in Hanford's underground waste storage tanks can lead to gas accumulation within the layer of settled solids (sludge) at the tank bottom. The gas, which typically has hydrogen as the major component together with other flammable species, is formed principally by radiation-driven chemical reactions. Accumulation of these gases within the sludge in a waste tank is undesirable and limits the amount of tank volume for waste storage. Further, accumulation of large amounts of gas in the sludge may potentially result in an unacceptable release of the accumulated gas if the sludge-layer density is reduced to less than that of the overlying sludge or that of the supernatant liquid. Rapid release of large amounts of flammable gases could endanger personnel and equipment near the tank. For this reason, a thorough understanding of the circumstances that can lead to a potentially problematic gas accumulation in sludge layers is needed.

A study by van Kessel and van Kesteren (2002) generates a theoretical prediction of how gas retention might change with depth. Their study implies that for sludge of sufficient shear strength, there is a sludge depth (denoted as d_{max} and measured from the sludge surface[1]) that marks a transition between two types of gas retention behavior. They suggest that at depths less than d_{max} (the region of the sludge between the surface and d_{max}), connected cracks and channels allow gas to escape the sludge and gas is prevented from accumulating. Specifically, van Kessel and van Kesteren (2002) state on page 24:

> "In the upper part of an artificial sludge depot, channel formation has an important contribution to drainage of gas; at depths below d_{max} **this mechanism is not relevant**, however [emphasis added]."

At depths greater than d_{max}, however, the work of van Kessel and van Kesteren (2002) argues that overburden stress (created by the self-weight of the material) is sufficient to prevent formation of the connected-channel network and any generated gas will tend to accumulate in the sludge until the sludge bulk density is low enough that the layer becomes unstable and the gas is released. Again, on page 24 of van Kessel and van Kesteren (2002) this is described as follows:

> "In the lower part of a depot, outflow of gas **will only occur** when the gas content is increased up to a level at which the sediment matrix becomes unstable [emphasis added]."

The predicted behavior of van Kessel and van Kesteren is strictly theoretical and has not been verified experimentally. Experiments of the type required to observe d_{max} are rare and to date the theory has not, based on a review of available information, been directly challenged. As discussed further in Section 1.1, Wichman et al. (2000) present data for gas void fraction as a function of depth to a depth of 17 to 20 m in the Slufter disposal site. Although never specifically analyzed, the depth of the Slufter sediment probably exceeds the depth for channel closure (d_{max}) but the void data show no significant increase in gas retention with depth, which is predicted for depths below d_{max}.

Therefore, as the d_{max} theory has not been empirically tested, its applicability to the waste sludge in the Hanford Tank Farms is unknown and cannot be ruled out. Accumulating gas at depths below d_{max}

[1] If another liquid layer, such as a layer of water, is present on top of the sludge layer, it is not included in the d_{max} calculation. The depth is referenced from the surface (top) of the sludge layer.

would not be a favorable waste sludge configuration. Gas accumulation could be a precursor to a deep-sludge gas release event (DSGRE). Thus, the tests and associated support activities described in this report were designed to evaluate the accuracy of the d_{max} theory presented by van Kessel and van Kesteren at full-scale Hanford tank depths. Several experiments were planned using waste depths expected to be reached in double-shell tanks (DSTs) AN-101 and AN-106 after retrieval campaigns. These two receiver tanks are intended to be filled to the greatest waste depths (compared to any other vessels) as waste transfers continue. The current safety basis for those vessels restricts the waste depths that can be achieved in AN-101 and AN-106, threatening to halt waste retrieval from other tanks. An increase in the waste depths that are permitted in these vessels depends in part on assessing whether d_{max} theory is or is not applicable to the sludge waste.

Target simulant shear strengths were selected that are representative of the waste in these tanks. These experiments are similar to a set of tests performed using a column of intermediate height (approximately 20 ft with a sludge depth of 14 ft) and shear strength (~350 Pa) that has already been performed by PNNL (see Powell et al. [2014] for a description of the completed testing and results). By comparison, the full-scale height (hereafter typically referred to as "tall") column is 5 ft in diameter and can hold simulant slurry depths of 30 ft or more (the column having a total height of 45 ft). The column of sludge simulant was designed to be deep enough to detect gas retention behavior changes (if they exist) at depths below d_{max}. The sludge simulant column tests used kaolin/water/iron mixtures with shear strengths of approximately 500 or 1000 Pa. Simulants similar to this have been used previously to evaluate gas retention and release (Gauglitz et al. 2012; Powell et al. 2014).

The experiments were performed at the Cold Test Facility (CTF), operated by Washington River Protection Solutions (WRPS), to accommodate the tall column and the equipment required to conduct testing at full scale.[1] Preparation for the tests and test operation was a collaborative effort between PNNL, WRPS, and WRPS subcontractors. Performing the tests at full scale alleviates the need to verify or validate any scaling relationships related to sludge depth. Full-scale tests also provide the opportunity to compare the results with those of the already completed intermediate column testing. Conducting tests with shear strengths that are representative of AN-101 and AN-106 sludge, though on the lower end of the range of shear strengths measured by a cone penetrometer (Follett 2014), also reduces the amount of extrapolation of actual waste behavior.

An important feature of the tall column experiments was measuring void as a function of time and elevation as the test progressed. The change in gas retention behavior suggested by van Kessel and van Kesteren (2002) would result in, presumably, a region at greater depths with both different bubble morphology and higher gas fraction (see the conceptual diagram given in Figure 1.1). Accurately measuring gas retention was important for quantitatively evaluating retained gas behavior above and below d_{max}. Thus, the column tests had several methods by which gas retention behavior (or more precisely, the void fraction at various sludge depths) was determined: an acoustic measurement technique, sampling the sludge in the column, and various analyses of images and videos collected during each experiment. These were also compared to the bulk void fraction as determined by the measured change in surface level as a way to assess their accuracy.

[1] Any reference to the tall column testing as "full scale" does not imply that the entire test system (i.e., the column diameter or any supporting equipment) was full scale. It refers only to the depth of the waste simulant, which was targeted to be the same as the highest expected depth in retrieval tanks AN-101 and AN-106.

The measurements of void fraction with sludge depth performed during the tall column tests, along with visual observation of gas transport and morphology in the column, quantify whether gas retention behavior varies with depth and, more specifically, if there is a transition in this behavior at or below d_{max}. As such, the testing program was designed to empirically determine if d_{max} theory predicted the correct gas retention behavior, with one of two possible outcomes:

- If a large or sudden increase in gas fraction is observed and/or calculated from measurements at depths deeper than d_{max}, then the d_{max} theory will be supported.
- If no significant change in gas retention is observed and/or calculated from measurements deeper than d_{max}, then the conclusion will be that the d_{max} theory does not reliably predict an increase in gas retention behavior in the simulant sludge, and by extension, sludge waste in AN-101 and AN-106.

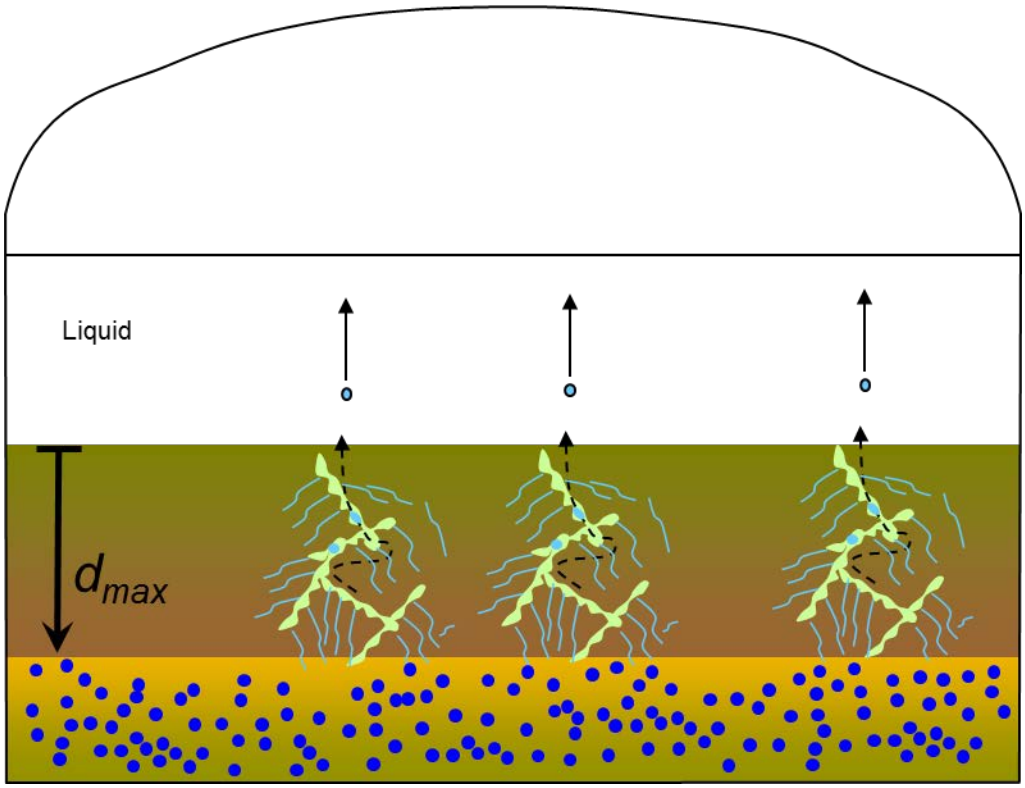

Figure 1.1. Conceptual Diagram of How a Change in Gas Retention Behavior below D_{max} Might Manifest in a Waste Tank. The exact nature of the gas volume fraction and morphology in this diagram is speculative as it is not described in any previous work.

In the following subsection, we discuss additional previous work on gas retention and release in sediments, waste simulants, and actual waste. The balance of this report then describes the methods and results of the tall column testing. Section 2.0 describes the test objectives. Section 3.0 outlines the quality assurance (QA) program under which the testing was conducted. Section 4.0 contains the technical approach used to conduct the testing and the analysis techniques. Section 5.0 describes the simulant used in this work. Section 6.0 presents the experimental systems that were used and how the tests were conducted. The data from the tests are presented in Section 7.0, followed by a discussion of void fraction data for each test in Section 8.0. Section 9.0 summarizes the testing and the conclusions. Section 10.0 lists all the work cited in this report. Finally, there are three appendices that provide

supplementary information (A – Supplementary Tall Column Test Data, B – Core Sampling Method for Determining Void Fraction, C – Supplementary Ultrasonic Information).

1.1 Previous Studies of Gas Retention and Release

Retention of bubbles is known to occur in a variety of materials, ranging from yield-stress fluids and pastes (Chhabra 1993) to ocean sediments (Wheeler 1988a, 1990; Judd and Hovland 1992), in addition to radioactive waste slurries which are the focus of the current study. Beginning with studies focused on bubbles in natural sediments, the early studies generally considered the retention of roughly spherical bubbles that displaced the sediment particles and the impact of the bubbles on sediment properties (Wheeler 1988a, 1988b, 1990; Wheeler and Gardner 1989; Wheeler et al. 1990; Sills et al. 1991; Sills and Wheeler 1992). More recent studies have recognized that the bubble shapes are more complicated and, for fine-grained sediments where bubbles displace the sediment particles, a number of images show bubbles that form as cracks and slits in the sediment (Sills and Gonzalez 2001; Best et al. 2004; Winterwerp and van Kesteren 2004; Boudreau et al. 2005; Algar et al. 2011a; Boudreau 2012). In general, the shape of the bubbles being cracks is associated with the bubbles growing by a process of initiating and extending fractures within the sediment, and this mechanism of bubble growth has been described and modeled in a number of studies (Johnson et al. 2002; van Kessel and van Kesteren 2002; Gardiner et al. 2003; Winterwerp and van Kesteren 2004; Algar and Boudreau 2009; Jain and Juanes 2009; Barry et al. 2010; Algar and Boudreau 2010; Katsman et al. 2013).

A number of studies have discussed the overall gas bubble retention and release behavior of sediment beds or columns. Sills and Gonzalez (2001) and van Kessel and van Kesteren (2002) both describe similar overall behavior of gas retention increasing to a level where additional generated gas escapes through cracks, fissures, or channels and the void fraction reaching a peak level and then decreasing with continued gas generation. Both of these studies also note accelerated compaction of the sediment beds after the peak void fraction due to the connected gas channels providing a pathway for pore water to escape. Algar et al. (2011b) specifically discuss that once a bubble release path is formed, initially by bubbles expanding by fracture growth, additional bubbles can readily re-open closed channels and this provides a pathway for bubble release. For all the studies discussed in the section, the bubble behavior is treated as being governed by local conditions. The work of van Kessel and van Kesteren (2002) is unique in that this work specifically predicts a role for the macroscopic property of sediment depth where the weight of the material will close channels below a specific depth (d_{max} in their work). Scandella et al. (2011) also discuss the closing of channels (or conduits) with increasing total vertical stress (increasing sediment depth) but further argue that an increase in the local bubble pressure can overcome the total stress and re-open closed conduits to initiate bubble transport.

Finally, both Wichman et al. (2000) and van Kessel and van Kesteren (2002) discuss gas retention in large laboratory or field experiments associated with contaminated lake bottom sediment and disposal sites in the Netherlands. The large laboratory tests discussed in van Kessel and van Kesteren (2002) used a sediment bed about 5 m deep and the peak gas void fraction was about 8% and decreased with continued gas generation to about 5% at the end of the test. For this test they estimated the depth for channel closure, d_{max}, of 8 to 10 m, so this experiment was not sufficiently deep to evaluate the predicted channel closure below d_{max}. Wichman et al. (2000) give gas void fraction as a function of depth for sediment that is 17 to 20 m deep in the Slufter disposal site. The data are given for the volume fraction of gas, expanded to atmospheric pressure, and the mean value is 10% to 11% (the in situ gas fraction would

be less due to the increase in pressure with depth). The gas void data were generally the same for measurements taken two years apart. Although never specifically analyzed, the depth of the Slufter sediment probably exceeds the depth for channel closure (d_{max}) but the void data show no significant increase in gas retention with depth, which is then consistent with having gas channels connected, perhaps periodically, to release gas at all depths in this large field test.

For studies that have focused on evaluating bubble retention and release in radioactive waste, there are a number of studies using simulants and actual waste samples (see for example, Powell et al. 2014; Gauglitz et al. 1994, 1995, 1996, 2001, 2012; Stewart et al. 1996; Rassat et al. 1997, 1998, 1999, 2014; Bredt et al. 1995; Bredt and Tingey 1996; and Walker et al. 1994). There are many common observations between these studies and the evaluation of bubble behavior in natural sediments. Gauglitz et al. (1996) showed images of retained bubbles in bentonite clay simulants that progressed in shape from spherical in weak material (~ 6 Pa), to distorted spheres in intermediate strength material (67 Pa), and to slits and cracks in stronger materials (1040 Pa).[1] One notable difference is that the peak gas retention measured in the bentonite clay simulants is consistently higher than in the natural sediments. In particular, the bentonite had a maximum gas void fraction of about 40% at intermediate strengths (about 50 Pa) and then decreased with increasing strength to about 30%. For the stronger clay (1040 Pa) with slit-shaped bubbles, while gas transport could not be directly visualized, video recordings showed the slit-shaped bubbles expanding and contracting as gas was being generated, indicating periodic interconnection of the slit-shaped bubbles (Gauglitz et al. 1996). Similar bubble retention tests were also conducted in actual waste samples, and round bubbles were seen in weaker waste and distorted and slit-shaped bubbles were observed in stronger samples that visually appeared to be sludge; gas retention decreased with increasing strength, the bubbles had a more pronounced slit-shape above 1000 Pa, and the lowest gas retention measured for actual waste was ~ 25% for the strongest material that was described as stiff-sludge (Gauglitz et al. 1996; Rassat et al. 1997; 1998).

In a more recent study, Gauglitz et al. (2012) focused specifically on studying gas retention and release in strong sludge simulants with an overall objective of understanding the conditions when comparatively low gas retention will occur, such as the 8% peak retention reported by van Kessel and van Kesteren (2002) for lake-bottom sediment. In this study, bubble shape and gas retention and release were observed in kaolin clay simulants for a range of strengths, test vessel sizes, and methods of generating in situ gas bubbles. A key finding of this work was the observation of bubble release channels, similar to those described by van Kessel and van Kesteren (2002) and Sills and Gonzalez (2001). In the gas channels that could be visually identified, gas movement repeatedly started and stopped, suggesting that the pressure in the gas would increase until the bubble could open a blocked region of the channel and allow gas to escape along the channel.

Finally, Powell et al. (2014) conducted experiments on gas retention and channel formation with kaolin clay simulants similar to the material used by both Gauglitz et al. (2012) and in the tall column tests reported here. In column studies with a 14-ft-deep simulant bed, crack-shaped bubbles were

[1] The categorization of the material as weak, intermediate, and strong in this report (and this section in particular) refers to the shear strength of the material. The delineation between weak, intermediate, and strong is not formally defined but the approximate shear strength ranges are: weak (~10 Pa), intermediate (~100 Pa), and strong (~1000 Pa).

observed throughout the column and gas transport through connected bubbles also occurred throughout the column.

Based on these previous tests, the overall expected behavior in strong sludge materials is for bubbles to grow as slits and crack, at all depths, and interconnect to form pathways for gas release. A gas release channel may temporarily be blocked, but a local increase in the pressure of a gas bubble will either reopen the previously open channel or will expand by extending a fracture in some other direction and eventually connect with an open channel. While this behavior is expected at all depths, because bubbles should be able to expand and interconnect at all depths, the predicted closing of the gas release channels below d_{max} by van Kessel and van Kesteren (2002) is an uncertainty that needs to be evaluated. Based on available information in the literature, the d_{max} prediction has not been observed experimentally.

If van Kessel's and van Kesteren's theory is applicable to sludge waste tanks, it prevents waste transfers from continuing in order to avoid unsafe waste configurations. Thus, conducting tests to assess whether the predictions of d_{max} are relevant to sludge wastes is the overall objective of the tall column studies reported here. The objectives of the testing that support the overall objective are discussed in more detail in the next section.

2.0 Objectives

The principal objective of the tall column tests was to evaluate the accuracy of the d_{max} theory described by van Kessel and van Kesteren (2002) at a representative DST sludge depth. The tall column tests challenged the d_{max} theory directly by determining whether gas retention changes significantly at sludge depths below d_{max}. The overall testing objectives were as follows:

- Measure the retained gas (void) fraction in a column with a simulant depth and strength that is representative of a typical full-scale DST.
- Quantify the distribution of retained gas fraction as a function of depth to confirm or refute the applicability of d_{max} theory to full-scale DSTs.

In support of the two overall objectives, several supporting objectives were defined:

- Define a sludge simulant composition and gas generation method that will match typical shear strengths observed in DST waste and produce representative void fractions during testing. The gas generation method needs to be feasible to implement operationally and continue producing gas over the duration of a test, even after a peak or steady-state void fraction has been reached.
- Produce a correlation between ultrasonic attenuation and gas void fraction for the selected kaolin clay sludge simulants with shear strengths of approximately 500 to 1000 Pa; use these data to interpret the measurements made during the tall column tests.
- Develop a secondary (backup) measurement of gas void fraction at selected locations in the tall column to support ultrasonic measurements, such as a sampling method.
- Deploy cameras and/or video systems to directly observe and record the bubble morphology, retention, and gas transport behavior as a function of simulant depth over the full test duration.
- Measure gas generation rate or volume as a function of time to verify that gas is still being generated after a peak or steady-state surface level is achieved.
- After peak gas retention is achieved, increase the water layer depth above the clay simulant by approximately 5 to 10 ft and quantify, using video images, the downward motion of simulant due to compression of retained gas bubbles. Use the data to estimate the retained gas volume as a function of simulant depth.

Section 4.0 describes how the studies were used to satisfy the overall objectives and the supporting objectives. Testing and analysis to meet the objective described above were performed at the QA technology level of Applied Research (see Section 3.0).

There are important assumptions in the technical approach described in this document. The key assumptions, evaluated in later sections of the report, are as follows:

- The rheological and bubble-retention behavior of the sludge simulants used for the tests is assumed to be representative of radioactive tank waste sludge. Originally, work was planned to study the

behavior of actual waste compared to simulants as described in Fiskum and Daniel (2013)[1], but it was not completed due to budget constraints.

- The gas generation rates in the tall column experiments, which are orders of magnitude greater (see Yarbrough 2013, Meacham et al. 2014) than gas generation rates in Hanford tanks containing sludge wastes, do not significantly impact gas morphology, retention, and transport (i.e., similar gas phenomena occur in both the tall column and the waste tanks).
- No vessel-spanning bubbles were formed during the tests. This assumption, if incorrect, carries risk that test(s) did not generate data that support the objectives.
- Measurement of void fraction across the column diameter using ultrasonic sensors encompasses a large enough volume to be insensitive to local heterogeneities in bubble distribution. The uncertainty due to this assumption was assessed by performing correlation work with the ultrasonic sensors prior to tall column testing.
- Simulant gas retention behavior was not significantly influenced by protrusions or equipment (such as the camera column discussed in Section 6.1.2) that create asymmetries in the tall column. Instrumentation and equipment were designed to minimize protrusions into the tall column, but intrusions could not be completely eliminated.
- As gas is evolved in the tall column, an ultrasonic signal-to-noise ratio was achieved to produce interpretable data. This uncertainty was also assessed by performing correlation work.

[1] Fiskum SK and RC Daniel. 2013. *Gas Release Testing in AY-102 Sludge*. TP-DSGREP-013, Rev 0.0, Pacific Northwest National Laboratory, Richland, WA.

3.0 Quality Assurance

Work performed by Deep-Sludge Gas Release Event Project (DSGREP) staff is done in accordance with the *Support to Evaluation of Gas Release Mechanisms in Deep Sludge Project Quality Assurance Plan* (64405-QA-001). The DSGREP uses the WRPS Waste Form Testing Program (WWFTP) QA program (QA-WWFTP-001) at the Applied Research level as the basis for performing work. The WWFTP QA program implements an NQA-1-2000 Quality Assurance Program, graded on the approach presented in NQA-1-2000, Part IV, Subpart 4.2. This QA program and implementing procedures meet the quality requirements of NQA-1-2004, NQA-1a-2005, and NQA-1b-2007 as provided in the statement of work authorizing PNNL to conduct these studies.[1] When needed, analyses performed by the Analytical Support Operations (ASO) organization are conducted under the ASO QA Plan, which complies with the requirements of Hanford Analytical Services Quality Assurance Requirements Documents (HASQARD) and NQA-1.

Table 3.1 lists the implementing procedures identified in the WWFTP QA program plan (QA-WWFTP-001) that govern the work conducted under this study. Listed below is a summary of key procedures.

- All staff members contributing to the work described in this report received proper technical and QA training prior to commencing quality-affecting work in accordance with QA-NSLW-0201, *Training.*
- The planned studies were conducted in accordance with QA-NSLW-1102, *Scientific Investigation for Applied Research*.
- The studies were planned and conducted in accordance with QA-NSLW-1104, *Test Plans*, and QA-NSLW-1107, *Test Instructions*.
- Test materials and samples were identified and controlled in accordance with QA-NSLW-0801, *Item Identification and Sample Control.*
- Measuring and testing equipment used to generate quality-affecting data was properly procured, controlled, calibrated, handled, and maintained in accordance with QA-NSLW-1201, *Calibration and Control of M&TE*.
- All data and calculations used in this report were reviewed in accordance with QA-NSLW-1108, *Data Entry and Data Review*, QA-NSLW-0301, *Management of Electronic Data*, and QA-NSLW-0304, *Calculations*.
- This technical report was generated in accordance with QA-NSLW-1109, *Reporting*, and an independent technical review was performed and documented in accordance with QA-NSLW-0601, *Document Preparation and Change*, and QA-NSLW-0603, *Independent Technical Review.*

[1] This program has been independently evaluated by Acquisition Verification Services (AVS) of Mission Support Alliance (MSA) to specified requirements of NQA-1:2004 (including NQA-1a-2005 and NQA-1b-2007 Addenda) and is operating under a WRPS-approved Supplier Quality Assurance Program Implementation Plan (SQAPIP) (QA-WWFTP-002).

Table 3.1. QA Implementing Procedures (from QA-WWFTP-001)

Document Number	Title
QA-NSLW-0201	*Training*
QA-NSLW-0202	*Surveillances*
QA-NSLW-0203	*Management Assessments*
QA-NSLW-0301	*Management of Electronic Data*
QA-NSLW-0302	*Software Control – Applied Research*
QA-NSLW-0304	*Calculations*
QA-NSLW-0305	*Safety Software*
QA-NSLW-0401	*Control of Procurements*
QA-NSLW-0501	*QA Implementing Procedures*
QA-NSLW-0601	*Document Preparation and Change*
QA-NSLW-0602	*Document Control*
QA-NSLW-0603	*Independent Technical Review*
QA-NSLW-0801	*Item Identification and Sample Control*
QA-NSLW-0901	*Special Processes*
QA-NSLW-1001	*Inspections*
QA-NSLW-1102	*Scientific Investigation for Applied Research*
QA-NSLW-1104	*Test Plans*
QA-NSLW-1106	*Operating Procedures*
QA-NSLW-1107	*Test Instructions*
QA-NSLW-1108	*Data Entry and Data Review*
QA-NSLW-1109	*Reporting*
QA-NSLW-1110	*General Documents*
QA-NSLW-1201	*Calibration and Control of M&TE*
QA-NSLW-1301	*Handling and Storage*
QA-NSLW-1401	*Status and Tagging*
QA-NSLW-1501	*Nonconformances*
QA-NSLW-1502	*Deficiency Reporting*
QA-NSLW-1601	*Significant Quality Issues*
QA-NSLW-1602	*Trending*
QA-NSLW-1701	*Record System*
QA-NSLW-1801	*Project Audits*

4.0 Technical Approach and Analyses

The tall column tests were designed to empirically challenge the d_{max} theory by directly observing regions of a sludge simulant layer that were below the predicted d_{max} values. However, given the scale and complexity of the tests, only a limited number of tests were conducted. A number of analysis approaches were developed and implemented to get the maximum amount of data from the tests.

The following sections discuss the technical approach for conducting the tall column tests and the data analysis techniques used to estimate void fraction. Section 4.1 describes the test strategy and test matrix. Section 4.2 describes how estimated values of d_{max}, based on target parameters for the tall column tests, were generated. Section 4.3 outlines how observations of gas transport and analysis methods for generating estimates of void fraction in the tall column were used to assess the gas retention behavior, and more specifically, if they supported or undermined the theory of van Kessel and van Kesteren (2002). More detailed descriptions of the testing, including equipment and operations, are provided in Section 6.0.

4.1 Tall Column Tests: Strategy and Test Matrix

The tall column tests were conducted using typical DST simulant depths and shear strengths. The tests involved large-scale equipment but were performed without the benefit of a shakedown period or other large-scale preliminary tests. Thus, selecting the tests that were performed and the order in which they occurred required careful consideration of the balance between technical and operational factors. The primary technical consideration was conducting tests that obtain defensible, quality data on gas retention behavior as a function of waste depth. In particular, tests needed to challenge the predictions of the d_{max} theory, which are discussed in more detail in the next section, for the simulant depths that were planned to be tested. The primary operational concerns were minimizing column or equipment reconfiguration (loading the simulant, cleaning out the column, etc.), performing the tests safely, and avoiding upset conditions that render a test unrepresentative or the data unusable. The test matrix had to balance technical need and operational risk while selecting test conditions (simulant shear strength, test method) and test order. The uniqueness of the experimental program also warranted a flexible test strategy.

Originally, two methods of conducting the test were planned. In the first, the sludge simulant is mixed to a target shear strength and loaded in a single batch to full-scale DST sludge height. The simulant then generates gas until steady-state or peak gas retention is achieved (observable via changes in liquid level height). In the second method, the sludge simulant is loaded in two stages. In the first stage, it is loaded to approximately half of the full-scale DST height. This initial sludge layer generates gas until steady-state or peak gas retention is achieved, and then a second layer (of simulant at the same shear strength) is added on top of the first layer to represent the actual sequence that occurs during waste retrieval operations. In aggregate, the total layer height after the second stage will be the full-scale DST height (the same as the initial height in a single-batch test). The second layer then begins generating gas until a second steady-state or peak gas retention is achieved. The second method was initially intended for a planned but optional test or tests, but due to the complexity of operations and the uncertainty that any additional data of interest would be acquired in a two-load test, this method was not implemented.

The most significant technical results of the tall column tests were observations and measurements of gas retention behavior at depths below d_{max}. The target sludge depth in the planned experiments was

fixed to that of a typical DST. Therefore, using a sludge simulant with lower shear strength was a more definitive test of the d_{max} theory, since d_{max} has a leading order proportionality to shear strength (see Section 4.1). A lower-shear-strength sludge simulant, if used in a tall column experiment, has a smaller predicted value of d_{max}. Consequently, there would be more observable sludge depth in which to determine gas void below d_{max} than there would be at higher shear strengths. For this reason, tests with a target shear strength of 500 Pa were planned, as they represent the best test of the theoretical prediction while still using shear strengths that are similar to DST waste(s). Note that 500 Pa would be similar to material near the top sludge layers in AN-101 and AN-106 (see Follett [2014], which presents recent cone penetrometer measurements in these two DSTs).

However, a shear strength of approximately 1000 Pa was considered more representative of sludge waste in DSTs, i.e., closer to the median shear strength observed historically, and more recently, in the receiver tanks AN-101 and AN-106. Given this, at least one test with 1000 Pa shear strength was also planned. Depending on the parameters used to estimate d_{max}, the tall column had several feet of simulant depth below d_{max} even at a shear strength of 1000 Pa, so the gas retention behavior could still be observed above and below d_{max} in the tall column.

Shear strengths greater than 1000 Pa, which would further probe the DST waste shear strength parameter space, were considered. There were concerns about handling simulants of strengths >1000 Pa with the equipment that was available to mix and move the simulant. Another concern was the potential for the occurrence of process upset conditions. One upset condition in particular that was evaluated against the test design and parameters was the formation of a vessel-spanning bubble (VSB) in the tall column during the generation of gas in the simulant. In the event of a VSB, the test would no longer be representative of the physical phenomenon of interest and the data collected would not satisfy the test objectives. A VSB is also a potential hazard and should be mitigated once it is detected. Thus, the test would have to be discontinued immediately. It is important to point out that a VSB in the tall column experiment would be an artifact of the test design; it would not be reasonable to expect a VSB to also occur in a much larger vessel, e.g., a 75-ft-diameter DST.

Predictions for the conditions under which a VSB would occur were developed based on experimental measurements made by Epstein and Gauglitz (2010) and Gauglitz et al. (2010). These predictions were based on empirical stability criteria for the gravity yield parameter, Y_G. The gravity yield parameter is the dimensionless ratio of the force necessary to yield the sludge to its weight, defined as

$$Y_G = \frac{\tau_s}{\rho_s g D} \ , \tag{4.1}$$

where τ_s is the shear strength of the sludge, ρ_s is the sludge density, g is gravitational acceleration, and D is the vessel diameter. The sludge simulant selected for use in the tests was a kaolin-water slurry (discussed in more detail in Section 5.0). Both the shear strength and density of the sludge were estimated using previously established correlations (see Gauglitz et al. 2010, 2012) for shear strength of a kaolin slurry, for example

$$\tau_s = 0.018 e^{\left(0.1915 (x_k \times 100)\right)} \ , \tag{4.2}$$

where x_k is the mass fraction of the kaolin in the simulant. For a given shear strength, the density of the sludge (assuming the balance is water) was calculated. Thus, Y_G was computed for various column diameters using Equation 4.2.

The criterion for stability of a VSB ranges from 0.04 to 0.12. The recommended value from Epstein and Gauglitz (2010) is $Y_G = 0.09$, but testing across several vessel diameters in Gauglitz et al. (2010) suggested that Y_G could be as low as 0.04 and may also depend on H/D, where H is the height of sludge in the vessel (note that for the tall column $H/D \sim 5$). To ascertain whether a VSB might occur, a range of stability criteria were plotted, formulated as the minimum vessel diameter where the sludge would be stable (no VSB) as a function of shear strength. This result is given in Figure 4.1. For a given value of Y_G, a vessel with a diameter larger than the minimum at a given shear strength would not be expected to have a VSB.

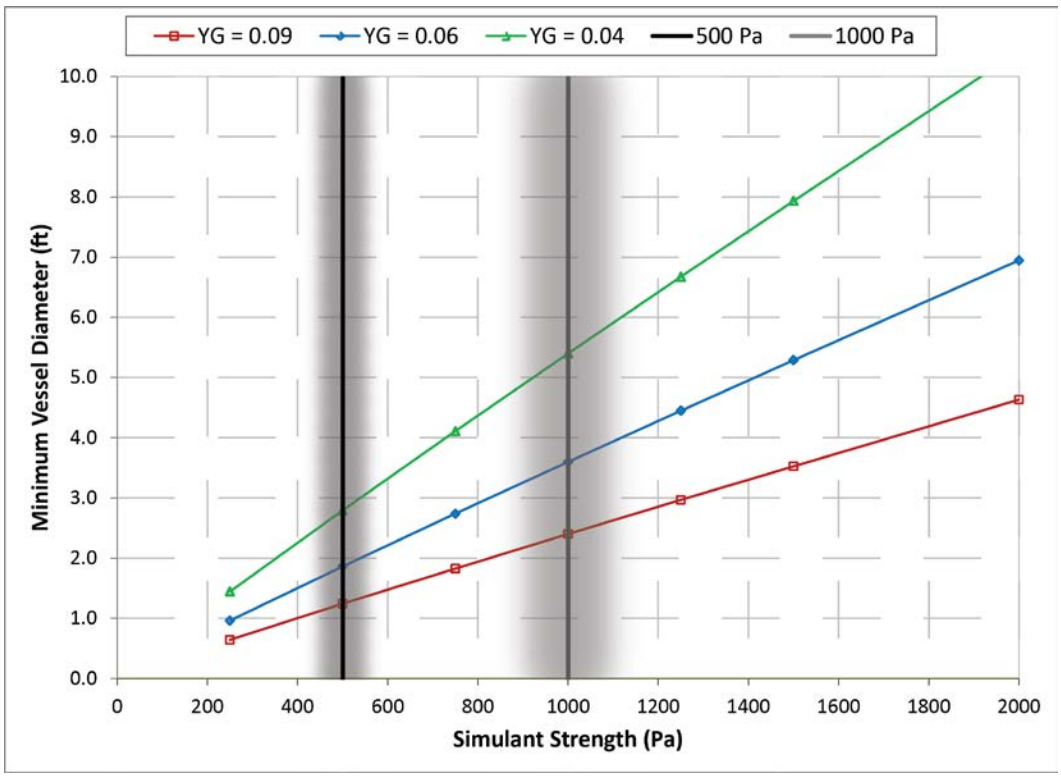

Figure 4.1. Vessel-Spanning Bubble Stability Criterion as a Function of Simulant Strength (Pa). The vertical lines are for two simulant strengths and the shaded area is ±10% (representing uncertainty in simulant formulation and actual shear strength distribution in the column).

Figure 4.1 demonstrates that the uncertainty in the gravity yield parameter Y_G results in a wide range of minimum vessel diameters. Compared against the specified diameter of the tall column, which was 5 ft, a VSB was not expected at 500 Pa even if the appropriate value for Y_G was 0.04. This remains true even when accounting for the presence of the 1 × 1 ft square column[1] inside of the 5 ft column, which reduced the effective D to 4 ft (i.e., the behavior is controlled by the smallest effective diameter).

[1] This is the viewing column that housed the cameras used to observe the simulant directly during testing. The viewing column and its configuration are discussed in more detail in Section 6.0.

Avoiding stable VSBs in a 1000 Pa simulant was less certain. For a Y_G = 0.06, a VSB was not expected if the effective D is ~ 4 ft or larger, but a VSB could become stable for a vessel with an effective D of 4 ft if the simulant compacted such that some regions of the simulant had τ_s > 1000 Pa. For values of Y_G < 0.06, which were difficult to rule out, especially if Y_G decreases with vessel scale as the results suggest, and/or compaction of the simulant resulted in shear strengths >1000 Pa, the results predict the formation of a stable VSB. The risk of a VSB occurring would be aggravated by the two-stage loading method, which creates an interface between two sludge layers where gas can be trapped and grow to form a VSB (this being another reason why the two-stage loading method was not performed). Increasing the vessel diameter reduces the risk of a VSB; however, the diameter of the tall column was limited to 5 ft due to other constraints such as heating and instrumentation requirements and the challenges of preparing and loading large simulant batches.

The planned tall column tests, to varying degrees, satisfied technical needs and had some probability of a VSB (negligible for 500 Pa, very small for 1000 Pa) or another process upset. Based on weighing these factors, a test matrix was proposed that is shown in Table 4.1. The rationale for conducting the tests in the order given in Table 4.1 can be summarized as follows:

- A test (Test 1) with a sludge simulant of 500 Pa shear strength that involved only a single load was chosen to be conducted first because it is the most definitive test of d_{max}, was the easiest to conduct operationally, and had the smallest risk of a VSB. To get some information as quickly as possible, this test was planned to be conducted when the column was ready for testing even if all the planned instrumentation was not yet available for deployment. The minimum instrumentation required to perform a test were the load cells that track the column mass and the video cameras.
- For all the same reasons as above, the 500 Pa single-load test was selected to be repeated (Test 2) with full instrumentation. This provided the opportunity to correct any issues identified during the first test and confirm the result with all instruments operational.
- The third and final test (Test 3) was chosen to be performed with a 1000 Pa shear strength simulant, added in a single load. This was more risky (it carried a higher probability of a VSB occurring and the stronger simulant was more difficult to mix and load) than the 500 Pa tests, but not as risky as a double-load test (highest probability of having a VSB and more complicated to load simulant into the column a second time), and it still permitted observation of gas release behavior at depths near to or greater than d_{max}. It was a test with a target shear strength more representative of DST waste than Tests 1 or 2.
- The fourth and fifth tests (considered optional) are shown in the test matrix for completeness but they were not planned to be attempted. It was unclear if tests of that nature would have additional technical benefit. Some flexibility was intentionally built in, in the event that the results of Tests 1–3 required modifications to the approach. For example, if a VSB had occurred in Test 3, Test 4 could have been modified to be a second attempt of Test 3 conditions or the shear strength could have been decreased slightly.
- Note that aside from simulant handling concerns at shear strengths >1000 Pa, Figure 4.1 also shows that higher simulant τ_s further increases the risk of a VSB occurring in a test. With the risk of a VSB added to the operational uncertainty and the observation that testing the d_{max} theory does not necessitate going to higher τ_s, tall column tests with τ_s >1000 Pa were not planned.

The test matrix in Table 4.1 was devised with the above rationale in mind. It describes a test strategy that collected the most critical data first at the lowest operational risk, then sought to confirm that data at the same conditions before conducting a final test (that was more challenging and had higher risk). Tests considered to have limited additional benefit relative to their complexity were ultimately discarded from the test matrix as indicated.

Table 4.1. Planned Tall Column Test Matrix

Test Number	Target Shear Strength (Pa)	Target Total Waste Depth (in.)	Simulant Loading	Instrumentation Level
1	500	310	Single load to 310 in.	Partial[(a)]
2	500	310	Single load to 310 in.	Full
3	1000	310	Single load to 310 in.	Full
4 [np][(c)]	1000[(b)]	310	Double load[(b)]: first to 170 in., second to 310 in.	Full
5 [np][(c)]	<1000	310	Double load: first to 170 in., second to 310 in.	Full

(a) Minimum level of instrumentation required was the load cells and video cameras. Ultimately Test 1 (see Section 7.1) had all instruments installed except the pressure transducers.

(b) During test planning, the option of revising the shear strength and loading approach was dependent on results of Tests 1–3. Ultimately these tests were not conducted, see note (c).

(c) Optional tests that were not performed [np]. Given the outcomes of Tests 1–3, it was not necessary to perform more complex tests to support the objectives. They are shown here for completeness.

The nature of the full-scale tall column testing made it difficult to modify the test approach to respond to off-target parameters. Repeating a test that failed to have parameters within an acceptable range was also not desirable for the same reason. Thus, the acceptance criteria or requirements for the key test parameters were designated to be as broad as possible, while still resulting in a set of tests that accomplished the objectives. The important test parameters and the criteria that apply to each are given in Table 4.2. The shear strength acceptance criterion for each test, in particular, was wide enough to account for the uncertainty in mixing the simulant in large quantities, obtaining a representative sample, and errors in the shear strength measurement itself.

Table 4.2. Parameter Requirements or Acceptance Criteria for Tall Column Tests

Quantity (Purpose of Measurement)	Requirement or Acceptance Criterion
Simulant Solids Content (Batch Quality)	As-made-up solids content within ± 1.0 wt% of recipe
Simulant Shear Strength for d_{max} Sludge Column Tests (Target Parameter)	Tests 1 and 2: 350 – 800 Pa [500 Pa target] Test 3: 800 – 2000 Pa [1000 Pa target]
Simulant Temperature, T (Operating Condition)	Preferred: $72 \le T \le 78$ °F ($22.2 \le T \le 25.6$ °C) Acceptable: $\Delta T < 10$ °F (5.5 °C) over a 24-hour period, i.e., hold simulant temperature approximately constant. Note: Controls were established during simulant mixing to restrict simulant temperature before loading into the column.
Simulant Layer Thicknesses For Tall Column Tests (Representative of DST)	The simulant shall be loaded into the tall column to a depth of 310 ± 10 in. for a single-load test.
Gas Generation Rate for d_{max} Sludge Column Tests (Test Characteristic)	No requirement; gas generation rate was measured. Expected to be 3 to 6 L/min based on previous experiments.
Gas Void Fraction (Test Characteristic)	In each test, measure void fraction, at minimum, at one simulant depth above and below d_{max} both initially and after steady-state or peak void fraction has been achieved.

4.2 Estimation of d_{max} for Target Parameters

The tall column tests were devised to have target sludge depths greater than or equal to the expected depths that will be reached in the AN-101 and AN-106 DSTs. In these tall column tests, a 5 ft (1.52 m) inside diameter steel column was filled with gas-generating sludge simulant to a depth greater than the target of 310 in. (25.8 ft, 7.9 m). The target simulant depth was chosen to represent a full-scale DST sludge depth, specifically that of tank AN-101 (Uytioco 2010).[1] The expected test behavior was that gas bubbles form in the simulant and the sludge column expands, increasing the simulant height beyond its initial level. The column height should continue increasing until the rate of gas release from the top surface of the simulant column equals the rate of gas generation in the simulant. At or near this point, the simulant reaches a peak void fraction, i.e., retains a maximum amount of gas. Based on this expectation, assessing the gas retention behavior at or near peak void fraction was important data that either supports or does not support d_{max} theory. Note that the peak void fraction may not necessarily result in a steady-state column height, as the simulant can compact over time as the kaolin solids consolidate.

To properly observe and collect data on gas retention behavior, the tall column tests were designed to ensure that the initial (target) sludge simulant height was significantly greater than d_{max}. Thus, if d_{max} theory is correct, these tests should reveal a significant change in the simulant's gas retention behavior at depths deeper than d_{max}. At depths shallower than d_{max}, the theory predicts that a network of connected channels forms that allow generated gas to escape. At depths deeper than d_{max}, the theory predicts the absence of a connected-channel network and, consequently, a much higher volume fraction of retained gas. Thus, it was important to assess the theoretical prediction of d_{max} for the tall column experiments.

[1] The reference gives a maximum final (post-additions) sludge depth of 303 in., which is rounded up to 310 in. for the tall column experiments. This is consistent with the approach taken in Rassat et al. (2014) – see, for example, Section 4.2.1 in that report.

The value of d_{max} was predicted by the following equation from van Kessel and van Kesteren (2002):

$$d_{max} = \frac{\tau_s(1+e)}{K_0(\rho_p-\rho_w)g} \times \left[1 + \ln\left(\frac{r_0^2-d_f^2}{d_f^2}\right) + \ln\left(\frac{E}{2\tau_s(1+\nu)}\right)\right] \quad (4.3)$$

where τ_s = undrained shear strength (note this is written c_u in the original work)
e = void ratio (e.g., ρ_p/ρ_w)
K_0 = ratio between horizontal and vertical effective stress
ρ_p = dry (material) density of the sediment particles
ρ_w = water density
g = gravitational acceleration
r_0 = radius of the undisturbed channel
d_f = average floc size
E = modulus of elasticity
ν = Poisson's ratio

For the tall column tests an estimate of d_{max} was generated using Equation 4.3 and the target conditions. In order to adequately test the validity of d_{max} theory, the physical properties in Equation 4.3 needed to be carefully identified for the kaolin simulant used in this work. These can be compared to d_{max} values calculated using as-measured properties from each test, which are presented in Section 7.0. The shear strength (τ_s) was a target parameter in the experiments, and the weight fraction kaolin was adjusted to target a shear strength of 500 or 1000 Pa. The void ratio (e) was calculated based on the known weight fraction solids and the densities of kaolin and water; for the planned simulants the values of e were 2.31 for the 500 Pa simulant and 2.00 for the 1000 Pa simulant. According to Wells et al. (2010, Figure 3.1), values for kaolin/water K_0 range from about 0.4 to 0.75, depending on the simulant shear strength and for τ_s = 500 to 1000 Pa the data predicts K_0 ranging from 0.48 (minimum) to 0.70 (maximum). The dry density of kaolin particles (ρ_p) is 2650 kg/m^3 (Wells et al. 2010) and the density of water at room temperature (ρ_w) is 998 kg/m^3 (Lide 2003). The radius of the undisturbed channel was taken to be 0.5 cm based on both visual observations of typical gas channel sizes (Gauglitz et al. 2012) and on the r_o used by Crosato (1998) for d_{max} calculations.

The average floc size (d_f) has not been measured at PNNL for kaolin/water mixtures. However, d_f must, at minimum, be larger than the mean particle size of kaolin, which is approximately 5.5×10^{-6} m (Bontha et al. 2010). To generate a conservative estimate of d_{max} for the testing, $d_f = 5.5 \times 10^{-6}$ m was used. This approach is conservative since smaller values of d_f result in increased values for d_{max}. Note that the floc size used by van Kessel and van Kesteren (2002) was 200×10^{-6} m.

A typical or representative value of the floc size of kaolin in water was also used to develop a "representative" estimate of d_{max}. Some data on the floc size of kaolinite are available in the literature. However, floc size is a function of the environment in which the kaolinite resides, for example: pH, ionic strength, presence of other chemicals, and shear rate (various aspects of these issues are summarized in Mietta 2010 and Son and Hsu 2009). This list is not exhaustive but represents the complexity involved in determining d_f. Despite this limitation, measurements given by Mietta (2010) on kaolin in water suspensions support a $d_f > 50 \times 10^{-6}$ m for a wide array of conditions. In particular, measurements of

mean floc size are shown to approach 100×10^{-6} m when the kaolin is suspended in water with a pH ~4, which most closely represents conditions for the sludge simulants used in the planned testing.

A theoretical prediction of mean floc size has also been suggested by Khelifa and Hill (2006), with a similar prediction presented by Maggi et al. (2007) that is calibrated against empirical data for flocculated kaolinite minerals. The prediction of Maggi et al. (2007) is expressed as

$$d_0 = \delta \left(\frac{L}{L_p}\right)^{\xi}, \tag{4.4}$$

where d_0 is the capacity dimension (also called the fractal or Housdorff dimension), L is the floc size, and L_p is the primary particle size. The quantities δ and ξ were estimated by data fitting to have values of 3 and -0.1, respectively. Following the approach of Mietta (2010), the capacity dimension for kaolin was estimated to be 2.0, which is a typical value for sediments from estuaries and coastal waters (see Winterwerp 2002). Using Equation 4.4 and a value of $L_p = 5.5 \times 10^{-6}$ m (i.e., the d50 of kaolin), L was estimated to be 317×10^{-6} m. Using a value of $d_0 = 2.2$, which is on the upper end of the typical range for cohesive sediments, $L = 122 \times 10^{-6}$ m. These predicted values added some confidence that d_f was likely to be closer to 100×10^{-6} m or greater. However, to avoid underestimating d_{max} based on the uncertainty surrounding the value of d_f, a typical value for kaolin floc size was taken to be 50×10^{-6} m.

Values for E and ν were estimated from τ_s using a correlation given in Wells et al. (2010) for shear modulus. The quantity $E/2(1+\nu)$ is equal to the shear modulus, so the shear modulus estimate from Wells et al. (2010) was used in place of this expression in Equation 4.3. By interpolating based on the data in Figure 3.5 (also given in Table 3.2) from Wells et al. (2010), the shear modulus for a τ_s = 500 Pa kaolin/water mixture was approximately 105 to 115 kPa, and for τ_s = 1000 Pa the shear modulus was 350 to 400 kPa. The values for shear modulus obtained by interpolation depend on the selection criteria used to define the data set. Accounting for this uncertainty, conservative values for the shear modulus are 120 kPa and 410 kPa, respectively.

Table 4.3 shows various calculated values for d_{max} based on different assumptions for the various parameters (K_0, d_f, and τ_s) in Equation 4.3. Calculations are included using a range of K_0 spanning the minimum (0.48), median (0.62), and maximum values (0.70). The d_f values are conservative (5.5×10^{-6} m) or an estimate of a "representative" d_f (50×10^{-6} m) based on data in the literature.[1] The calculated d_{max} values for a 500 Pa sludge simulant range from about 2.29 m (7.52 ft) to as high as 4.32 m (14.17 ft). The best-estimate d_{max} (based on $d_f = 50 \times 10^{-6}$ m, $K_0 = 0.62$) for 500 Pa is 2.61 m (8.56 ft). Recall that the sludge simulant height planned for these tests was 310 in. (25.8ft), which is greater than all the d_{max} values in Table 4.3 for 500 Pa, so the simulant was deep enough to allow observation of a change in gas retention behavior at depths below d_{max}.

The 1000 Pa sludge simulant had a larger calculated d_{max}, with values ranging from 4.29 m (14.07 ft) to 8.02 m (26.33 ft). The best-estimate d_{max} (based on $d_f = 50 \times 10^{-6}$ m, $K_0 = 0.62$) for 1000 Pa is 4.88 m (16.02 ft). Provided the predicted d_{max} for the 1000 Pa strength was approximated well by the best estimate, the 25.8 ft simulant depth was also deep enough to observe changes in gas retention behavior.

[1] It is worth noting that even the representative value is still conservative relative to the body of flocculation diameter measurements available in the literature for kaolin in water.

However, the most conservative estimate of d_{max} was on the order of the planned sludge height in the column. If the input parameters used to generate the conservative estimate accurately capture the physics governing the predictions of d_{max} theory (which was not expected), a test with 1000 Pa simulant would not have a sludge depth below which different gas retention behavior would be expected.

The validity of d_{max} theory was assessed against the predictions in Table 4.3 by measurements of gas void as a function of height. Gas fractions were assessed using several methods that are described in Section 4.3. Based on the data observations, the tall column tests either supported or did not support the theory of van Kessel and van Kesteren (2002).

Table 4.3. Calculated d_{max} for Various Assumed Input Parameter Values

Sludge Simulant Strength[(b)]	d_f = 5.5 micron, d50 of kaolin[(a)]		d_f = 50 micron, an estimated value	
	500 Pa	1000 Pa	500 Pa	1000 Pa
d_{max}, K_0 = 0.48	4.32 m	8.02 m	3.37 m	6.31 m
	14.17 ft	26.33 ft	11.06 ft	20.70 ft
d_{max}, K_0 = 0.62	3.34 m	6.21 m	2.61 m	4.88 m
	10.97 ft	20.38 ft	8.56 ft	16.02 ft
d_{max}, K_0 = 0.70	2.94 m	5.46 m	2.29 m	4.29 m
	9.64 ft	17.90 ft	7.52 ft	14.07 ft

(a) The d50 of kaolin particles is the most conservative value possible for mean floc diameter.
(b) Target sludge simulant strengths to be tested.
Note: Range of K_0 covers minimum, median, and maximum values determined from available data.

4.3 Gas Retention and Void Fraction Analyses

4.3.1 Observations of Gas Transport in Cohesive Sediments

As noted in Section 2.0, one of the supporting objectives was to directly observe bubble morphology and gas retention behavior in the tall column experiments. Though visual observation is a qualitative measure of how gas is retained and released in the simulant, it was the most direct method of investigating the behavior in the sludge. The bubble morphology that develops as gas is generated is also an important part of the framework upon which the d_{max} theory is built. The theory assumes that cylindrical channels form, with radius r_0. These channels remain open (and potentially expand if the gas generation rate is great enough) to permit the transport of gas and interstitial fluid (Crosato 1998). The gas and fluid (as the sediment consolidates) both tend to move upward toward the surface as long as the channel remains open. Open channels may be fed by other tributary channels that are also cylindrical. However, channels that are closed, i.e., suffer a reduction in radius down to the flocculation diameter d_f, will not permit transport of gas. Pockets of void below these closed channels would be expected to have a different morphology as they would have no place to escape and would continue to retain gas.

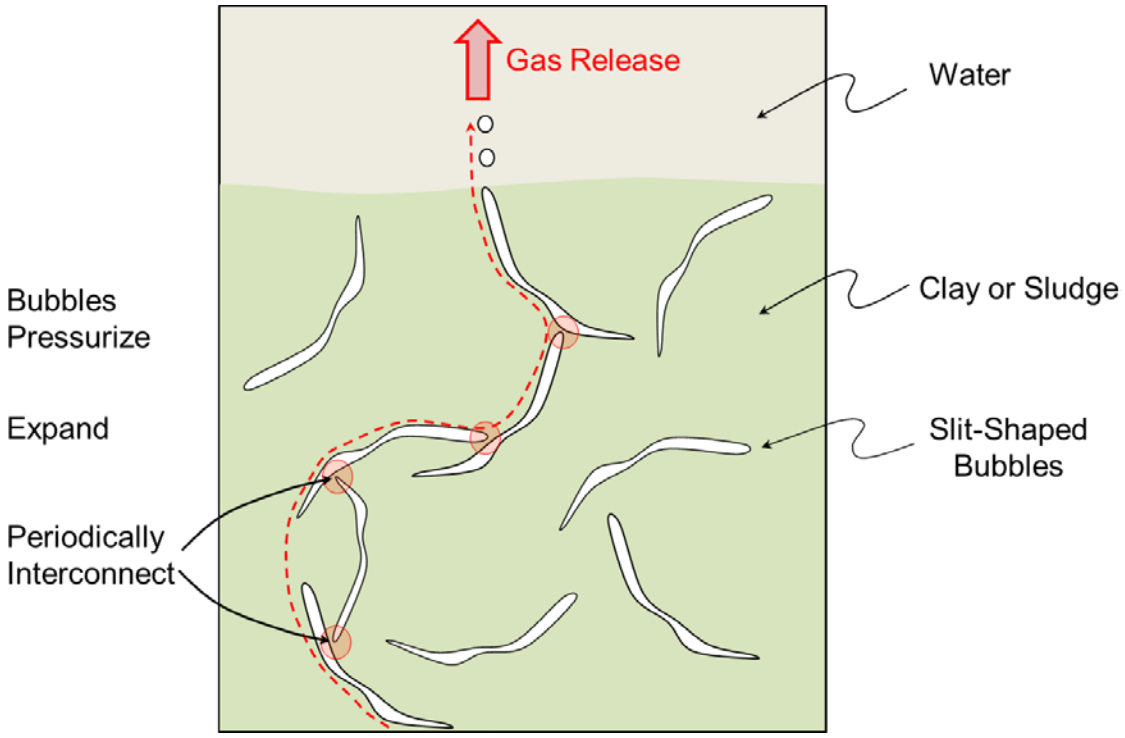

Figure 4.2. Diagram Illustrating the Anticipated Gas Release Mechanism That Dominates Gas Transport in Deep Sludges or Finely Grained Cohesive Simulants

In contrast to a series of cylindrical channels, the anticipated gas release mechanism was expected to be more dynamic, as discussed in Section 1.1. Figure 4.2 illustrates the dominant gas release mechanism that was expected to be observed in the tall column experiments. The bubbles begin to grow and will eventually form slits and cracks as enough gas is generated locally. The slit or crack-like shape evolves as the gas builds up enough pressure to yield some of the sediment particles around it and occupy the space vacated by them. These slit-shaped bubbles have been observed in previous PNNL work (Gauglitz et al. 1996, 2012) and in other studies of cohesive sediments (Sills and Gonzalez 2001; Best et al. 2004; Winterwerp and van Kesteren 2004; Boudreau et al. 2005; Algar et al. 2011a; Boudreau 2012). The slit-shaped bubbles may be connected over significant length scales but, in this conceptual model, do not necessarily have to be interconnected constantly to transport gas. The gas can periodically generate enough pressure locally to expand in regions where slit-shaped bubbles are in proximity, thereby migrating upward through the network of slits and cracks as shown in Figure 4.2. A similar mechanism has been proposed for marine wetland or seafloor sediments (e.g., Algar et al. 2011b; Jain and Juanes 2009) and gassy soft soil (Sills and Gonzalez 2001). Algar et al. (2011b) suggest that fractures or cracks transporting gas can be partially annealed and provide a preferential path for further transport. Regardless, this type of gas transport would be expected to be manifested visually as bubbles "stopping and starting" while they periodically cross between various slits and cracks. Note that gas evolution by this process does not require stagnant slits and cracks, but could facilitate gas transport provided there were enough slits in proximity to one another to periodically permit the movement of gas.

Thus, if only visual observation was available to assess gas retention in the tall column experiments, the validity of the d_{max} theory could be judged based on observed gas morphology and transport. If the d_{max} theory was supported by the experimental observations, it was expected that long, connected channels would form above a certain depth and remain relatively static while transporting gas to the

surface. Below this depth another, unknown bubble morphology would be observed and there would be minimal gas transport. If gas bubbles are observed to form arrays of slits and cracks that do not appear continuous over long distances, but gas is still being evolved from the simulant, the fundamental framework of d_{max} theory would be violated. The theory would further be called into question if there was no perceivable change in gas morphology at elevations predicted to be below d_{max} in the column.

4.3.2 Estimating Bulk Void Fraction

As gas is generated in the tall column experiments, it expands the simulant matrix around it and forces it to rise upward. Collectively, all the gas in the simulant increases the simulant level by an amount proportional to the volume fraction of gas that is present. To get a more accurate measure of the changes in level, a water layer was placed on top of the simulant. The bulk void fraction during the test is related to the initial void fraction and the water layer position as a function of experimental elapsed time *t* via the expression

$$\phi_{bulk} = \frac{\phi_o h_{s,o} + (h_{w,t} - h_{w,o})}{h_{s,t}}, \tag{4.5}$$

where ϕ_{bulk} is the bulk void fraction, ϕ_o is the initial void fraction at time = 0; $h_{s,t}$ and $h_{s,o}$ are the slurry simulant levels at t = t (current elapsed time) and 0, respectively; and $h_{w,t}$ and $h_{w,o}$ are the water levels at t = t (current elapsed time) and 0, respectively. As discussed in Section 7.0, except for the initial slurry level at time = 0, the slurry level as a function of time, $h_{s,t}$ used in Equation 4.5 was very uncertain and could not be accurately determined during each of the tall column tests. Due to a lack of acceptable slurry level data as a function of time, ϕ_{bulk} was approximated by using the initial slurry simulant level, $h_{s,o}$, as an estimate for $h_{s,t}$. With this approximation, the measurement of the bulk void is calculated with the following expression:

$$\phi_{bulk} = \phi_o + \frac{(h_{w,t} - h_{w,o})}{h_{s,o}}. \tag{4.6}$$

Depending on whether the slurry height as a function of time is larger or smaller that the initial height, the bulk void fractions approximated by Equation 4.6 overestimates or underestimates the actual void fraction. Early in the tests when the majority of the void was generated, the slurry height was larger than the initial height, and Equation 4.6 slightly overestimates the bulk void. The bulk void calculation in Equation 4.6 can be simplified to using level changes because a level-volume correlation was performed that demonstrated that the volume changes constantly with height in the tall column apparatus (discussed further in Section 6.0). The level (height) measurements were taken throughout the test. The initial void is the estimate of the amount of void present in the simulant at t = 0 as the experiment begins. It is computed by using the level-volume correlation of the column, i.e.,

$$\phi_o = 1 - \frac{\rho_o}{\rho_{act}} = 1 - \frac{M_{s,o}/V_{s,o}}{\rho_{act}}, \tag{4.7}$$

where ρ_o and ρ_{act} are the initial (implied) and actual (using as-measured quantities for the gas-free simulant) densities of the simulant when it is loaded into the column. The initial density is calculated by taking the ratio of the mass of slurry simulant measured by the load cells ($M_{s,o}$) and using the initial

simulant level to calculate the initial volume ($V_{s,o}$). Since there is some uncertainty in the calculation of the actual density of the gas-free simulant, the initial void was calculated as a range, i.e., $\rho_{act,min} \le \rho_{act} \le \rho_{act,max}$, which results in $\phi_{o,min} \le \phi_o \le \phi_{o,max}$, all calculated using Equation 4.7. Note that the minimum and maximum values were not typically symmetric about the central value of ϕ_o.

The bulk void fraction allows tracking of the global void growth in the simulant with time. It does not, by itself, distinguish the gas retention behavior of the simulant with depth. However, if there was a lower region in the column where higher gas fractions were being retained and not being transported to the simulant surface, the bulk void fraction would continue to rise with time. The increase would continue until it became visually obvious that there was more gas at lower elevations than at higher elevations (which, if d_{max} theory is correct, would have relatively stable amounts of gas/void) or an instability would occur due to a large density difference in the sediment (likely leading to a sudden drop in level as a significant quantity of gas escapes). Conversely, the bulk void fraction could stabilize (or at least not continue to increase) with time even though gas continues to be released from the simulant. Therefore, the bulk void time series cannot by itself specify the gas retention behavior, but it can help support other data and observations in confirming or refuting d_{max} theory.

The bulk void fraction during tall column testing is also a helpful benchmark for assessing the measurements of void fraction as a function of simulant depth presented in the next section. The various methods can be integrated with height and compared against the bulk void fraction to get an idea of their accuracy. The integration of the void fraction data is subject to some uncertainty due to the relatively low resolution in elevation since the methods are based on no more than 10 discrete heights in the column. Nevertheless, method(s) that are in good agreement with the bulk void computed by Equation 4.6 will be considered more representative of the actual void profile in the column.

Equation 4.6 describes an instantaneous measure of bulk void fraction. A second estimate that is a discrete measure in time was originally discussed in Powell et al. 2014 (see Equation 3.4 and surrounding text). This calculation method uses the data from compression of the simulant, which was performed in each tall column test at the end of data collection, to iteratively solve for the bulk void fraction at the time compression was performed. Note that the equation was derived assuming zero friction between the simulant and the column, and the gas is assumed to undergo isothermal compression as an ideal gas. The average retained gas fraction ϕ_{avg} can then be computed from the compression test data using the expression

$$\phi_{avg} = \frac{1}{\Delta P}\left[\frac{\Delta h_c \rho_{gf}(1-\phi_{avg})g}{\ln\left(\frac{P_{atm}+P_{hyd}+\Delta P+\rho_{gf}(1-\phi_{avg})gh_s}{P_{atm}+P_{hyd}+\Delta P}\right)}\right] \tag{4.8}$$

where
- Δh_c = measured elevation change of simulant surface upon compression
- ρ_{gf} = gas-free density of the sludge simulant
- ΔP = change in pressure at simulant surface upon compression
- P_{atm} = atmospheric pressure
- P_{hyd} = hydrostatic head above simulant surface before compression
- h_s = simulant depth before compression

Note that Equation 4.8 has to be implicitly solved for ϕ_{avg}. In contrast to the intermediate column work, the simulant depth h_s was highly uncertain and thus the calculation was performed with upper and lower bounds on h_s. At the time of the compression, ϕ_{avg} can be compared to ϕ_{bulk} (as calculated in Equation 4.6). This provides some feedback on the validity of the assumptions used to perform the calculation in Equation 4.8.

4.3.3 Determining Void Fraction at Various Simulant Depths

To probe the gas retention behavior as a function of elevation (or simulant depth), it was necessary to devise some methods that would permit void fraction to be estimated in sub-regions of the tall column. The bulk void fraction only calculates the overall average void fraction and not the void distribution, which conceivably could be configured so that most of the gas is in a few regions of the column, with the lowest elevations in the column of particular interest. At the outset of testing, three methods were planned: ultrasonic measurements, core sample measurements, and analysis of post-test compression data. Uncertainty regarding the accuracy of these methods led to the development of two other techniques after the tests were conducted, both of which depended on still images extracted from the video files collected during the tests: feature tracking during void growth and image analysis for void fraction.

The five methods listed above that were implemented to generate void measurements are described in the rest of this section. Known uncertainties and limitations of each technique are presented to help assess the void data that is presented in Section 8.0. If appropriate, a brief discussion of the utility of a void fraction measurement technique is included, as it was discovered that not all five methods were of equal value for accomplishing the test objectives.

Note that the terms gas fraction and void fraction are used interchangeably throughout the text. Techniques described in this section all purport to determine the gas fraction. Methods based on visual information from the cameras interpret observed voids only as gas-filled, whereas some of the voids may contain liquid. No attempt was made to distinguish between gas and liquid-filled voids in any visually-based analyses. Any void that was observed was assumed to be solely due to gas, which may contribute to some differences between visual and non-visual based techniques.

Ultrasonic Measurements

Ultrasound is a high-frequency, oscillating sound pressure wave that can be transmitted through opaque or transparent media that include solids, liquids, gases, or a combination thereof. Ultrasonic measurements are often performed in process-monitoring applications to non-invasively probe fluids in vessels and pipes to measure the physical properties of the fluid or detect certain physical phenomena. The sound field properties of ultrasonic velocity and attenuation are commonly measured via ultrasound and used to characterize concentration, density, and other physical properties for fluid mixtures and slurries.

Ultrasonic velocity is calculated by measuring the time required for an ultrasonic pulse to traverse a known distance (e.g., pipe diameter) and dividing it by the known distance. Ultrasonic attenuation is calculated by measuring the reduction in ultrasonic signal amplitude over a known distance and quantifying the change in amplitude relative to the starting material (e.g., gas-free sludge simulant) or a reference fluid (e.g., water). Ultrasonic attenuation measurements were ultimately used to quantify gas-void fraction (GVF) in the intermediate-scale column due to the sensitivity of attenuation to changes

in GVF and the practicality of their application. The bubble-laden kaolin slurries did not lend themselves to ultrasonic velocity measurements due to the large gas bubble geometries and their sizes relative to the intermediate column diameter.

Ultrasound can be very sensitive to the presence of gas bubbles in a liquid and this sensitivity can be used to characterize bubble-laden media. However, great care must be taken when selecting the ultrasonic measurement frequency or frequencies used to meet the measurement objective. Gas bubbles have resonance frequencies that, when excited by a sound wave of equivalent frequency, result in vibratory motion of the bubbles with a sharply peaked resonance at the fundamental pulsation frequency. Measurements performed over the resonance frequency or frequencies of gas bubbles in a liquid result in non-linear ultrasonic attenuation and velocity measurements. Figure 4.3 shows an example of the effect of bubble resonance on ultrasonic attenuation over a range of ultrasonic frequencies for gas bubbles in water. Bubble resonance is clearly achieved between 25 and 30 kHz, although the range of frequencies affected is broader than this.

Figure 4.4 shows an example of the effects of bubble resonance on ultrasonic velocity for a range of ratios of ultrasonic frequency to bubble resonance frequency. The ultrasonic measurement frequency equals the bubble resonance at a frequency ratio of 1.0 along the plot's abscissa. At ultrasonic frequencies well below the bubble resonance (i.e., frequency ratio is <<1.0), the velocity is independent of ultrasonic frequency, is less than that of bubble-free water, and can be accurately predicted by Wood's emulsion equation (Wood 1955); at ultrasonic frequencies in the range of bubble resonance (i.e., frequency ratio ~1.0), the velocity first decreases and then rapidly increases to a value above that for bubble-free water; and at frequencies above resonance (frequency ratio is >>1.0), the velocity decreases until it reaches the value for bubble-free water.

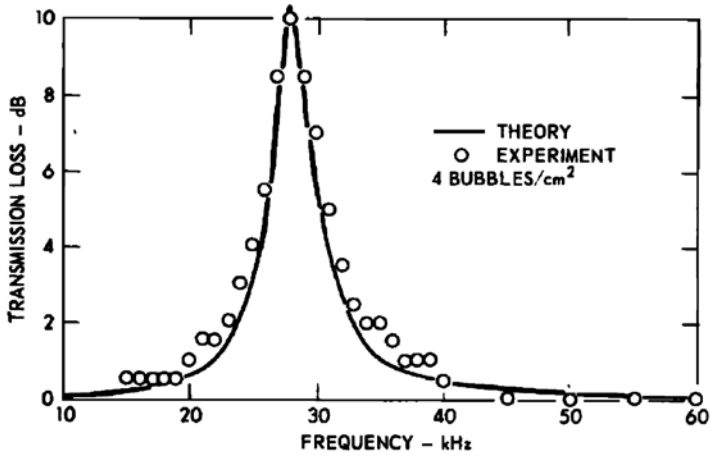

Figure 4.3. The Attenuation of Sound through a Screen of Bubbles (four per square centimeter) of Uniform Size for Frequencies Ranging from 10 to 60 kHz (Anderson and Hampton 1980)

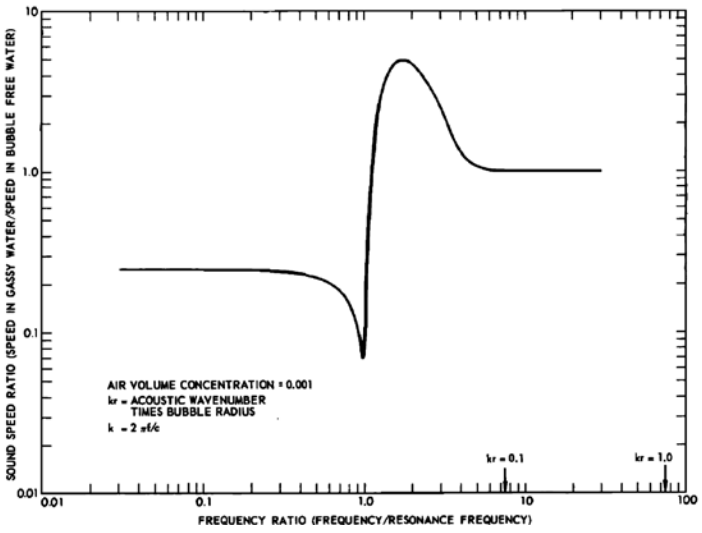

Figure 4.4. Ultrasonic Velocity for a Range of Ultrasonic Frequencies in Water Containing Bubbles of Uniform Size (Anderson and Hampton 1980)

The non-linear effects of bubble resonance on ultrasonic velocity and attenuation can be valuable for characterizing bubble sizes (or particle sizes) when that is the objective of the measurement. However, when the objective of ultrasonic velocity or attenuation measurements is to quantify gas concentration, great care must be taken to select ultrasonic measurement frequencies that are either well below or well above the range of bubble resonances in the bubble-laden medium for a monotonic relationship to exist between gas concentration and these sound field properties.

Ultrasonic attenuation is the reduction of the pulse amplitude due to the absorption, scattering, and/or reflection of sound energy by the gas bubbles as the pulse propagates through the bubbly medium. In general, attenuation increases with increasing gas concentration. In addition, a monotonic relationship exists between attenuation and gas concentration at ultrasonic frequencies well below and well above the bubble resonances in a bubble-laden medium. The velocity of an ultrasonic pulse in a bubbly medium can either be affected by the change in bulk compressibility when gas is added to a liquid or not affected at all. The ultrasonic velocity will only be influenced by the gas concentration if the ultrasonic measurement frequency is well below the lowest bubble resonance frequency in a bubbly medium; the velocity will remain essentially constant if the ultrasonic measurement frequency is above the highest bubble resonance frequency.

Previous investigators have developed theoretical models for ideal bubbly media that allow gas concentrations to be determined based on ultrasonic measurements. The ideal bubbly media contained bubbles that had spherical or spheroidal shapes, uniform gas bubble sizes, and uniform distribution in the supporting liquid. For example, Wilson et al. (2008) performed ultrasonic measurements at ultrasonic frequencies below gas-bubble-resonance frequencies in kaolin sediment. The gas concentrations of the kaolin sediment could be accurately predicted based on the ultrasonic velocity measurements and a simplified version of Wood's equation (Wood 1955). However, the predictions were much less accurate for real (referred to as non-ideal) gas-bearing media having non-spherical bubble shapes and heterogeneous bubble distributions. A working theory for non-ideal slurries with non-spherical bubbles has not been developed, rendering currently available direct inversion algorithms for ideal slurries unreliable.

Non-ideal bubbly media require empirically derived correlations between gas concentration and ultrasonic measurements with test configurations that represent the fluid mixture and the pipe or vessel characteristics. Investigators have developed empirically derived correlations between gas concentration and ultrasonic measurements for bubbly mixtures and gas-bearing sediments, sands, and muds. Kepkay and Cooke (1978) measured ultrasonic velocity through gas-bearing silty clay at frequencies below bubble resonance and generated a decreasing step-down relationship between acoustic velocity and GVF; Wilkens and Richardson (1998) measured ultrasonic velocity and attenuation over a wide range of acoustic frequencies in gassy seafloor sediments. They reported the sensitivity of ultrasonic velocity to the presence of gas bubbles only at ultrasonic frequencies below bubble resonance and the high sensitivity of attenuation to the presence of gas at frequencies well above and below the range of bubble resonance frequencies.

An example of an empirical relationship developed between ultrasonic attenuation and a 25 wt% kaolin/bentonite slurry during oxygen bubble generation from hydrogen peroxide decomposition[1] is provided in Figure 4.5.

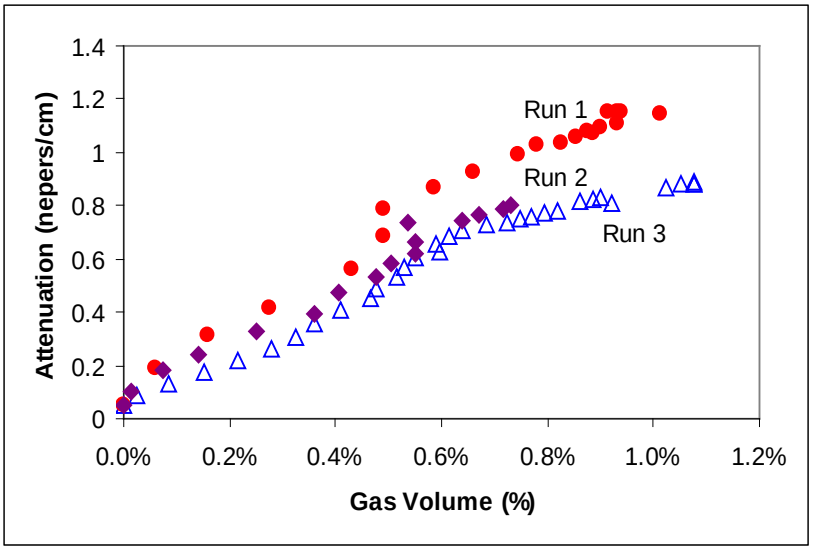

Figure 4.5. Example of a Trend between Ultrasonic Attenuation and GVF in a Kaolin/Bentonite Slurry

Bubbly kaolin mixtures are known to yield non-ideal gas bubbles with a wide range of shapes and dimensions that include relatively small-diameter spheroidal bubbles to large gas-filled cracks/slits that are several inches wide. See Figure 4.6 for an example of the gas void sizes and geometries in 500 and 1000 Pa kaolin.

[1] The data in the figure are from Panetta PD, BJ Tucker, KM Judd, and AA Diaz. 2004. *Ultrasonic determination of gas volume fraction (proof of principle results)*. Unpublished data, Pacific Northwest National Laboratory.

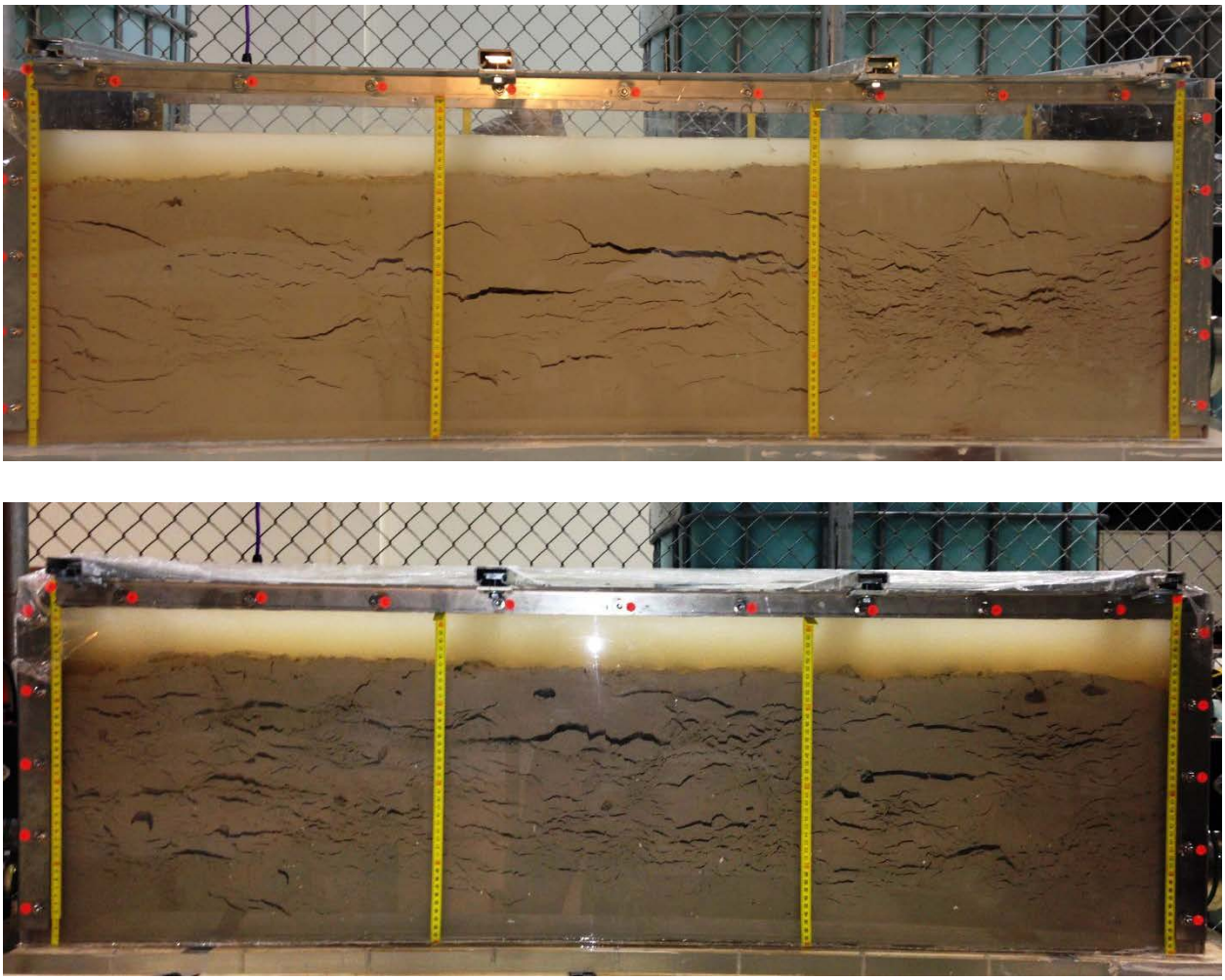

Figure 4.6. Photographs of Gas Void Sizes and Geometries in the Test Vessel for 1000 Pa Kaolin Clay Simulant (top) and 500 Pa Kaolin Clay Simulant (bottom)

The wide range of possible bubble sizes is accompanied by a wide range of possible bubble resonance frequencies that have to be avoided when selecting ultrasonic measurement frequencies. The larger bubbles precluded the use of low ultrasonic measurement frequencies for ultrasonic velocity measurements because a measurement frequency that would be well below the lowest bubble resonance frequency would have a wavelength larger than the diameter of the tall column and would be impractical to use. Ultrasonic attenuation measurements that could be performed above the range of bubble resonance frequencies were determined to have a good likelihood of success based on research published in the literature as well as in previous laboratory testing at PNNL. Therefore, ultrasonic attenuation measurements were ultimately selected to quantify the GVF in the tall column.

Additional considerations made when selecting the ultrasonic frequency for attenuation measurements were 1) the total attenuation of the sound field by the bubbly kaolin medium at its highest gas concentration and 2) the geometry of the tall column. The ultrasonic frequency selected for measurement had to be sensitive to changes in gas concentration without being completely attenuated by the bubbly medium at its highest gas concentration and had to result in at least three wavelengths across the measurement path (test vessel length). Early testing was performed to evaluate three candidate

frequencies for their abilities to meet these measurement requirements: 20 kHz, 100 kHz, and 250 kHz. A frequency of 250 kHz was ultimately selected for yielding the highest attenuation change per change in GVF.

In the absence of an available working theory to facilitate direct inversion analysis, i.e., a direct determination of GVF based on attenuation measurements, a relationship between ultrasonic attenuation and GVF had to be empirically developed through laboratory testing. The "calibration standards" used to develop the relationship between ultrasonic attenuation and GVF were kaolin slurries with the same composition intended for the tall column tests. Details on the correlation development tests are provided in Section 6.1.3.

Core Sample Measurements

The core sampler was intended as a backup measurement should ultrasonic measurements or the post-test compression data analysis be delayed in development or have large uncertainties. The principle behind the core sampler was to take in-situ slurry samples that contained gas from the tall column, remove them, and determine the gas fraction by application of a reference pressure in a known volume. This is quite similar to the approach used in the deployment of an in-situ void fraction instrument in Hanford DSTs, described in Stewart et al (1995, 1996). The gas in the slurry compresses when the reference pressure is applied, resulting in a change in pressures in the sample and the reference pressure. The void fraction can be calculated using an equation of state.

A mechanical sampler was designed and built for this purpose, but it did not accurately measure known gas fractions during the development of the sampler that occurred prior to the tall column tests. The core sampler was still deployed during testing, as it also provided useful data on the in-situ shear strengths and total solids of the simulant. Unfortunately, the source of the discrepancy between the void fractions as determined using the core sampler and known void fractions has not been determined. The inaccuracy and uncertainty in the core sample void fraction data made it unsuitable for assessment of void fraction profiles, and it is not discussed further in Section 8.0. For completeness, the core sampler design, method, and void fraction results are discussed separately in Appendix B.

Analysis of Post-Test Compression Data

At the end of each tall column test, approximately 4540 kg (10,000 lb) of water was added to the existing water layer above the simulant. The weight of the added water increased the hydrostatic pressure acting on the top of the simulant layer by about 0.25 bar (3.7 psi). The increased pressure compressed the gas contained within the simulant. With the reduction in gas volume that results from compression, the simulant layer compressed downward in the column. The magnitude of the simulant-surface elevation change indicates the average void fraction in the simulant. Equation 4.8 can be used to estimate the average void fraction based on the observed change in elevation of the simulant surface in response to a change in applied hydrostatic head.

During each simulant compression test, the nine, fixed-position video cameras in the viewing mast were used to monitor the change in elevation of visually distinct features (bubbles and cracks). Still images taken from the video recordings before and after each compression test were analyzed to determine how the simulant elevation changes varied with elevation above the bottom of the column.

These data can be used to determine how void fraction varies with elevation in the simulant because regions with a higher gas fraction will exhibit larger elevation changes than those with lower gas fraction.

For each before-compression camera image, a visually distinct feature was selected and its elevation determined by measuring its location on the photograph and then correcting for parallax and lens-distortion effects in a manner identical to that used for the feature tracking method for determination of void (see the following section). Similar measurements and corrections were then made for each corresponding feature in the after-compression camera images. Once complete, this analysis yielded data showing the observed compression as a function of elevation in the simulant.

In general, one feature was selected and tracked for each of the nine camera elevations. Tracking multiple features in each set of images was judged unnecessary because the real-time video showed uniform movement of simulant in response to compression in almost all cases. The exceptions were cameras 4, 5, 6, 8, and 9 during the Test 3B compression. Cameras 4, 5, 6, and 8 showed movement of the simulant features in parts of the image but no movement in other parts. Camera 9 showed movement at two different rates in two different regions as well as regions with no movement. Camera 7 showed no simulant movement for Test 3B in any region. This behavior was attributed to adhesion of simulant to the viewing windows. Cameras 1 through 5 in Test 1 exhibited similar behavior in that no simulant movement was evident upon compression. Because of these hypothesized simulant-adhesion effects, the compression-vs.-elevation data for Tests 1 and 3B were not used to develop vertical void fraction profiles.

The simulant compression-vs.-elevation data for Test 2 appeared uniform within each camera image and there was no indication of problematic simulant adhesion. Further, the measured trend of increasing compression with increasing elevation, when projected to the elevation of the simulant surface, agrees well with the simulant surface elevation change calculated from the observed liquid-level change during the compression test. Even though it is uncertain whether the Test 2 data were affected by simulant-adhesion effects, the consistency of the measured elevation changes with that of the simulant surface provides added confidence that the Test 2 compression data are reliable.

The Test 2 compression-vs.-elevation data were used to estimate the void fraction in the simulant at various elevations. The approach used involves first assuming a void fraction profile and then calculating the resulting combined hydrostatic/lithostatic pressure throughout the simulant layer. All retained gas is assumed to be at the same local, combined hydrostatic/lithostatic pressure as the surrounding simulant. The amount of increased pressure used in the tall column compression test is then applied throughout the simulant layer. The pressure increase results in a corresponding reduction of the local gas volume throughout the simulant as predicted by the ideal gas law. The reductions in local gas volumes result in a prediction for how much the simulant should compress at each elevation. For these calculations, the simulant is assumed to move without friction on the column walls or the viewing mast. Further, any effects of the simulant yield stress on the change in gas volume with increased pressure are ignored.

The assumed void fraction profile is adjusted as needed until the simulant compression-vs.-elevation predicted by the calculations matches the values measured by analysis of the before- and after-compression photographs.

Feature Tracking During Void Growth

The variation of retained-gas fraction with elevation was determined for each test by a feature tracking technique that involved measuring the movement of visually identifiable features (e.g., cracks and bubbles) throughout each test. Digital images taken from the fixed-position video cameras in the viewing mast were used for this analysis. The method used to determine the retained-gas-fraction profile implied by the feature tracking technique is described in this section.

The average retained-gas fraction in the simulant column is estimated based on the observed change in level of the liquid/air interface throughout the test. The initial average retained-gas fraction (ϕ_o) is calculated based on the as-loaded density of the simulant (see Section 4.3.2). The initial retained gas fraction is assumed to be uniformly distributed throughout the simulant. The volume of the initially retained gas is equal to the initial simulant volume multiplied by ϕ_o. As gas is generated thereafter and the liquid level rises, the volume associated with that level rise is a direct measure of the quantity of gas retained within the simulant. The average volume fraction of gas (ϕ_{avg}) is calculated by adding the initial gas volume to the volume indicated by the level rise and then dividing by the total simulant volume.

A similar approach can be used to determine how the retained gas fraction varies vertically in the column. Suppose, at the beginning of a d_{max} test, a visually distinct tracer particle is loaded into the simulant column at a level h above the bottom of the column. As the test proceeds, the level of the tracer particle varies with time from its initial level (h_{init}) and the tracer level changes by $\Delta h(t)$, which is given by this equation:

$$\Delta h(t) = h - h_{init} \tag{4.9}$$

The average retained-gas fraction in the simulant between the bottom of the column and level h can be calculated[1] by

$$\phi_{avg,h}(t) = \frac{\phi_o h_{init} + \Delta h(t)}{h_{init} + \Delta h(t)} \tag{4.10}$$

where $\phi_{avg,h}(t)$ = average retained-gas fraction up to level h
ϕ_o = initial gas volume fraction in the simulant (assumed uniform)

Testing d_{max} theory requires an assessment of whether the *local* retained-gas fraction increases at depths below d_{max}. Values for the local retained-gas fraction (ϕ_{local}) can be computed between any two depths (h_1 and h_2) based on their respective values of $\phi_{avg,h}$ using the equation

$$\phi_{local} = \frac{(\phi_{avg,h_2})h_2 - (\phi_{avg,h_1})h_1}{h_2 - h_1} \tag{4.11}$$

This equation provides the average retained-gas fraction between depths h_1 and h_2. To illustrate use of this equation, consider a hypothetical case where, during a d_{max} test, analysis of the movement of visually distinct tracer particles yields $\phi_{avg,h}$ = 0.1 for h = 0.5 m and $\phi_{avg,h}$ = 0.15 for h = 1.0 m. Using

[1] The equations in this section apply specifically to the case where the simulant is contained in a column of constant cross-sectional area. The cross-sectional area of the tall column is constant.

these values in Equation 4.11 yields ϕ_{local} = 0.2. Again, this value is the average retained-gas fraction in the column between heights 0.5 and 1.0 m.

In the tall column d_{max} tests, no visually distinct tracer particles were intentionally loaded into the sludge simulant. However, when the column was loaded with simulant, some bubbles and cracks were present due to entrained air and gas generated during column loading. As gas generation continued during the test, additional bubbles and cracks formed in the simulant that could be tracked as they moved vertically in response to changing quantities of retained gas. Figure 4.7 shows an example of visibly identifiable bubble shapes (for a more typical image seen during the tall column testing, see Figure 4.8 or Figure 8.1). These photographs were taken 1 hour apart during Test 1 at 8:00 a.m. and 9:00 a.m. on 12-30-2013. As shown in the photographs, the bubble indicated by the white arrow moves from the 9 ft 1 in. level at 8:00 a.m. to approximately 9 ft 1.75 in. at 9:00 a.m. Photographs used for the feature tracking analysis were extracted from the video files at 1-hour intervals until after peak void was reached. Thereafter, the photographs were extracted at 8-hour intervals. The longer interval after peak void was justified because feature movement is much slower after peak void is reached.

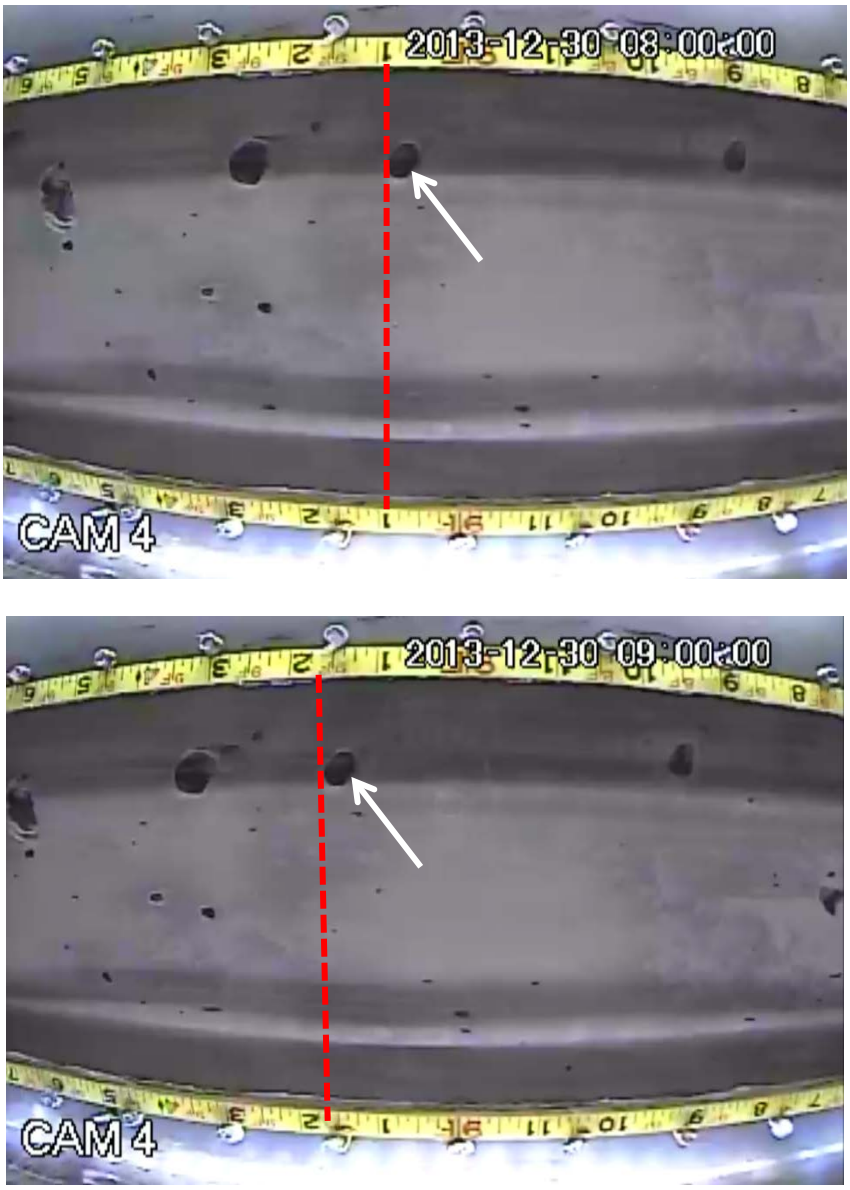

Figure 4.7. Example Bubble/Crack Movement between Subsequent Photographs. Note that right-to-left motion in the images corresponds to upward motion in the tall column.

For the analysis of images, the measured bubble/crack elevations had to be corrected for parallax errors and barrel distortion introduced by the wide-angle lenses on the video cameras. The magnitude of these corrections was determined based on measurements and images collected during the level-volume correlation test that preceded the d_{max} tests.

In most cases, it was not possible to track a single feature for the duration of the test. As the simulant moves in response to generated gas, new features appear and existing features often disappear. Additionally, at the higher elevations, features sometimes move out of the field of view of the camera and can no longer be tracked. To address these issues, it was often necessary to switch partway through the test from tracking one feature to tracking an alternative feature. When switching from one feature to another, the distance between the two features was carefully measured and that distance used to adjust all

subsequent elevation measurements for the new feature to, in effect, allow calculation of the expected elevation for the feature that was first selected for tracking. After all the required adjustments were made, for each of the cameras used in each test, the resulting data show the change in elevation with time for a feature present in the video image at the beginning of the test.

The feature tracking method depends on motion of gas features at the viewing window representing the growth in gas content at those elevations and below. Thus, an uncertainty in the method is how similar near-wall feature motion is to the gas behavior (and unobservable motion) in the middle of the column. This uncertainty is considered to be relatively small for three reasons:

- In previous studies with kaolin simulants of similar strength that were generating gas (Gauglitz et al. 2012; Powell et al. 2014), the simulants have been observed to move as a plug in the column, suggesting that the gas grows similarly at all radial locations.

- When the change in water level (indicating the bulk void) was plotted against time, the data for each test was similar in shape to the data describing changes in features at various column elevations (presented in Section 8.3). That is, the observed data are internally consistent with one another.

- Computed tomography images of column cross-sections presented in Gauglitz et al. (2012) demonstrate that a simulant of similar strength (~680 Pa) has gas distributions that are relatively uniform at different elevations.

These three observations support the idea that near-wall visible features, and in particular their motion as gas is generated, are a good representation of the column cross-section at the measurement elevations. This does not preclude the existence of local variation in gas fraction throughout the cross-section of the column, but significant differences between near-wall and bulk bubble motion were not expected.

Image Analysis

The simulant selected for the tall column tests has a beige or light brown color, whereas gas bubbles or void pockets show up black (or very dark). The contrast in light intensity between the gas and the simulant was used to implement a straightforward, image-based method to determine void fraction as a function of elevation in the tall column. The method required still images extracted from the continually collected video stream of all nine fixed location cameras at discrete times during each test. These images were converted to grayscale, cropped to include only a region that has uniform lighting, and a threshold value was computed for each image.[1] The image resolution was such that small adjustments (reductions of around 10%) had to be made to the threshold value to reduce the prevalence of false detection of void. The false detections occurred due to gradients in the simulant matrix, i.e., a region of the simulant that was darker than other regions was slightly lower than the global threshold. The adjusted threshold was then used to create a binary image, or more precisely, a matrix of ones and zeroes where white (not void = 1 and black (void) = 0. The process is illustrated in Figure 4.8 using an example image from tall column Test 1.

[1] The threshold algorithm uses Otsu's method (see Otsu 1979) on the global image in anticipation of selecting for pixels that are below the threshold, i.e., are dark and indicate void.

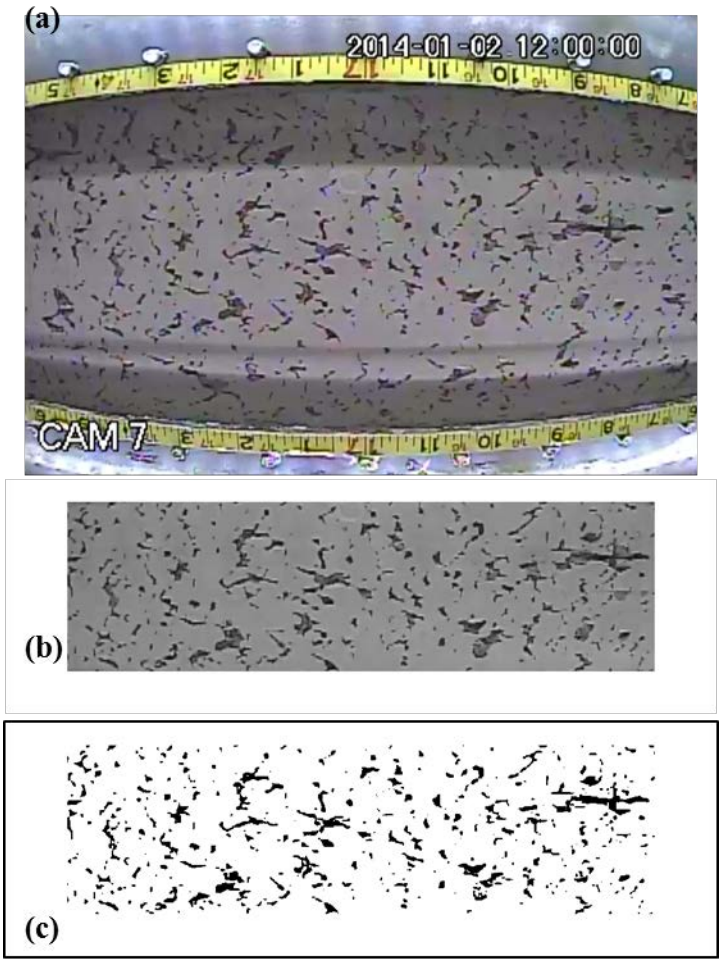

Figure 4.8. Example of the Image Analysis Process for an Image from Test 1. (a) The original image taken from Camera 7 on 01/02/14; (b) The cropped region that takes only the center portion when the illumination is uniform; (c) The cropped image after calculating a threshold and converting the image to a binary matrix where black (pixel is 0) = void and white (pixel is 1) = not void.

The matrix representing the binary image can be used to determine the void fraction ϕ_A via the simple formula

$$\phi_A = \frac{\sum_{j=1}^{n} n_V + 1[p_j = 0]}{n}, \tag{4.12}$$

where n is the total number of pixels in the matrix, j is the index of the current pixel, p_j is the value (either 0 or 1) of the pixel j, and n_V is the number of pixels indicating void. The sum is conditional on $p_j = 0$ and n_V increments by one every time the conditional is true. The void fraction is denoted ϕ_A to indicate it is an area fraction (two-dimensional) that assumes the third dimension (which cannot be interrogated by this technique) is represented by the planar space that is visible. Though the method is straightforward, it is subject to the following caveats:

1. It only observes the void (which has a three-dimensional shape) in a plane.

2. It assumes the void (as long as it is present) in the viewing plane remains visible and no appreciable smearing of the slurry occurs on the viewing surface.
3. The threshold adjustment factor that was selected is appropriate for the duration of all the tall column tests, i.e., to maintain consistency in the approach, it was not optimized for individual image sets.
4. The cropped region of each image that was analyzed is considered rectangular, but the image has some curvature and this assumption introduces small errors; no attempt was made to correct for the curvature.
5. The image quality may not be sufficient to resolve pixels on the boundary of regions containing void, resulting in underestimates of void. Attempts to sharpen the image without compromising the integrity of the information were not successful.

After consideration of all the caveats, the uncertainty in the void fraction determined by this technique is estimated to be ±1% (absolute). It should be considered a qualitative method where relative changes in magnitude (with time or elevation) are significant but the accuracy of the absolute magnitude is less certain.

Method Comparison Summary

The major features of the five void profile calculation methods are summarized in Table 4.4 for comparison. Each method has limitation(s) or caveat(s) that require consideration when comparing void fraction data in Section 8.3.

Table 4.4. Summary of the Distinguishing Elements of Each Void Fraction Profile Calculation Method

Method	Features
Ultrasonic	Volume average (in-situ) over radial path length at 10 elevations in the column; high resolution in time; duplicates at each elevation; requires correlation development to translate collected data
Core sampling	Local in-situ measurement at five elevations; low resolution in time; method could not be correlated with measurements of known void fraction (apparent high bias)
Post-test compression analysis	Differential measure using camera images of local void fraction (assumes all void is gas-filled) using motion of void features during compression event; only provides void fraction at one instant in time; requires observable motion that is unimpeded by the viewing area; does not directly evaluate the bulk simulant
Feature tracking	Differential measure using camera images of local void fraction (assumes all void is gas-filled) using motion of void features during growth in a test; analysis complicated by consolidation of the slurry later in the test; requires observable motion that is unimpeded by the viewing area; does not directly evaluate the bulk simulant
Image analysis	Local, two-dimensional measure of area fraction (assumes all void is gas-filled) at the nine fixed camera elevations; sensitive to changes in simulant coloration since it uses a threshold technique; depends on observable voids at viewing area being representative of the surrounding simulant volume; does not directly evaluate the bulk simulant

5.0 Simulant Selection and Properties

The selection of the simulant for the tall column tests for evaluating gas retention and release in deep sediment layers followed the guidelines set in ASTM C1750-11 (2011), which provide a methodology for selecting a simulant that is relevant to the test objectives. This section discusses the specific simulant selection criteria and the selection of kaolin and zero valent iron slurries for the tall column tests. Results of bench-scale tests that were used in developing specific simulant recipes and the final simulant recipes for the tall column testing are presented. Additional bench-scale tests were conducted to support selection of preferred test operating conditions, such as temperature, and the role of key test operational considerations such as the method of addition of simulant components.

5.1 Selection of Kaolin and Zero Valent Iron for Tall Column Tests

The principal objective of the tall column tests was to evaluate the accuracy of the d_{max} theory for gas transport from deep sediment beds described by van Kessel and van Kesteren (2002) at a representative DST sludge depth. The key selection criteria for the simulant to meet this overall testing objective are as follows:

- The shear strength of the material can be controlled in the range of 500 to 1000 Pa, preferably by a simple change in solids concentration.
- Simulant properties are available or can be measured to calculate d_{max} for each test.
- Representative gas bubbles (slits and cracks) can be generated in situ in a controlled manner.
- Gas generation will continue over the duration of a test, even after a peak or steady-state void fraction has been reached, and will occur over a reasonable period of about a week (slow enough to allow column loading but fast enough to be complete within one to two weeks to allow multiple tests to be completed).
- Gas bubble retention and release mechanisms reasonably match what is known for Hanford sludge waste, which is low gas retention and release of gas through what is thought to be interconnected slit-shaped bubbles. (Note that the evaluation of the d_{max} theory does not require the simulant to match Hanford radioactive sludge waste behavior, but this was still preferred.)
- Simulant preparation and column loading are feasible to implement operationally in large-scale tests.

As discussed in Section 1.1, previous gas retention studies have used natural sediments (mud), kaolin and bentonite clays, sand and crushed glass, and combinations of these materials. The gas generation methods have been the formation of oxygen bubbles from the decomposition of hydrogen peroxide, the formation of hydrogen bubbles from the corrosion of zero valent iron particles, and the formation of methane, carbon dioxide, and other biogenic gases from biological activity. In the previous studies using biological gas generation reported by van Kessel and van Kesteren (2002) and Sills and Gonzalez (2001), the peak gas retention occurred between 20 and 40 days and the overall tests were completed after about 100 days. This test duration is too long to meet the criterion of doing multiple tests. In the recent study by Gauglitz et al. (2012), gas generation from hydrogen peroxide in kaolin reached peak gas retention in about a day and corroding iron particles in kaolin clay slurries reached a peak generation between one and seven days. Both of these durations are suitable for large-scale testing. For both these methods of gas

generation, in materials in the 500 to 1000 Pa target range, bubbles formed that were slits and cracks and the bubbles connected to form gas transport channels that were similar to those described by van Kessel and van Kesteren (2002) and Sills and Gonzalez (2001). In the study by Gauglitz et al. (2012), the bubble shapes generated using iron particles were more angular (sharper cracks) than those created by hydrogen peroxide. The overall gas retention was also lower and closer to Hanford sludge tanks with the iron particles.

Based on data obtained from historical PNNL studies, there were two significant problems with using hydrogen peroxide as the gas generation agent for the tall column tests. First, the hydrogen peroxide begins reacting very quickly to generate gas. Thus, to reduce initial void fraction and make column loading with simulant practical, the hydrogen peroxide needs to be at a low concentration (as a percent of the total simulant mass) and introduced to the kaolin slurry in a highly concentrated solution (to minimize the water withheld from the slurry and keep the kaolin slurry from being too difficult to mix). Second, to have a gas generation reaction that continues to produce gas for the duration of the experiment, the hydrogen peroxide should be at a high concentration (as a percent of the total simulant mass). Without a periodic injection of additional H_2O_2 into the simulant over the duration of the tall column experiments, which would have several challenges of its own, these two competing effects could not be reconciled.

Therefore, kaolin and iron particles were selected for use because gas retention was lower and closer to Hanford sludge tanks, the delay in the start of gas generation (which did not occur in the actual tall column tests as discussed in Section 7.0) made field implementation easier, and hydrogen bubbles are what are retained in the Hanford waste. The iron particles had also been demonstrated to continue generating gas over sufficiently long periods even at relatively low loadings (<1 wt% of the total simulant).

Based on the selection criteria, the tall column simulant was specified by examining candidate simulant components used in PNNL historical studies. The simulant selected contained four components: kaolin, water, iron, and biocide. Each component (except water) is briefly described in the following sub-sections.

5.1.1 Kaolin Used as Waste Physical Simulant

Kaolin-water slurries have been used as physical simulants for waste in a wide array of PNNL studies, including a series of gas retention studies (most recently Gauglitz et al. 2012). In general, kaolin simulants (after being mixed) are homogeneous and lack the chemical complexity of actual waste. However, the bubble retention behavior (particularly the bubble morphology) of the simulant is similar to the limited observations of gas retained in actual waste, especially for shear strengths of 500 Pa or greater. For this reason, kaolin was used as the physical simulant in the tall column tests.

The kaolin used in this study was EPK kaolin (Edgar Minerals Inc.), with a d50 particle size of 5.5 microns (Bontha et al. 2010).

5.1.2 Iron Used as Gas Generation Agent

The previous study by Gauglitz et al. (2012) demonstrated that the zero valent iron particles will corrode in kaolin slurries and generate hydrogen bubbles over a period of one to several days. The

corrosion of iron for yielding hydrogen gas proceeds in a series of steps (Reardon 1995) that can be summarized as follows:

$$Fe + 2H_2O \rightarrow Fe^{2+} + 2OH^- + H_2(g) \rightarrow \frac{1}{3}Fe_3O_4(s) + \frac{4}{3}H_2(g) + \frac{2}{3}H_2O$$

Depending on the chemistry and temperature of the simulant, the reaction will proceed to only the intermediate step or completely to form magnetite (Fe_3O_4), and the moles of hydrogen gas generated per mole of iron also depends on the extent of the reaction. The rate of reaction is expected to depend on temperature. In the previous study, Gauglitz et al. (2012) noted that the initiation of hydrogen generation reaction was delayed by about 5 days in tests that used iron that had been stored in the laboratory for a period of time and began immediately in one test that used a newly purchased supply of iron. While the cause of the different initiation period was never evaluated, it was suspected that a corrosion layer had formed on the older iron and this delayed the onset of further corrosion. The previous work also showed that during the period of gas generation, the generation rate of gas was similar for both the old and the new iron.

The iron particles used in both Gauglitz et al. (2012) and the tall column tests were S-3700 MICROPOWDER® iron (Ashland Incorporated), which have a median particle size of about 2 microns based on vendor literature.

5.1.3 Biocide Used for Biological Control

In the previous studies of gas generation and release with iron particles (Gauglitz et al. 2012), it appeared that some biological activity in the kaolin slurry occurred due to the presence of the iron particles; therefore, a small amount of biocide (Mt. Hood 480) was added and was found to be effective at minimizing this potential complication. In the tall column tests, 75 ppm of biocide was selected for the recipe and this was expected to provide a similar level of control of biological activity.

5.2 Bench Top Scoping Studies

Bench top scoping studies were conducted to determine target recipes for the planned tall column tests, to investigate an acceptable temperature range for conducting the tests, and to assess if the method of adding the iron particles to the kaolin slurry affected that gas generation behavior. The primary objective of specifying the target recipe was to understand how changing the kaolin solids concentration changed the shear strength and to pick an iron concentration that would generate an appropriate amount of gas to conduct the tests.

5.2.1 Kaolin Concentration Impacts on Shear Strength

The effect of kaolin solids concentration on the shear strength has been studied extensively, but before mixing the simulant at large scale, collecting additional data to confirm the relationship was warranted. Some uncertainty regarding the mixing of the simulant at different scales was also important to understand. With this understanding, a solids concentration could be defined in the recipe that would result in a kaolin simulant near the target shear strengths. The approach in the tests was to target a kaolin solids concentration that was expected to result in a shear strength slightly larger than either 500 or

1000 Pa. This approach made it more likely that the simulant would need to be diluted with water (rather than adding more kaolin solids) if the measured shear strength was not within the acceptance range.

Figure 5.1 shows some bench top results of shear strength measured with various kaolin concentrations. These results are "For Information Only (FIO)," as the data were collected prior to the completion of the Test Plan governing the work. The data have a similar functionality as previously developed correlations at PNNL (shown by the various lines, refer to the reference section for each source in the legend), where shear strength has a log-linear relationship with solids concentration. The data collected in this work are very similar to the expression in Gauglitz et al. (2001) when the leading coefficient is increased by 20%. The solid concentrations used in the recipe were adjusted down slightly (approximately 0.5 wt%) from the bench-top data to account for the differences in mixing at large-scale, which was expected to be more thorough than the mixing done to prepare the bench-top samples.

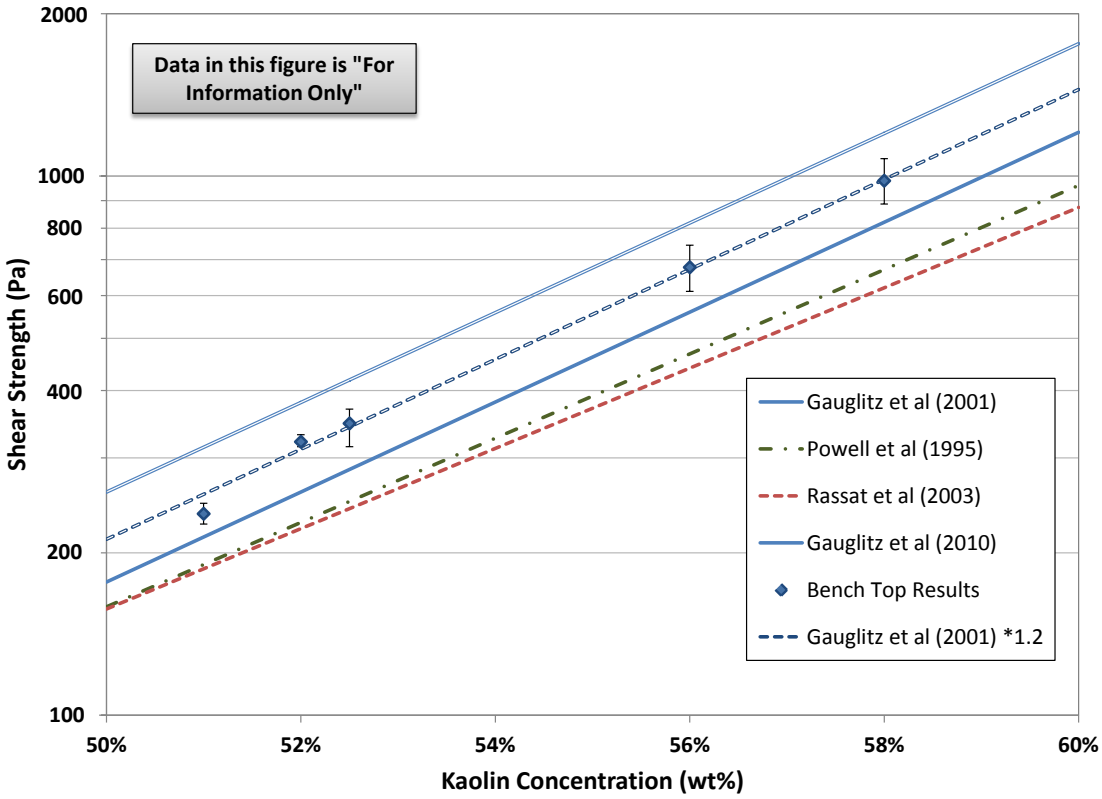

Figure 5.1. Comparison of Bench Top Results (FIO Data) to Reported Correlations of Shear Strength as a Function of Kaolin Clay Concentration

5.2.2 Temperature Impacts on Reaction Rate

Prior to the tall column tests, experiments were conducted to determine the effect of temperature on the gas generation rate from the corrosion of the iron particles. At the time, it was known that the simulant preparation for the tall column tests would be done outdoors during the winter using hot water and allowing for cooling during the mixing period, and therefore these tests were conducted to determine an acceptable temperature range for the simulant during mixing and column loading. Section 6.1.4 shows

the test systems used for conducting the gas generation rate tests and is essentially the same as used in previous studies (Gauglitz et al. 2012).

Figure 5.2 shows gas generation results for the effect of test temperature using a nominally 1000 Pa simulant. The results are shown in terms of the total volume of generated gas per initial volume of simulant. Additional data using a 500 Pa simulant that were collected at higher temperature (>75 °F) are shown in Figure 5.3, where duplicate temperature tests were performed using iron that was old (particles remaining from prior PNNL experimental work) and new (iron purchased specifically for the tall column tests). Both figures demonstrate that the primary effect of temperature was to change the length of the induction period. The lower the temperature, the longer it takes for the iron particles to start generating appreciable amounts of hydrogen gas. Since the experiments were to be conducted in the winter months, the long induction periods at temperatures <75 °F were a concern, and ultimately led to the use of a heating system in the tall column. The data at higher temperatures suggested that an induction period was still present even at 91 °F, but it had shortened to ~36 hours. Thus, it was decided not to add Fe particles if the temperature was >90 °F.

The tall column experiments did not have induction periods similar to those measured in the bench top testing. The cause of this discrepancy was difficult to ascertain. The data from the old and new iron in Figure 5.3 are in good agreement, suggesting that the discrepancy was not due to iron particles with different inherent reactivity. One possibility was the presence of a trace chemical acting as a catalyst, such as $CaCl_2$ (a concrete additive potentially present in the cement trucks used to mix the simulant used in the tall column tests). Small amounts of $CaCl_2$ were tested in a few scoping tests using the bench-top columns and found to reduce or eliminate the induction period. To verify this as the cause, further study would be required.

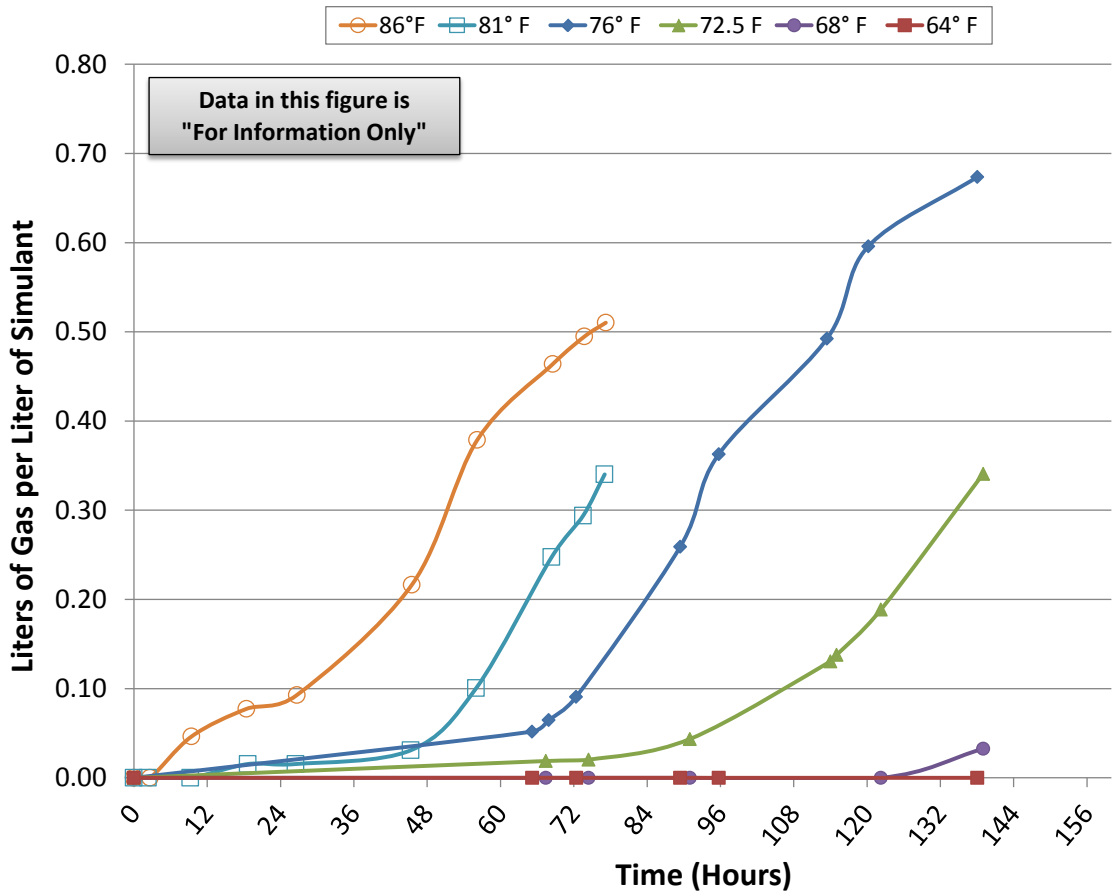

Figure 5.2. Effect of Test Temperature on the Cumulative Volume of Generated Gas per Initial Volume of 1000 Pa Simulant (For Information Only)

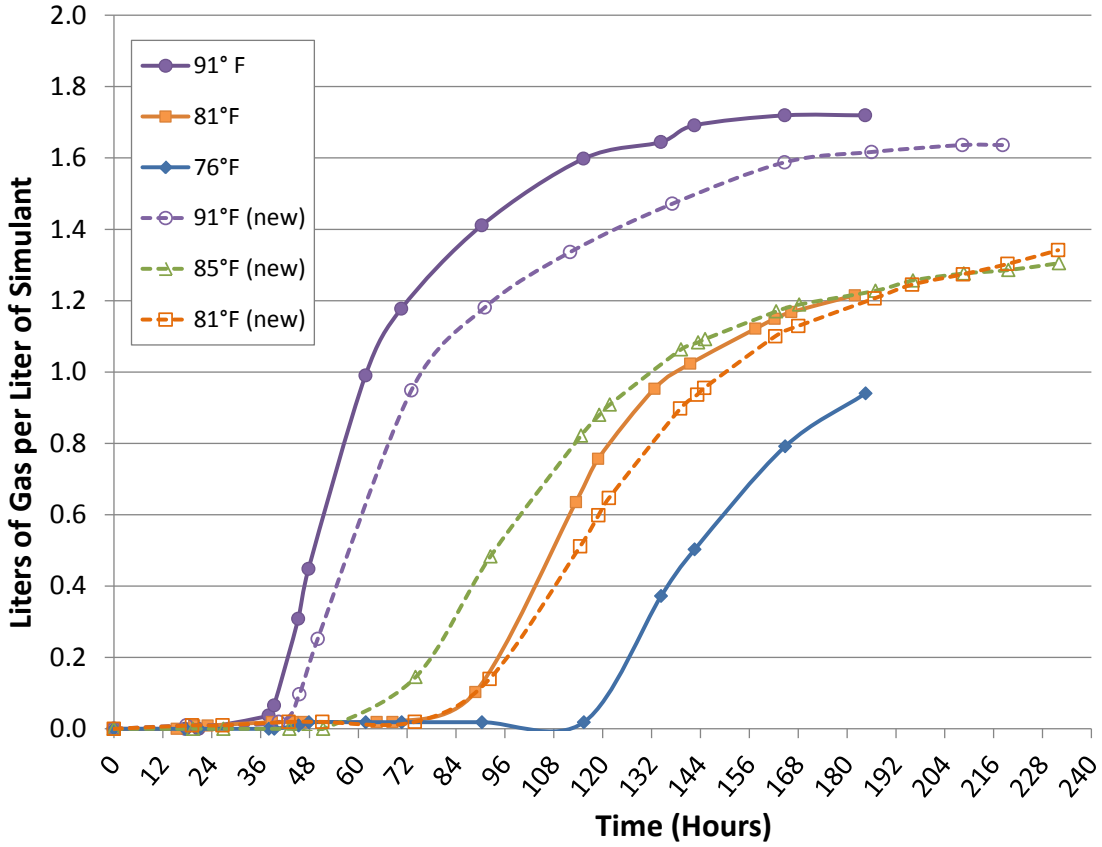

Figure 5.3. Effect of Higher Temperatures on the Cumulative Volume of Generated Gas per Initial Volume of 500 Pa Simulant, with Old and New Fe Particles

5.2.3 Iron Concentration and Addition Methods

Another uncertainty in the simulant recipe was the method of iron loading to use in the experiments. The choice of iron concentration is a balance between having the reaction occur slow enough to facilitate the experiment (mixing and filling the column), yet having enough iron present to continue generating gas even after the peak void fraction is achieved in the column. Data collected in bench top experiments for four iron concentrations (0.25, 0.5, 0.75, 1.0 wt%) are shown in Figure 5.4. The experiments are inconclusive with respect to how specific gas generation rate (volume of gas per volume of simulant) changes with iron loading, other than to state that the rate was lower at 0.25 wt%. The length of the induction period was also not clearly a function of loading, and this illustrates another uncertainty regarding the iron reaction—it appeared to depend on the extent of mixing, i.e., how homogeneously the Fe particles were distributed in the simulant.

The different induction periods observed when the iron loading was changed did not affect the void fractions that were measured in the simulant (see Figure 5.5). The simulant reached a maximum of 23 to 25 vol% void in the small bench-top scoping tests regardless of the induction period and the rate of reaction. All the reactions also continued until the specific gas generation rate was > 1. Thus, even though the data presented in Figure 5.4 did not exhibit any identifiable trends, the iron concentration

could be selected from a range between 0 and 1 wt% without affecting the capacity of the simulant to achieve a void fraction of ~25%.

Since the impact of Fe concentration did not appear to materially affect the gas generation behavior (aside from some variation in induction period), the iron loading was chosen for the tall column tests in order to provide a sufficient "supply" of gas during the tests. The gas generation rate and the quantity ("supply") of gas available at the lowest point in the tall column, i.e., the location where the pressure is at a maximum, is primarily governed by the concentration of Fe particles. This statement assumes the temperature would be approximately constant throughout the simulant and inhomogeneities in the dispersion of Fe particles are not significant. Given the requirement that an equivalent volume of gas should be generated for the simulant volume, the moles of hydrogen gas at the bottom of the column were calculated based on the ideal gas law. For both the 500 Pa and 1000 Pa simulants, the numbers of moles of Fe necessary to generate the required moles of hydrogen were calculated based on the reaction shown in Section 5.1.2 and an assumed conversion of 70%. On a mass basis, the Fe loading requirement was estimated to be 0.36 wt% for both simulants. A similar calculation using the average pressure in the column resulted in an iron concentration of 0.27 wt%. Based on these calculations, the Fe concentration was selected to be 0.35 wt% for the tall column tests.

The 0.35 wt% iron loading was tested in bench-top experiments with nominally 500 Pa kaolin clay. The data from these experiments are given in Figure 5.6. The data in the figure fall into two categories: 0.35 wt% experiments using iron PNNL had remaining from previous work, and 0.35 wt% experiments using iron purchased specifically for the tall column tests (labeled as "new" in the figure). The first set of 0.35 wt% tests had one simulant batch that incorporated the Fe particles dry and duplicate tests that incorporated the Fe slurried with water (wet). This set also included a 1.0 wt% experiment (prepared wet) for comparison purposes. In that set of experiments, the 1.0 wt% batch reacted earlier with a slightly larger specific gas generation rate. There was little difference between the duplicate wet tests and the dry test. From this data it was concluded that the method of introduction of Fe (dry vs. wet) did not significantly affect the reaction rate. The wet method was used in the tall column tests since it was considered safer (iron dust is a flammability hazard) and easier to implement. The second set of 0.35 wt% tests was conducted in triplicate with the new iron, with the Fe mixed in as a slurry in all three experiments. The data were all very similar, suggesting that the gas generation reaction was reproducible at the bench scale.

For reasons that are currently unknown, the induction period that was observed in the triplicate experiments using 0.35 wt% iron did not occur when the tall column experiments were conducted, despite the use of the same simulant components in the correct proportions. The induction period was expected in the tall column tests based on it transpiring in the majority of smaller scale experiments and in large laboratory column tests reported by Powell et al. (2014) using a very similar kaolin/iron simulant, but even the bench-scale tests had instances where the induction period was shorter than typical. Possible explanations for the difference are discussed in Section 7.4, but the elimination of the induction period in the tall column tests did not change the rate of reaction or the extent of reaction (see Figure 7.17 and Figure 7.18).

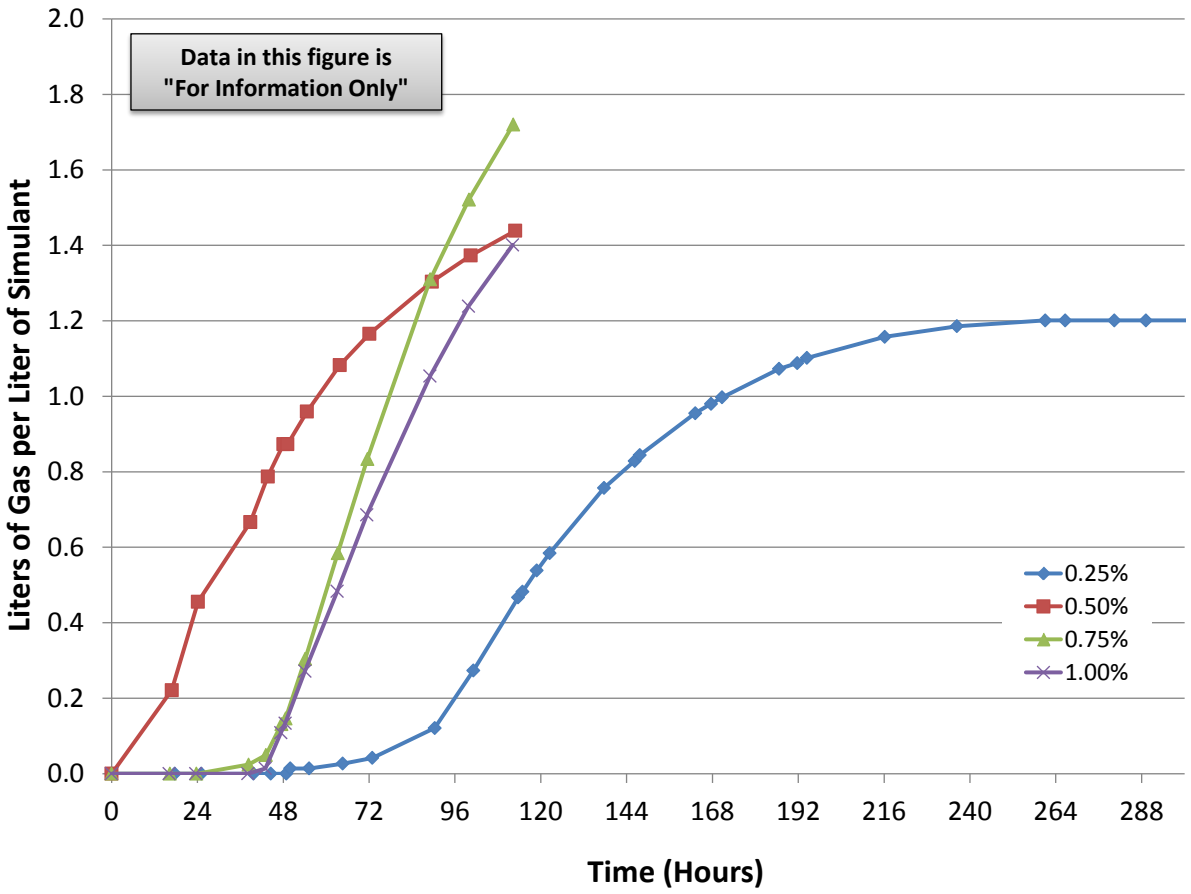

Figure 5.4. Cumulative Volume of Generated Gas per Initial Volume of 1000 Pa Simulant at Various Iron Concentrations (in wt%) (For Information Only)

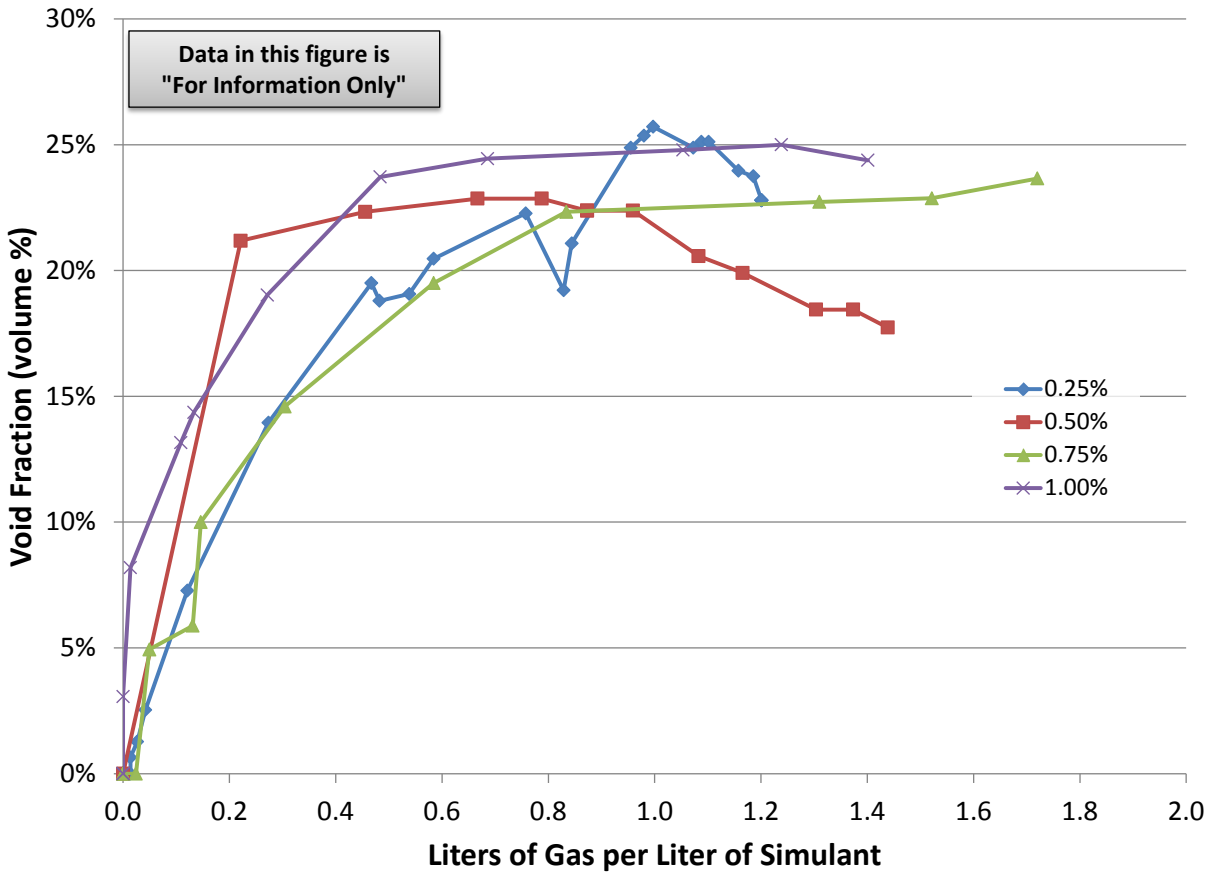

Figure 5.5. Bulk Void Fraction vs. Cumulative Volume of Generated Gas per Initial Volume of 1000 Pa Simulant for Various Iron Concentrations (in wt%) (For Information Only)

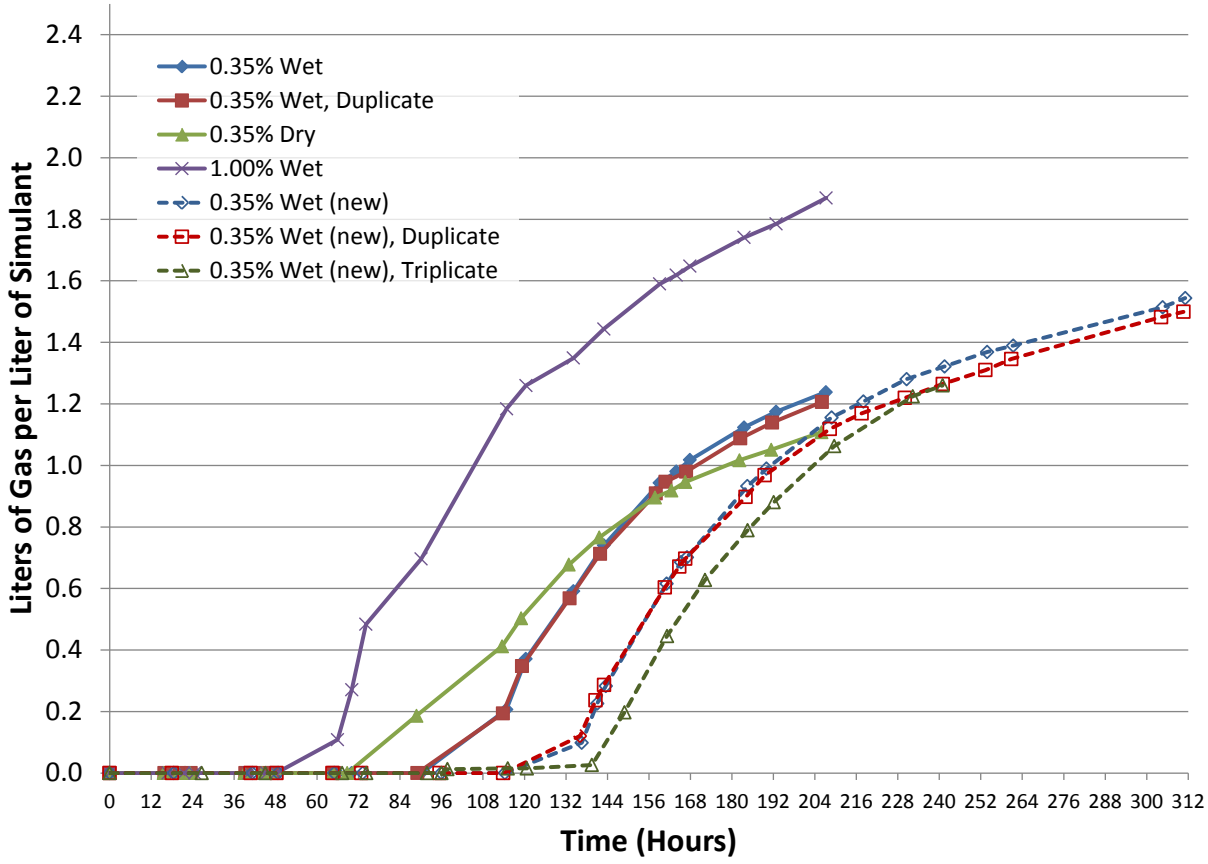

Figure 5.6. Cumulative Volume of Generated Gas per Initial Volume of Simulant for Bench-Scale Experiments Conducted to Assess Reproducibility of Results with Iron at the Target Concentration

5.3 Simulant Recipes for Tall Column

Based on the historical experience and the simulant development conducted prior to the tall column experiments, the target concentrations of the four simulant components (kaolin, water, iron, and biocide) were selected. For the simulants with target shear strengths of 500 Pa (Tests 1 and 2) and 1000 Pa (Test 3), the concentrations were chosen to produce a material with the appropriate shear strength and gas generation behavior. Note that a change to the recipe of the Test 3 simulant was required during the second attempt to conduct that test (see the description of the attempts in Section 7.3). Table 5.1 provides the simulant recipes on a weight percent basis, along with the estimated density of the simulant based on the proportions of the various components. The simulant recipe was divided into batches, where one batch was mixed in one cement truck. The size and number of batches varied between the three tests; however, as an estimate, reaching a target level of 310 in. in the tall column with material of 1.5 kg/L density requires a mass of 22,600 kg (49,800 lb).[1] In general, only ~50% of the simulant could be

[1] Based on early calculations assuming a 10% hold-up in the cement truck. Using the level-volume correlation, the required volume is 44*310 in. + 4.94 = 13,645 L, which would require 13,645 L × 1.5 kg/L = 20,468 kg (45,124 lb).

recovered from the cement trucks during tall column loading, so approximately 90,000 lb (45 tons) was prepared for each test.

Table 5.1. Target Simulant Recipes for Tall Column Tests

Component/Quantity	500 Pa Simulant	1000 Pa Simulant	~900 Pa Simulant[(b)]
Kaolin (wt%)[(a)]	53.7%	57.3%	56.7%
Water (wt%)	45.9%	42.3%	42.9%
Iron (wt%)	0.35%	0.35%	0.35%
Biocide (wt%)	0.000075% (75 ppm)	0.000075% (75 ppm)	0.000075% (75 ppm)
Estimated Density (kg/L)	1.51	1.56	n/a

(a) The kaolin weight fraction is "as-is," but kaolin is known to contain a small amount of moisture (~2%). This is not reflected in the kaolin or water weight percent in this table.
(b) Modification of the 1000 Pa recipe after first attempt at Test 3 was aborted.

The Fe particles were added by wetting the particles to make an iron-water slurry that was dispersed into the already-mixed kaolin-water slurry. Adding the iron with water required excluding some of the water from the initial kaolin-water slurry to achieve the ratios in the target recipes given in Table 5.1. The iron addition method impacted the determination of the simulant's shear strength acceptability range for the test. The shear strength, which was measured prior to iron addition to assess the simulant preparation, was greater than the target value. Therefore, the acceptance criteria for shear strength (τ_s) were adjusted to account for withholding 25 gallons of water (the amount used in the iron slurry). The adjusted acceptance criteria are given in Table 5.2. Once the Fe slurry was added and mixed in, the shear strength fell within the original shear strength range given in Table 4.2.

Table 5.2. Shear Strength Acceptance Criteria Adjusted for 25 Gallons of Withheld Water

Simulant	τ_s Lower Bound (Table 4.2)	Adjusted τ_s Lower Bound (25 gallons withheld)	τ_s Upper Bound (Table 4.2)	Adjusted τ_s Upper Bound (25 gallons withheld)
500 Pa Target	350 Pa	395 Pa	800 Pa	903 Pa
1000 Pa Target	800 Pa	896 Pa	2000 Pa	2240 Pa
~900 Pa Target	800 Pa	896 Pa	2000 Pa	2240 Pa

Had a different amount of water needed to be withheld, adjustments to the acceptance criteria could have been projected via the following expressions:

$$\tau_{s,bound} = \tau_{s0} e^{(5.73\times10^{-3})X} \text{ [500 Pa Target]}$$

$$\tau_{s,bound} = \tau_{s0} e^{(5.89\times10^{-3})X} \text{ [1000 Pa Target]}$$

where $\tau_{s,bound}$ is the adjusted shear strength acceptance criterion (each the lower or upper bound), τ_{s0} is the original acceptance criterion, and X is the amount of water (in gallons) withheld to make the iron slurry.

The primary reason for the broad acceptance range for shear strength as given in Table 5.2 was that very little scale-up data were available for a cohesive kaolin simulant mixed in cement trucks. The properties of kaolin have been studied extensively in bench-top quantities. However, in the tall column

experiments, the mixing occurred on a large scale and not all elements of large-scale preparation could be mimicked during the simulant development activities. The acceptance range was kept broad to allow for changes in shear strength with scale.

Another uncertainty was whether the iron reaction would proceed in a similar manner at a large-scale as it had in laboratory experiments. Particularly difficult to replicate in the laboratory was the mixing efficacy of industrial equipment such as cement trucks and pumper trucks. Another major element that was challenging to account for was the cleanliness of industrial mixing equipment before it was used. Ultimately, it was found that the induction period that was expected based on the simulant development work was absent in the tall column experiments. Hydrogen gas generation that starts shortly after introduction of the iron complicates the mixing and loading process, creating safety concerns before they can be managed using the controls described in Section 6.2.1. Given these concerns, attempting to reproduce the simulant behavior in the tall column tests reported in this work should be done with caution. If possible, a shakedown of the process (at the largest attainable scale) is advised.

Estimates of the hydrogen gas generation rate for the tall column experiments were generated prior to testing to specify nitrogen purge flow rates and specify some operational expectations. The estimate was calculated in two ways: 1) scaling-up the hydrogen generation rate from the intermediate column testing (Powell et al. 2014), and 2) using simulant data collected during simulant development work using nominally 500 Pa kaolin clay with 0.35 wt% Fe particles at ambient temperature (~75 °F).

The first approach assumed the following:

- The kaolin-water-biocide-iron simulant has a similar hydrogen generation rate despite small differences in kaolin loading (a couple weight percent).
- The generation rate scales directly with iron loading (0.25 wt% in the intermediate column vs. the planned 0.35 wt% for the tall column).
- The simulants in both columns are at similar temperature (~75 °F).

The scale-up calculation used the volume ratio between the two columns (tall column volume was larger by a factor of ~120). The intermediate column hydrogen generation rate ranged between 1 and 2 L of H_2 gas/h (Powell et al. 2014). Scaling up these values yields a range of 168 to 336 L/h of hydrogen gas generated, or 2.8 to 5.6 L/min.

The second approach used the test data collected from experiments in 5-inch-diameter acrylic columns and assumed that the specific rate in those tests would be similar in the tall column. A series of triplicate tests was used, where all of the tests were performed using a 0.35 wt% Fe loading and a nominally 500 Pa kaolin-water simulant. The generation rate was calculated using data of specific gas volume (L of gas per L of simulant) versus time. The highest rates occur when the reaction begins, so the slope of the specific gas volume over time was used in this initial period. The slope was then scaled up by the tall column simulant volume expected in the tests. On average, the small column test data projected a gas generation rate of 259 L/h (4.3 L/min).

Based on the two estimates, gas generation rates in the tall column were expected to range from 3 to 6 L/min. If deviation from this range occurred, one or more of the assumptions used in the calculation were not valid. The actual generation rates measured in the tall column tests are discussed in Section 7.0.

6.0 Experimental Methods

This section discusses the experimental methods used to conduct the tall column tests in two parts. First, the test equipment that was used to conduct tall column testing and various support activities is described. Second, the general operations of a tall column test are delineated. For deviations from the general test operations for a given test, refer to Section 7.1 (Test 1), Section 7.2 (Test 2), or Section 7.3 (Test 3).

6.1 Test Equipment

The description of the test equipment includes the tall column, installed instrumentation, the heating system, and the data acquisition equipment. Also described is the smaller-scale equipment used at PNNL to perform simulant testing and develop the core sampler and ultrasonic measurement methods. Auxiliary equipment that was not functionally part of the tall column but was used to assist in mixing the simulant, loading the column, and performing other test operations is described in Section 6.2.

6.1.1 Location of the Tall Column

The tall column was installed at the Cold Test Facility (CTF), which is managed and operated by WRPS. The CTF hosts a full-scale mockup of a Hanford waste tank surrounded by superstructure and other supports. The tall column was placed next to the waste tank on a cement pad and tied into the existing superstructure for support. The installation location is shown in Figure 6.1, where the mock waste tank and its superstructure can be seen on the right side of the image, the tall column is in the center, and on the left edge is the control trailer where the data acquisition equipment was housed. Work on the tall column performed at height was conducted using a boom lift that could be maneuvered around the column and reach any elevation that was required. The CTF site also afforded enough space to conduct the large-scale simulant preparation, mixing, and loading activities during testing.

Figure 6.1. Installation Location of the Tall Column at the CTF

6.1.2 Tall Column

The tall column was fabricated by HiLine Engineering & Fabrication, Inc. (Richland, WA) as directed by WRPS and advised by PNNL. PNNL provided guidance on the placement of PNNL instruments and equipment on the column. Schematics of the column are given in Figure 6.2 (with some dimensions included) and Figure 6.3 (with instrument identifiers).[1] The schematics show the elevations (side view) and angular locations (top view) of all the instruments on the column. There are a few instruments shown on Figure 6.3 that are not in Figure 6.2, namely the load cells, the wet test gas meters and their thermocouples, and the barometric pressure sensor. They are not shown in Figure 6.2 because their measurements are not specific to a column location. Note that one of the cameras (C10) is mobile and can be moved up and down the entire height of the column.

The column was constructed to a height of 45 ft with an internal diameter of 5 ft, and built out of 3/8-in.-thick carbon steel. It was placed on a scale (a set of four load cells calibrated to 100,000 lb) and supported by superstructure at the CTF at an elevation of 35 ft using struts (the location of the supports is visible in Figure 6.1). As shown in the column diagrams, there was a square column inside of the tall

[1] The diagrams describe the placement of instruments on the as-built column but are not scaled drawings.

column that was approximately 1 by 1 ft and ran the full height of the tall column. The square column housed an array of cameras that were deployed at nine fixed elevations (C1–C9) and look into the interior of the column (toward the center). The interior-facing plane of the square column (also referred to as the viewing column or viewing mast) was composed of rectangular acrylic windows that had a minimum unobstructed viewing area of approximately 8 by 24 in. The cameras were selected to allow observation of gas voids in the simulant over a minimum vertical distance of 6 in. (actual images were closer to >10 in.) with a resolution of approximately 100 pixels per inch.[1] The tenth camera (C10) in the viewing column was mobile (referred to as a "rover" camera) with the intent of tracking changes in the water surface level over the course of a test, which was a primary indicator of retained gas content. However, a mobile camera also allowed determination of the slurry surface level, scans of the entire simulant depth, and investigation of features of interest during the testing.

[1] The viewing area and resolution that is achieved by the cameras in the tests was estimated based on the images, which have a resolution of approximately 930 by 1360 pixels. There was typically a vertical distance of 10 in. (or more) in the image. If a conservative value of 12 in. is used, there were 1360/12 = 113.3 pixels per inch. The horizontal distance was typically a minimum of 8 in. (or more). Using a conservative value of 10 in., there were 930/10 = 93 pixels per inch in that direction.

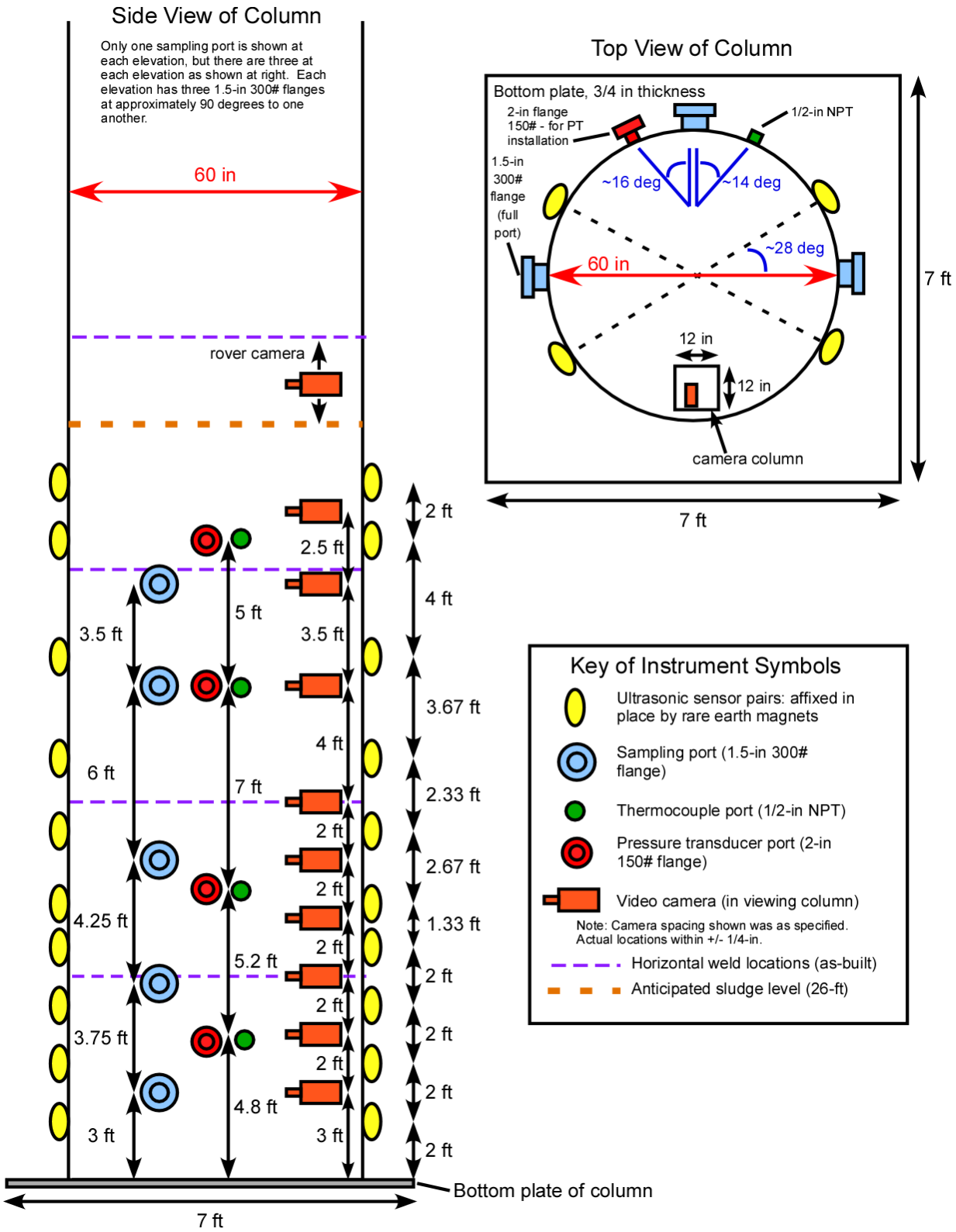

Figure 6.2. Schematic of the Tall Column with Most Instrument Locations. Note: The drawing is labeled with locations and/or dimensions of the instrumentation but it is not to scale.

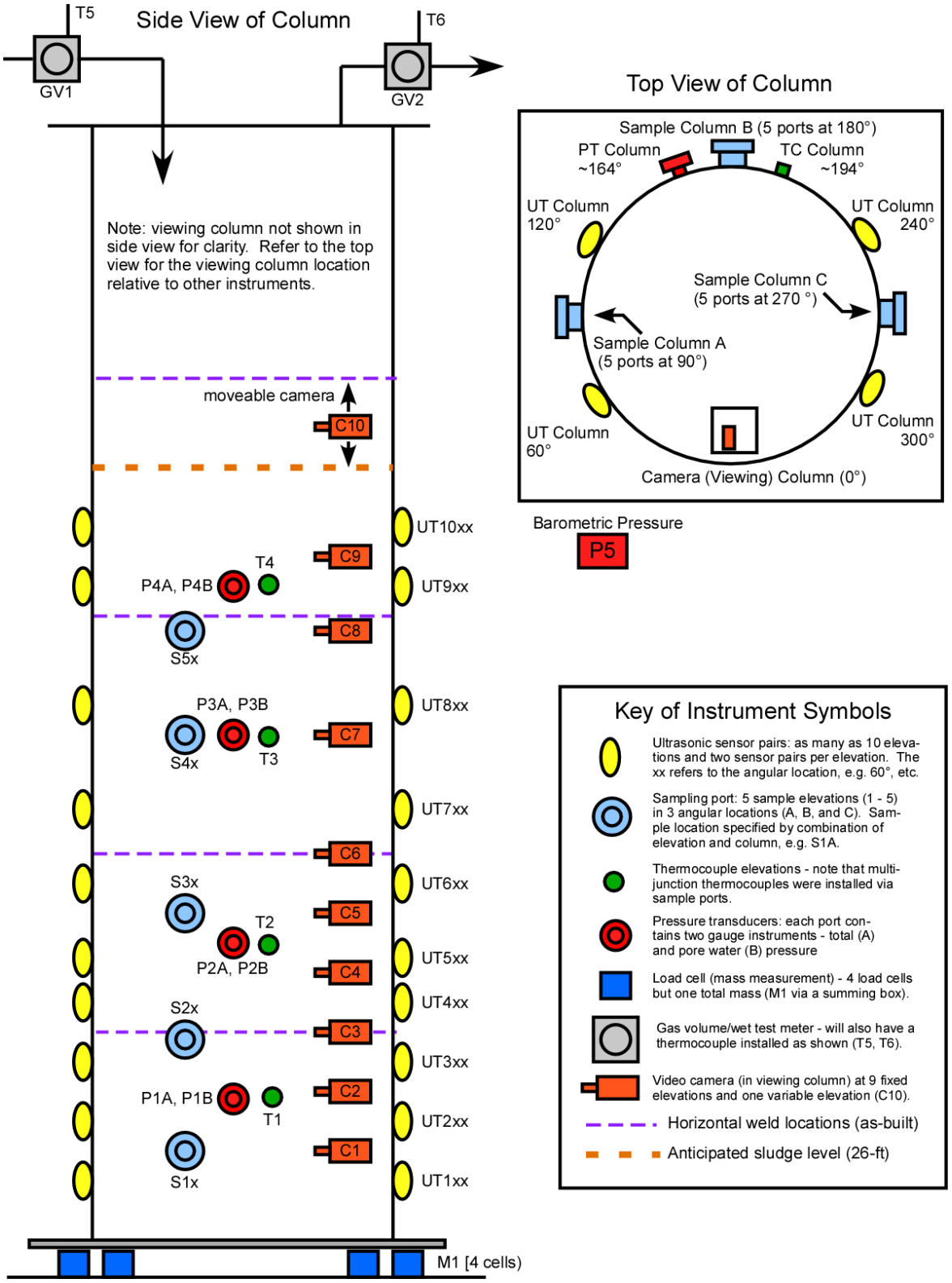

Figure 6.3. Schematic of Tall Column with All Instruments and Identifiers. The locations of the instruments can be determined by cross-referencing this figure with Figure 6.2.

The tall column had various ports and penetrations to accommodate instruments. As presented in Figure 6.3, there was a series of 1.5 in. flanges at five elevations. Each elevation had three 1.5 in. flanges at 90 degrees from one another (the fourth 90-degree location was occupied by the viewing column). Each of these flanges had a 300# ball valve attached to it. The core sampling system was connected at any one of these locations to take a sample from the tall column at that elevation. During a test, the sample ports could also be used to conduct a temperature measurement taken every 6 in. (radially, using a multi-junction thermocouple) to establish a radial profile. There were four elevations that had both a 0.5-in. NPT port (for thermocouples that extended approximately 6 in. into the column from the wall) and a 2-in. flange (for in-column pressure transducers), so that temperature and pressure measurements could be taken to get a coarse profile of the column during testing. The pressure transducers were installed in pairs at each elevation. One transducer measured the total pressure (it was vertically orientated in the column – the "B" transducer) and the other transducer measured the pore pressure (it was horizontally orientated in the column – the "A" transducer). The instrument wires were shielded in a steel tube and penetrated the column 2-in. flange through a modified (bored-through) blind flange (see the diagram in Figure 6.4). Both of the pressure transducers measured gauge pressure so the barometric pressure was also measured via a separate pressure transducer outside the column (P5).

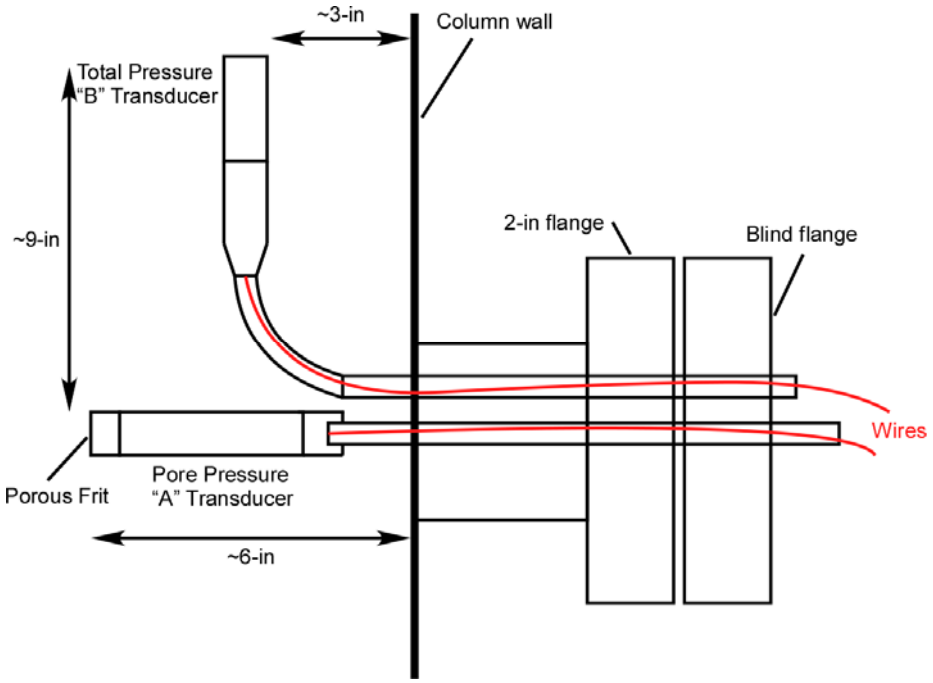

Figure 6.4. Installation Diagram of Pressure Transducers in the Tall Column

The ultrasonic transducer (UT) pairs were deployed at 10 elevations on the tall column. Each elevation had two UT pairs to make duplicate measurements across a different cross-section, i.e., radial path, of the column. The UT elevations were concentrated more heavily near the column bottom where measurements below d_{max} occurred. The angular locations are illustrative but may differ by a few degrees from what is shown in Figure 6.3; the major requirements were that a transducer pair was 180 degrees apart and the measurement area was a sufficient distance away from any obstructions that might have interfered with transmission of the ultrasonic waves (such as, for example, the viewing column). The UT installation and data collection system is described in more detail in Appendix C.

Not fully illustrated in either Figure 6.2 or Figure 6.3 is the configuration of the top of the column. The column was closed and sealed with a steel plate affixed to the top. A vent stack with a 10-ft-tall riser permitted gas to leave the column, where it was carried through flexible hose to more than 100 ft away from the tall column. The column also had a vent line in case of pressurization of the headspace (with a pressure relief valve set at ~5 psi). To prevent build-up of H_2 gas in the presence of air (oxygen), a N_2 purge was used to keep the headspace above the simulant and water layers oxygen-deficient. Initially (before loading or just after loading the simulant), the N_2 purge flow rate was as large as desired to replace oxygen in the headspace with nitrogen. During each test, the N_2 purge was lowered to be on the order of the expected H_2 generation rate. This facilitated the measurement of H_2 volume as it was produced and escaped into the headspace. To avoid using a measurement method that was composition-dependent, wet test meters were used on the inlet gas (GV1, the N_2 purge) and the outlet line (GV2, N_2 + H_2 gas leaving the column) to totalize the gas volumes and estimate the H_2 volume generated by difference. A diagram demonstrating the wet test meters installation on the inlet and outlet lines is given in Figure 6.5.

All possible permutations using the N_2 purge system are not shown in Figure 6.5. When the simulant was initially loaded, a high-flow purge of ~8 scfm was used to reduce the oxygen concentration to negligible levels. During the high purge, the wet test meters were not in service—the inlet meter was valved out and the outlet meter was valved out after the pea trap was drained. The pea trap was present to provide enough backpressure during testing to force the exiting gas to pass through the Ritter wet test meter. Thermocouples were installed on both wet test meters in the event that a temperature correction would be required. All the outlet lines from the column were insulated to protect the lines from freezing and minimize condensation (line plugging was not desirable in these tests). The viewing column was also purged with nitrogen as a safety precaution.

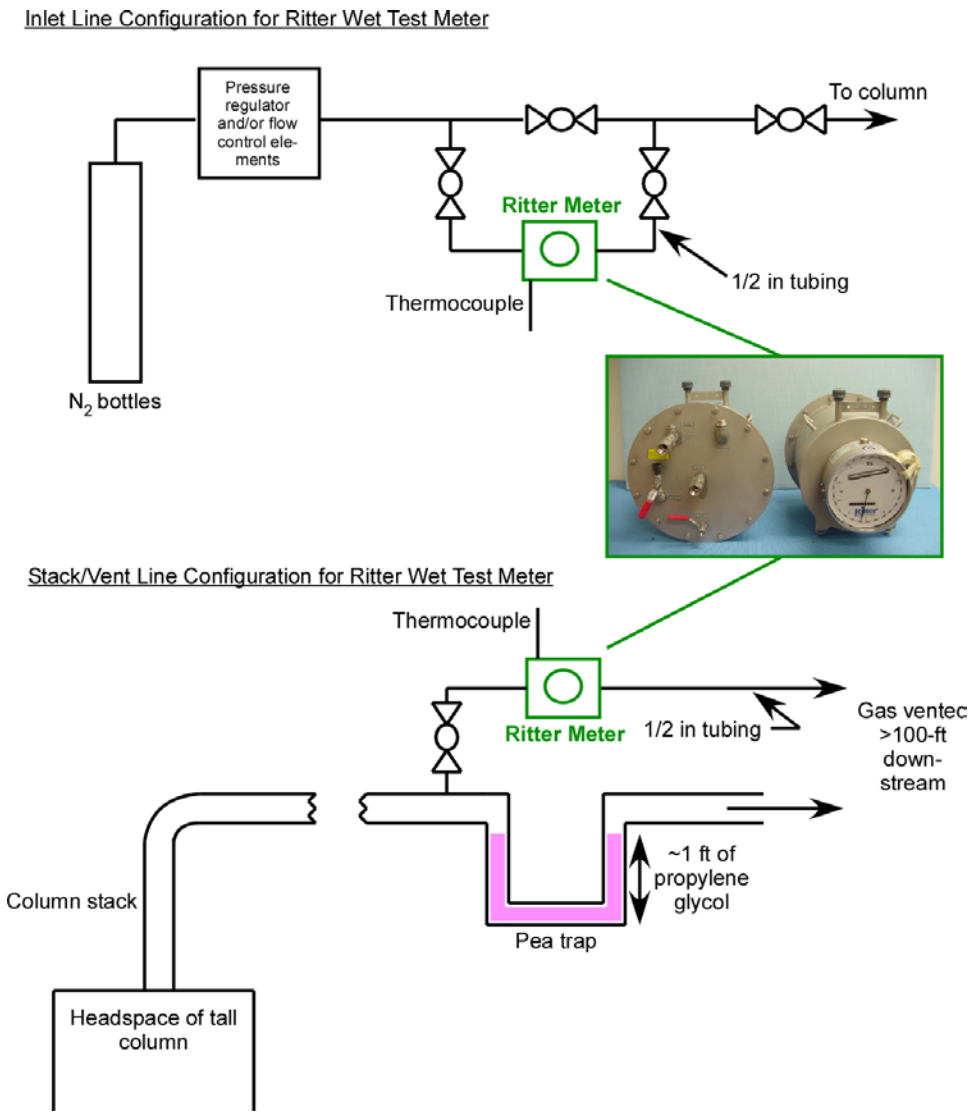

Figure 6.5. Wet Test Meter Configuration at the CTF during Tall Column Testing

Data collection from instruments was primarily performed remotely in a control trailer. For many of the instruments, significant lengths of cable were required (up to 200 ft) from the measurement location to the trailer, where a series of instrument displays and video monitors (for the cameras) were housed. Instrument data were recorded manually (on test instructions or associated data sheets) from these displays and captured by time-lapse photography of the displays at 5-minute intervals, which was planned as a backup record. Video was recorded at the highest bit rate available (192 kb/s) at 1 frame per second for the entire test, except at times when real-time video was to be collected. Real-time video was collected at 30 frames per second at a bit rate of 1024 kb/s or greater. Ultrasonic data was collected using a separate data acquisition system (DAS). The DAS cycled through the 20 pairs of sensors sequentially over the course of a few minutes. During Test 1, the DAS was not yet automated so measurements were taken manually approximately every 4 hours during the test (the manual measurements took 30 to 40 minutes to complete a cycle of all 20 sensor pairs). For Tests 2 and 3, the UT DAS was collecting a data cycle automatically every 15 minutes.

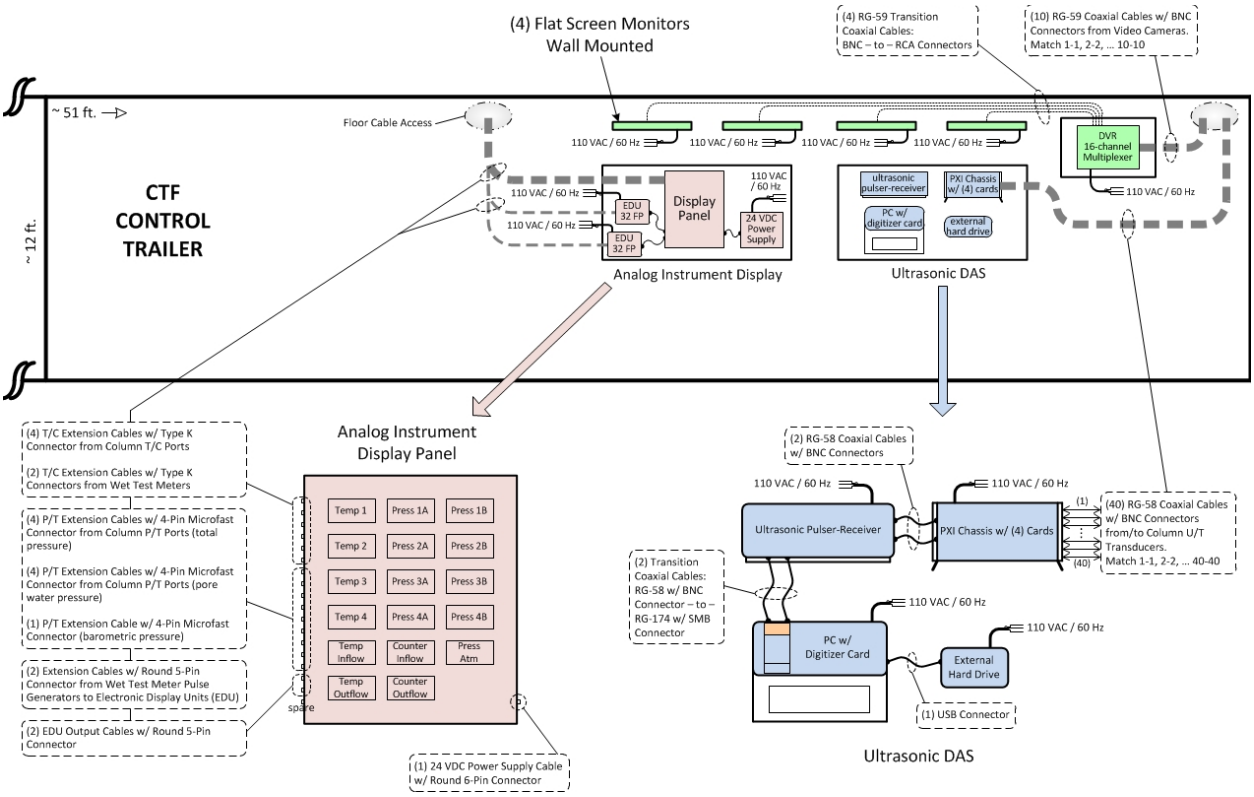

Figure 6.6. Diagram of the CTF Control Trailer with Data Monitoring Equipment (not shown in the diagram are the load cell display and a separate computer system used to interface with the DVR)

Based on simulant work described in Section 5.2.2, it was preferable to conduct the tests at approximately room temperature (~75 °F). Achieving and maintaining column temperatures in that range during winter environmental conditions necessitated a heating system for the column. However, the heating system also could not interfere with potential instrument reconfiguration or maintenance. The tall column was surrounded by a shell of insulating panels supported by a frame welded to the column exterior. The shell of insulating panels (garage door panels with an R-value of 19) created an annulus of 4 to 8 in. around the column (depending on the circumferential location), through which heated air was used to maintain column temperature by forced convection. The air was supplied by compressors, which heated the air sufficiently that a series of heaters were only required for finer control of the inlet temperature (dialed to a target of 75 °F). The hot air was sent into the bottom of the column annulus and vented out the top, with a target spread in temperature of 10 °F (e.g., 80 °F at the bottom and 70 °F exiting at the top). Refer to Figure 6.7 for a design drawing of the insulation panels where they are transparent purple to expose some of the internal components; in Figure 6.1 the insulation panels are visible as the white surface and give the column an octagonal appearance.

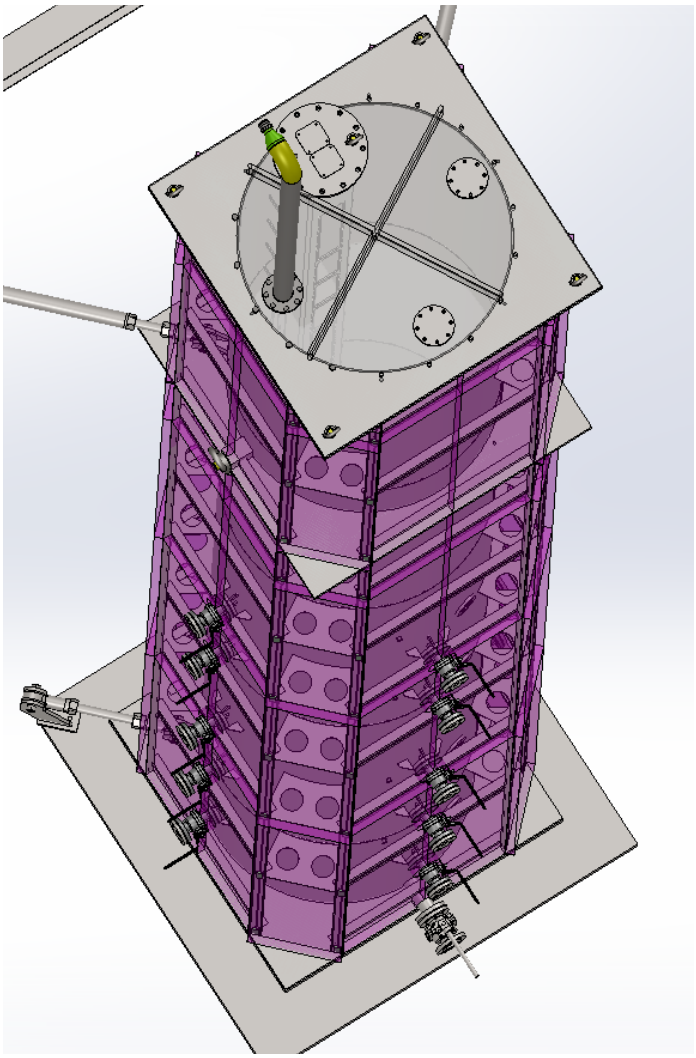

Figure 6.7. Top Down View of Column with Insulation Panels Colored in Transparent Purple

The camera system and the column load cells were used to perform a level-volume correlation before the first tall column test. The purpose of the level-volume correlation was to relate measured levels in the column to volumes in order to accurately estimate initial void fraction and analyze the post-test compression data. The level-volume correlation doubled as a leak test and a functional test of the camera system. The correlation was developed by filling the tall column up to its full height and then draining water from it, stopping at several different levels. Each time the draining process was halted, the level was measured by the rover camera and the volume was determined using the mass of water (measured by the load cells) and the density of the water (inferred from the temperature, which was measured using the installed thermocouples in the column). The resulting relationship is given in Figure 6.8, with the obtained data in red open circles and the correlation given by the solid black line. The tall column had a constant volume cross-section of 44 L per inch of change in height. A simple three-point check of the effect of parallax for a typical fixed camera (Camera 7 was used) was also conducted during the level-volume correlation. It indicated that measurements at the extremities of an image collected by a camera could have an error of almost 0.5 in. Whenever possible, data were collected with the rover camera centered on the level it was measuring to minimize the error. Other calculations discussed in this report correct for the parallax error more rigorously.

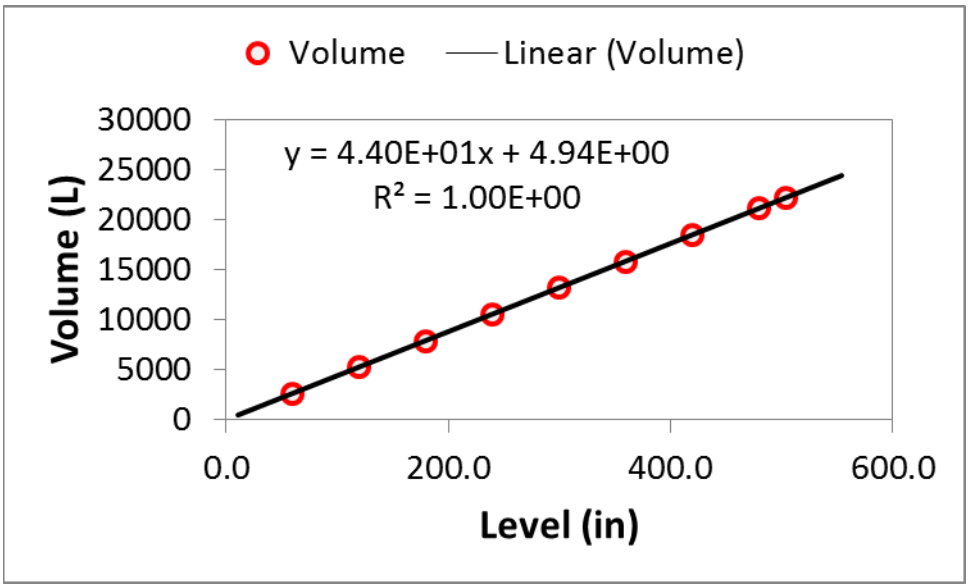

Figure 6.8. Level-Volume Correlation Data for the Tall Column

6.1.3 Acoustic Test Cell

The ultrasonic measurement method was developed using the acoustic test cell shown in Figure 6.9. The test cell was a mockup of the tall column cross-section. The end-plates were 3/8-in.-thick carbon steel with the same curvature that an equivalently sized section would have if it were part of the 5-ft-diameter column. The sides were acrylic to permit visual observation of the contents and lined with rulers to take level measurements. Each of the test cell end-plates had a 1.5-in. flange of the same type that was on the tall column (mimicking the sample ports). The top remained open to permit simulant loading from the top. It was placed on a floor scale to perform estimates of initial void during simulant testing using Equation 4.6 and a level-volume correlation that was performed with water. The test cell served three purposes: 1) help identify a transducer type that could be used in the tall column testing, 2) develop correlations for gas fraction with UT data, and 3) provide an independently known void fraction to test the core sampler method against.

In an initial scoping test, an approximately 1000 Pa kaolin-water slurry[1] with 1 wt% Fe particles was prepared and loaded to a height of ~12 in. (total height of the test cell is 18 in.). Three inches of water were added to the top. Average gas fraction of the simulant was estimated by tracking the level change. UT scoping measurements confirmed that sonic waves could be transmitted and received through the 5 ft of sludge simulant at void fractions between 0% and ~20%. As mentioned in Section 4.3.3, the UT transducer frequency selected based on the scoping test was 250 kHz.

Using the acoustic test cell in a similar manner to the scoping test, correlation development for the ultrasonic void fraction measurement technique was performed before tall column tests. Correlation tests were performed for both a nominally 500 Pa and a 1000 Pa kaolin-water simulant, each with 0.35 wt%

[1] The shear strength was not measured. The 1000 Pa simulant was prepared based on historical PNNL data for mass fraction of kaolin and shear strength (Gauglitz et al. 2012) and a small adjustment based on experience with preliminary simulant mixtures.

iron (these are described in more detail in Appendix C). As gas was generated in the simulant and the sludge/water interface changed, the level measurements using a series of rulers affixed to the test cell were used to calculate an average void fraction in the test cell. Ultrasonic measurements were made continually during the correlation test such that the observed ultrasonic attenuation could be correlated with the observed average void fraction in the test cell. The results of this investigation are shown in Figure 6.10 and Figure 6.11 for the 500 and 1000 Pa correlation tests, respectively. For a more detailed discussion of the correlation test results, refer to Appendix C. To summarize the implications of the correlation test data, the variable slopes in the attenuation-vs.-void fraction 500 Pa correlation data (Figure 6.10) mean the correlation can only be used to reliably quantify GVF from 0% to 2% GVF and 10% to 15% GVF and determine if GVF is "between 2% and 10% GVF" for tests with ~500 Pa kaolin. The 1000 Pa correlation data (Figure 6.11) has a monotonically increasing slope after ~2% GVF and can quantify GVF from 2 to 12% GVF.

Figure 6.9. Picture of Acoustic Test Cell Used for Correlating Void Fraction Measurements

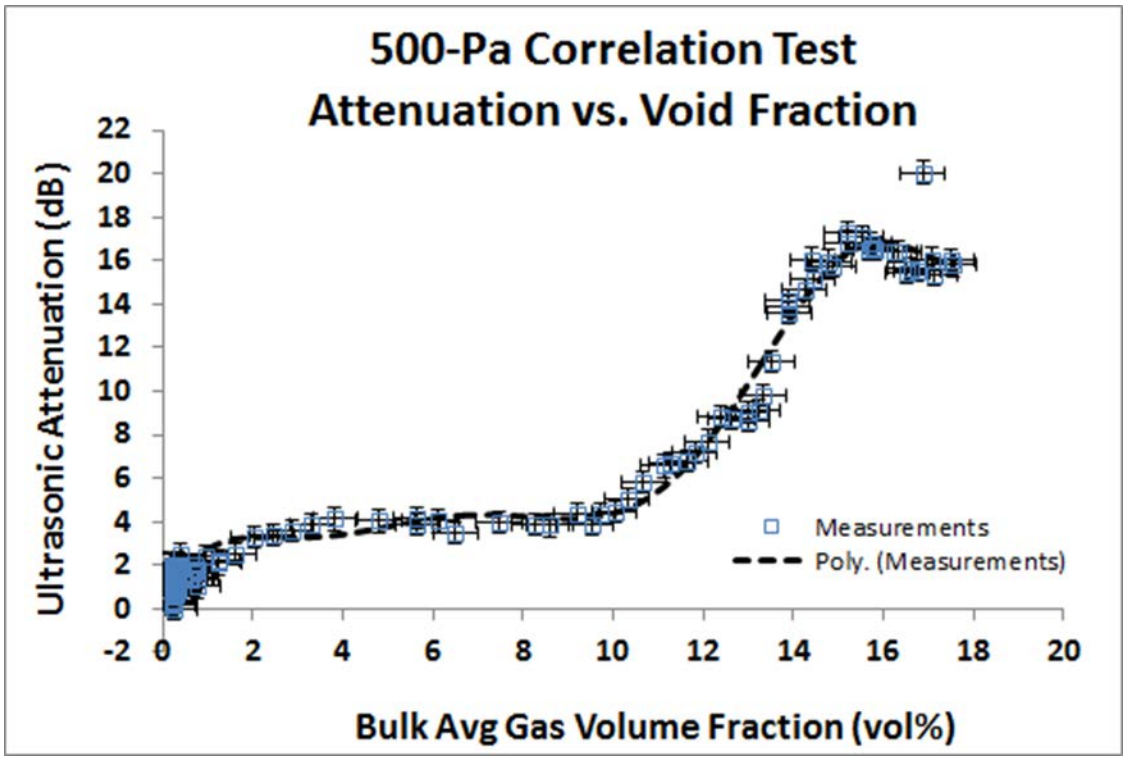

Figure 6.10. Attenuation as a Function of GVF for the 500 Pa Correlation Test

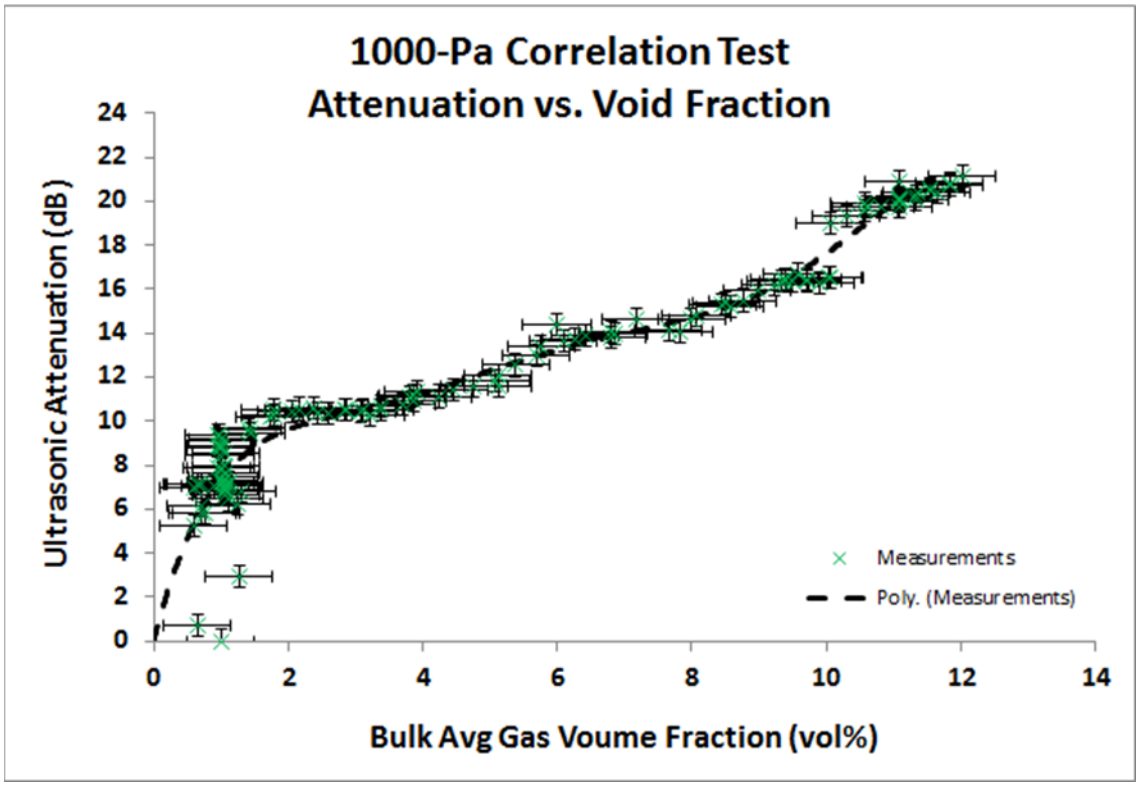

Figure 6.11. Attenuation as a Function of GVF for the 1000 Pa Correlation Test

The sample ports were used for testing the core sampling system once it was ready for a performance check. After the UT correlation data had been collected, the simulant in the acoustic test cell contained a bulk (average) void fraction that was known. The core sampler was attached to one of the available flanges and tested in an environment that simulated the tall column, i.e., a "prototypic-test" of the sampler. Aside from the geometry of the acoustic test cell, all other facets of operation were identical to how it was implemented in the tall column tests.[1] This evaluation of the core sampler was an opportunistic scoping test conducted during the sampler development, and in advance of conducting the formal tests discussed in Appendix B that followed the project QA plan. Accordingly, the results of this evaluation of the core sampler are FIO. The results of analyzing the core sampler data on the sample taken from the acoustic test cell gave a void fraction value that was compared against the bulk void fraction measured in the test cell. The core sampler void fraction was, as previously mentioned, significantly larger than the known void fraction. The source of the bias in the measurement is unknown. The core sampler was still deployed during testing but, based on these initial measurements, was not expected to provide quantitative measures of void fraction in the tall column experiments.

6.1.4 Small Column Testing

During simulant loading for each tall column experiment, ~5-L samples were removed from each batch mixed at the CTF and taken to PNNL where they were loaded into small acrylic columns. These parallel tests were run to see if there was significant variation in gas production between the batches loaded into the column. The acrylic columns had a nominal inside diameter of 5 in. and were approximately 12 in. tall. These columns were also used to perform the majority of the simulant development work described in Section 5.0, with the exception of the temperature studies (described in the next paragraph). Simulant was placed in the column and a water layer was added to monitor changes in gas content. An inverted graduated cylinder was used with the 5-in. acrylic columns to measure the gas as it was produced. An example of an acrylic cylinder loaded with simulant is shown in Figure 6.12.

[1] Meaning that the acoustic test cell was not a full cross-section nor did it have the full height of sludge (and thus the pressure that might be experienced at different depths) that the tall column had during testing. It was, however, a geometrically prototypic "slice" of the column and essentially axisymmetric.

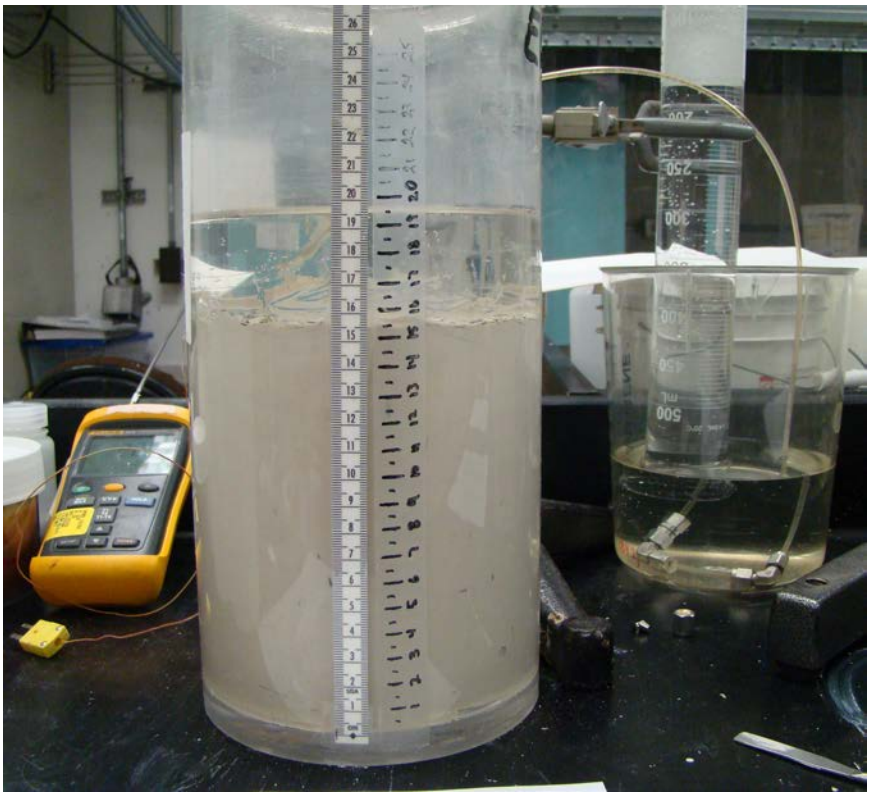

Figure 6.12. Acrylic Vessel (5 in. diameter) Used for Simulant Studies and Tall Column Parallel Testing

The simulant temperature studies discussed in Section 5.2.2 were performed using closed-top stainless steel vessels. These vessels had a working volume of around 150 to 200 mL and could be temperature-controlled by placing them in water baths. An example of the stainless steel vessel in use during a room temperature reaction study is shown in Figure 6.13. The figure also illustrates how the gas produced during a reaction was collected and measured—using an inverted graduated cylinder. A thermocouple monitors the simulant temperature as pictured. The stainless steel vessels do not allow visual observation of the simulant and thus reaction data were limited to gas volume measurements.

Figure 6.13. Stainless Steel Vessel Used for Simulant Temperature Testing

6.1.5 Characterization Measurements

The key properties of the simulant used in the tall column experiments that were determined with laboratory characterization tests were the total solids (moisture content) and the shear strength. The shear strength characterization and documentation followed the RPL-COLLOID-02 procedure,[1] and the moisture content measurements were conducted according to procedure OP-WTPSP-004.[2]

Shear strength, τ_s, was determined by the shear vane method using an instrument (e.g., Thermo Fisher Scientific HAAKE Viscotester 550) that was qualified with certified viscosity standards. The shear vane used had a cross-pattern (viewed from the end) and was 16 mm diameter by 32 mm high. For most samples, the shear strength was measured immediately after collection and then left undisturbed for a minimum of 30 minutes. After the ~30-minute period elapsed, another measurement was taken. In a few cases, samples were purposely disturbed or agitated prior to the initial measurement; this was typically after the sample had spent several days undisturbed. This was done to release bubbles and homogenize the sample.

Moisture analysis was conducted using a Mettler Moisture Analyzer, Type HR83, that was performance checked according to the relevant procedure. The moisture analyzer dried samples at 105 °C until the remaining weight was unchanged, i.e., mean weight loss <1 mg over 140 seconds. It reported %DC (percent dry content), which is equivalent to the total solids for a material with no dissolved solids in the liquid phase. This is a reasonable assumption for the kaolin-water simulant used in this work and the two terms are used interchangeably in this report.

[1] Daniel RC. 2011. *Measurement of Physical and Rheological Properties of Solutions, Slurries and Sludges*." RPL-COLLOID-02, Rev. 2, effective 03/11/2011.
[2] Burns CA. 2012. *Operation of the Mettler Moisture Analyzer*. OP-WTPSP-004, Rev 1.0, effective 09/04/2012.

6.1.6 Measuring and Test Equipment Summary

The various measuring and test equipment (M&TE) used in the tall column experiments is summarized in Table 6.1. The target accuracy and achieved accuracy for each measurement type are given in the table. Accuracies of M&TE used in support testing (acoustic test cell, small columns, and analytical measurements) are not presented in the table, but are discussed in the preceding sections where the support work was described.

Table 6.1. Tall Column M&TE Specifications and Requirements

Required Measurement	Instrument (General and/or Specific Examples)	M&TE Category[(a)]	Target Accuracy	Notes on Accuracy
Mass of Simulant Components	Dynamometer: MSI 4260, Electronic Scale: Ohaus CQ250XL11, Flow Rate Totalizer: John C Ernest Co. S20N	1	±1% of mass	Met using given equipment
Mass of Simulant in Column	Load cells (4): Mettler-Toledo Model SLC610	1	±20 lb	Met: This was the resolution of the load cells and display
Temperature of Simulant in Column	Thermocouple (type K) and Display/Readout	1	±2 °C	Thermocouples were ±2.2 °C from 0 °C to 100 °C
Pressure, Barometric	Druck Novus 1500	1	≤ ±0.2% of Full Scale (≤ ±1.0 mbar)	750 to 1000 mbar, ±2.5 mbar; >1000 to 1250 mbar, ±7.5 mbar
Pressure, Pore Water	PNNL-modified Druck UNIK 5000	1	≤ ±0.2% of Full Scale (≤ ±0.3 kPa)	±0.75 kPa (gauge), range 0 to150 kPa
Pressure, Total	Druck PXT 1290 transducer	1	≤ ±0.2% of Full Scale (≤ ±0.3 kPa)	± 0.685 kPa, (gauge), range 0 to 137 kPa
Images and Video	Array of 10 CSP-700BW Cameras with 16-channel HDMI Digital Video Recorder	n/a	Field of View ≥6 in. vertical; Resolution ≥2 pixels per mm	Achieved field of view ≥10 in. vertical; resolution was ~4 pixels per mm
Levels (Height or Depth)	Ruler and/or visible gradations in viewing column	3	±1/4 in.	Actual accuracy ±1/8 in.
Time	Commercial clocks, cell phones, and watches	3	Accuracy of ±5 s Synchronize before start of test	Met
Gas Volume In/Out of Column	Wet Test Meter (Ritter LitreMeter TG5/3-ER)	1	±0.2% (standard flow) ±0.5% (full range)	±3% (full range) for volume and ±14 L/h or 1.5% (whichever is greater) for flow rate
Temperature of Gas In/Out of Colum	Thermocouple (type K) and Display/Readout	1	±2 °C	Thermocouples were ±2.2 °C from 0 °C to 100 °C
Ultrasonic Gas Volume Fraction Measurement	Pulser-receiver, multiplexer, ultrasound transducers, and associated hardware	2	±3% gas fraction	Actual accuracy uncertain, dependent on correlation in use
Sampling System Gas Volume Fraction Measurement	Core sampler and associated instruments (pressure, temperature, volume)	n/a	±3% gas fraction	Not achieved, sampler gas fractions suspected of bias

(a) M&TE Categories:
Category 1 – M&TE that is calibrated with traceability to a nationally recognized standard or physical constant, performed under controlled conditions and by an evaluated and accepted calibration laboratory, agency, or metrology facility.
Category 2 – M&TE that can be calibrated prior to and verified prior to and after use, by the user, with certified standards traceable to a nationally recognized standard or physical constant. The calibration frequency shall be called out in the associated instrument operating procedure.
Category 3 – Commercial devices procured as normal commercial equipment that provide adequate accuracy, such as rulers, tape measures, and graduated glassware.

6.2 Test Operations

This section describes the general steps that occurred during test operations. Many of these test steps were performed by an amalgam of staff from several organizations: PNNL, WRPS, Total Site Services, American Rock Products, Harms Pacific Transport, Ralph's Concrete Pumping, Dade Moeller, Intermech, and others. The party or parties responsible for executing each operational step are not outlined below; rather, the operations are treated as if they were performed by a single entity. In general, the tests were directed by PNNL with support from all the other organizations. Deviations from these steps that occurred in one test but not others are discussed independently for that test in Section 7.0.

6.2.1 Hydrogen Management

The iron particles added to the kaolin slurry corrode to generate hydrogen gas, and the hydrogen flammability hazard was actively managed and controlled for all aspects of test operation. The overall approach was to meet the requirements in the National Fire Protection Association standards NFPA 496 and 497. The primary methods of actively controlling the hydrogen flammability hazard were the following:

1. Inert the column headspace prior to the kaolin/iron simulant generating and releasing hydrogen by purging the headspace with 5 volumes of nitrogen. This purge was done at approximately 8 cfm nitrogen.

2. Avoid any influx of air (oxygen) by having a purge of nitrogen during testing. The flow rate of this purge was set to approximately match the peak hydrogen generation rate of the kaolin/iron simulant (~ 0.15 cfm).

3. During the initial cleanup activities of draining simulant from the column, avoid influx of air (oxygen) by increasing the nitrogen purge to exceed the withdrawal rate of simulant from the column (the operation used ~ 8 cfm nitrogen with a maximum removal rate of ~ 25 gpm from the column).

4. At the end of testing and prior to switching to purging with air for cleanup activities, purge the column headspace with nitrogen to reduce the hydrogen concentration to below 1 vol% (note that 1 vol% hydrogen in air is 25% of the lower flammability limit, so this purge was done to prepare for allowing air to enter the column). This purge was done at approximately 8 cfm nitrogen.

5. Direct vent discharges from the tall column through hoses that would not collect static charge and vent the gas to the atmosphere in an exclusion area away from the tall column.

6. Minimize spark sources for work on or near the column by using spark-resistant hand tools and non-sparking equipment, and by point-discharging tools, equipment, and personnel at grounding locations near specific work areas.

7. Monitor the work area for hydrogen gas during simulant preparation and loading, tall column testing, and column cleanout activities. This includes monitoring the headspace of the cement truck drums during mixing and loading.

Note that the multi-day delay in the onset of hydrogen generation that was observed in the laboratory studies (See Section 5.0) did not occur in the tall column tests (See Section 7.0), and this complicated the hydrogen management during simulant mixing and column loading. The cause of the fast onset of hydrogen generation has not been determined. Ideally, any future testing using large industrial equipment, similar to what has been described here, should determine how to delay the onset of hydrogen generation so the hydrogen generation begins after the kaolin/iron slurry is inside an inert column.

6.2.2 Simulant Preparation

The simulant in the tall column testing was prepared using industrial equipment, including cement trucks, a hot water truck, and forklifts. A diagram that illustrates the mixing and loading process is given in Figure 6.14. The diagram contains all the major elements of the process; however, the mixing sequence was more dynamic than a figure can convey. Many of the steps were conducted simultaneously as different batches (cement trucks) were in different parts of the process. The general flow of steps was as follows:

1. Kaolin solids were pre-weighed into sacks of 1000 to 2500 lb each using a dynamometer attached to a forklift; the sacks were divided into sets that made up the amount required for a batch (usually 5 or 6 sacks made up a batch).

2. The heating system of the column was started to increase the skin temperature of the column to the ~75 °F set point before the simulant was loaded.

3. Hot water was added into a cement truck using a flow totalizer attached to a hot water truck (~140 °F water) and blended with cold water that was added from a supply of Richland city water, again using a flow totalizer (~45 °F water). Some water was withheld from the recipe amount, often both for temperature adjustments and an aliquot of 25 gallons for loading in the iron particles.

4. Biocide was added into the cement truck using a small container.

5. The kaolin solids were loaded into the cement truck using a forklift and staff on scaffolding.

6. The slurry temperature was measured using a long thermocouple to assess what temperature adjustments might be required. This also occurred periodically for the rest of the preparation process.

7. Additional cold and/or hot water was added for temperature adjustment as described in Step 3.

8. The trucks mixed the slurry after the additional water was added for at least 30 minutes, then a ~500 mL sample was taken from the cement truck.

9. The shear strength of the sample was measured immediately on-site to assess if the slurry had shear strength values within the desired range of acceptance. Adjustments could be made if this was not the case (not required for Tests 1, 2, or 3B).

10. The iron was not to be added if the temperature was greater than 90 °F, and preferentially the temperature would be closer to 75 °F to 85 °F. The simulant continued to be mixed until the temperature dropped into this range. For some of the simulant batches, the cement trucks were positioned under a large cold water spray to reduce the temperature more quickly.

11. The iron was loaded by measuring dry Fe particles on a scale (often done prior to this step), then wetting the particles in 25 gallons of water and pumping the slurry into the cement truck through a nozzle (distributor).

12. The batch was mixed for at least 30 minutes to incorporate the iron into the simulant.

At this point in the process, the simulant preparation was complete and the loading process began. The corrosion reaction of the iron can theoretically occur whenever it is contact with water, so from Step 11 onward, work areas were monitored continuously for the presence of hydrogen gas.

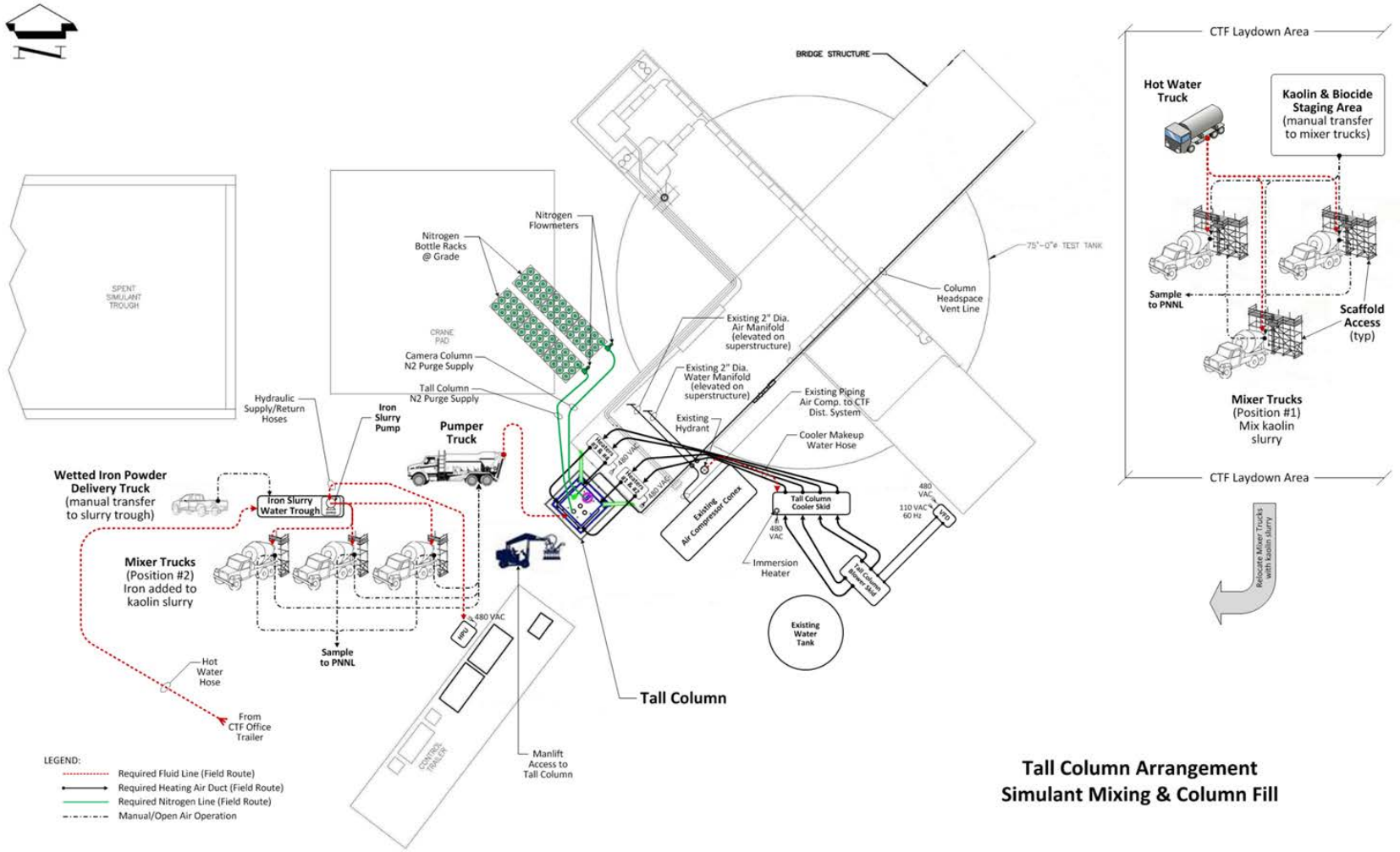

Figure 6.14. General Diagram Illustrating the Simulant Mixing and Filling Process and Approximate Equipment Configurations. Variations from this diagram did occur in some tall column tests.

6.2.3 Simulant Loading

Continuing from Section 6.2.2, the simulant loading process had the following general steps:

1. A pumper truck was staged near the tall column, approximately as shown in Figure 6.14.

2. Cement trucks with prepared batches were staged to load into the pumper truck intake, sometimes with two trucks at the same time (but more often one at a time).

3. The batch was loaded into the pumper truck intake. During the removal of simulant from the cement truck, two samples were collected. One sample (~500 mL) was for immediate measurement of shear strength to confirm the as-prepared shear strength, and the other (~5 L) was for parallel small column tests described in Section 6.1.4.

4. The pumper truck with an equipped boom pumped the simulant into the column from a valve at the column bottom. The camera system was used to monitor the progress of the fill.

5. When a cement truck batch was done loading into the pumper truck, it was replaced with another truck and the process continued.

6. The fill proceeded until the level as seen on the rover camera reached the target level for the test. The pumping stopped immediately and the bottom valve was closed. Excess material in cement trucks and the pumper truck was discarded.

7. A water layer was added on top of the simulant layer through a ball valve on the top of the column. This was also monitored using the rover camera until the target level was reached.

8. The headspace was purged using a high flow rate of nitrogen gas to render the space above the simulant oxygen-deficient. Note that in Test 3, this step was done before the slurry was loaded.

9. After a sufficient number of headspace volume exchanges, the purge flow rate was reduced to a lower flow rate for the rest of the test.

Upon completion of these steps, the column was loaded with simulant and the test proceeded as outlined in the next section.

6.2.4 Test Monitoring

The test monitoring phase did not consist of a prescribed set of steps that were conducted in a certain order, as the primary task was to observe the column and its contents. However, the test monitoring phase included activities such as the following:

- Maintaining the annulus temperature using the heated air system (keeping the temperature around 75 °F on the column skin).

- Checking the functionality of the nitrogen purge system (the primary safety system of the tall column as it was producing H_2 gas).
- Monitoring the water and slurry levels using the rover camera.
- Recording data (mass, temperature, pressure, gas volumes, etc.) from instrument displays.
- Observing gas generation and void formation in the simulant using the video system.
- Collecting ultrasonic data or confirming the UT DAS was functioning properly.
- Taking core samples at predetermined times. Core sample collection required the use of the man lift and additional support for sample analysis.
- Using "real-time" data to determine when the test was completed and could be discontinued.

The tall column was staffed continuously 24 hours a day while the column was filled with simulant that was actively generating hydrogen gas.

6.2.5 Post-Test Compression

The test was considered complete if a peak bulk void was observed and no additional significant gas generation or increases in level were occurring (roughly 2 to 3 days past peak void). The test was run long enough (i.e., the simulant was exposed to a sufficient quantity of in-situ-generated gas from the iron) to give the simulant every opportunity to exhibit changes or variations in gas retention behavior. Once the test was completed, a post-test compression was performed. The general steps of the post-test compression were as follows:

1. The current water level and column mass were obtained; preparations were performed to add additional water through the top of the column.

2. All the video cameras were directed to record in real-time (30 frames per second) if they weren't already recording at that rate.

3. Approximately 8 to 9 ft of additional water was added to the existing water layer to supply a change in hydrostatic pressure in the column. The new water level and column mass were measured.

4. The gas in the column was compressed with the additional pressure. The resultant downward motion of void was observed on the fixed cameras.

5. The simulant was monitored for several hours after the compression event; data continued to be collected and the column simulant was watched for signs of any peculiar behavior.

The test was complete once the monitoring in the last step ended. The simulant was removed from the column while the purge system was switched back to a high flow rate. After being emptied, the tall column was cleaned in preparation for the next test.

7.0 Tall Column Test Data

The equipment described in Section 6.0 was used to conduct three tall column tests.[1] The tests were conducted according to the test matrix presented in Table 4.1 and are described in chronological order. For each test, a brief narrative of the test and any departures from general test operations (as delineated in Section 6.2) are given, followed by a discussion of the key parameters (temperature, shear strength, gas production, d_{max} estimates) of the test. After presenting data from the three tests, a comprehensive discussion of the gas generation characteristics of the tests is made. The data of primary interest, the gas void fraction measurements and evidence of gas transport below estimates of d_{max} for each test, are of sufficient importance that they are discussed separately in Section 8.0.

7.1 Tall Column Test 1

Tall Column Test 1 began on 12/28/2013. The only instruments not installed for Test 1 were the pressure transducers described in Section 6.1.2; all other instrumentation was in use. The first day, three batches of sludge simulant (slurry) were prepared, each with a volume of approximately 6.5 yd^3. Temperature control of the simulant as it was being mixed in the cement trucks, which was a concern prior to testing, was achieved despite low outside air temperatures (30 °F or less). In fact, the simulant retained enough heat that a few hours were spent waiting for the slurry to cool down to the target temperature range (<85 °F) before the iron was added. Upon loading the column after the iron was added to each batch, the target level of 310 in. was not achieved. The suspected cause of the shortfall was that a significant amount of the simulant, which is cohesive, stuck to the inside of the cement truck mixing drums and could not be moved to the pumper truck intake. Estimated holdup of simulant based on the as-mixed batch masses suggested that around 40% to 45% of the simulant by weight remained behind in each truck. Though some simulant loss was accounted for in the batch recipe (which included an excess of 10% by weight), it had not been expected to occur to that magnitude. The slurry was loaded only to a height of approximately 182 in. the first day. A ~26 in. water layer was added to the slurry and the column was monitored overnight. A small amount of gas generation, indicated by the presence of new voids, was observed on a few of the cameras over the first 12 hours, but the total amount of gas generated in this initial period was small. Any initial gas generated in this period is included in the estimate of initial void for Test 1.

To make up the remaining required simulant amount, on 12/29/2013 two additional batches were prepared that were each approximately 8.0 yd^3. The larger batch size used on the second day was to adjust for the greater amount of simulant holdup that was observed on the first day. After loading the column the second day, a slurry level of 320.25 in. was reached (compared to a target of 310 ± 10 in., putting the level at the upper end of the target range). The loading process is illustrated in Figure 7.1, where the approximate size and location of each batch, along with the initially measured shear strength and temperature, are shown in the column. The as-mixed batch compositions for all five batches are shown in Table 7.1, along with the shear strength measured before and after iron addition. Recall that the target shear strength for the test was 500 Pa. The shear strength values in Table 7.1 can be averaged to

[1] This does not include an aborted first attempt of Test 3, which was followed by a mixing pre-test that preceded the second (successful) attempt at Test 3. For this reason, Test 3 is also interchangeably referred to as Test 3B.

compute a bulk as-loaded shear strength of 594 ± 84 Pa,[1] which was within the acceptable range for the test (350 to 800 Pa). Loading on the second day was completed on 12/29/2013 at 22:26, which serves as the t = 0 marker when the elapsed time of the test is discussed.

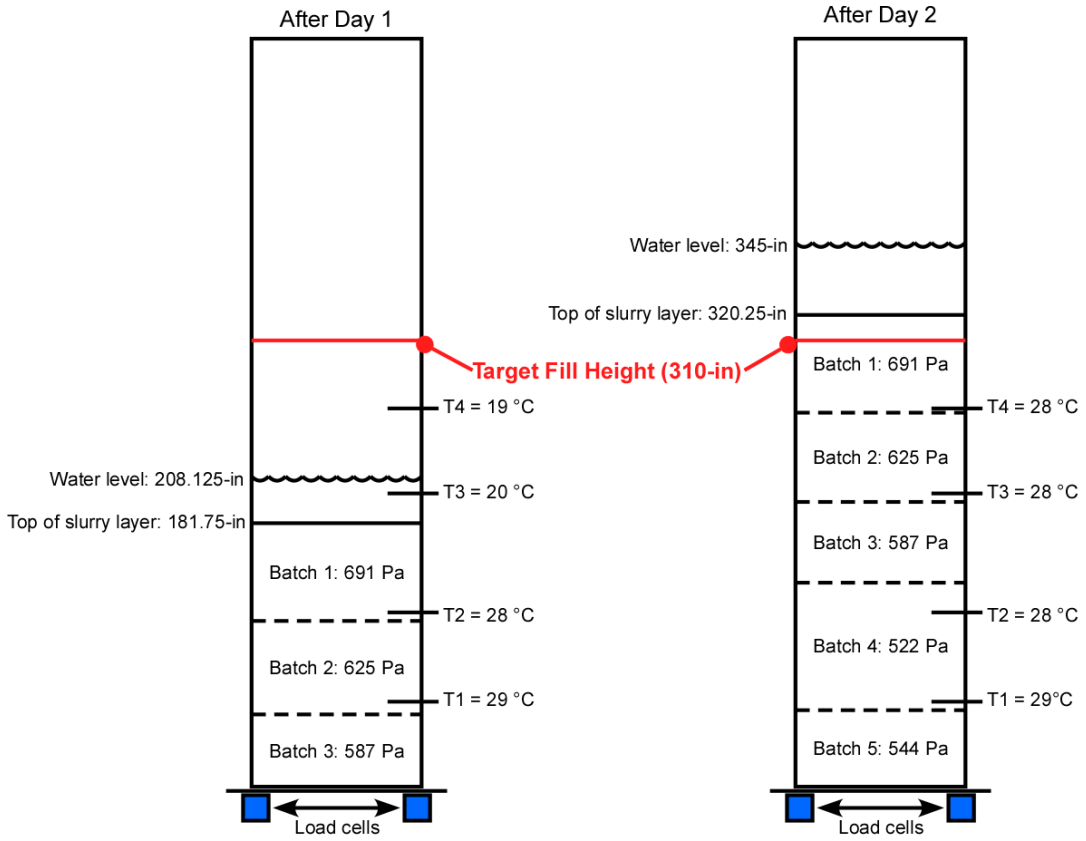

Figure 7.1. State of the Tall Column after Completion of Loading on Day 1 (left) and Day 2 (right) of Test 1. The dotted lines are estimated batch sizes and locations based on test observations – they do not represent quantitatively measured amounts.

[1] The uncertainty given is an estimate of the standard error in the average at the 95% confidence level.

Table 7.1. Simulant Batch Properties for Tall Column Test 1

	Batch 1	Batch 2	Batch 3	Batch 4	Batch 5
Date Batch Mixed	12/28/13	12/28/13	12/28/13	12/29/13	12/29/13
EPK Kaolin	8913.9 lb	8931.9 lb	8923.1 lb	11,102.5 lb	11,121.9 lb
Water[(a)]	7509.8 lb	7509.9 lb	7509.7 lb	9623.2 lb	9597.1 lb
Zero Valent Iron	58.2 lb	58.0 lb	58.0 lb	72.6 lb	72.6 lb
Mt. Hood 480 Biocide	1.3 lb	1.3 lb	1.3 lb	1.6 lb	1.6 lb
Shear strength (before Fe addition)[(b)]	626 Pa	566 Pa	564 Pa	553 Pa	573 Pa
Total solids (before Fe addition)[(c)]	54.9 wt%	54.7 wt%	55.3 wt%	52.9 wt%	53.5 wt%
Shear strength (after Fe addition)[(b)]	691 Pa	625 Pa	587 Pa	522 Pa	544 Pa
Total solids (after Fe addition)[(c)]	55.9 wt%	52.9 wt%	54.6 wt%	53.3 wt%	52.4 wt%

(a) Not all the water used to make up Batches 1–3 was measured with calibrated instrumentation. The water mass for those batches is For Information Only. When making quality-affecting calculations, the as-measured water content for those batches should be inferred from the total solids measurements.

(b) The shear strengths presented here were measured after a 30-minute period where the sample was left undisturbed. The 30-minute undisturbed period followed an initial shear strength measurement made immediately after the sample was collected (data not shown). The differences between the initial and 30-minute measurements were typically negligible (within the uncertainty of the measurement technique).

(c) The total solids measurements were not conducted immediately after the sampling, giving the samples opportunity to evaporate some moisture over time. This is the likely reason for the variability in the total solids measurements and values that are elevated relative to Test 2 (Table 7.3) and expectation.

From t = 0 h and onward, the test was constantly monitored via the cameras and instrumentation. Core samples were taken near the start of the test over a two-day period (one sample each from elevations S1, S2, and S3 at approximately 16 h elapsed time, and one sample each from elevations S4 and S5 at approximately 33 h). These samples were assessed for void fraction (see Appendix B) and later aliquots were taken and analyzed for shear strength and total solids. The water level presented in Figure 7.2 increased slowly in the first several hours and then steadily increased (reflecting gas accumulation in the simulant). A peak in water level was reached at approximately 65 h elapsed time. A peak level is also reflected in the more sparse measurements of slurry level. The slurry level was initially well-resolved but measuring it was more challenging as the test progressed due to the evolution of gas from the slurry. The release of gas bubbles smeared the interface between the slurry and the water, in addition to suspending solids in the water and giving it a “muddy” appearance. This was observed in all three tests and makes the slurry level measurements very uncertain, especially data collected after the peak water level was observed.

After the peak water level at t = 65 h, the slurry began to noticeably consolidate (or compact). The extent of the consolidation is difficult to quantify, but it was observed both in the slurry level data (though

with higher uncertainty) and when viewing the video images collected during the test. Time-lapse video shows the slurry, or rather the gas trapped in the slurry, moving downward with time as it compacts. Since the consolidation process results in dewatering of the slurry, the water level did not drop in proportion to the amount of compaction that was occurring. Core samples taken near the end of the test (at approximately 129 to 133 h) were analyzed in the same manner as at the start of the test. The end-of-test core samples also support that consolidation was taking place, as the total solids were higher at the end of the test, especially at the two highest sample elevations (S4C and S5C) where the video images showed the most downward motion (see Appendix A for the core sample data). Following the test, a post-test compression was performed by adding an additional water layer on top of the exisiting water layer. Water was added until the level reached 464.75 in,. adding almost nine additional feet of head to the simulant column. The data collected during the compression is tabulated in Appendix A and analyses conducted using the data are discussed in Section 8.0.

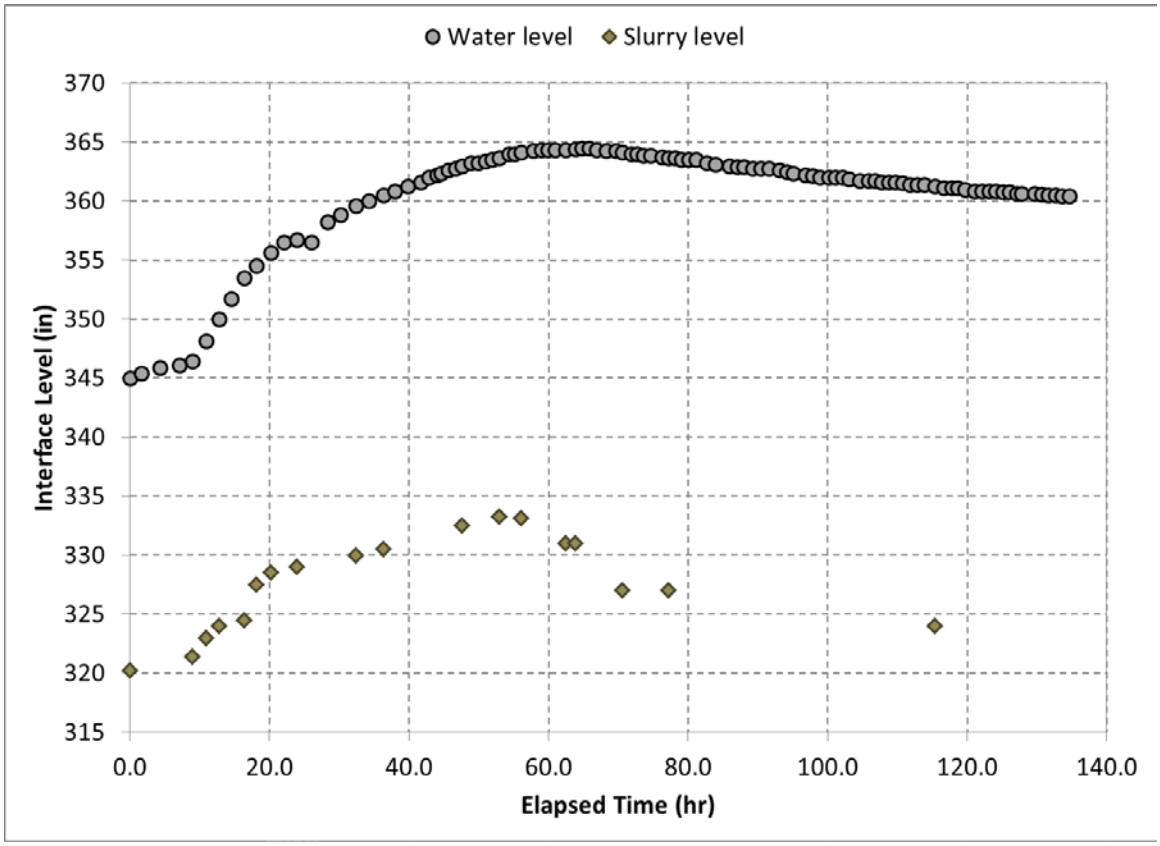

Figure 7.2. Water and Slurry Levels Measured During Tall Column Test 1

As mentioned in Section 6.0, the gas in-flow and out-flow were monitored and this data was collected to estimate the generation rate of H_2 gas during the experiment. The hydrogen gas generation rate versus elapsed time for Test 1 is given in Figure 7.3, where each data point represents the average rate over the period elapsed since the previous data point. The peak rate was approximately 4.5 L/min and it nearly corresponds to the peak water level, occurring about 5 hours before. After the peak rate was observed, the gas generation rate slowly decayed to around 1 L/min by the end of the test, in accordance with how the iron corrosion reaction has been observed to slow down in the small column experimental studies. The peak rate was very close to the expected peak rate based on laboratory studies and the intermediate column experiments (see Section 5.3).

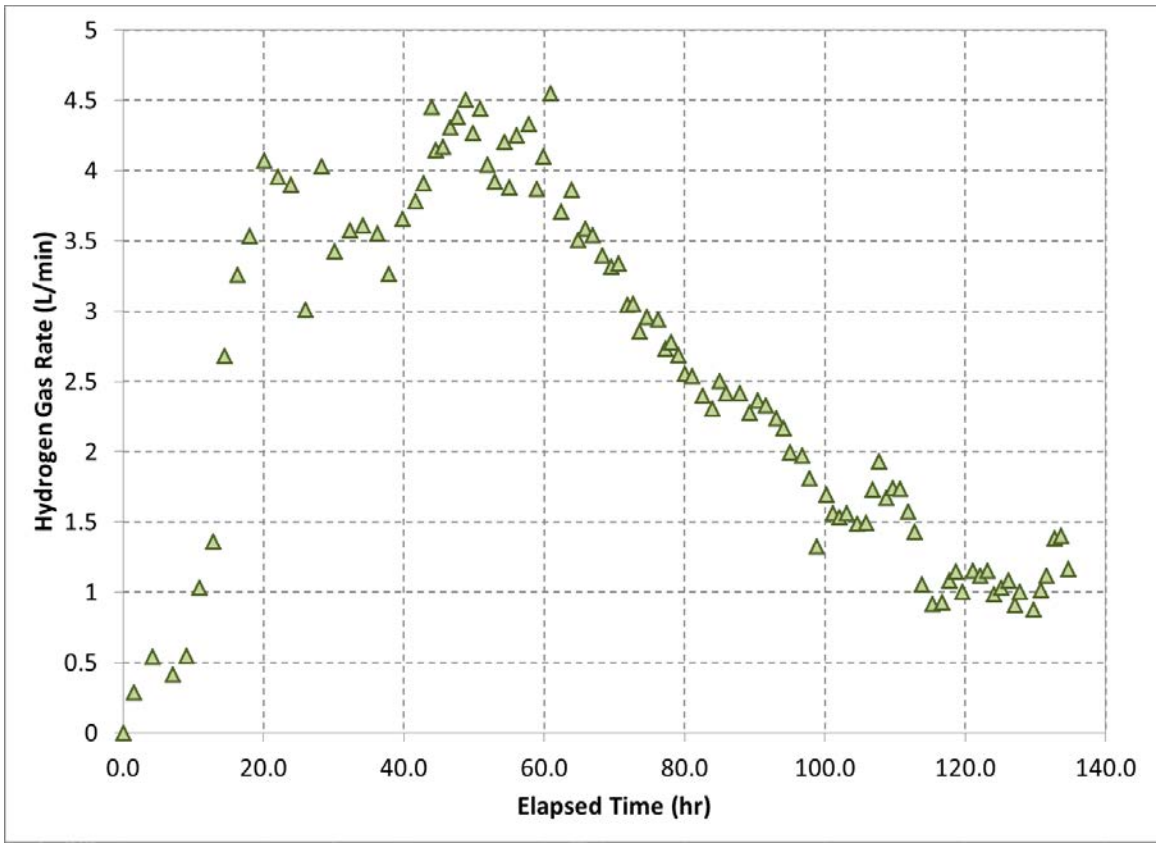

Figure 7.3. Hydrogen Generation Rate Estimated for Tall Column Test 1

The other important distinction that the measurement of gas in-flow and out-flow volumes can provide is whether the gas that is generated in the simulant caused primarily expansion of the slurry (all or most of the gas is retained), venting of gas into the column headspace and out the stack (all or most of the gas is released), or some combination of both. Since the iron concentration was chosen to generate enough gas to achieve approximately 50% void at the column bottom if all the gas was retained, the slurry had ample amounts of generated gas available to reach high void fraction if such retention mechanisms were present. Comparison of the amount of gas retained (inferred from the water level data) and the amount of gas released (using the gas volume measurements) is shown in Figure 7.4 as a function of elapsed time in Test 1. The data indicate that the majority of gas produced in the simulant was released and only a small fraction was retained. The data also do not imply that there were any episodic releases as the net gas volume leaving is smooth and monotonically increasing. These data observations are also supported by the void fraction data measured during Tall Column Test 1 (see Section 8.3).

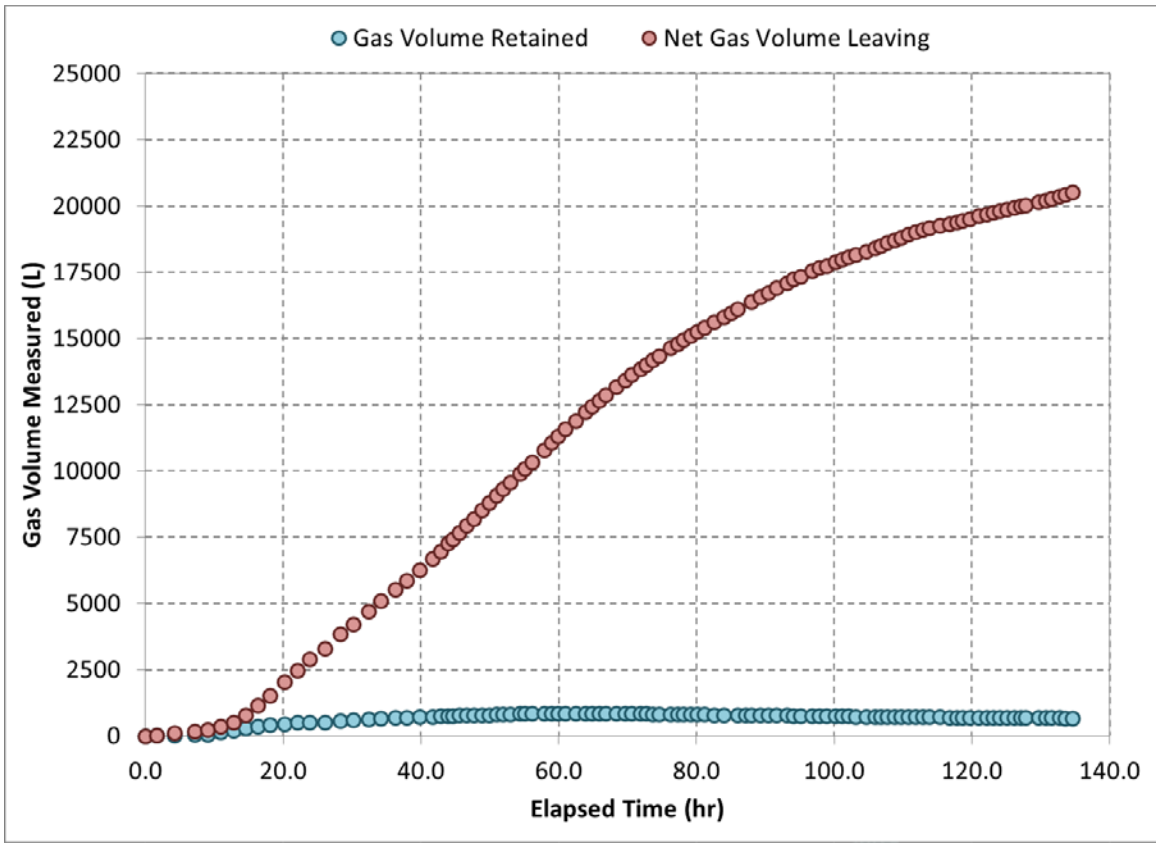

Figure 7.4. Comparison of Gas Volume Retained and Net Gas Volume Leaving the Tall Column During Test 1. The net gas volume is calculated by difference from the in-flow and out-flow wet test meters and was assumed to be only hydrogen.

As the primary objective of the tall column tests was to challenge the predictions of van Kessel and van Kesteren (2002), estimates of d_{max} were repeated using the methodology discussed in Section 4.2 with the as-measured parameters for Test 1, using properties from both the bulk (average) and the batch with the greatest shear strength. These estimates are given in Table 7.2, along with the minimum amount of depth below d_{max} that would be present based on the initial slurry level. By even the most conservative measure, there was initially at least 98 in. (8.2 ft, 2.5 m) of simulant below d_{max} in Test 1; recall from the description of the column that at least three fixed cameras (C1, C2, and C3) were below this level.

Table 7.2. Comparison of d_{max} Estimates for Target, Bulk, and Highest Batch Properties in Tall Column Test 1. The minimum depth below d_{max} indicates the minimum amount of simulant below d_{max} that would be expected based on the basis parameters.

Basis	Shear Strength (Pa)	Waste Depth (in.)	Conservative d_{max} Estimate (in.)	Representative d_{max} Estimate (in.)	Minimum Depth Below d_{max} (in.)
Target properties	500	310	170.0	102.7	140.0
Bulk properties[(a)]	594	320.25	200.9	121.6	119.3
Highest shear strength[(b)]	691	320.25	221.3	134.0	98.9

(a) "Bulk properties" indicates that the mean properties (shear strength, kaolin mass fraction) of all the batches loaded in the test were used to determine d_{max} via Equation 4.3.

(b) "Highest shear strength" indicates that the batch with the greatest shear strength (Batch 1 from **Table 7.1**) and its corresponding kaolin mass fraction were used to determine d_{max} via Equation 4.3.

Tall Column Test 1, from a gas generation perspective, was unique due to the two-day loading process. The various batches of simulant were all observed to react (create gas) at different elapsed times, with the formation of voids in the slurry occurring less simultaneously than it did in the other two tests. This is also clear when comparing the gas generation rates of the various tests – see Section 7.4). This is largely due to the top half of the simulant having contact with zero valent iron almost 24 more hours than the bottom half. There was, however, heterogeneity of gas generation even when comparing material loaded on the same day. This was attributed primarily to the difficulty in homogeneously mixing a small fraction of Fe particles into a large simulant matrix using larger industrial equipment over short timescales. This reaction heterogeneity did not completely disappear in later tests but was less prominent.

7.2 Tall Column Test 2

Tall Column Test 2 began on 01/16/2014. As mentioned earlier, all instrumentation, including the pressure transducers, was in use. Based on experience with simulant holdup in Test 1, four batches of sludge simulant (slurry) were prepared, each with a volume of approximately 8.5 yd^3. As before, temperature control of the simulant was achieved despite low outside air temperatures (45 °F or less). The slurry was loaded to a height of 318.75 in., which was within the criterion for initial simulant fill level. A ~24.5-in. water layer was added to the slurry and the monitoring period began immediately after the addition of water. The initial state of the column is illustrated in Figure 7.5, where the approximate size and location of each batch, along with the initially measured shear strength and temperature, are shown. The as-mixed batch compositions for all four batches are shown in Table 7.3, along with the shear strength measured before and after iron addition. Recall that the target shear strength for the test was 500 Pa. The shear strength values in Table 7.3 can be averaged to compute a bulk as-loaded shear strength of 627 ± 36 Pa,[1] which was within the acceptable range for the test (350 to 800 Pa).

[1] The uncertainty given is an estimate of the standard error in the average at the 95% confidence level.

Table 7.3. Simulant Batch Properties for Tall Column Test 2

	Batch 1	Batch 2	Batch 3	Batch 4
Date Batch Mixed	01/16/14	01/16/14	01/16/14	01/16/14
EPK Kaolin	11,540.1 lb	11,559.5 lb	11,549.8 lb	11,552.1 lb
Water[(a)]	9943.2 lb	9963.8 lb	9968.8 lb	10,012 lb
Zero Valent Iron	75.5 lb	75.5 lb	75.5 lb	75.5 lb
Mt. Hood 480 Biocide	1.6 lb	1.6 lb	1.6 lb	1.6 lb
Shear strength (before Fe addition)[(a)]	605 Pa	677 Pa	673 Pa	603 Pa
Total solids (before Fe addition)	52.8 wt%	52.5 wt%	53.1 wt%	53.0 wt%
Shear strength (after Fe addition)[(a)]	598 Pa	642 Pa	620 Pa	648 Pa
Total solids (after Fe addition)	52.6 wt%	52.8 wt%	52.6 wt%	52.1 wt%

(a) The shear strengths presented here were measured after a 30-minute period where the sample was left undisturbed. The 30-minute undisturbed period followed an initial shear strength measurement made immediately after the sample was collected (data not shown). The differences between the initial and 30-minute measurements were typically negligible (within the uncertainty of the measurement technique).

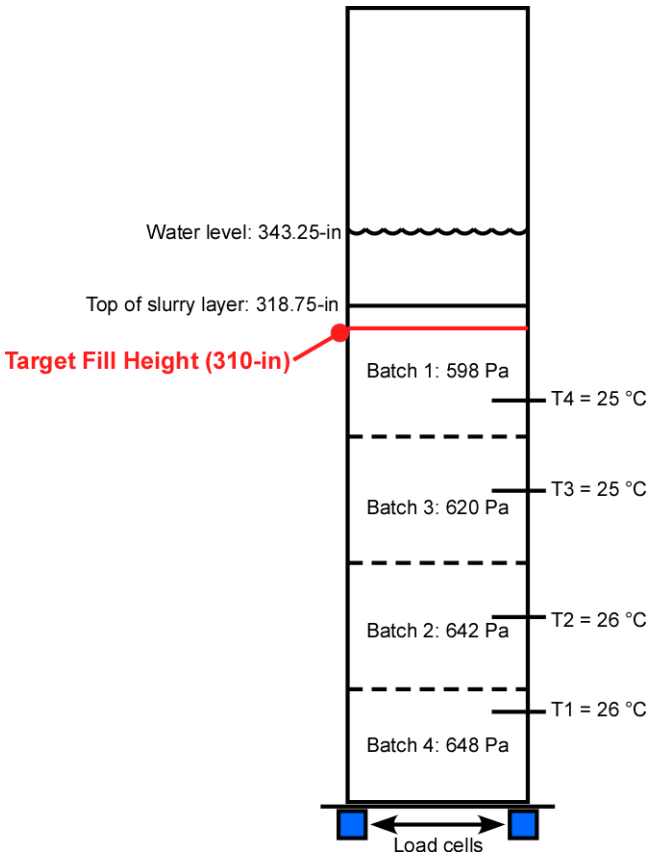

Figure 7.5. State of the Tall Column after Completion of Loading in Test 2. The dotted lines are estimated batch sizes and locations based on test observations—they do not represent quantitatively measured amounts.

The t = 0 h marker for Test 2 elapsed times was 01/16/2014 20:46. As in Test 1, core samples were taken near the start of the test (four successful samples[1] taken at four elevations between 11 and 16 h elapsed time). These samples were assessed for void fraction (see Appendix B) and aliquots were taken and analyzed for shear strength and total solids. While the samples were taken, radial temperature measurements were also made through all five sample ports using a multi-junction thermocouple that was temporarily inserted into the simulant. The measurements indicated that there was a small radial temperature gradient of ~2 °C (3.6 °F) that was similar at all five elevations, i.e., the center of the column was approximately 2 °C (3.6 °F) warmer than the near-wall region. Given the significant mass of the simulant, a small gradient was expected, and a 2 °C (3.6 °F) difference would not be signficant enough to have gas generation kinetics that were appreciably faster in the center than at the wall of the column.

In contrast to Test 1, the water level increased steadily immediately after the loading was completed (reflecting immediate gas production and accumulation in the simulant) until the peak was reached at approximately 47 h elapsed time (see Figure 7.6). Slurry level was measured more frequently in the beginning of Test 2 than it was in Test 1. Despite this, slurry level data collected after ~40 h elapsed time are also highly uncertain for the same reasons described in Section 7.1. The slurry level prior to the time the peak water level was achieved implies that the slurry begins consolidating even before a peak water level is reached in the experiment.

[1] The core sampler jammed twice and was unable to sample: once when sampling from S1A, a sampling event that was repeated at the same elevation with a different sample port (S1B), and once when sampling from S3A, a sampling event that was not re-attempted.

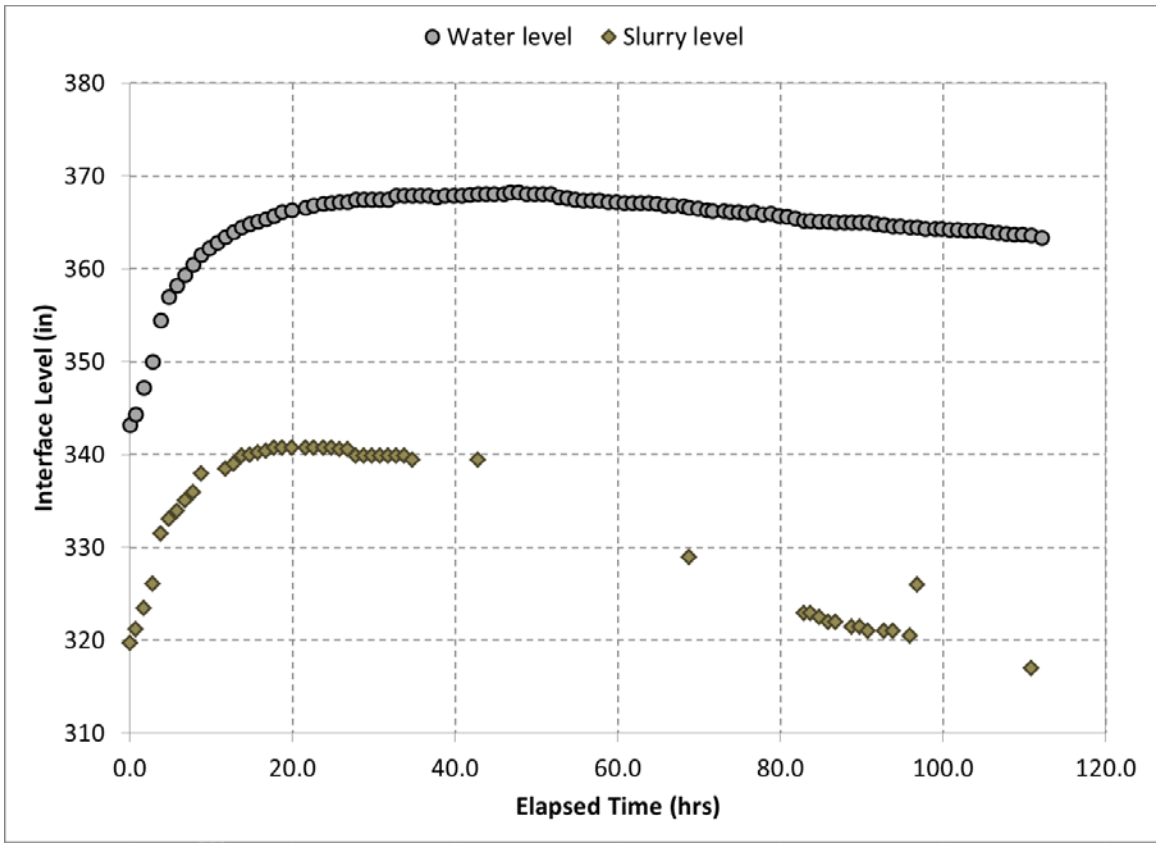

Figure 7.6. Water and Slurry Levels Measured During Tall Column Test 2

Following the peak water level at t = 47 h, the slurry continued to consolidate (or compact). Visually, the compaction was less noticeable than in Test 1. However, if the slurry level data are accurate, the slurry had already compacted back to its initial level by the end of the test (at least as significant a compaction as in Test 1). The extent of the consolidation is difficult to quantify for reasons already mentioned. Duplicate core samples taken near the end of the test (duplicates taken at three elevations between 85 and 90 h elapsed time and duplicates taken at two elevations between 107 and 112 h elapsed time) were analyzed in the same manner as at the start of the test. The end-of-test core samples, as before, support the conclusion that consolidation was taking place, as the measured total solids were higher at the end of the test (data given in Appendix A). The increase in total solids was less pronounced than in Test 1 and, in contrast, was not strongly segregated between the upper elevations (S4, S5) and the lower elevations (S1, S2, S3).

Another indication of the progress of the consolidation process is the pressure measurements that were collected in Test 2. The data from the pressure transmitters (PTs) is given in Figure 7.7. Note that the pressure data have been converted to pounds per square inch absolute using data from a barometric gauge (the PTs in the column measure gauge pressure). The initial transient response in the pore water measurement is likely due to the time it takes for the PTs to communicate with the pore water as it migrates through a porous frit in the sensor housing. Over the course of the test, the pore and total pressure measurements are of a similar magnitude. As the consolidation occurs, the pore water and total pressure measurements slowly drift in opposite directions. This is particularly noticeable at the lowest elevation (P1). It is not known what caused the sawtooth pattern on the P2 pore pressure, and the presence of gas bubbles in the simulant complicates interpretation of the data. The similarity of the pore

and total water pressure for the first part of the test suggests that using the bulk density to estimate pressure with depth is a reasonable assumption for unconsolidated (or perhaps slightly compacted) simulant.

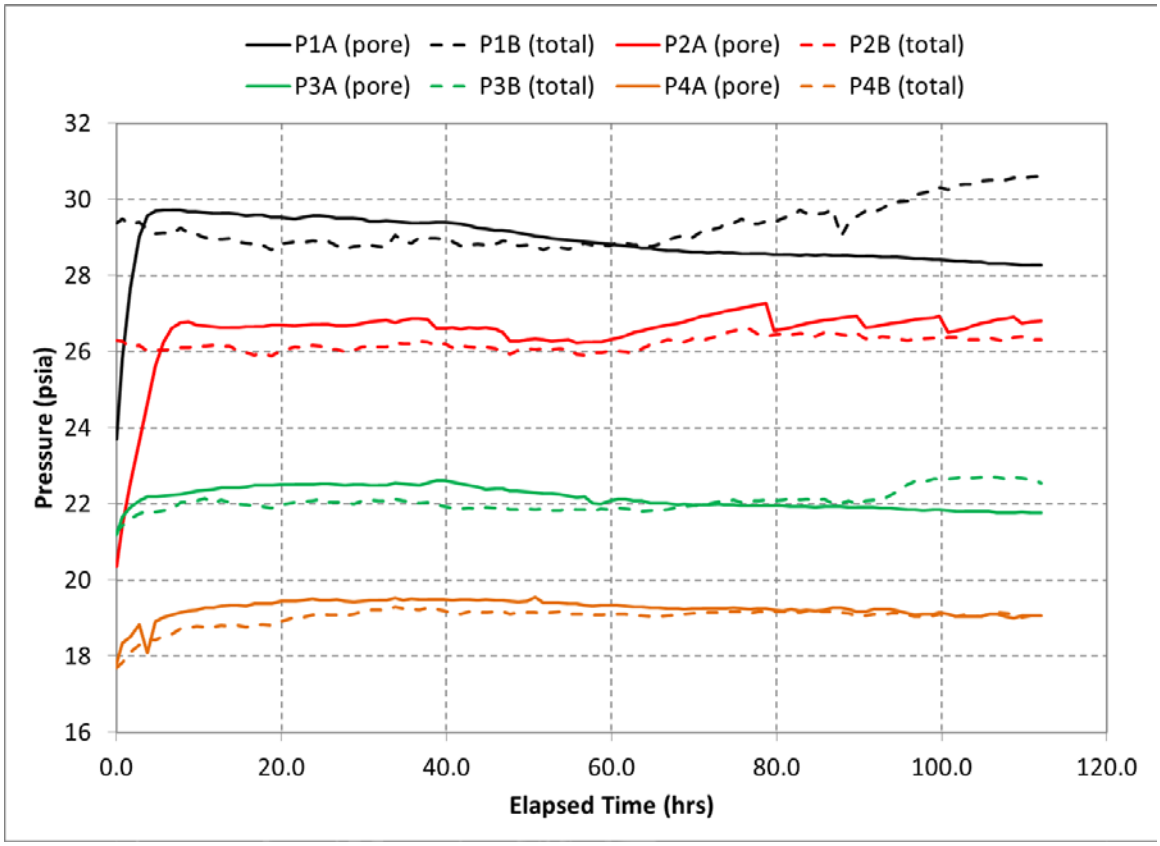

Figure 7.7. Pore Water and Total Pressure Measured at Four Elevations During Tall Column Test 2. The pore water (dashed lines) and total (solid lines) pressures were measured at elevations of ~5 ft (P1), ~10 ft (P2), ~17 ft (P3) and ~22 ft (P4).

Following the test, a post-test compression was performed by adding an additional water layer to the top of the existing water layer. Water was added until the level reached 463.875 in., adding about 8.5 additional feet of head to the simulant column. The data collected during the compression is tabulated in Appendix A and analyses conducted using the data are discussed in Section 8.0. Following the post-test compression, the column was monitored for approximately 24 more hours to collect additional pressure data, which is also compiled in Appendix A.

The hydrogen gas generation rate versus elapsed time for Test 2 is given in Figure 7.8, where each data point represents the average rate over the period elapsed since the previous data point. The peak rate was approximately 6 L/min and occurs almost immediately during the test. Note that this is significantly different from the gas generation rate data of Test 1. The rapid initial gas generation was not expected, based on both Test 1 and the laboratory studies discussed in Section 5.2, and thus for the first several hours the column headspace was being purged (during which the wet test meters conducting the gas volume measurements cannot be in use). It is possible that the peak generation rate was even greater than 6 L/min, but the early data is not available. However, the long, slow decay in gas generation rate to around 1 L/min by the end of the test was also observed in Test 1. The peak rate in Test 2 was on the

order of the expected peak rate based on laboratory studies and the intermediate column experiment (Section 5.3).

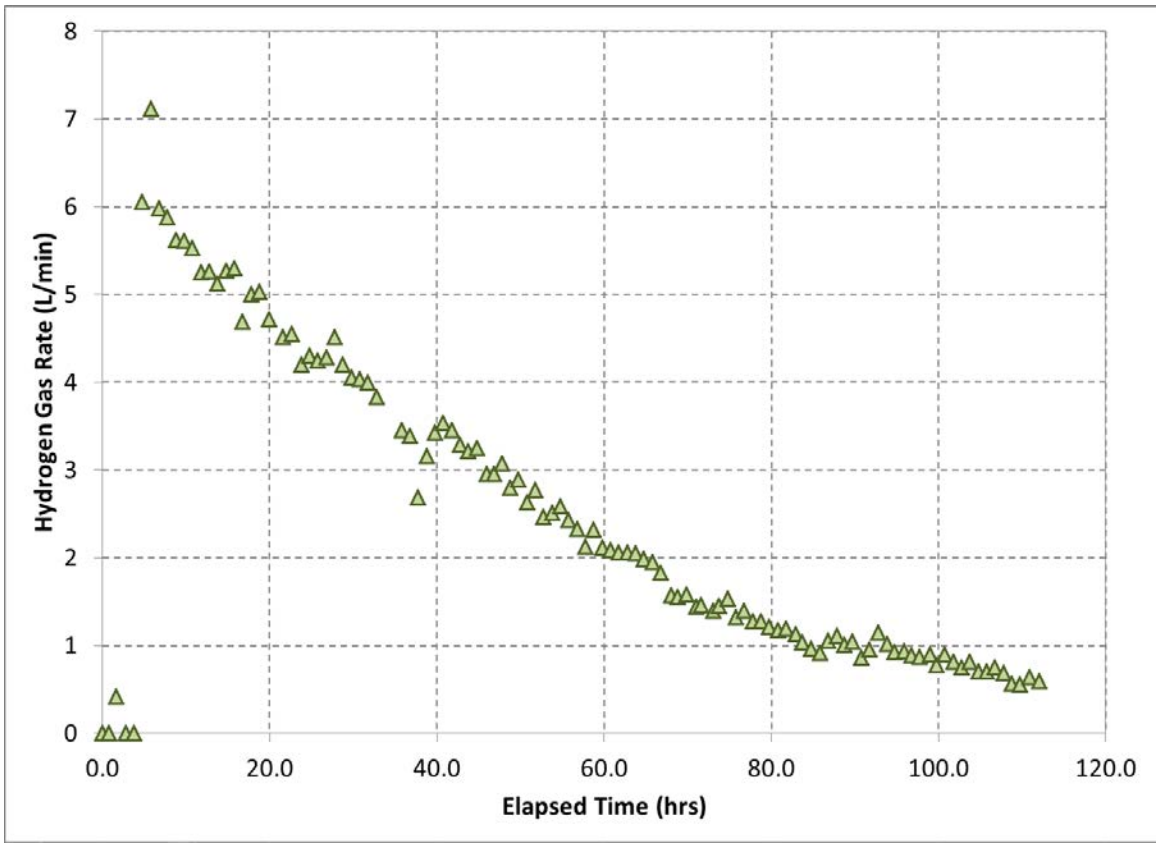

Figure 7.8. Hydrogen Generation Rate Estimated for Tall Column Test 2

Based on the observed behavior in Test 1, it was expected that gas generated in the simulant matrix would predominantly be released and not retained. This was confirmed by the data shown in Figure 7.9, in which the amount of gas retained (inferred from the water level data) reaches a near-constant value early in the test and is only a small fraction of the amount of gas released (using the gas volume measurements). As before, the data also do not imply that there were any episodic releases as the net gas volume leaving is smooth and monotonically increasing. These data observations are also supported by the void fraction data measured during Tall Column Test 2 (see Section 8.3).

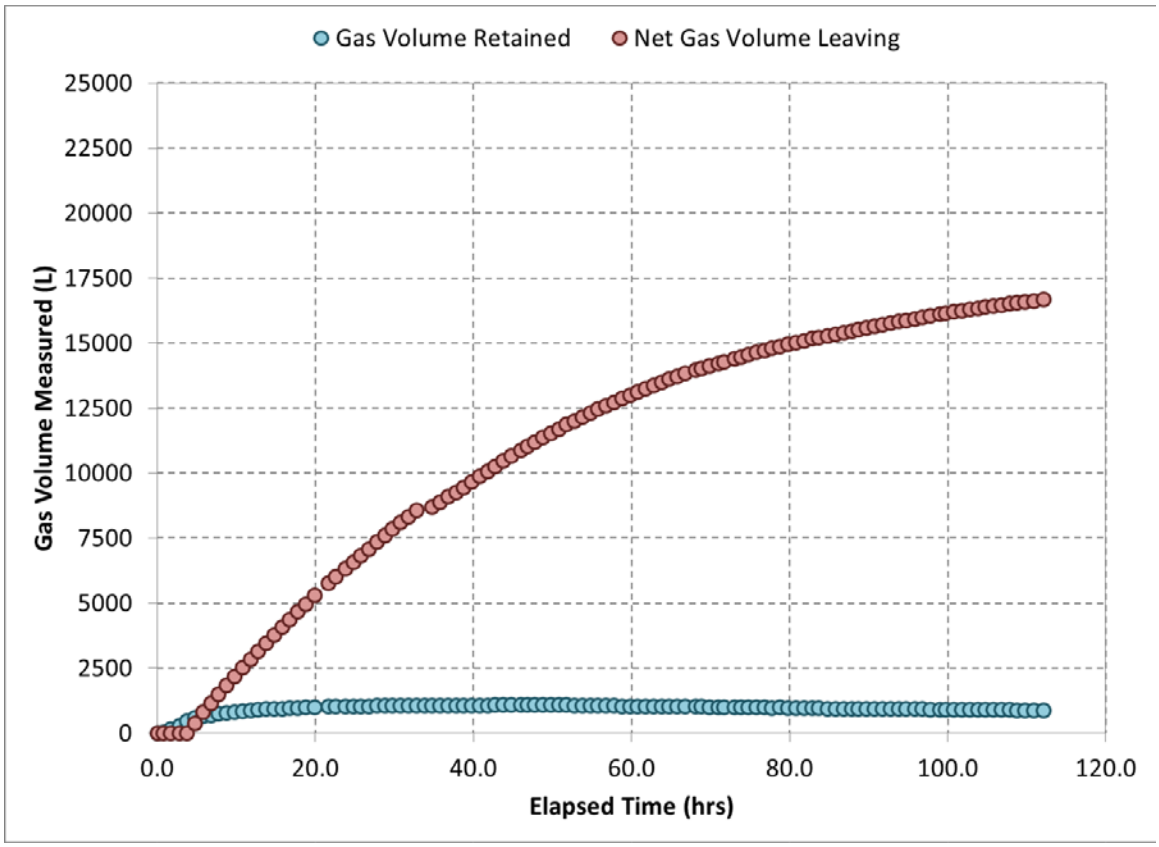

Figure 7.9. Comparison of Gas Volume Retained and Net Gas Volume Leaving the Tall Column During Test 2. The net gas volume is calculated by difference from the in-flow and out-flow wet test meters and was assumed to be only hydrogen.

Following the approach used in Test 1, estimates of d_{max} were repeated using the methodology discussed in Section 4.2 with the as-measured parameters for Test 2, using properties from both the bulk (average) and the batch with the greatest shear strength. These estimates are given in Table 7.4, along with the minimum depth below d_{max} that would be present based on the initial slurry level. By even the most conservative measure, there was initially at least 92 in. (7.7 ft, 2.3 m) of simulant below d_{max} in Test 2; recall from the description of the column that at least three fixed cameras (C1, C2, and C3) were below this level.

Table 7.4. Comparison of d_{max} Estimates for Target, Bulk, and Highest Batch Properties in Tall Column Test 2. The minimum depth below d_{max} indicates the minimum amount of simulant below d_{max} that would be expected based on the basis parameters.

Basis	Shear Strength (Pa)	Waste Depth (in.)	Conservative d_{max} Estimate (in.)	Representative d_{max} Estimate (in.)	Minimum Depth Below d_{max} (in.)
Target properties	500	310	170.0	102.7	140.0
Bulk properties[(a)]	627	318.75	220.2	133.2	98.6
Highest shear strength[(b)]	648	318.75	226.3	137.0	92.5

(a) "Bulk properties" indicates that the mean properties (shear strength, kaolin mass fraction) of all the batches loaded in the test were used to determine d_{max} via Equation 4.3.

(b) "Highest shear strength" indicates that the batch with the greatest shear strength (Batch 4 from Table 7.3) and its corresponding kaolin mass fraction was used to determine d_{max} via Equation 4.3.

Tall Column Test 2 was intended to be a repeat of Test 1 with the pressure transducers installed; with the exception of the two-day loading procedure that was required in Test 1, the test parameters were all reasonably similar. The same simulant recipe was used in both tests, with a slightly larger batch size in Test 2. The initial slurry and water levels were less than 2 in. apart. There were minor differences in initial temperature (Test 2 started a few degrees lower than Test 1) and shear strength (Test 2 bulk shear strength was around 30 Pa higher than Test 1). Despite these similarities in properties between the two tests, the gas generation rates were quite different. In particular, the peak gas rate was observed at much different times, with Test 2 reaching a maximum gas generation rate immediately and Test 1 almost three days after $t = 0$. Another implication of the earlier peak rate in Test 2 is that a larger volume of gas was produced in a shorter amount of time than in Test 1. The explanation for this difference is not clear, as several factors that affect iron reaction rate or the data interpretation are harder to quantify, for example:

- extent of mixing in each batch
- local gradients in shear strength, or more directly, moisture content
- difficulty in obtaining representative samples of the simulant
- variation in reactivity of iron particles
- unintentional introduction of trace components that acted as catalysts or retardants in the corrosion reaction.[1]

It is significant that despite this difference in generation rate, the retention behavior of the two tests was very similar, for example:

- overwhelmingly, the gas volume was released from the simulant and not retained
- the shapes of the water and slurry level curves between the tests are very similar

[1] One example would be $CaCl_2$, which might have been present in trace amounts in the cement trucks (this is also discussed in Section 5.2.2) despite efforts to remove aggregate and perform cleaning in order start the process with mixing drums that were as clean as possible. In practice, removing all trace chemicals from the mixing drum was difficult.

- gas release is not episodic and occurs throughout both tests
- the water levels and slurry levels reach a peak and do not continue to increase with time.

The similarities in gas retention behavior are also exhibited in estimates of void fraction for Tests 1 and 2. The bulk void and void profiles calculated by various methods are presented and compared in Section 8.0.

7.3 Tall Column Test 3

Tall Column Test 3 was attempted twice, the first attempt being aborted immediately after failed loading of the column. This first attempt was conducted on 02/04/2014 on a day where the air temperature was very cold (<20 °F). The simulant was mixed in four batches to a shear strength of approximately 1100 Pa prior to loading the column. During the loading process, extracting the simulant from the cement trucks proved to be exceedingly difficult, and only ~7 ft of slurry was pumped into the column.[1] As this was far below the target level and some equipment failures made mitigation of the problem intractable, the loading process was stopped and the column was cleaned out in preparation for a second attempt. When the slurry was diluted with water, removing the simulant from the truck became easier. To determine the maximum shear strength that could be used (operationally) in Test 3, a mixing pre-test was performed before the second attempt. The pre-test demonstrated that 5 to 6 ft of simulant could be loaded into the column from a single cement truck (batch) if the shear strength was reduced to ~900 Pa. Since 900 Pa was still within the acceptance criterion for Test 3 (see Table 4.2), this was used as the new target for the second attempt (i.e., Test 3B.) For flexibility during the loading process, the preparation of five batches was planned for Test 3B so the target fill level could be reached.

Test 3B, which will be interchangeably referred to as Test 3 throughout the report, began on 02/21/2014. All the same instrumentation used in Test 2 was still in use, with the exception that the core sampler was not deployed during Test 3B. As mentioned, five batches of sludge simulant (slurry) were prepared, each with a volume of approximately 8.5 yd^3. Temperature control of the simulant was achieved in the same way as in other tests, helped by some warmer air temperatures (~50 °F). The slurry was loaded to a height of 353.5 in., which was well above the criterion for initial simulant fill level. The target level was exceeded by more than 40 in. because the shear strength measurements for the first two batches that were loaded measured far below the target of 900 Pa. Since the third batch was close to the target shear strength, it was desirable to inject as much of the stronger simulant as possible. Ultimately, the simulant was mobilized from the cement trucks better than expected and the fifth batch was not needed.

A~24.5 in. water layer was added to the slurry and the monitoring period began immediately after the addition of water. The initial state of the column is illustrated in Figure 7.5, which shows the approximate size and location of each batch, along with the initially measured shear strength and temperature. The as-mixed batch compositions for all four batches that were loaded are shown in Table 7.5, along with the shear strength measured before and after iron addition. Recall that the target

[1] The difficulty appeared to be due primarily to the slurry "sticking" or adhering to the walls of the cement truck. The rotational shear in the truck barrel was not enough to force the slurry to migrate back to the chute. Only when the slurry was diluted with water (in the process lowering its shear strength) did it begin to mobilize in the barrel.

shear strength for the test was ~900 Pa. The shear strength values in Table 7.5 can be averaged to compute a bulk as-loaded shear strength of 692 ± 269 Pa,[1] which was outside of the acceptable range for the test (800 to 2000 Pa). The bulk shear strength is below the target because the first two batches were abnormally low, and the cause of the lower shear strength measurements warrants additional discussion.

Table 7.5. Simulant Batch Properties for Tall Column Test 3B

	Batch 1	Batch 2	Batch 3	Batch 4
Date Batch Mixed	02/21/14	02/21/14	02/21/14	02/21/14
EPK Kaolin	12,744.3 lb	12,735.5 lb	12,776.9 lb	12,734.5 lb
Water[(a)]	9736.4 lb	9996.4 lb	9777.5 lb	9766.1 lb
Zero Valent Iron	78.3 lb	78.3 lb	78.3 lb	78.3 lb
Mt. Hood 480 Biocide	1.7 lb	1.7 lb	1.7 lb	1.7 lb
Shear strength (before Fe addition)[(a), (b)]	937 Pa	1039 Pa	965 Pa	1041 Pa
Total solids (before Fe addition)[(c)]	54.6 wt% 54.8 wt%	54.7 wt% 54.9 wt%	54.7 wt% 55.1 wt%	55.2 wt% 55.2 wt%
Shear strength (after Fe addition)[(a), (b)]	380 Pa	391 Pa	917 Pa	929 Pa
Total solids (after Fe addition)[(c)]	54.4 wt% 54.0 wt%	54.1 wt%	53.8 wt% 54.2 wt%	54.8 wt% 54.8 wt%

(a) The shear strengths presented here were measured after a 30-minute period where the sample was left undisturbed. The 30-minute undisturbed period followed an initial shear strength measurement made immediately after the sample was collected (data not shown). The differences between the initial and 30-minute measurements were typically negligible (within the uncertainty of the measurement technique).
(b) Average of two shear strength measurements, with the exception of Batch 2, after Fe addition.
(c) The two measurements of total solids that correspond to the two shear strength measurements, with the exception of Batch 2, after Fe addition.

When the samples from the first two batches were collected, it was noted that the slurry appeared to be weaker than expected, as if it had entrained a lot of air (or in this case, likely hydrogen gas). Gas continued to be generated after the samples were collected, in sufficient quantities to push some of the simulant sample out of the vent hole in the sample containers. The presence of gas, and gas that was actively growing during the shear strength measurement, is the suspected cause of the lower shear strength measurements. The presence of gas reducing the shear strength measurement has been observed before in PNNL work with cohesive simulants (Gauglitz et al. 1995), but it did not reduce the shear strength by more than 50% as the samples in question were, instead reducing the shear strength approximately in proportion to $(1 - \phi)$, with ϕ = the volume fraction of gas. Other work (Wheeler 1988b) with reconstituted soils suggests that the presence of gas can both increase and decrease (up to 40%) the shear strength depending on consolidation and initial pore water pressure. Related work (Duffy et al. 1994) conducted with kaolin slurry containing methane bubbles noted reductions in shear modulus (note: applicable assuming shear modulus is correlated to shear strength for kaolin) of up to 50% with only small fractions of gas present. In general, however, the literature is sparse on this topic and only provides anecdotal support for the suspected behavior.

[1] The uncertainty given is an estimate of the standard error in the average at the 95% confidence level.

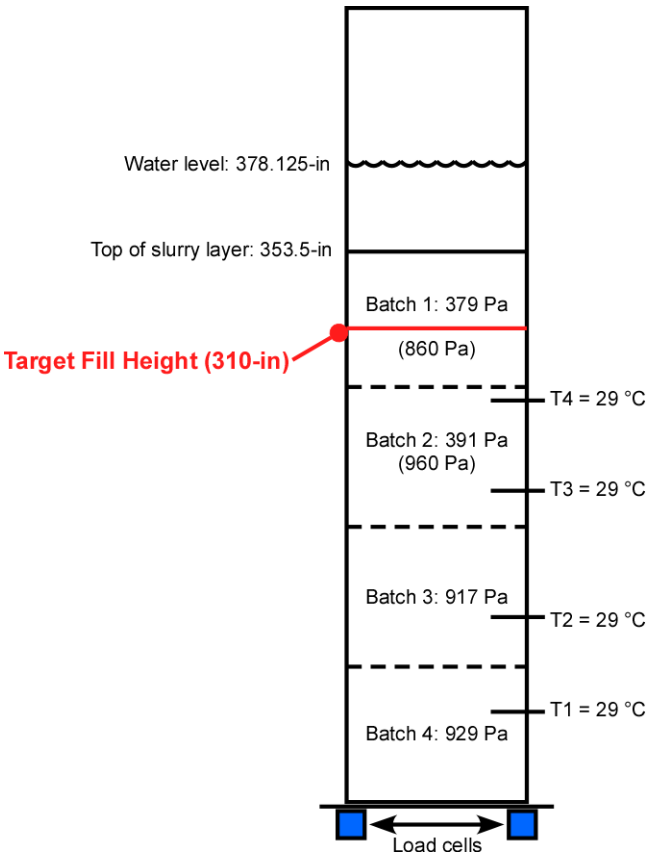

Figure 7.10. State of the Tall Column After Completion of Loading in Test 3. The dotted lines are estimated batch sizes and locations based on test observations—they do not represent quantitatively measured amounts. For a discussion of the shear strength values in parentheses, see the discussion below.

The four batches in Test 3 all had similar shear strengths prior to the addition of iron (refer again to Table 7.5). Then, once the iron slurry was added (same for all four batches), two batches had large drops in shear strength and two did not. Since the same amount of iron and water was added, the only plausible causes of a reduction in measured shear strength are 1) the presence of hydrogen gas actively being generated, 2) significant heterogeneities in mixing, or 3) a very unrepresentative sample. Poor mixing and poor sampling are possible causes but are highly unlikely to occur to the extent that a sample has a reduction in shear strength greater than 50% (when it had previously been as expected). The case is strengthened when a large data set of shear strength and total solids (e.g., kaolin weight percent) is examined. These data are presented in Figure 7.11. The data sets shown in black closed and red open circles encompass all the measurements performed on samples taken prior to Test 2 and Test 3B, including samples with and without iron particles. The “bubbly” samples from Test 3B are outliers relative to the rest of the data set. Note how the Test 2 and 3B data are clustered tightly together near the target lines for each test. They also follow the expected behavior provided by the correlation line in the figure, which is adapted from previous work at PNNL (a rounded version of Equation 4.2). Furthermore, the samples taken before Test 3B were re-measured several days later after being degassed by tamping down the samples in their containers (the closed blue and open orange triangles). The re-measured shear strength versus total solids data for the samples are in agreement with the correlation. This includes the

same samples that were "bubbly" prior to the test and measured lower than expected (as indicated by the labels in Figure 7.11).

Once the gas was removed, the shear strengths of the simulant were as expected. Thus, it was concluded that the shear strengths measured for Batches 1 and 2 were apparently lower but, if it had been measured, the gas-free simulant had a shear strength comparable to the third and fourth batches. The estimates of what the shear strengths would have been if they had changed similar to Batches 3 and 4 (after the addition of the iron slurry) are shown in parentheses in Figure 7.10. Incorporating these estimates into a bulk average for the Test 3 simulant results in an average shear strength of ~920 Pa[1] for Test 3B.

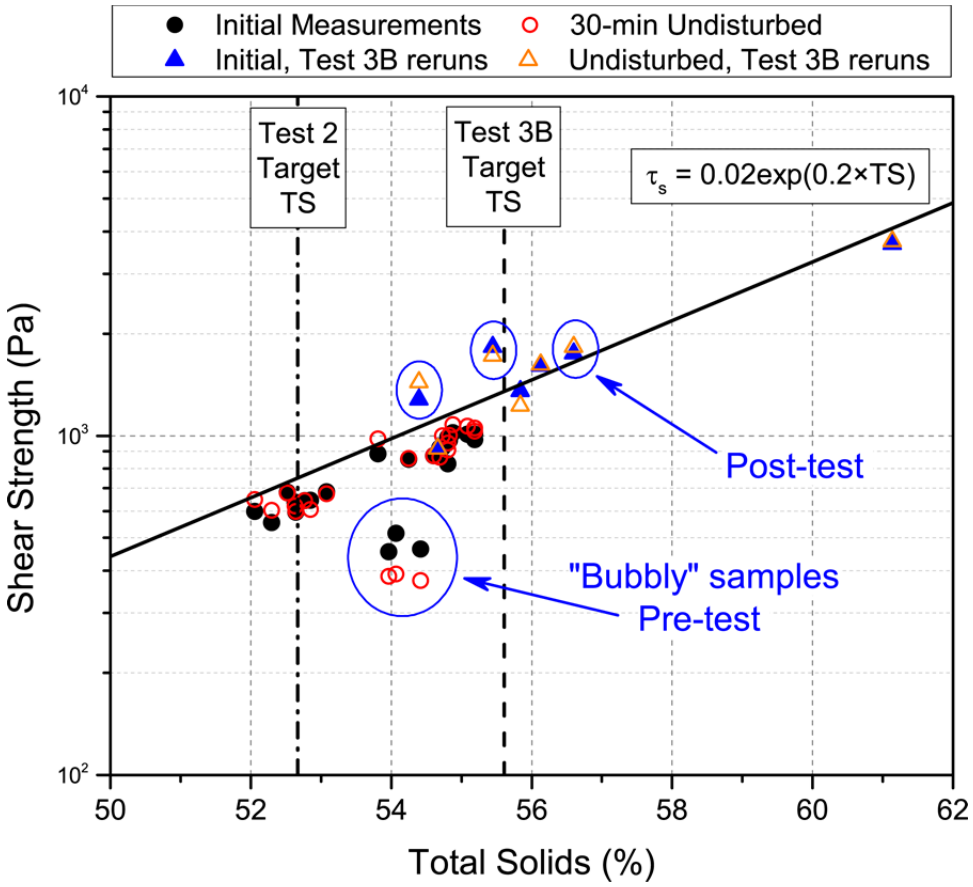

Figure 7.11. Shear Strength Measurements for Tests 2 and 3B with Outlier Data (both prior to and after Test 3B) Circled in Blue. The vertical dotted lines indicate the total solids values that were expected based on the target shear strength and simulant recipe. The solid line is a correlation similar (see Equation 4.2) to historical PNNL shear strength-kaolin wt% correlations that has arbitrary constants.

The t = 0 h marker for Test 3B elapsed times was 02/21/2014 15:20. No core samples or radial temperature measurements were collected. Following the trend of the previous two tests, the simulant

[1] The standard error was not calculated since this is an estimate. The value comes from using the average of 860, 960, 917, and 929 Pa = 916.5 Pa, rounded to 920 Pa.

level was observed to be increasing before the water layer could even be added. The water level increased rapidly immediately after the loading was completed (reflecting immediate gas production and accumulation in the simulant) until the peak was reached at approximately 21 h elapsed time (see Figure 7.12). Following the approach in Test 2, the slurry level was measured more frequently in the beginning of the test. Despite this, slurry level data collected after ~25 h elapsed time is highly uncertain for the same reasons described in Section 7.1. The slurry level prior to peak water level implies that the slurry begins consolidating even before a peak water level is reached in the experiment. The sudden increase in water level at ~70 h elapsed time was due to a small amount of water that was added to keep the water level visible, as it had been dropping steadily and was approaching the location of a visual obstruction (metal crossbar) in the viewing column.

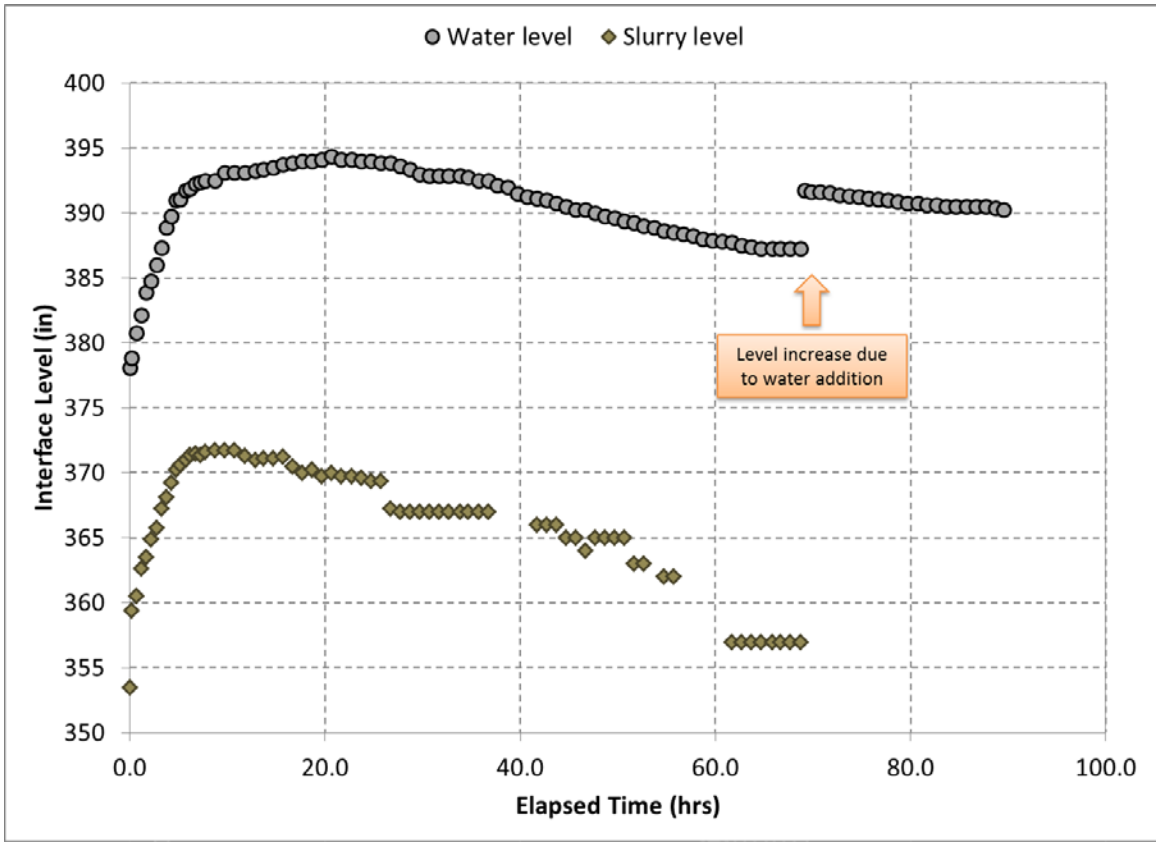

Figure 7.12. Water and Slurry Levels Measured During Tall Column Test 3

Following the peak water level at t = 21 h, the slurry continued to consolidate (or compact), but again less noticeably than in Test 1. The extent of the consolidation is difficult to quantify for reasons already mentioned; however, if the slurry level data are accurate, the slurry had already compacted back to near its initial level by the end of the test. End-of-test samples were not taken using the core sampler; pressure data that hints at the degree of consolidation was collected in Test 3. The data (shown in Figure 7.13.) are analogous to the Test 2 data. There was an initial transient response in the pore water measurement. Over the course of the test, the pore and total pressure measurements are of a similar magnitude. As the consolidation occurs, the pore water and total pressure measurements drift in opposite directions swiftly (P1 and P2) or gradually (P3 and P4). The P2 pore pressure has an unexplained increase approximately halfway through the test that remains for the duration of the test. The similarity of the pore and total water pressure for the first part of the test suggests that using the bulk density to estimate pressure with

depth is a reasonable assumption for unconsolidated (or perhaps slightly compacted) simulant. Some of the apparent consolidation at lower elevations (both in Tests 2 and 3) could also be attributed to the "collapse" of the simulant as the gas bubbles no longer are produced in large enough quantity to support some of the self-weight of the material.

Following the test, a post-test compression was performed by adding an additional water layer to the top of the existing water layer. Water was added until the level reached 486.75 in., adding about 8 additional feet of head to the simulant column. The data collected during the compression are tabulated in Appendix A and analyses conducted using the data are discussed in Section 8.0. Following the post-test compression, the column was monitored for approximately 24 more hours to collect additional pressure data (this data is also compiled in Appendix A).

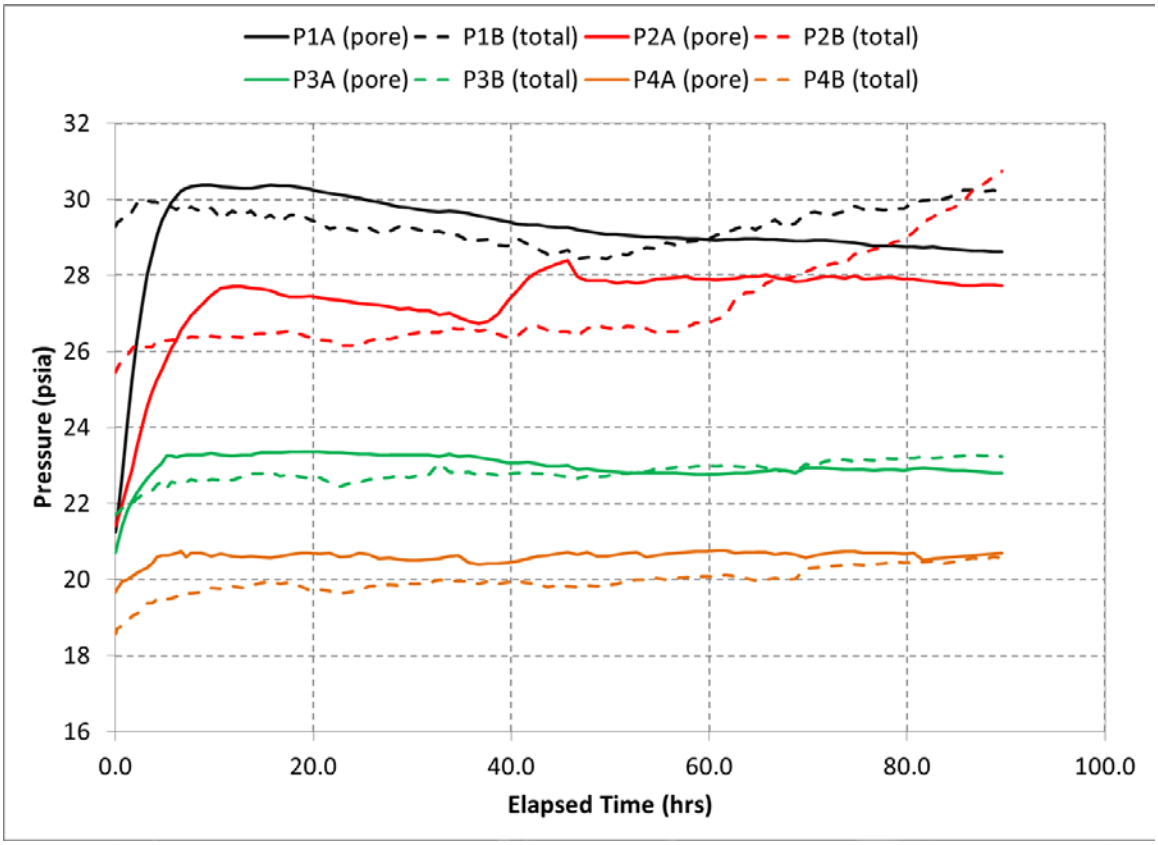

Figure 7.13. Pore Water and Total Pressure Measured at Four Elevations During Tall Column Test 3. The pore water (dashed lines) and total (solid lines) pressures were measured at elevations of ~5 ft (P1), ~10 ft (P2), ~17 ft (P3) and ~22 ft (P4).

The hydrogen gas generation rate versus elapsed time for Test 3 is given in Figure 7.14, where each data point represents the average rate over the period elapsed since the previous data point. The peak rate was approximately 12 L/min and occurs immediately during the test. Note that this is a significant increase even over Test 2, although the characteristics of the data are similar. Since it was observed previously in Test 2, the rapid initial gas generation was planned for and the column had already been purged prior to simulant loading. There was a long slow decay in gas generation rate to around 1 L/min by the end of the test. The peak rate in Test 3 was slightly larger than the expected peak rate based on laboratory studies and the intermediate column experiments (Section 5.3). As discussed near the end of

Section 7.2, the explanation for the rapid generation rate in this test and the lack of induction time before the gas production began is unclear.

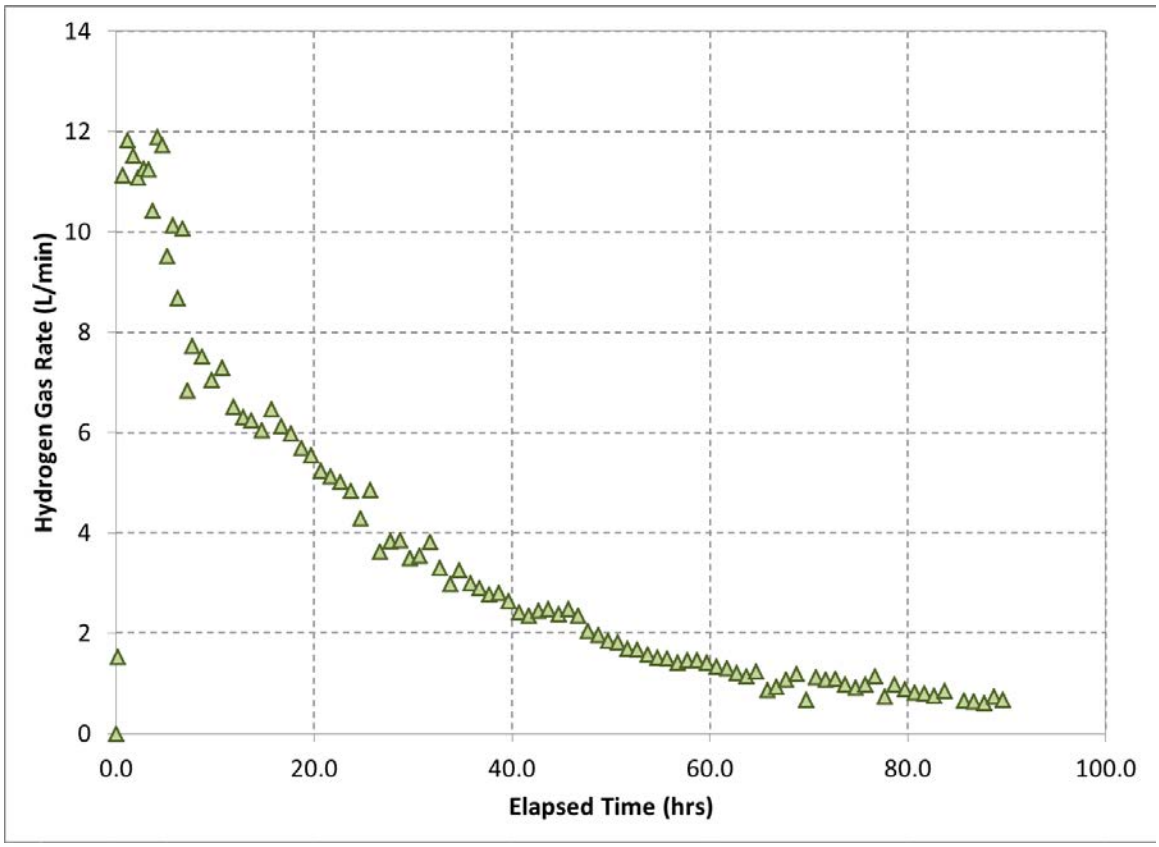

Figure 7.14. Hydrogen Generation Rate Estimated for Tall Column Test 3

Based on the observed behavior in the previous two tests, it was expected that gas generated in the simulant matrix would predominantly be released and not retained. This was confirmed by the data shown in Figure 7.15, in which the amount of gas retained (inferred from the water level data) reaches a near-constant value very early in the test and is only a small fraction of the amount of gas leaving the column (using the gas volume measurements). As before, the data also do not imply that there were any episodic releases as the net gas volume leaving is smooth and monotonically increasing. These data observations are also supported by the void fraction data measured during Tall Column Test 3B (see Section 8.3).

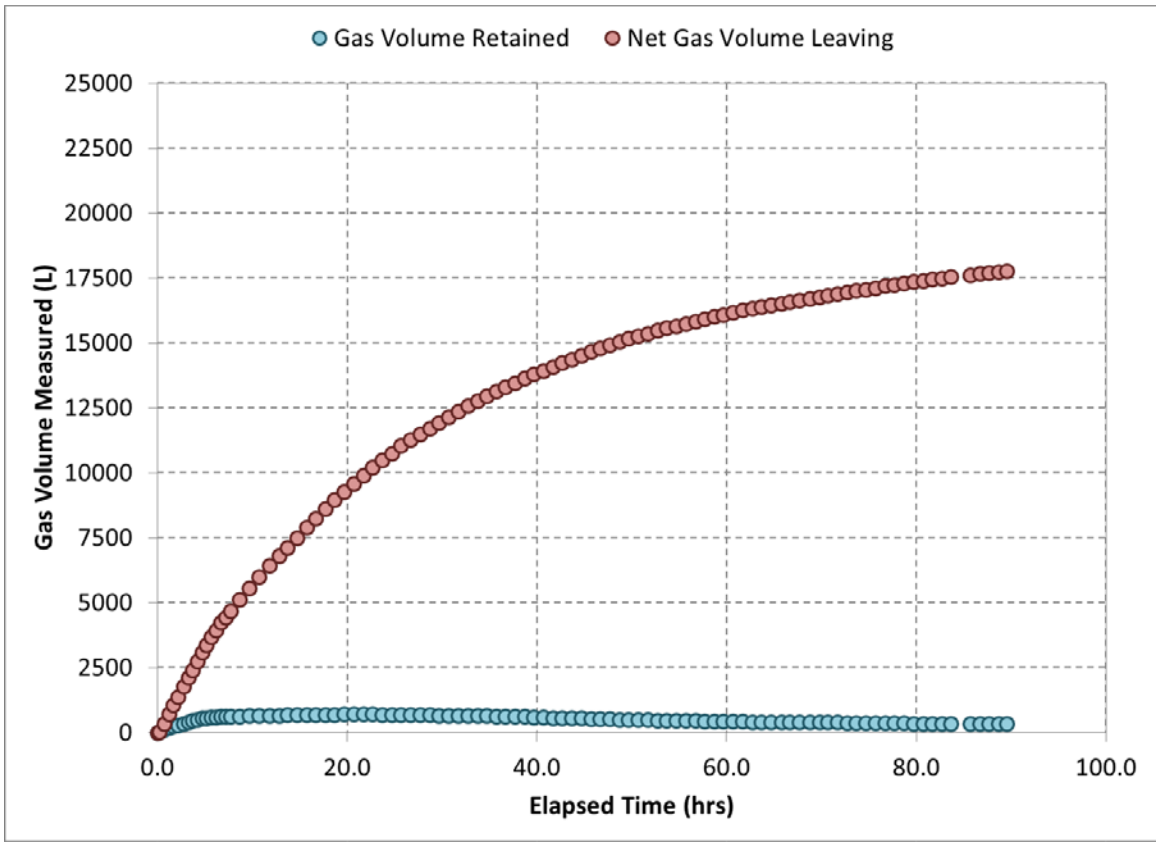

Figure 7.15. Comparison of Gas Volume Retained and Net Gas Volume Leaving the Tall Column During Test 3. The net gas volume is calculated by difference from the in-flow and out-flow wet test meters and was assumed to be only hydrogen.

Following the approach used in the other tests, estimates of d_{max} were repeated using the methodology discussed in Section 4.2 with the as-measured parameters for Test 3B, using properties from both the bulk (average) and the batch with the greatest shear strength. As discussed earlier, the bulk average is not expected to be representative of the simulant shear strength and is simply provided for reference. The highest shear strength was very close to the estimated bulk average (~920 Pa), making it an excellent proxy for the suspected average shear strength in Test 3. The d_{max} estimates are given in Table 7.6, along with the minimum depth below d_{max} that would be present based on the initial slurry level. By even the most conservative measure, there was initially at least 42 in. (3.5 ft, 1.1 m) of simulant below d_{max} in Test 3B; recall from the description of the column that one fixed camera (C1) was below this level.

Table 7.6. Comparison of d_{max} Estimates for Target, Bulk, and Highest Batch Properties in Tall Column Test 3B. The minimum depth below d_{max} indicates the minimum amount of simulant below d_{max} that would be expected based on the basis parameters.

Basis	Shear Strength (Pa)	Waste Depth (in.)	Conservative d_{max} Estimate (in.)	Representative d_{max} Estimate (in.)	Minimum Depth Below d_{max} (in.)
Target properties	~900[a]	310	287.1	174.4	22.9[b]
Bulk properties[c]	692	353.5	231.6	140.3	121.9
Highest shear strength[d]	929	353.5	310.8	188.9	42.7

(a) Reflects that the target value was adjusted down due to the aborted first attempt at Test 3.

(b) To remove confusion due to the much greater actual waste depth in Test 3, the minimum depth is based on the target depth of 310 in. – 287.1 in. = 22.9 in.

(a) "Bulk properties" indicates that the mean properties (shear strength, kaolin mass fraction) of all the batches loaded in the test were used to determine d_{max} via Equation 4.3.

(b) "Highest shear strength" indicates that the batch with the greatest shear strength (Batch 4 from **Table 7.5**) and its corresponding kaolin mass fraction was used to determine d_{max} via Equation 4.3.

It is important to point out that while Test 3 did not have all the same target parameters as Tests 1 and 2, once the test was conducted the only major differences were a shear strength estimated to be approximately 50% greater and a slurry level that was more than 30 inches higher. The gas generation rate was noticeably more rapid than the previous two tests, and yet the gas retention behavior of Test 3 was very similar to the previous tests. Discussion of the void fraction data from this test is given in Section 8.0.

7.4 Comparison of Gas Production in the Tall Column Tests

The three tall column tests described in the previous three sections each had unique aspects, the most substantial difference being the gas generation rates measured in the tests. Table 7.7 summarizes the differences in the gas rates, along with a comparison of the average (over four thermocouples) initial and final temperatures in the column. The same comparison of gas generation rates with the entire data set is shown in Figure 7.16. All the tests had approximately equal bulk temperatures, with no large changes over time; the initial and final temperature measurements were, at a minimum, 90 h apart. Test 3 had the largest peak gas generation rate, but it decayed the fastest of any of the tests. Test 2 had some similarities to Test 3 but the peak was lower and the decay was slower. Test 1 is significantly different since it did not attain a peak gas rate instantaneously, but rather peaked later and then the rate decreased slowly; it is nearly three times the Test 3 rate at 72 h elapsed time.

Table 7.7. Comparison of Initial and Final Temperatures and Gas Generation Rates at Selected Elapsed Times for All Three Tall Column Tests

Test No.	Initial Temperature (°C / °F)	Final Temperature (°C / °F)	Maximum Gas Rate (L/min)	Gas Rate at 12 h (L/min)	Gas Rate at 24 h (L/min)	Gas Rate at 48 h (L/min)	Gas Rate at 72 h (L/min)
1	28.3 / 82.9	26.3 / 79.3	4.55	1.36	3.90	4.39	3.05
2	25.5 / 77.9	23.5 / 74.3	7.12	5.25	4.20	3.07	1.46
3	29.0 / 84.2	24.8 / 76.6	11.90	6.53	4.84	2.05	1.08

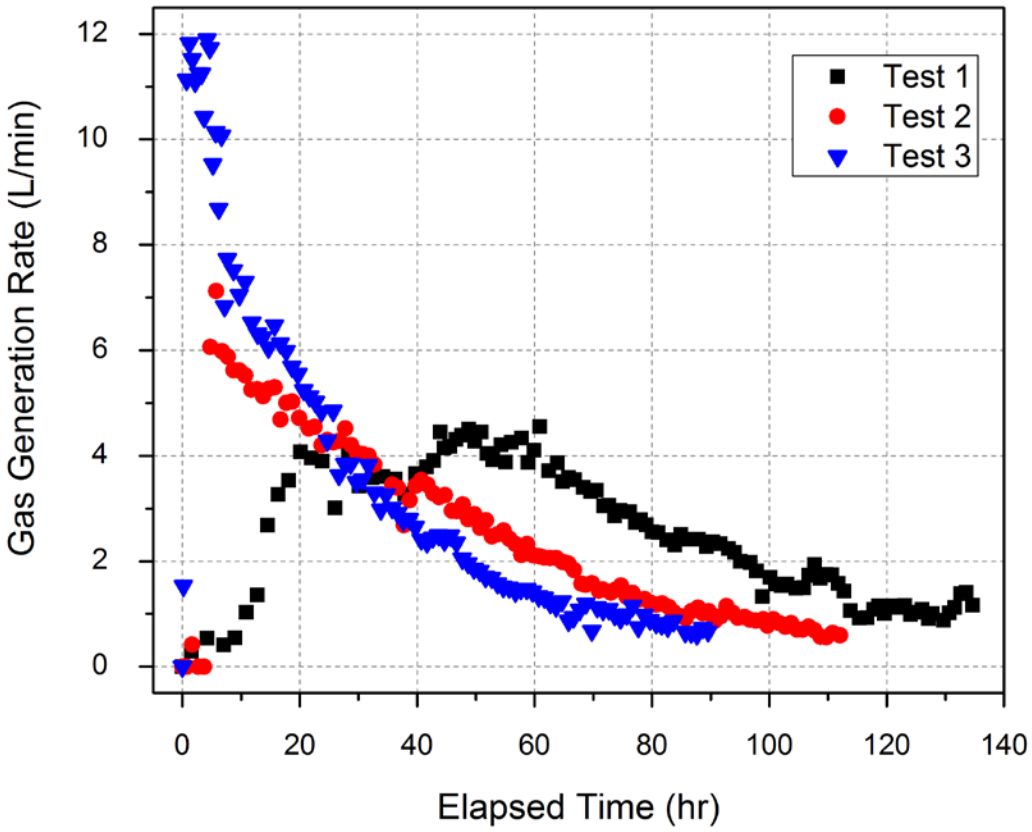

Figure 7.16. Comparison of the Gas Generation Rates for the Tall Column Tests

Based on the preponderance of data from laboratory studies performed with kaolin-water simulants using iron as a gas generation rate agent (see Section 5.0), an induction period of a few days was expected. Typically, there is no appreciable gas production during the induction phase. As Figure 7.16 demonstrates the gas generation rates measured during the tall column tests did not meet this expectation. Essentially, none of the tall column tests had an induction period. The contrast between what is typically observed in smaller-scale experiments in the laboratory[1] and the tall column tests is illustrated in Figure 7.17. The figure shows the specific gas volume (volume of gas generated/volume of the gas-free

[1] The intermediate column results also showed an induction period of several days (Powell et al. 2014) that was similar to the bench-top experiments in this work.

simulant slurry) produced by the iron reaction as a function of elapsed time. The small column experiments were performed in the laboratory in a 5-inch-diameter column using the same iron content (0.35 wt%) as the tall column tests and approximately the same kaolin/water ratio (the small column target shear strength was 500 Pa). The difference in induction period is large (several days); however, once the gas generation begins, the gas generation rate (which is the slope of the gas volume vs time) appears to be comparable between the small and tall columns.

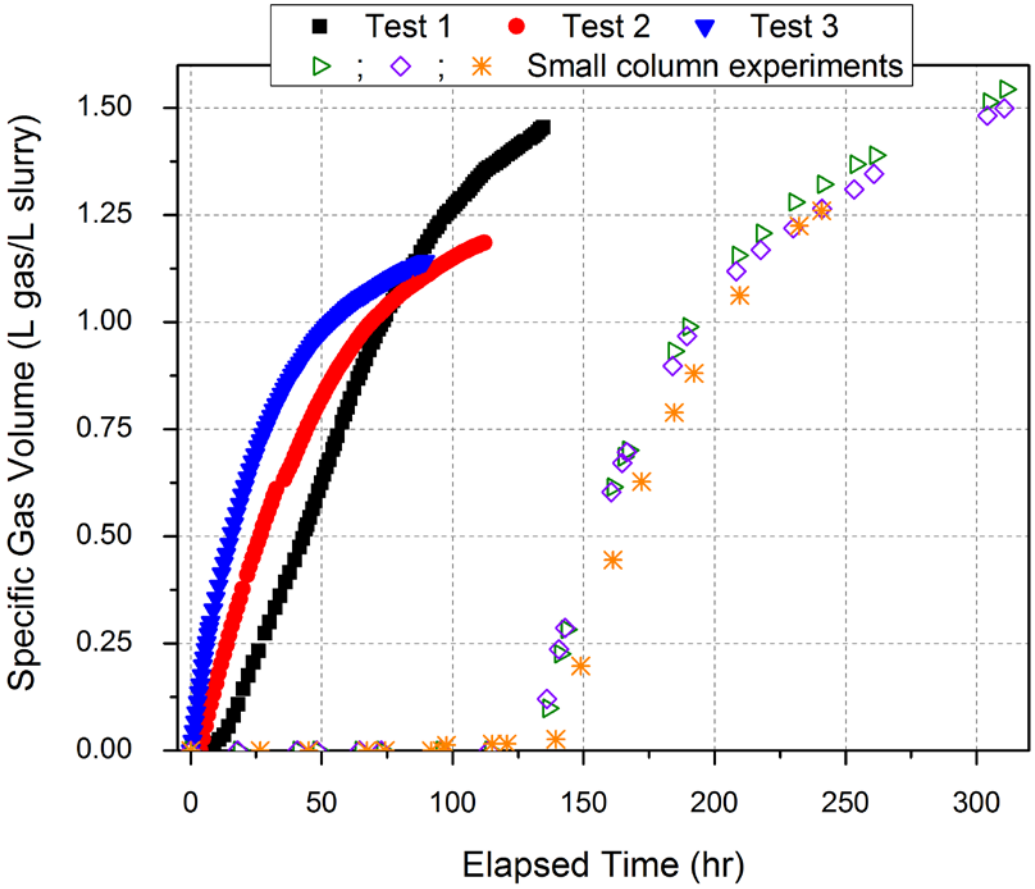

Figure 7.17. Specific Gas Volume Generated in the Three Tall Column Tests and Small Column Laboratory Experiments. The iron loading in all cases was 0.35 wt%. The small column experiments were conducted with kaolin slurries that had shear strengths of approximately 500 Pa.

To assist with comparing the data that represent the period when gas is being generated, the small column data were shifted left by subtracting the induction period. The adjusted elapsed time for the small columns was selected to be normalized to when gas is first measurable, in keeping with the behavior in the tall column tests. The resultant comparison is shown in Figure 7.18—note that the tall column test data have been replaced with lines so all the data can be resolved. The data are in very good agreement, which is a crucial point. It implies that the tall column tests had nearly identical reaction rates and extents of reaction to earlier experimental work. Unidentified causes in the tall column simulant preparation eliminated the induction period but did not fundamentally change the reaction behavior.

The figure supports a second important point regarding the extent of reaction. The iron loading specified for use in the tall column testing was selected to generate at least an equivalent volume of gas to volume of slurry at the column bottom (where the pressure was estimated to be approximately 33 psia). The equivalent volume specification was chosen so that the simulant would have every opportunity to retain large fractions of gas if there was a mechanism that allowed it to do so. The data show that the iron, which was still producing gas (albeit slowly) at the end of the test, exceeded this criterion. Both the small column and the tall column data are all trending towards values of 1.25 to 1.50 L of gas per liter of slurry. This observation is an essential point when considering the implications of the data shown in Figure 7.4, Figure 7.9, and Figure 7.15. Volumes of hydrogen gas were generated in the tall column in excess of the slurry volume; notwithstanding, the simulant retained only a small fraction of the ample quantity of generated gas that was available.

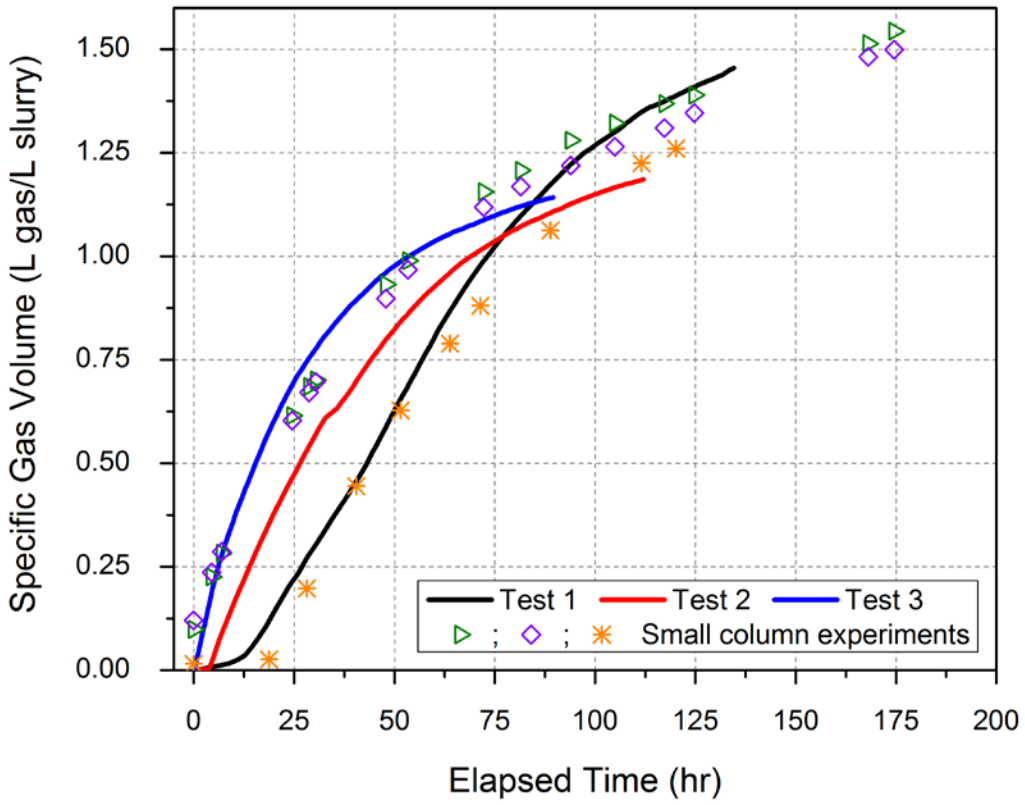

Figure 7.18. Data of Figure 7.17 Where the Induction Period for the Small Column Experiments Has Been Removed to Compare the Data During the Gas Generation Phase. The tall column test data is shown as lines in this plot for clarity.

8.0 Void Fraction Results and Discussion

This section discusses the void fraction data from the tall column tests. The section has three topic areas. The first topic is a short discussion of observations of gas transport and void in the tall column tests. The second topic presents the bulk (or average) void fraction data of each test and discusses the implications of the average measurement. The third topic presents void fraction profile data, where the results of the various methods described in Section 4.3 are shown and compared with one another. An important discussion in the third section is selecting a recommended best estimate of void fraction in the simulant as a function of elevation. Finally, a brief summary of the key results is provided.

8.1 Observations of Gas Transport and Void Morphology

The objectives of the tall column tests were established to assess quantitatively whether the d_{max} theory correctly predicted gas retention behavior. Quantitative measures (primarily void fraction measurements) are the subject of subsections 8.2 and 8.3. However, the visual observations made using the video camera system, either during tests or during post-test examination, supply compelling evidence of the gas retention and transport characteristics of deep sludges. The description below is a summary of information that is presented in the supplemental video (can be viewed at http://youtu.be/aBBJnmsWQgs) included as part of this report. The ~8-minute video contains, in the following order:

- Real-time video of three elevations (Cameras 2, 3, and 6) during Test 2.
- A one-frame-per-second time-lapse video from three elevations (Cameras 2, 4, and 9) during all three tests in order, playing at 5000x speed.
- A scan from the top of the column to the bottom of the column using the rover camera for all three tests, playing at about 4x speed.
- Real-time video showing bubbling at the surface of the water layer during Test 3.

There were three major questions that visual observations (both from the video and during real-time observation) can help answer:

1. What do the bubbles and voids look like and how do they compare in appearance with previously observed voids in kaolin-water simulants?

2. Does void morphology change with the depth from the surface of the simulant?

3. Does the simulant release gas readily at all depths and what does observable gas transport look like?

The first question is significant to the basis of the d_{max} theory itself, which was devised using the idealized assumption that gas channels forming in a sediment matrix are cylindrical tubes intersecting with one another. In recent work at PNNL, networks of cylindrical tubes have not been observed in kaolin simulant experiments, most notably studies by Gauglitz et al. (2012) and the intermediate column

experiments described in Powell et al. (2014).[1] The gas voids in the tall column tests viewable from the cameras also do not have cylindrical shapes, instead having shapes that can be described as slits, cracks, or elongated ellipses that were not connected continuously in the plane of the viewing window. Figure 8.1 shows two representative examples of images selected from Test 1. Both images are from an elapsed time that came after the peak bulk void fraction was reached in the column. There are distributions of rounder bubbles (these are typically small) dispersed among some of the longer bubbles, but the majority of the bubbles have a slit- or crack-like shape. The visual appearance of the bubbles does not hint at a network of tubular channels in the simulant.

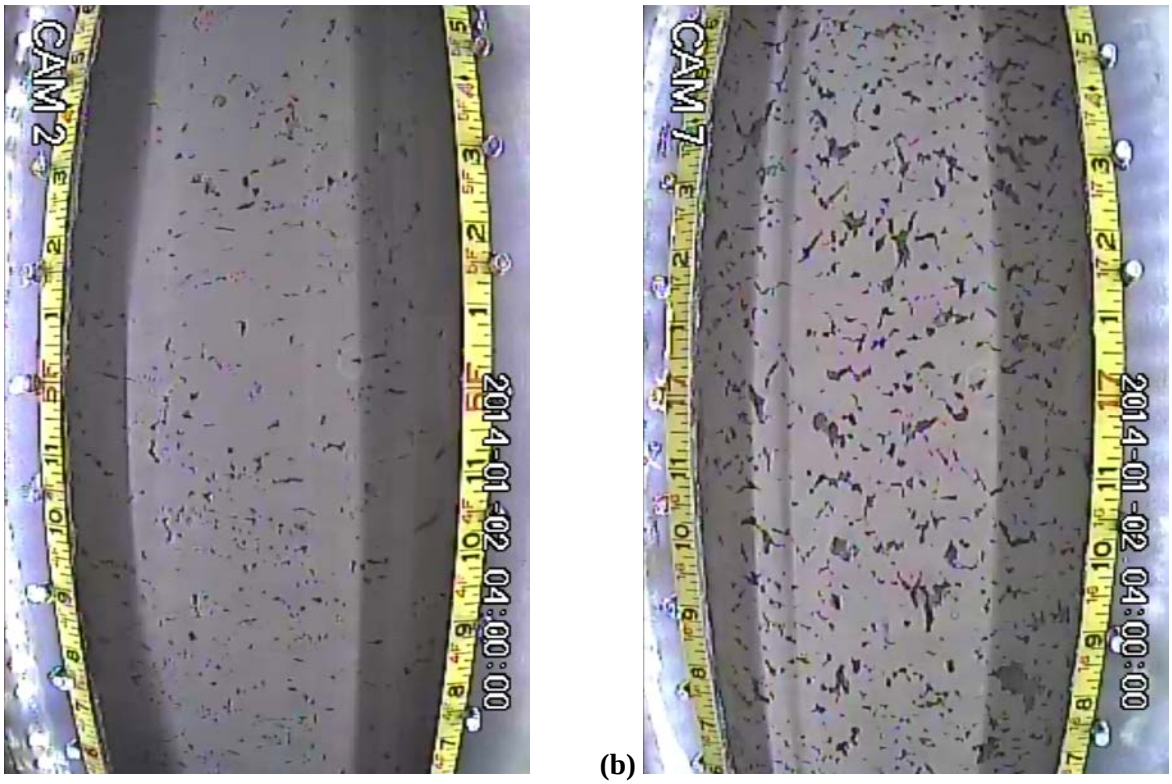

Figure 8.1. Example Images from Test 1: (a) Camera 2 at an elevation of 5 ft from the column bottom, and (b) Camera 7 at an elevation of 17 ft from the column bottom. The images occurred at 04:00 on 01/02/2014 at an elapsed time of approximately 78 h.

Answering the second question offers an approach to assessing the validity of d_{max} theory using strictly visual observation data. In each tall column test, the rover (mobile) camera was used to examine the appearance of the gas voids over the entire simulant depth. Near the end of the test, well after the peak in bulk void, the rover camera was moved slowly from the top of the simulant to the very bottom. These top-to-bottom scans are included in the supplemental video.[2] Although there were variations in the

[1] Also of relevance is the conclusion from Powell et al. (2014) that even if cylindrical channels are created in kaolin simulants, they had open channel depths that were smaller than the depth that was predicted by d_{max} theory. This casts further doubt on the validity of using an idealized cylindrical tube network to predict the gas retention, as Equation 4.3 was not accurate even when an experiment was designed to be consistent with the physical model governing it.

[2] The video can be viewed at http://youtu.be/aBBJnmsWQgs.

amount of void in a given video frame and subtle differences in bubble morphology between elevations in the column, these are randomly distributed throughout the top-to-bottom scan. The lowest elevations do not consistently have higher void densities or vastly difference void shapes than any other location in the column. It was expected that if some different gas retention behavior existed at the bottom, either very large voids or a high density of smaller, rounder voids would be observed. There were no visual observations fitting that description in any of the three tests.

Addressing the third question is another way to confirm or refute the predictions of d_{max} theory by visually observing gas transport behavior in the tall column tests. A change in gas retention behavior implies that gas would be retained more readily at the bottom of the column and therefore would not be transported out of the simulant. Evidence of gas being transported throughout the column, especially at the lowest elevations, would stand in stark contrast to this prediction. Gas transport was seen in all three tests at even the lowest elevations in the column (see the supplemental video[1] for one example from Test 2 in real-time). Periodic movement of gas was observed; trains of gas bubbles migrated vertically toward the simulant surface, sometimes motion occurred for only a few seconds and other times for a few minutes. Gas often stopped moving and then started again, a phenomenon that supports the expected gas transport mechanism described in Section 4.3.1. Though it was challenging to trace the movement of gas continually from the very bottom to the very top, bubble motion was occasionally observed at several locations simultaneously, suggesting gas transport was not impeded anywhere in the simulant. The gas transport can also be seen in the time-lapse videos from all three tests, where the gas motion shows up as flickering in the void spaces on the cameras. The flickering that indicates bubble motion was observed at elevations above and below d_{max}. Consistent with the other visual observations, unrestricted gas transport does not support the existence of d_{max}.

8.2 Bulk (Average) Void Data

The bulk void fraction is acquired directly from the water level and the calculation of initial void fraction as given in Section 4.3.2. There is some uncertainty in the initial void calculation since it depends on knowledge of the gas-free density of the simulant that is loaded into column. The density was bounded by calculating it using three methods (the methods differ depending on the simulant data that was used).[2] The results of the calculations for the three tests and the resultant initial void fraction estimates are given in Table 8.1. The best estimate of initial void fraction is based on the mean density, but the bulk void fraction results are shown with error bars derived from the minimum and maximum estimates of initial void fraction. The estimate of ϕ_o is the dominant source of uncertainty in the calculation of void fraction.

[1] The video can be viewed at http://youtu.be/aBBJnmsWQgs.

[2] The three methods available to calculate an initial gas-free density are: 1) use total solids measurement data from pre-loading simulant samples prior to the addition of iron, 2) use total solids measurement data from pre-loading simulant samples after the addition of iron, and 3) estimate the density based on the as-prepared batch masses of the simulant components and known component densities. Note that to perform this estimate, the bulk kaolin mass was corrected to a dry basis (in order to use the dry kaolin density) by accounting for the water content of the bulk kaolin.

Table 8.1. Estimates of Gas-Free Simulant Density and Initial Void Fraction (ϕ_o) for Tall Column Tests

Test No.	Test 1		Test 2		Test 3	
Quantity	Density (kg/L)	Initial Void Fraction (%)	Density (kg/L)	Initial Void Fraction (%)	Density (kg/L)	Initial Void Fraction (%)
Minimum	1.494	1.99%	1.481	1.00%	1.502	6.51%
Median	1.496	2.16%	1.485	1.29%	1.510	7.01%
Mean	1.498	2.25%	1.485	1.28%	1.513	7.22%
Maximum	1.503	2.60%	1.489	1.55%	1.528	8.12%

The bulk void fraction data are shown for Tests 1, 2, and 3 in Figure 8.2, Figure 8.3, and Figure 8.4, respectively. Since the calculation was based on the water level observations, the shapes of the curves are the same as in Figure 7.2, Figure 7.6, and Figure 7.12, respectively. In all tests the void peaked and then declined slowly with elapsed time. The decline in bulk void fraction was caused by a combination of voids shrinking as the gas production rate began decreasing, evaporation (likely minor), released gas bubbles entraining water (likely minor), and penetration of water into channels from the surface. It is significant that the decline was not caused by some small episodic releases of gas, as the net gas volume leaving the column declined over the same period.

The bulk void peaked at 8.3% in Test 1, which had the lowest gas generation rate. In Test 2 (intermediate gas generation rate), the bulk void peaked at 9.1%, and in Test 3 (highest gas generation rate), the peak was 11.8%. The available data on void fraction from sludge waste tanks estimate that the bulk void fraction is approximately 6% to 8% (Meacham et al. 2014). The experiments with contaminated lake bottom sediments conducted as part of van Kessel's and van Kesteren's (2002) work also exhibited peak gas fractions of 7% to 8%. Another set of measurements on a different depot of contaminated mud estimated gas volume percentages (referenced to atmospheric pressure) ranging from 7% to 13% (Wichman et al. 2000). The bulk void data from the tall column experiments, even at the peak values, were similar to those values. The intermediate column tests had higher void fractions, likely due to the much smaller diameter of approximately 7.25 in. (Powell et al. 2014).

While the data imply a correlation between gas generation rate and bulk void fraction, there were enough differences between the tests (particularly shear strength and the two-day loading process in Test 1) to complicate the comparison of the tests and this trend could simply be coincidental. It is important to note that the gas generation rates in the tall column tests were several orders of magnitude larger than the historical estimates of waste tank generation rates (compare, for example, the values from Yarbrough 2013 and Meacham et al. 2014 with the plots in Appendix A). If the speculation was accurate, it supports the notion that deep sludge wastes cannot achieve bulk void fractions larger than those observed in the tall column tests.

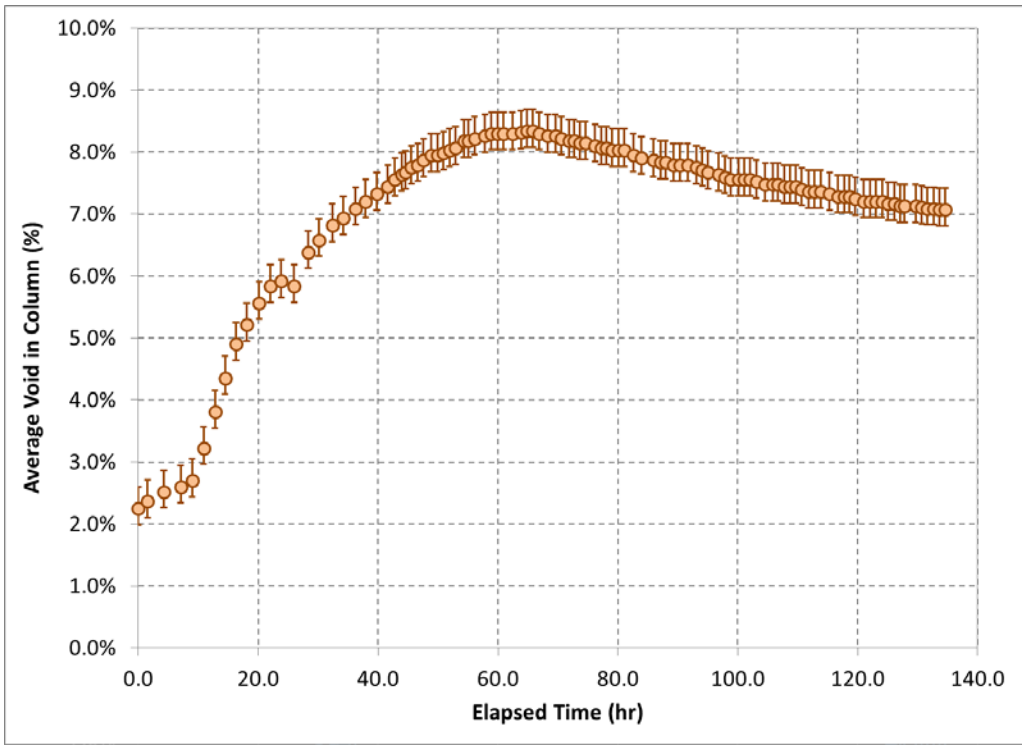

Figure 8.2. Bulk (Average) Void for Tall Column Test 1. The error bars represent the uncertainty in the calculation of initial void (difference between minimum and maximum values of initial void and the mean value).

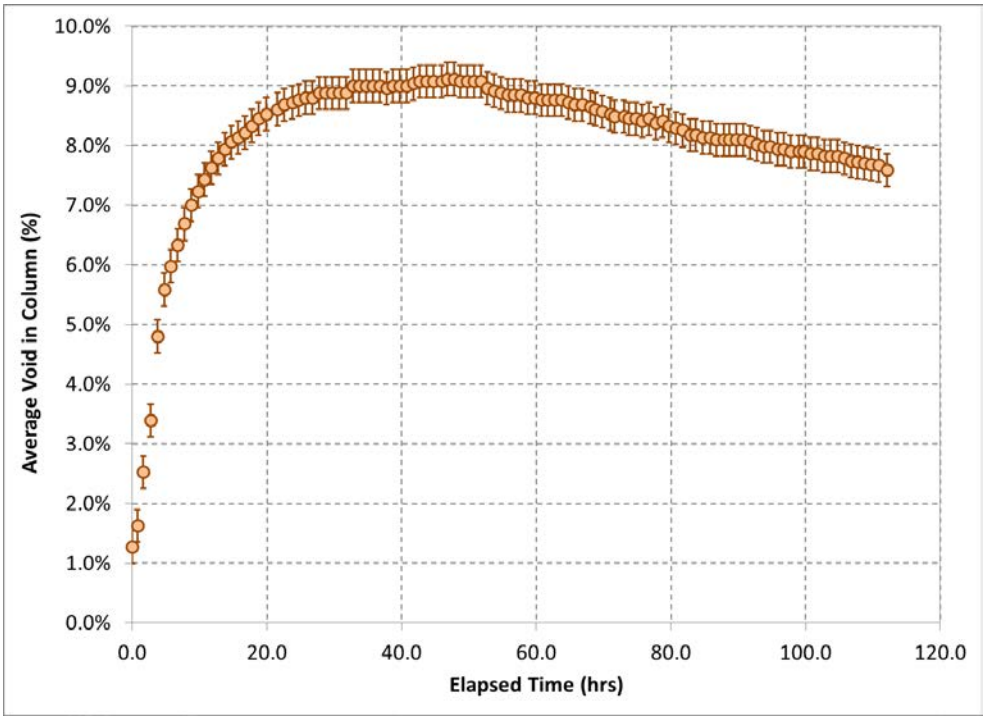

Figure 8.3. Bulk (Average) Void for Tall Column Test 2. The error bars represent the uncertainty in the calculation of initial void (difference between minimum and maximum values of initial void and the mean value).

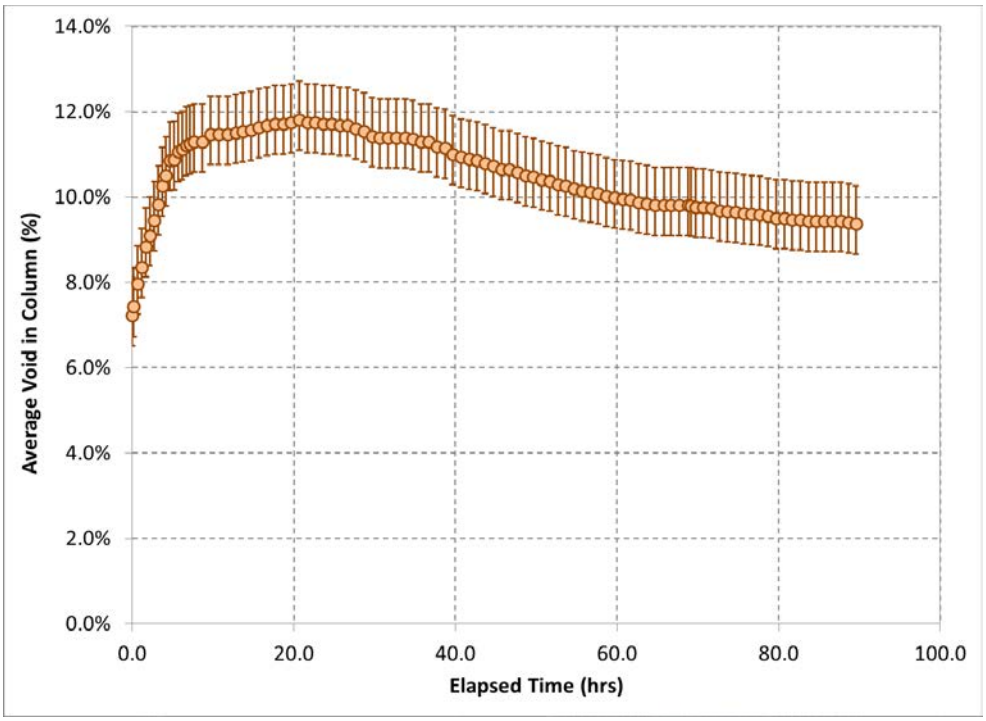

Figure 8.4. Bulk (Average) Void for Tall Column Test 3. The error bars represent the uncertainty in the calculation of initial void (difference between minimum and maximum values of initial void and the mean value).

The three bulk void fraction data sets are plotted together in Figure 8.5. The dotted lines in the figure represent the ranges in uncertainty of ϕ_{bulk} that were plotted in preceding figures with error bars. The shapes of the curves are all analogous; the distinguishing characteristic between the tests is that the features of the data become compressed in elapsed time as the generation rate increases. The portion of the data where the bulk void fraction declined appears to have the same slope in each test. The characteristics of the bulk void data for each test are tabulated in Table 8.2. Note that the term "end of test" refers to the time when data collection stopped and does not indicate that there was no longer any gas generation in the simulant. In each test, the time designated as "end of test" occurred after the gas generation had declined for a few days and there were no significant changes in observable voids. Running the tests longer would have provided additional information on the consolidation behavior of the simulant but would not be expected to change the conclusions regarding gas retention and release behavior. Some interesting features of note include the following:

- The void fraction in Test 3 returned closer to its starting value by the end of the test than in the other two tests.
- Test 2 had the greatest growth in bulk void fraction, e.g., $\Delta\phi_{bulk}$ (start to peak).
- Test 3 increased the least (smallest $\Delta\phi_{bulk}$ (start to peak)) but declined the most (largest $\Delta\phi_{bulk}$ (peak to end)). The smaller increase is largely due to the much higher initial void fraction (reflecting that the gas production reaction was occurring before loading was completed).
- Near-peak changes in void with time ($\Delta\phi_{bulk}/\Delta t$ (near-peak)) are similar in magnitude between tests; likewise for the changes in void in the decline phase ($\Delta\phi_{bulk}/\Delta t$ (peak to end)).

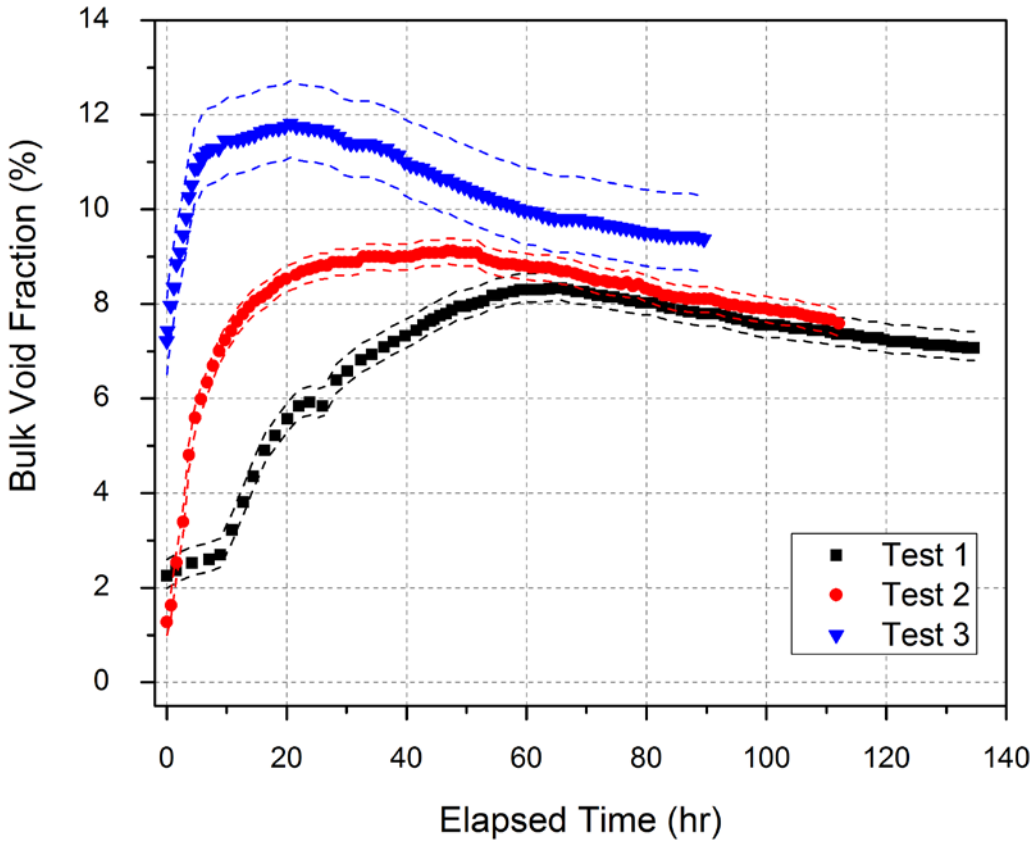

Figure 8.5. Comparison of Bulk Void for all Three Tall Column Tests. The dotted lines represent the error bars due to the uncertainty in the initial void calculation.

Table 8.2. Bulk Void Fraction Characteristics of the Tall Column Tests

Test No.	ϕ_{bulk} (peak)	$\Delta\phi_{bulk}$ (start to end)	$\Delta\phi_{bulk}$ (start to peak)	$\Delta\phi_{bulk}/\Delta t$ (near-peak)[(a)]	$\Delta\phi_{bulk}$ (peak to end)	$\Delta\phi_{bulk}/\Delta t$ (peak to end)
Test 1	8.34%	4.82%	6.09%	0.01% h^{-1}	1.27%	-0.02 % h^{-1}
Test 2	9.12%	6.31%	7.84%	0.02% h^{-1}	1.53%	-0.02 % h^{-1}
Test 3	11.82%	2.15%	4.60%	0.04% h^{-1}	2.45%	-0.04 % h^{-1}

(a) Estimated over the 10 data points up to and including the peak ϕ_{bulk}.

A final important point is that there was not, at any time during any test, a point after the peak void fraction was reached where the bulk void starting increasing again. If d_{max} theory was an accurate predictor of gas retention behavior in these tests, it would be expected that some lower region of the simulant would have continued to accumulate gas. Continued accumulation of gas, by necessity, would cause the simulant level and the water level to increase and be interpreted as an increase in bulk void. As this was not observed, d_{max} theory does not appear to hold for the simulant strengths and depths studied in the tall column tests. Additional support of this point is discussed in Section 8.3 when the void fraction profile data is presented.

Table 8.3. Bulk Void at Test End Compared to Bulk (Average) Void Calculated from the Post-Test Compression Data (Equation 4.8)

Description	Test 1	Test 2	Test 3	Basis
Bulk void at test end: ϕ_{bulk} (by water level)	7.1%	7.6%	9.4%	Water level just before compression
Maximum void: ϕ_{avg} (by compression)	7.3%	8.7%	12.5%	Based on initial slurry level
Best estimate of void: ϕ_{avg} (by compression)	7.2%	8.7%	12.3%	Based on best estimate of slurry level
Minimum void: ϕ_{avg} (by compression)	6.9%	8.1%	12.0%	Assumes no compaction of slurry

One other calculation of the bulk void was conducted using the post-test compression data (discussed in Section 4.3.2, see Equation 4.8). The post-test compression only provided an estimate of the bulk void at the end of each test. The calculation was performed for a range of slurry level values to bound the result—the slurry level is a parameter that affects the calculation and it was not well known. The results of the calculations are shown in Table 8.3 and are compared to the value of the bulk void (determined using the water level) at the end of the test. Given the assumptions used to perform the calculation, the agreement between the two measurements of bulk void (within 1%) is excellent for Tests 1 and 2. Overall, the post-test compression results are slightly higher than the bulk void determined by the water level. This is especially true of the comparison in Test 3, and the reason for the larger difference in Test 3 is not evident from the data. Regardless, the two calculations confirm that much larger bulk void fractions (i.e., 20% or greater) were not present in the simulant during the tall column tests.

8.3 Void Fraction Profile Data

This section presents data for each of the various methods used to determine void fraction with elevation in the tall column. The methods are discussed independently and then compared. A recommendation for the method that supplied the best estimate of void fraction in the tall column tests follows the comparison. For more details on some of the analyses used to generate the data presented here, refer to Section 4.3.3. Note that of the five methods discussed earlier in the report, one was discarded and will not be discussed (core sampling) and another does not give void fraction profile data as a function of time (post-test compression, which only results in a void profile at a discrete point in time).

Post-Test Compression Results

Analysis of photographic images as described in Section 4.3.3 yielded measurements of the elevation change of features resulting from water addition to the column and compression of gas bubbles as part of each compression test. Figure 8.6 through Figure 8.8 show the elevation changes in response to compression measured using the before- and after-compression photographs (red circles). Also shown is the elevation change of the simulant surface based on the change in liquid level upon compression (blue triangles). The pink line in each graph shows the expected variation of elevation change throughout the simulant layer assuming all the simulant has a gas content equal to the average gas content as determined by the liquid-level measurement method (see Equation 4.6 in Section 4.3.2).

The elevation change data for Test 1 and Test 3B show less elevation reduction in response to compression than expected for many of the measurements. For Test 1, only the three highest-elevation feature tracking values are reasonably consistent with the expected elevation change profile (pink line) or the simulant surface elevation change. Similarly, for Test 3B, only the two values measured at the 23-ft level (from Camera 9) are consistent with expectation. As discussed in Section 4.3.3, these discrepancies are due to the simulant adhering to the viewing windows and, therefore, not moving along with the bulk of the surrounding simulant. Because the compression-induced elevation change data for Tests 1 and 3B are suspect, no attempt was made to generate local void fraction estimates for these tests. Note that the suspect results for Tests 1 and 3B show essentially no elevation change in the lower region of the column. Negligible changes in elevation correspond to negligible amounts of retained gas, so the unanalyzed results from Tests 1 and 3B do not show high gas retention. The elevation change data for Test 2, shown in Figure 8.7, exhibit a trend that is reasonably consistent with both the expected trend for the assumed constant-void case and the change in simulant surface level based on the measured liquid level change during the compression test. This consistency implies that the simulant near the viewing mast in Test 2 moved in response to compression in a manner similar to that of the bulk of the simulant. If this was the case, then the data in Figure 8.7 can reasonably be used to calculate the vertical variation of retained gas fraction throughout the simulant.

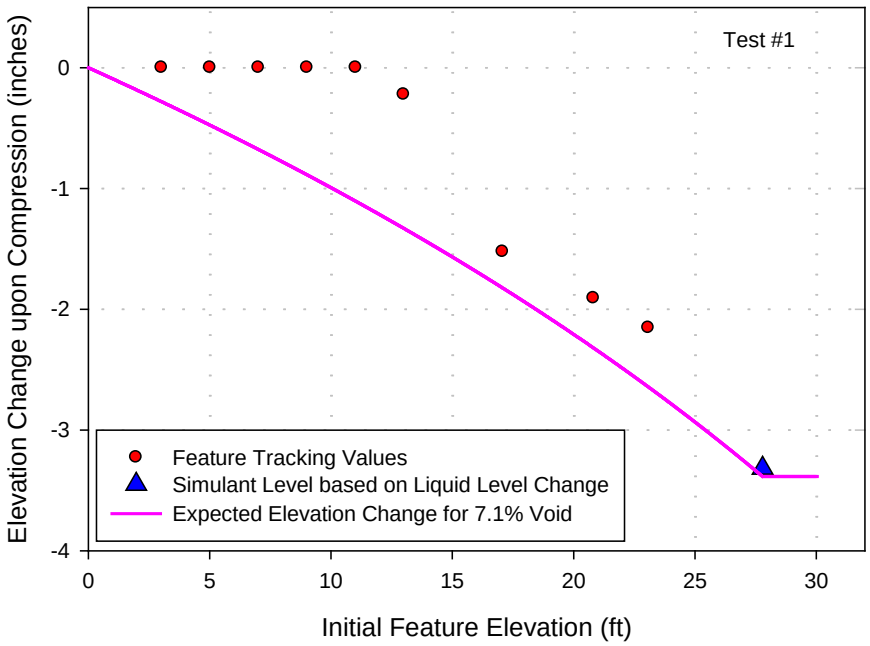

Figure 8.6. Elevation Change Measurements and Predictions for Test 1 Compression

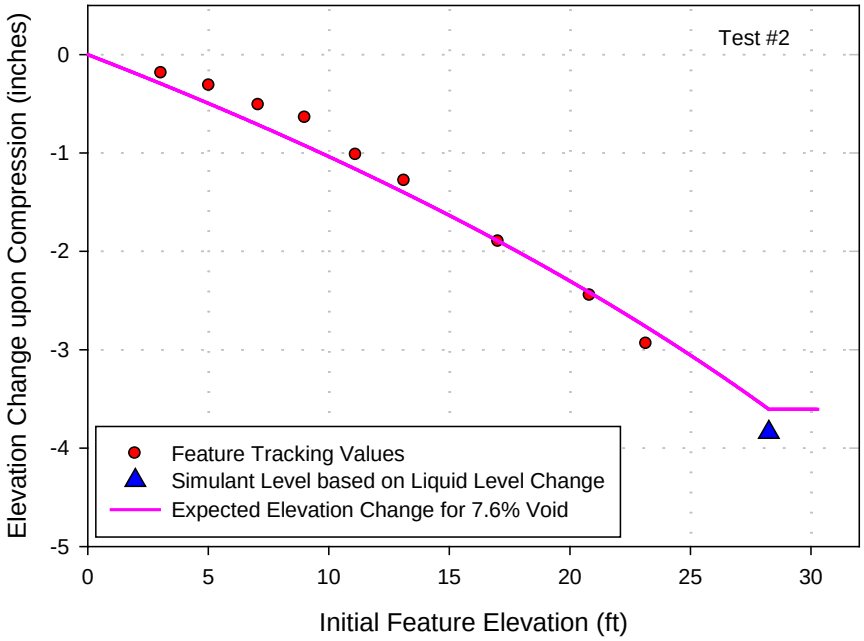

Figure 8.7. Elevation Change Measurements and Predictions for Test 2 Compression

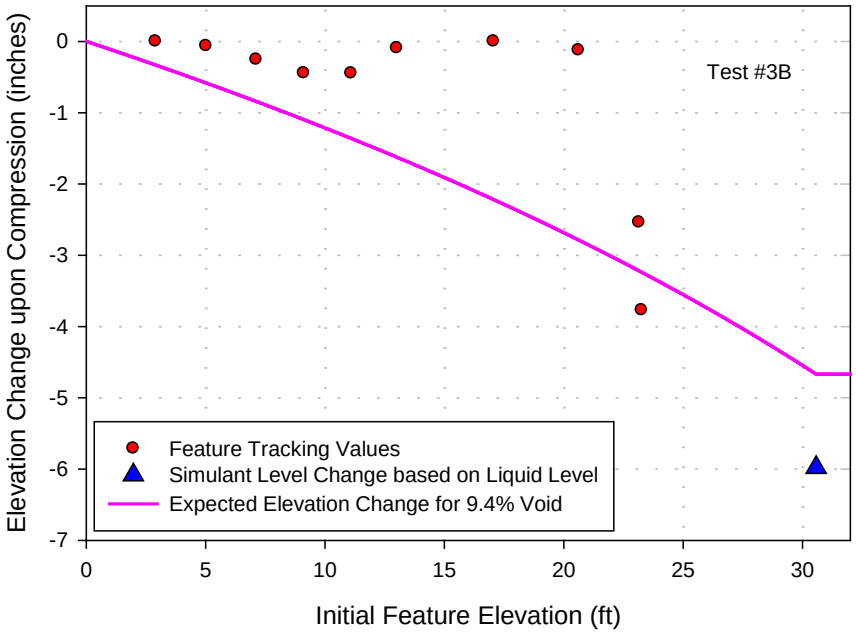

Figure 8.8. Elevation Change Measurements and Predictions for Test 3B Compression

Figure 8.9 shows the void fraction profile for Test 2 implied by the elevation change data in Figure 8.7. Each data point (black circles) represents the locally averaged void fraction, which is expressed as a percentage in the figure. The void fraction for each point is averaged over an elevation range corresponding to the distance between successive tracked features, which roughly corresponds to the difference in elevation between each camera and its nearest neighbors. The red line in the plot connecting the data points is intended to aid the eye and is not intended to imply that the gas content varies in the stair-step fashion shown in the plot.

The void fraction profile in Figure 8.9 compares favorably with overall average void fraction calculated by two other methods. The average void fraction based on liquid level measurements before the compression test is calculated by Equation 4.6 to be 7.6% (black dashed line). The average void fraction based on the change in simulant surface elevation upon compression is calculated by Equation 4.8 to be 8.1% (blue dashed line). For comparison, the integrated average of the void fraction profile shown in Figure 8.9 (green dashed line) is 7.9%. This agreement between the void fraction profile and the average void fraction determined by alternative calculations gives additional confidence that the void fraction profile estimated for Test 2 based on the compression test results is reliable.

The void fraction profile for Test 2 shown in Figure 8.9 is consistent with the void fraction profiles developed by other methods (discussed later in this section) in that the void fraction near the bottom of the column is lower than the void fraction at higher elevations. This result is not consistent with d_{max} theory, which predicts the void fraction should be higher at depths below d_{max}.

The calculated local void fraction values are sensitive to relatively small variations in compression-induced elevation change. For the feature tracked using the bottom-most camera, for example, the measured elevation change was only 5 mm (0.2 in.). Similarly, the relatively small variations in slope between successive data points in Figure 8.7 result in the comparatively large swings in void fraction shown in Figure 8.9. Every effort was made to ensure accurate measurement of the compression-induced elevation changes. However, the limit of measurement accuracy on the digital photographs is estimated to be about ±1 mm, which is large enough to affect the calculated local void fractions. Despite this high sensitivity to small elevation changes, the resulting void fraction profile for Test 2 is consistent with the average void fraction determined via alternative techniques. This consistency gives some confidence that the void fraction profile was not adversely affected by measurement errors.

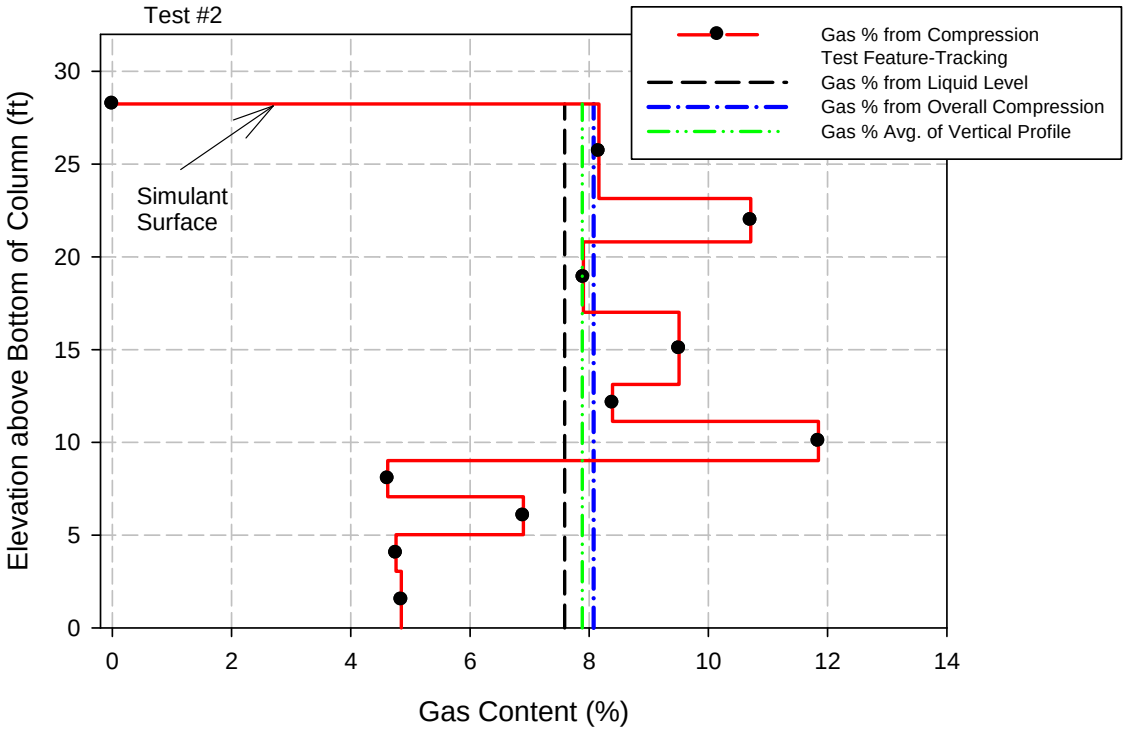

Figure 8.9. Gas Content Profile Estimated from Compression for Test 2

Ultrasonic Results

The 500 Pa correlation given in Section 6.1.3 was applied to the tall column Test 1 and Test 2 data to determine GVF at each elevation containing a pair of UT sensors. All 10 elevations contained two sensors pairs. Attenuation data for the two transducer pairs at each elevation for a given time increment were averaged to generate one GVF value for the elevation per time increment. The data plot of tall column elevation vs. GVF for tall column Test 1 is in Figure 8.10. The data plot of tall column elevation vs. GVF for tall column Test 2 is in Figure 8.12.

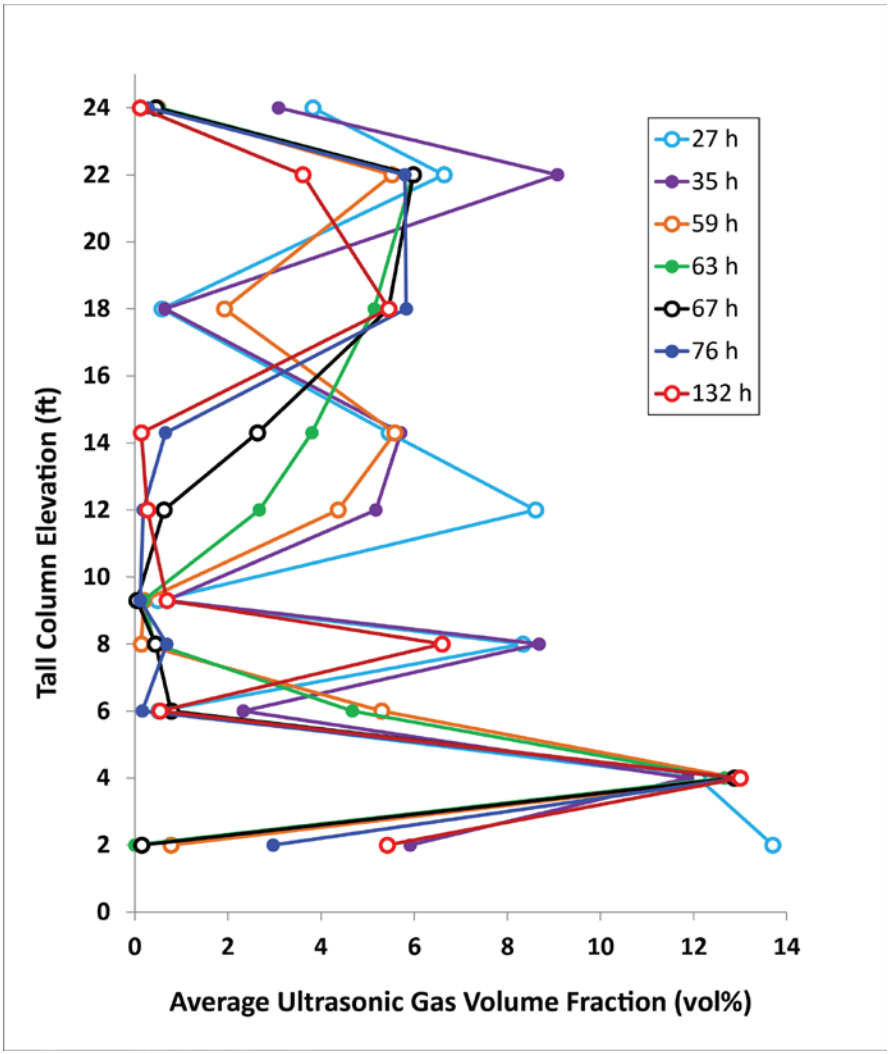

Figure 8.10. Tall Column Test 1: Elevation vs. Ultrasonic GVF for a Subset of Time Intervals

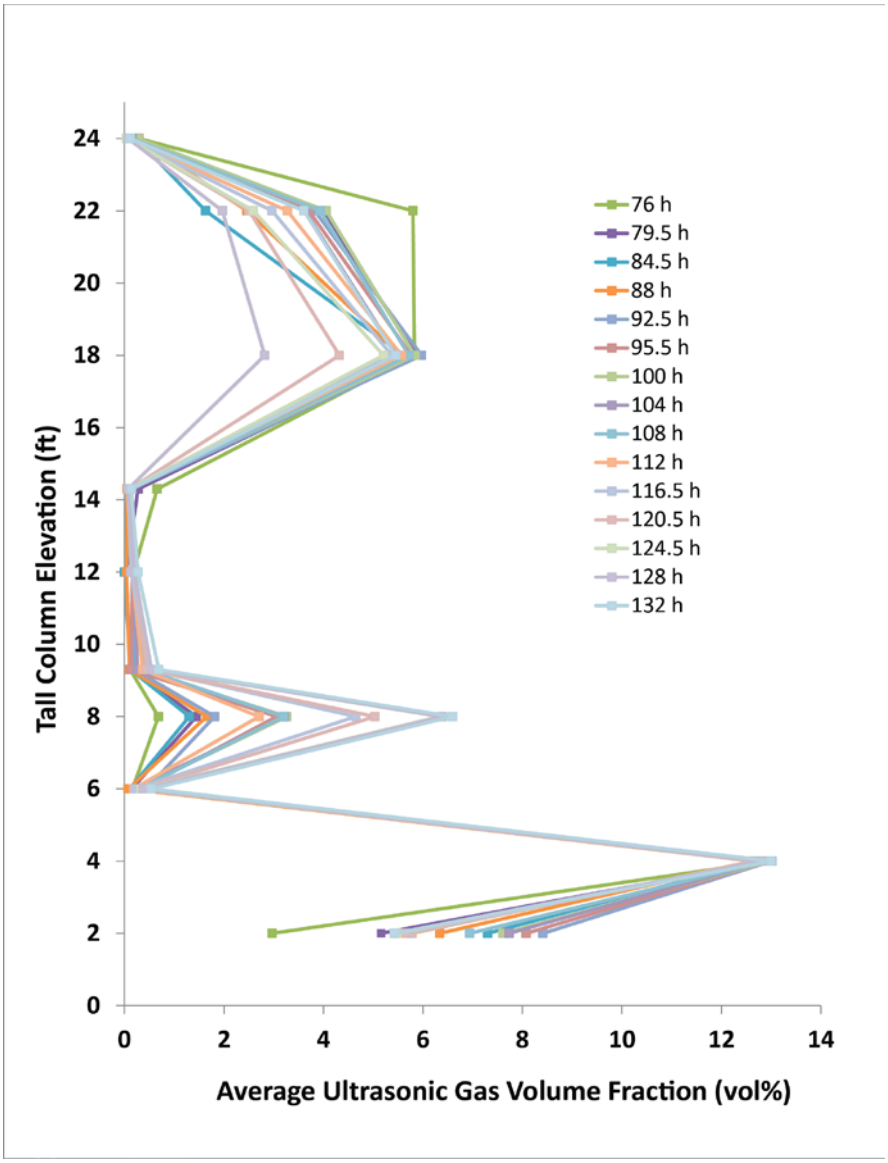

Figure 8.11. Tall Column Test 1: Elevation vs. Ultrasonic GVF for a Later Portion of the Test

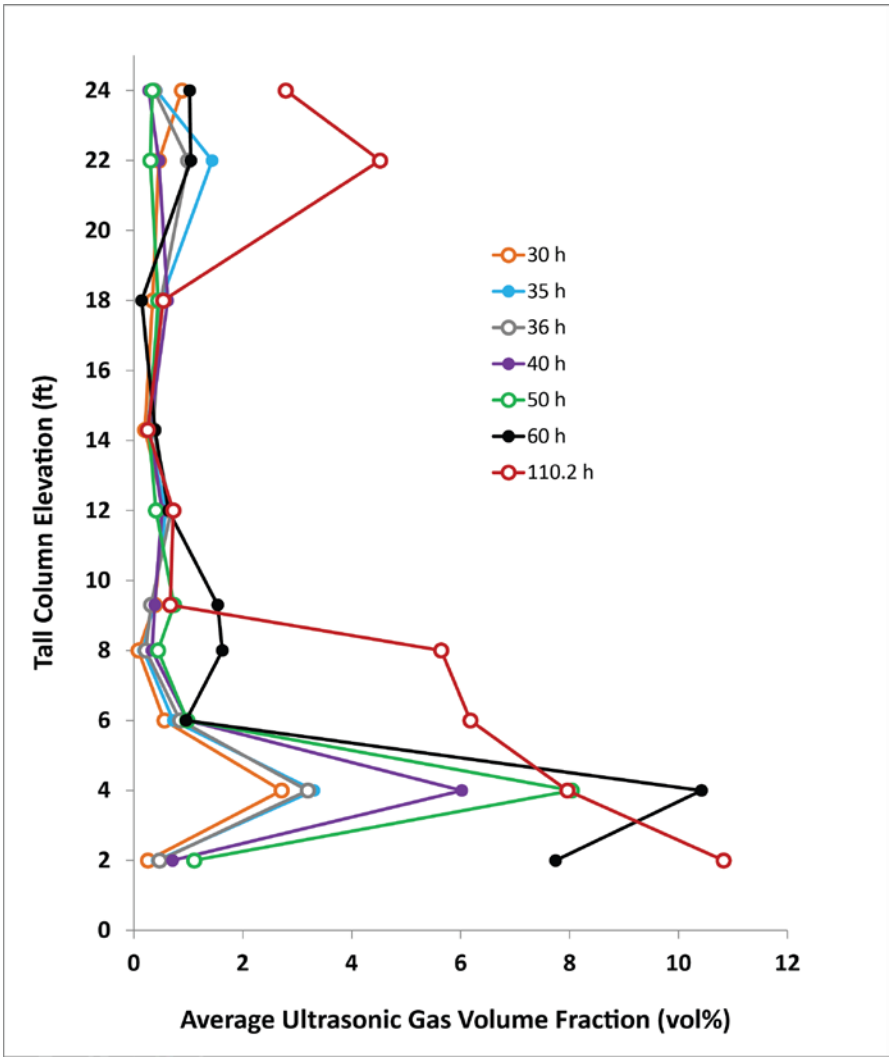

Figure 8.12. Tall Column Test 2: Elevation vs. Ultrasonic GVF for a Subset of Time Intervals

The tall column Test 1 and Test 2 ultrasonic profile data with GVF values between 2% and 10% have high uncerainty due to the near-zero slope in the 500 Pa correlation in this region. However, GVF values below 2% and above 10% have higher certainty because there are positive slopes in the 500 Pa correlation in these regions. The elevation vs. GVF data plot in Figure 8.11 for tall column Test 1 for the time period of 76 to 132 hours shows two important features:

1. A contiguous region of sustained GVF below 2% detected by the transducers located at the 9.3, 12, and 14.3 ft elevations. A GVF below 2% was also detected by the transducers at the 6 ft elevation.

2. A sustained GVF of 13% detected by the transducers located at the 4 ft transducer elevation.

A GVF profile similar to the ultrasonic profile determined for Test 1was observed during tall column Test 2 as shown in Figure 8.12. However, the region of sustained GVF below 2% was detected by most of the transducers for most of the test with the exception of the transducers at the 4 ft elevation. The transducers at the 4 ft elevation detected a GVF greater than 2%, but lower than 10% for most of the test

until the 55 h mark when the transducers began to detect a GVF greater than 10%. The transducers detected a shift from this trend at 100 hours (near the end of the test) when the GVF at the 2, 6, 8, 22, and 24 ft elevations began to increase while the GVF at the 4 ft elevation began to decrease. The test was concluded at approximately 112 hours.

The GVF profile for Test 3 shows very little difference in GVF along the tall column as shown in Figure 8.13. A review of the ultrasonic signals collected by the transducer pairs during Test 3 showed very little change in signal amplitude during the test, which results in low attenuation and low GVF values.

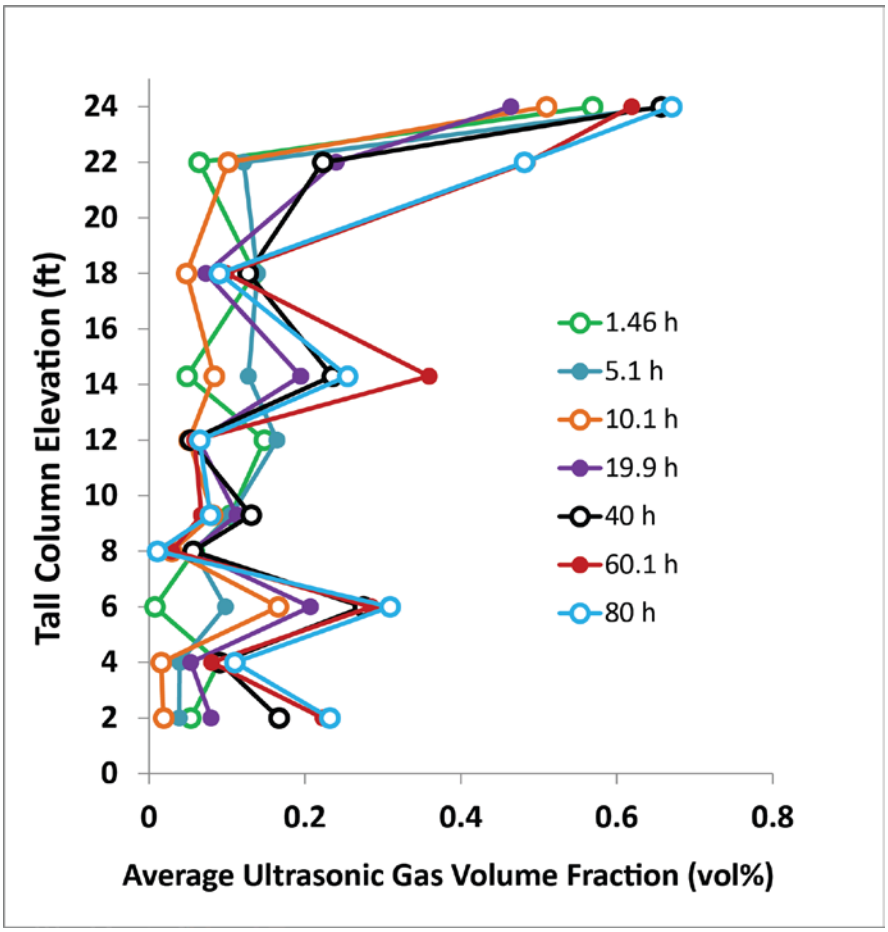

Figure 8.13. Tall Column Test 3: Elevation vs. Ultrasonic GVF for a Subset of Time Intervals

The purpose of performing ultrasonic measurements on the tall column was to determine if high GVFs existed in the lower elevations of the column during testing. The accuracy of the GVF values determined by ultrasonic attenuation measurements rely heavily on the correlation data for the 500 Pa and 1000 Pa kaolin simulants and how well the simulated conditions in the laboratory represented those in the tall column. The shear strengths of the simulants used in the correlation tests were representative of those loaded into the tall column during Tests 1, 2, and 3. However, other factors such as uneven gas distributions in the test vessel used to develop the correlation may have affected the accuracy of the correlation between attenuation and GVF. The correlation equations were therefore more valuable in distinguishing between “low” and “high” GVF values and less valuable for quantifying GVF with high

resolution or accuracy. Using the 500 Pa correlation in this capacity for tall column Tests 1 and 2 suggests there were areas with relatively higher GVFs toward the 4-foot elevation during both tests. The consistency and trend toward this profile over the course of both tests suggests the phenomenon is not due to other slurry property changes, such as slurry compaction, or system errors such as transducer malfunction. Applying the 1000 Pa correlation to data obtained for Test 3 suggests very little difference in GVF along the tall column and determined no areas of high GVF at the lower elevations of the tall column.

Feature Tracking Results

Images from all nine fixed-position cameras were analyzed for Tests 1 and 2. For Test 3B, however, only images from Cameras 1 through 6 were analyzed. The images from Cameras 7 through 9 for Test 3B were not utilized because there was considerable smearing and sticking of the simulant on the viewing windows. As a result, it was not possible to track features for those cameras. As a proxy for the elevation change data from Cameras 7 through 9, changes in liquid level were used instead to allow estimation of the void fraction in the region between Camera 6 and the simulant surface.

Figure 8.14, Figure 8.15, and Figure 8.16 show the measured changes in elevation throughout the three tests for each of the features tracked. In addition to the feature tracking elevations from each of the cameras, the figures also include the changes in elevation for the water surface and the simulant surface. The location of the water/air interface is very distinct, so the water-surface elevation changes are known with comparatively good accuracy. The location of the simulant surface, however, is much less distinct and subject to greater measurement error. The "initial elevation" shown in the legend of each figure refers to the initial elevations of the features tracked in the images, except in the case of the simulant and water surfaces where the measured initial elevations are indicated.

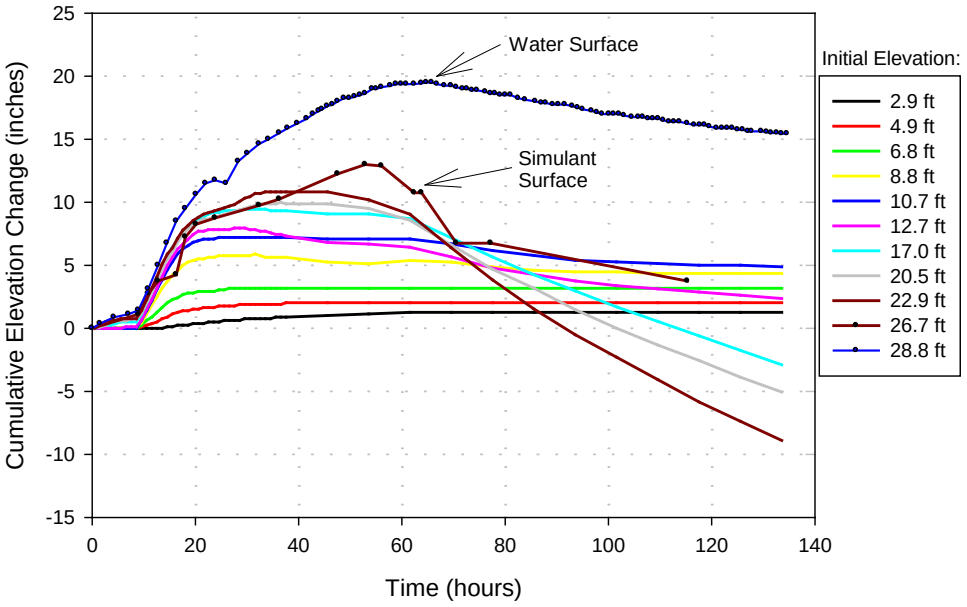

Figure 8.14. Feature Elevation Changes Throughout Test 1

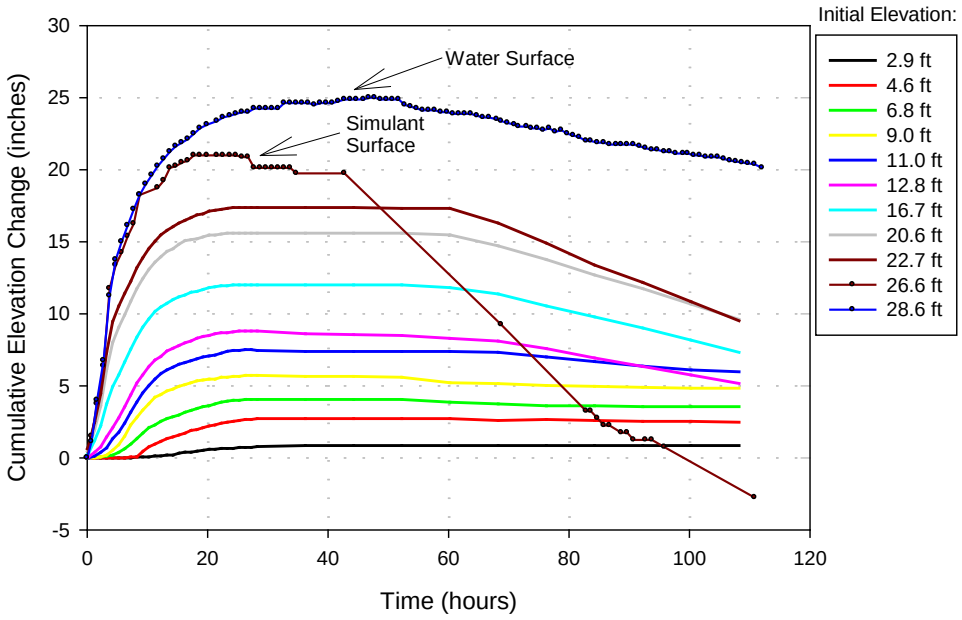

Figure 8.15. Feature Elevation Changes Throughout Test 2

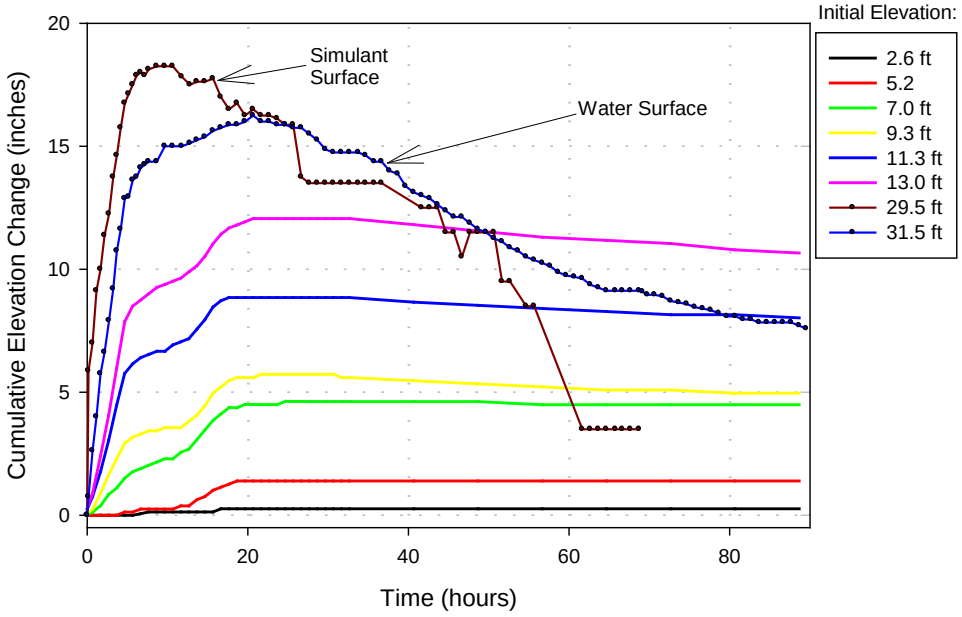

Figure 8.16. Feature Elevation Changes Throughout Test 3B

During each test, a combination of gas-flow-driven dewatering and gravitational consolidation resulted in increased simulant density for some elevations (see Appendix A, Section A.4). These density changes were large enough to affect the magnitude of the feature elevation changes observed during the tests. As shown in Figure 8.14, Figure 8.15, and Figure 8.16, the cumulative elevation changes for the features in the upper portion of the column reach a peak and then decrease significantly. In some cases,

the resulting elevation change is sufficient to result in the feature having a negative net elevation change by the end of the test. These reductions in elevation gain are driven partly by the density increase of the simulant during the test. The negative elevations may also correspond to a drop in void below the initial void present at the start of the test. Due to the uncertainty in measuring the simulant level, similarities in the shape of the cumulative elevation change curves with the simulant surface level change curve would only be expected prior to the time when the simulant surface level reaches its peak value.

To correct for the effects of the density change, the core sample data were used to determine the magnitude of the density change and its variation with elevation. The cumulative elevation change data were then adjusted to estimate the elevation changes that would have been observed in the absence of density changes. Figure 8.17 and Figure 8.18 show the density-adjusted elevation change data. The variation of simulant density at the end of Tests 1 and 2 was estimated based on the measured solids content of the end-of-test core samples. No core samples were collected during Test 3B, so no density-based adjustments to the feature-elevation data were made for Test 3B.

The density adjustment was applied to all feature elevations after the initial elevation measurement. This approach undoubtedly results in too much density correction being applied to the data collected early in the test before most of the consolidation and dewatering occurred. However, there is no independent means of determining when and how much of the density correction to apply, so the approach taken here is to apply all of the density correction to essentially all of the data. This approach results in the predicted gas contents being higher than they would be in the absence of the applied density correction.

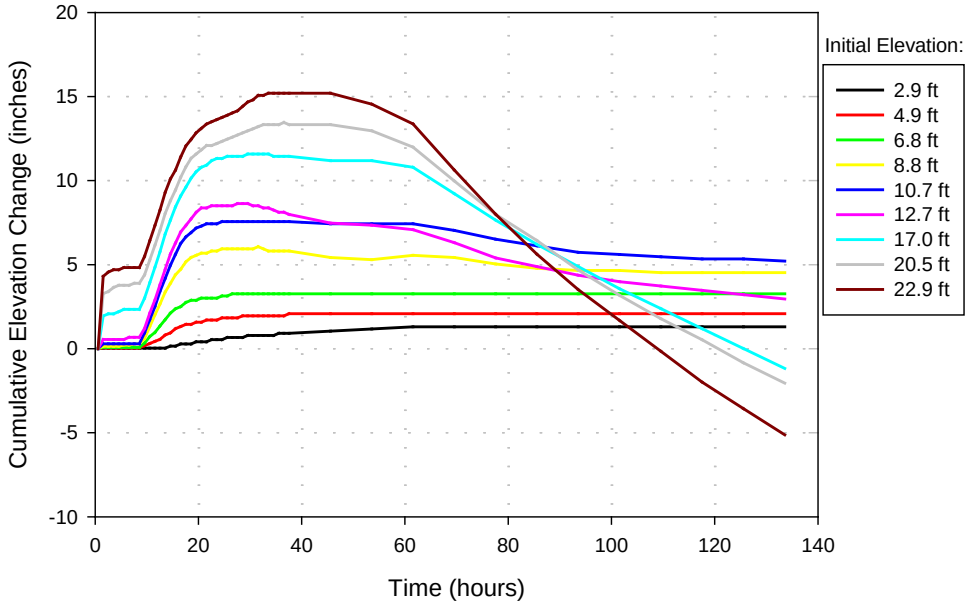

Figure 8.17. Density-Corrected Feature Elevation Changes Throughout Test 1

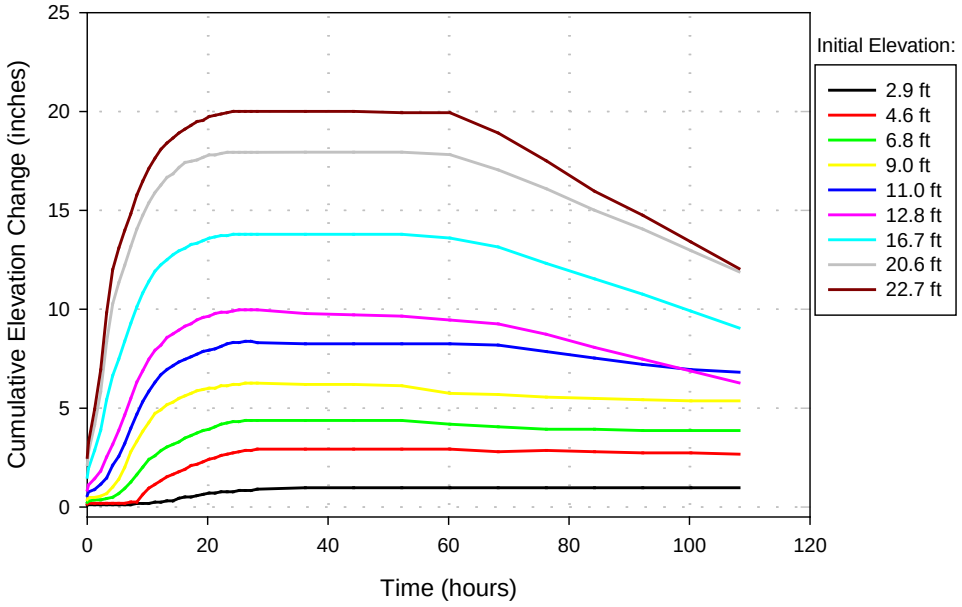

Figure 8.18. Density-Corrected Feature Elevation Changes Throughout Test 2

The data in Figure 8.14 through Figure 8.18 can be used directly in Equation 4.9 to calculate $\Delta h(t)$, which can then be used in Equations 4.10 and 4.11 to determine ϕ_{local} over the elevation ranges between each pair of tracked features. Figure 8.19 through Figure 8.23 show the evolution of the ϕ_{local} vertical profiles at selected times throughout each test. Figure 8.19, Figure 8.21, and Figure 8.23 are the ϕ_{local} values based on the elevation changes without density corrections applied for Tests 1, 2, and 3B, respectively. Figure 8.20 and Figure 8.22 show the ϕ_{local} vertical profiles for Tests 1 and 2 based on the density-corrected elevation change data. No density-corrected ϕ_{local} data were generated for Test 3B because no core samples were taken during Test 3B.

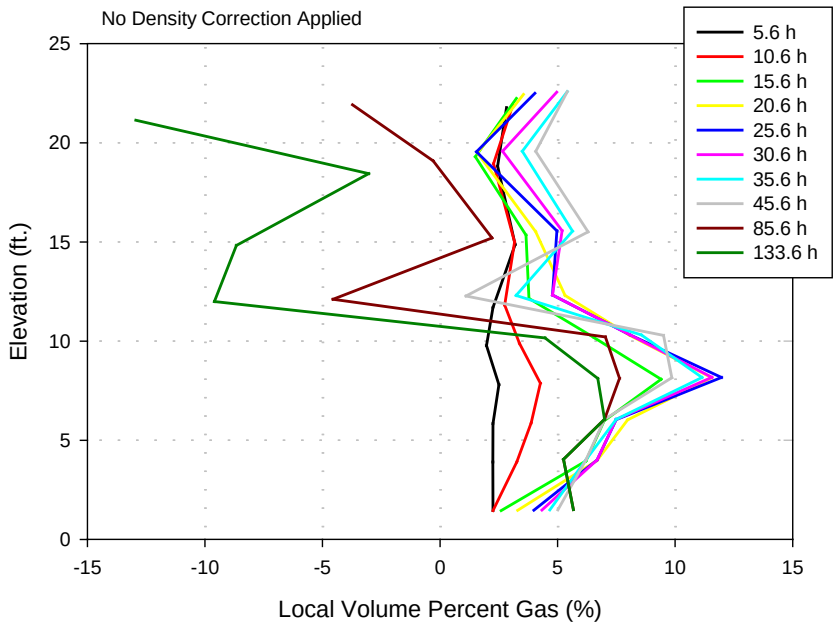

Figure 8.19. ϕ_{local} Vertical Profiles (no density correction) for Test 1

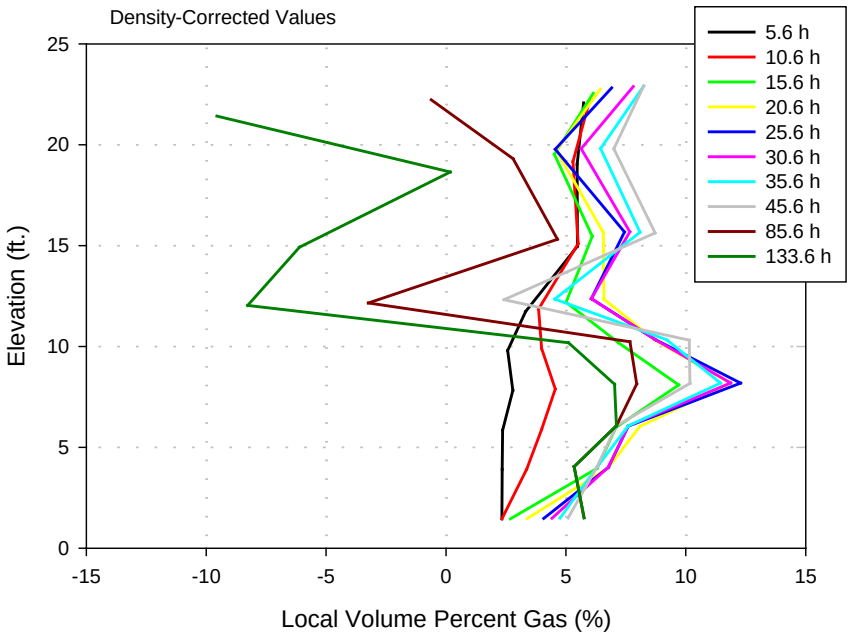

Figure 8.20. ϕ_{local} Vertical Profiles (with density correction) for Test 1

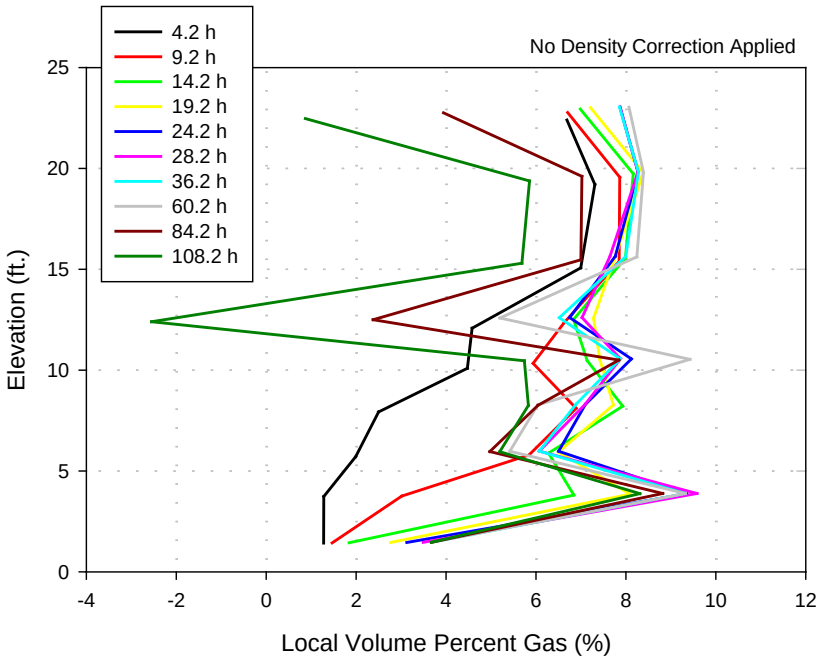

Figure 8.21. ϕ_{local} Vertical Profiles (no density correction) for Test 2

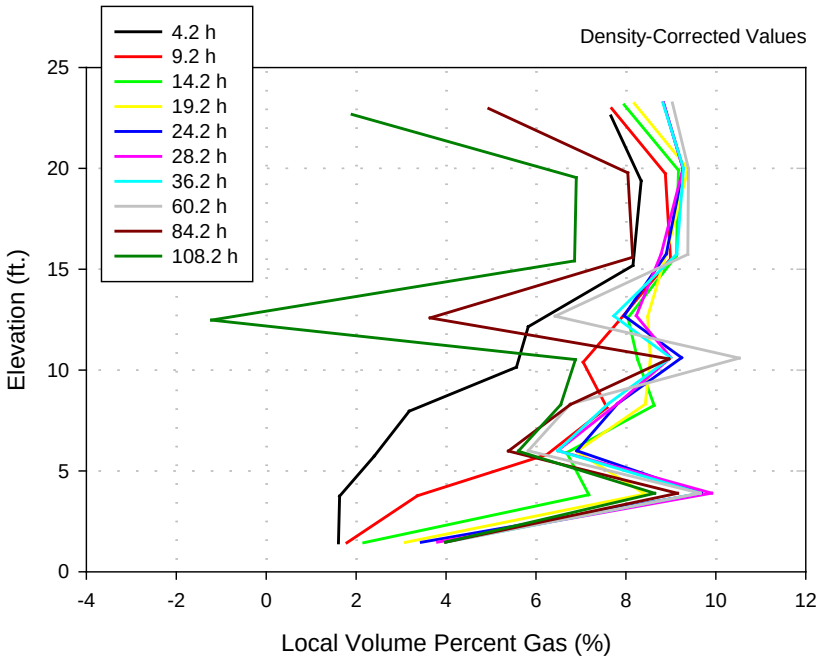

Figure 8.22. ϕ_{local} Vertical Profiles (with density correction) for Test 2

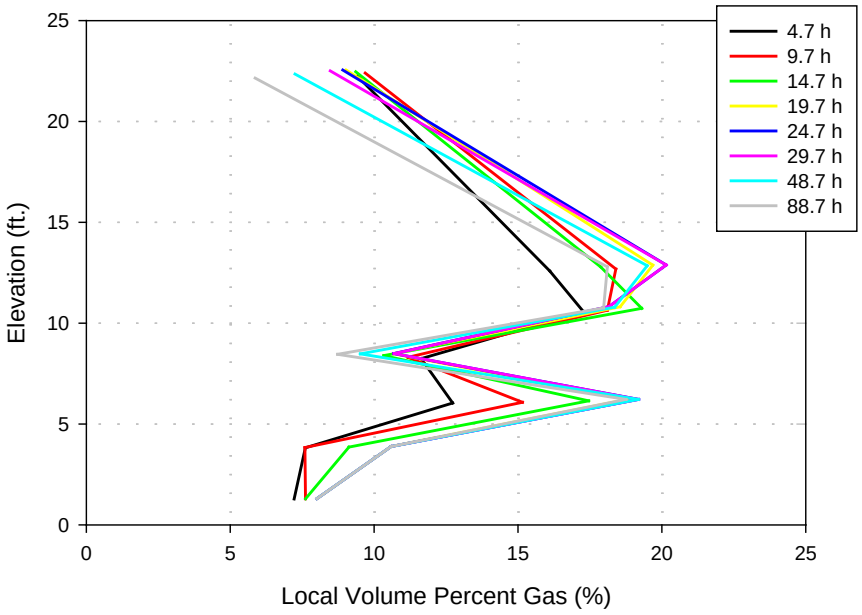

Figure 8.23. ϕ_{local} Vertical Profiles (no density correction) for Test 3B

The ϕ_{local} data shown in Figure 8.19 to Figure 8.23 are reasonable-looking profiles up through the time roughly corresponding to peak void fraction. Thereafter, some regions show marked reductions in void fraction until negative void fraction is indicated. A negative void fraction is not physically possible, so the results for these times are erroneous. The negative void fractions result from the excessive downward movement of the tracked features due to compaction in the regions near the top of the simulant column. Figure 8.14 through Figure 8.16 show the downward movement of the upper regions of simulant even when the liquid level is comparatively stable.

In addition to gravity-driven consolidation and gas-flow-driven dewatering, the simulant was also apparently affected by upward movement of simulant in some regions that resulted in downward movement in other regions. During Test 1, it appears the simulant near the viewing windows was forced downward due to this effect by an amount that is significantly greater than can be accounted for by the density-changing effects of consolidation and dewatering. The data from Tests 2 and 3B were affected to a lesser degree, but the effect is still evident near the end of both tests (see Figure 8.15 and Figure 8.16).

The downward movement of simulant features complicates interpretation of the feature tracking analysis and it is not clear whether the affected data are useful. However, early in each test the measured elevation changes track well with the liquid level and do not show the problematic elevation reductions until after peak void is achieved. Up until roughly the point at which peak void fraction is reached, the ϕ_{local} estimates based on the feature tracking technique should be reliable because the downward-motion and consolidation/dewatering effects should be relatively small.

Figure 8.24 through Figure 8.26 show the ϕ_{local} profiles for times specifically selected to be at or slightly before peak void. These void fraction profiles are judged to be the most reliable estimates that can be generated using the feature-tracking technique. For Tests 1 and 2 (Figure 8.24 and Figure 8.25), each plot includes ϕ_{local} values (expressed as a percentage) both with and without the density correction

applied. The data for Test 3B (Figure 8.26) have no density correction applied. As discussed earlier, the density-corrected values likely overestimate the void fraction while the uncorrected values likely underestimate the void fraction. The actual void fraction is expected to be between the corrected and uncorrected values for each elevation. Also shown on each plot for comparison is a vertical dashed line indicating the average void fraction determined from the liquid level measurements.

Agreement between the void profile and the liquid-level-determined average void fraction is generally good for Tests 2 and 3B. The feature tracking-based void fractions for Test 1 are lower than implied by the liquid-level-based average void. This difference is likely due to the downward-simulant-motion effect, which was clearly active before peak void (refer to Figure 8.14). In all tests, however, the feature tracking-based void fraction estimates do not show increased void fraction near the bottom of the column as is predicted by d_{max} theory.

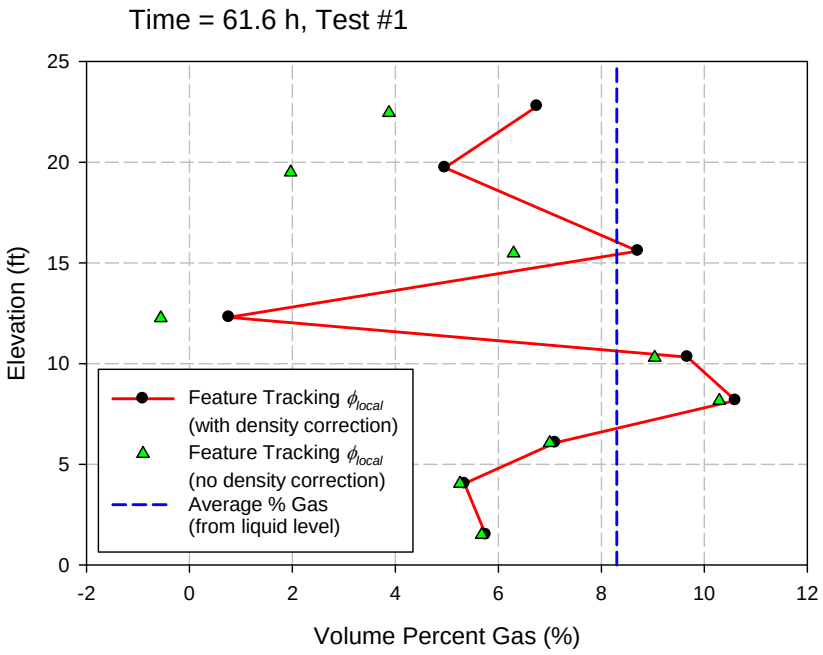

Figure 8.24. ϕ_{local} Vertical Profile for Test 1 at 61.6 Hours

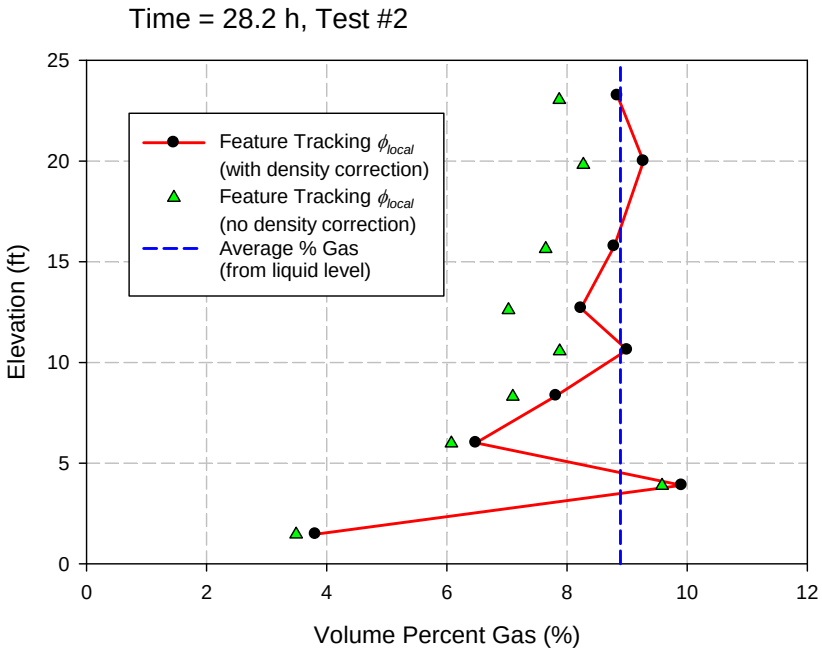

Figure 8.25. ϕ_{local} Vertical Profile for Test 2 at 28.2 Hours

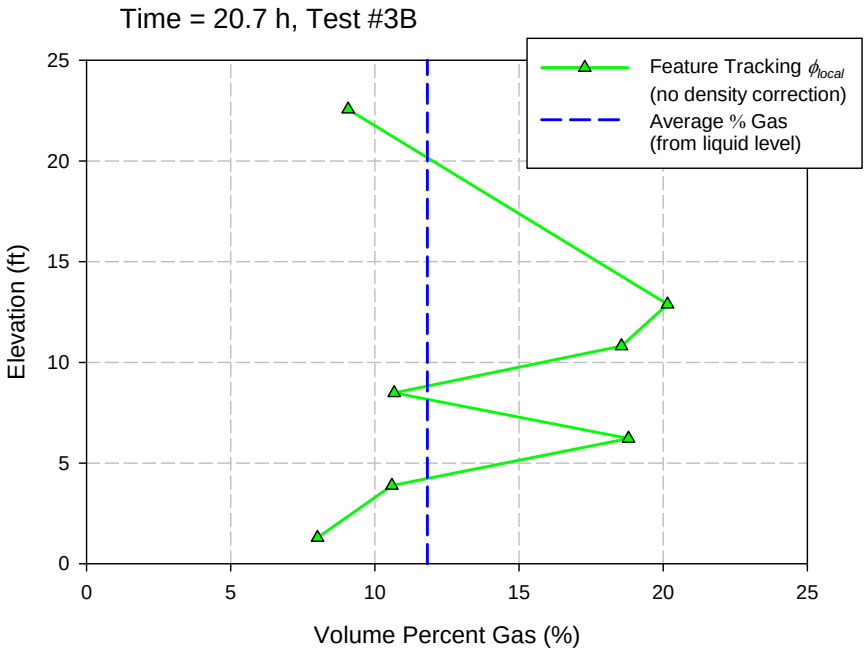

Figure 8.26. ϕ_{local} Vertical Profile for Test 3B at 20.7 Hours

Image Analysis

The image-analysis method was applied to the same set of images that were used in the feature-tracking technique described previously. The techniques used the same images at the same times using different information. Note that the image analysis generates an estimate of the void fraction over an area and is a two-dimensional measure; the uncertainty was ascribed to be ±1% (absolute). The uncertainty

bands are not shown in figures to avoid inconveniencing the interpretation of the data. The image analysis was conducted using the video camera images, so the elevations given are the centerline locations of the nine fixed cameras in the viewing column.

The void fraction data for Test 1 are shown in Figure 8.27. The void profiles near the start of the test indicate a void fraction of ~1%, with the exception of the middle of the column (between 10 and 15 ft), which was higher. The middle region in the column continued to grow and peaked at around 15 h before falling back to void values similar to those found at the other column elevations by the 25-h mark. This region was approximately where the interface between the two loads was in Test 1—determining whether that had a role in the initial spike in the void data is complicated. Near the peak of the bulk void (t = 53.57 h), the void is approximately 3% to 5% at all but the two highest elevations. The void stays in this range until the end of the test, while there was an increase in void at the higher elevations. The void profile in Test 1 does not suggest that there was increased gas retention at the bottom of the tall column relative to higher elevations.

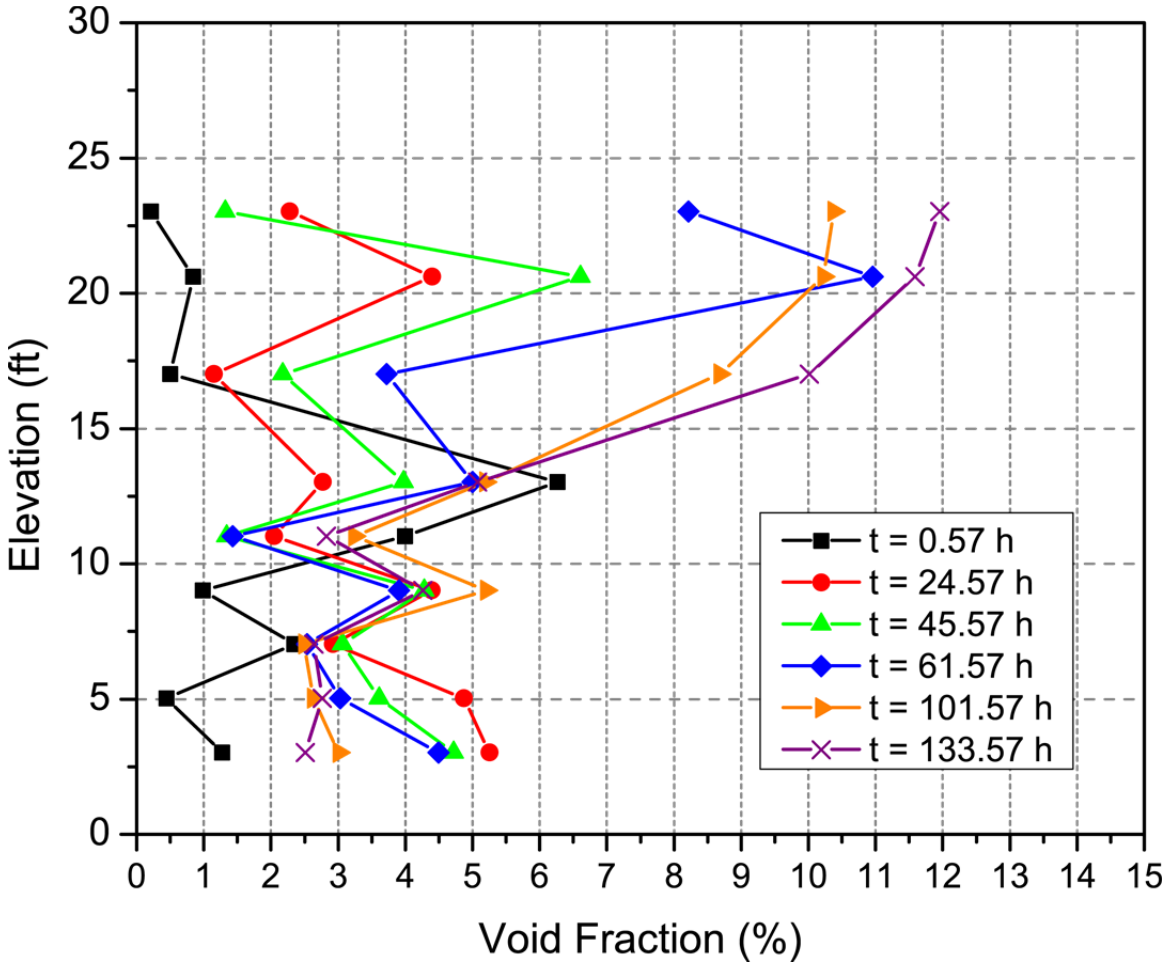

Figure 8.27. Void Fraction (Area) Determined by Image Analysis for Test 1

The void data determined by image analysis for Test 2 are displayed in Figure 8.28. The initial void is very low and consistent with the estimate of initial void given in Table 8.1. Following a small spike in void at elevations between 5 and 9 ft at around 10 h elapsed time, the void profile remained around 3% to

6%, depending on elevation, for the majority of the test. Later in the test (after the peak bulk void was achieved) the void increases, most dramatically at the upper elevations in the column. Careful examination of the images analyzed at these times indicated that some of the areas interpreted by the image analysis algorithm as void were due to discolorations (regions of slurry that were noticeably darker) in the simulant. In the interest of maintaining a consistent calculation method, the algorithm was not adjusted for Test 2 to eliminate some of the "false positives"; this also runs the risk of overcorrecting in the opposite direction and underestimating void in other images earlier in the test. Nonetheless, even if the increase in void at the end of Test 2 was real, the data do not indicate that more gas was retained at the column bottom than at other elevations. In all likelihood, if the "false positives" could be properly accounted for without significantly affecting the analysis, the void profile at the end of Test 2 would be much closer to the t = 28.23 h curve than either of the curves from later elapsed times.

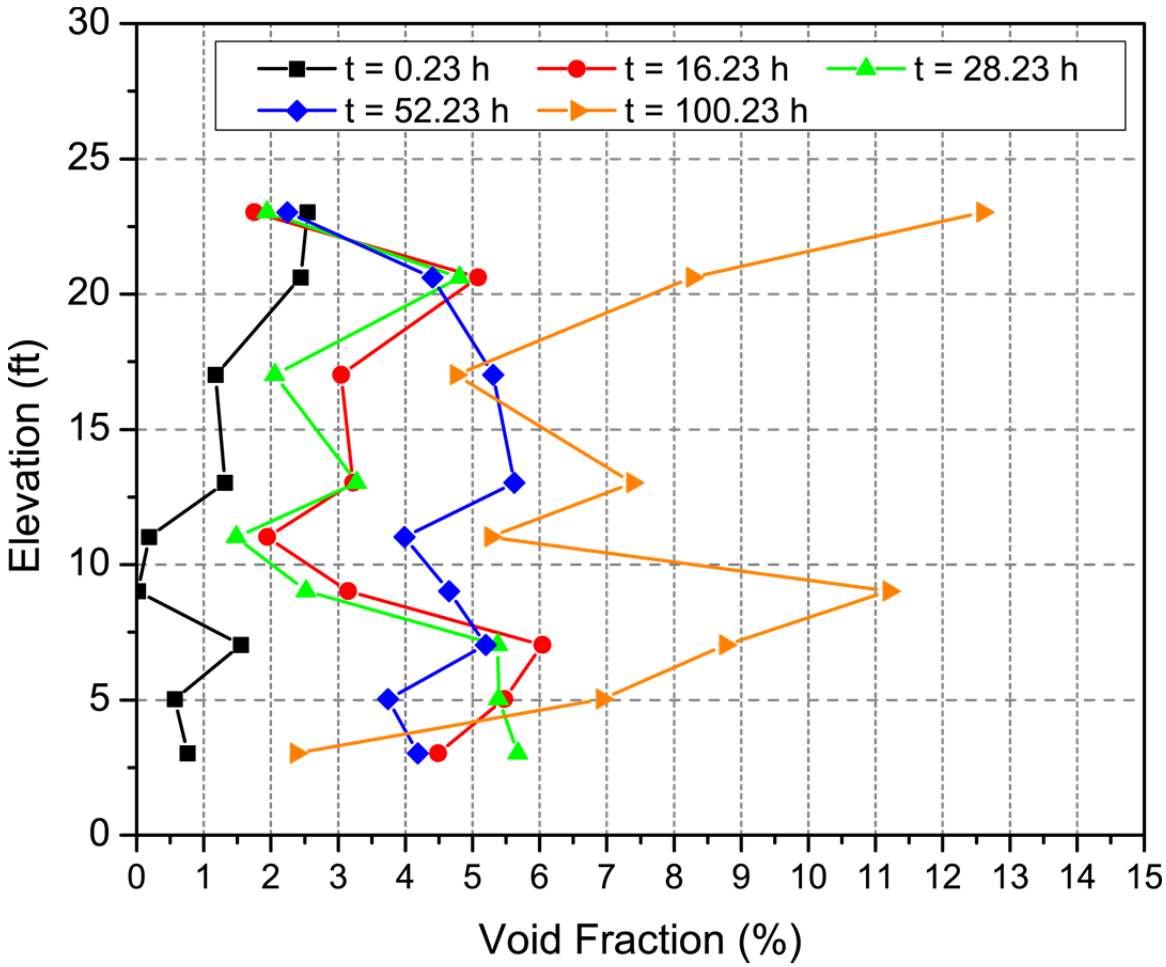

Figure 8.28. Void Fraction (Area) Determined by Image Analysis for Test 2

Test 3 void fraction data determined by image analysis are given in Figure 8.29. The same problem that plagued the feature tracking data (adhesion of simulant to the viewing window, wall smearing) also affected the image-analysis approach, so only images from the bottom six cameras were analyzed. The initial void was estimated to be very low, which does not agree well with the calculated initial void of around 7%. For essentially the entire data set, aside from Camera 6 (13 ft) at early times, the void is bounded between approximately 2% and 6% void at all six elevations. A small increase in void at some

lower elevations appears in the t = 112.67 h curve, but the later data has a similar shortcoming as in the Test 2 data—the problem of "false positives" occurring as the simulant compacts and darkens during the test. Overall, there is nearly a vertical void profile (implying constant void over the entire simulant depth[1]) at all elapsed times, and no large increases in void were seen at the lowest elevations.

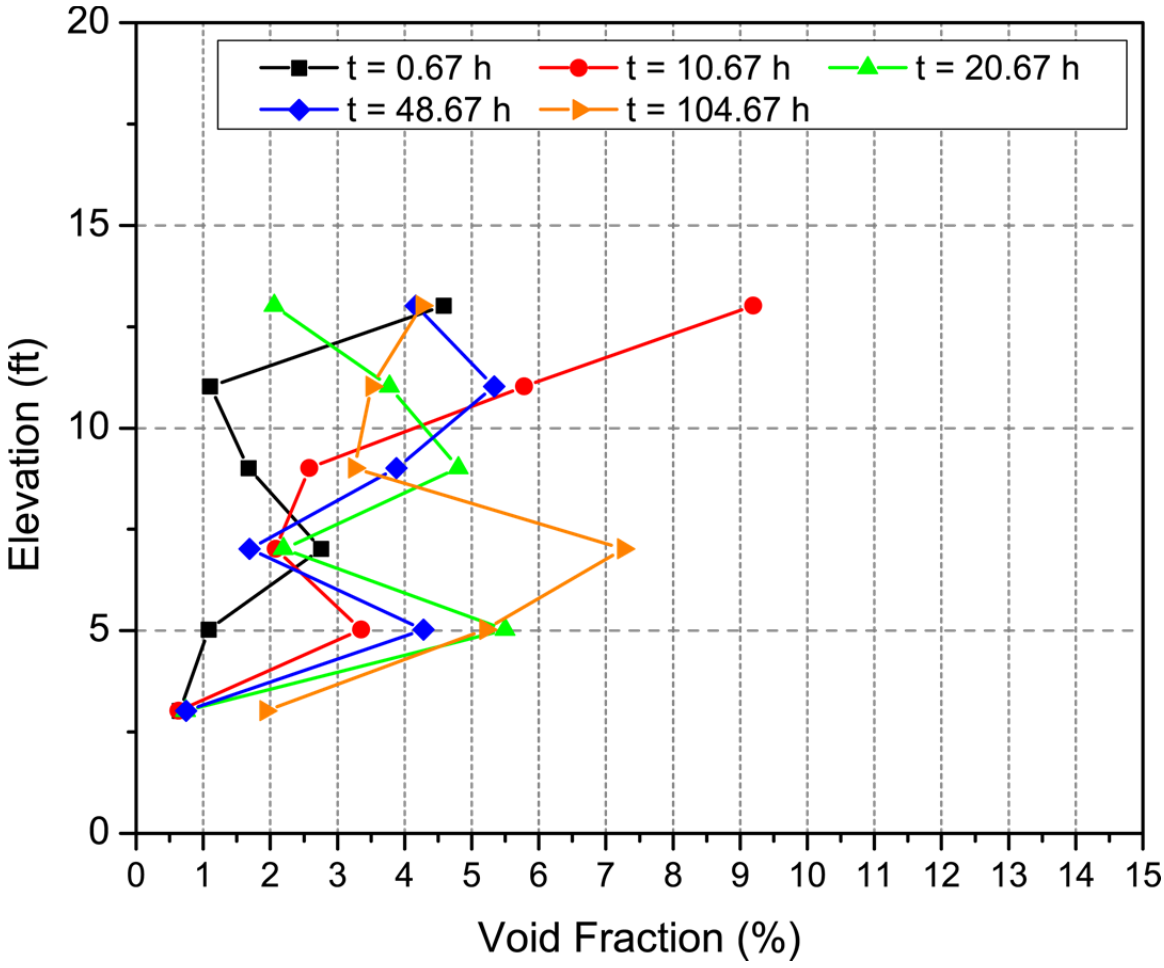

Figure 8.29. Void Fraction (Area) Determined by Image Analysis for Test 3

The Test 3 data most clearly illustrate how the image analysis data suffered from relying on a planar image to estimate a volume-based quantity. The void fractions, at least at the six elevations where data were available, are all lower in magnitude than the bulk void measured during the test. The method, on the basis of comparing the bulk void implied by the void profile with the measured bulk void, appeared to be biased low in all three tests. Given the caveats listed in Section 4.3.3, the qualitative nature of the analysis was foreseeable. The bias in the data indicates that the image-analysis technique was less accurate than the feature tracking approach in estimating the void. This does not invalidate it as a useful approach for assessing the relative magnitude in void fraction at various elevations, and the data from the three tests all support the notion that there was no increase in retained gas at the column bottom.

[1] Assuming, in the case of Test 3, that the data from the bottom six cameras is representative and can be extrapolated to the images from the highest three cameras that could not be analyzed.

Comparison of Void Profiles

The preceding sections present three methods that calculated the void fraction profile in the tall column as a function of elapsed time. This does not include the void fraction profile obtained from analysis of post-test compression data, which is only applicable at the time the compression occurred (the end of the test). Comparing the void profiles for all elapsed times was intractable given the size of the data sets. In the authors' estimation, the most instructive comparison is when the simulant in the column is at or near the peak bulk void measured in each test. The void profiles determined by the three methods were compared by plotting the elevation against the void fraction. The elevation is plotted at the mid-point of the local region where the given void fraction was estimated.

The comparison for Test 1 is given in Figure 8.30. The void profiles were compared at approximately 61 h elapsed time, which is just before the peak void was achieved (t = ~65 h). This comparison was slightly different from the other two tests because the UT data were collected manually every 4 hours, so the elapsed times are not as tightly clustered as in the other two tests. The UT data, which were demonstrated to be insensitive (see Figure 6.10) in the range encompassing the peak void, have a significant degree of variability with elevation. These data do not permit clear conclusions to be drawn on the behavior of the profile. The image-analysis data, in general, appear to underestimate the void. These data do not indicate any large increases of void at the lower elevations. Data from the feature tracking method also have some variability but on average appear to be similar to the bulk void at the selected elapsed time. Void fractions at the lowest elevations are similar to those near the top, and no increase in void with depth was apparent in the data.

The comparisons for Test 2 and Test 3 are presented in Figure 8.31 and Figure 8.32, respectively. By and large, the void profile data for both Test 2 and Test 3 indicate more convincingly that the feature tracking method was the most accurate of the three methods. Image analysis and UT underestimate relative to the peak bulk void measured at the same time, though they generally indicate that there are no increases in void at the lowest depths. Feature tracking compared much more favorably to the peak bulk void, especially in Test 2. The Test 3 data suffer from a lack of information from Cameras 7, 8, and 9 (elevations of 17 ft and higher), making the data set more sparse. However, the most conservative estimate of d_{max} suggests that only the lowest elevation would be below it, and this elevation has the smallest void of the profile.

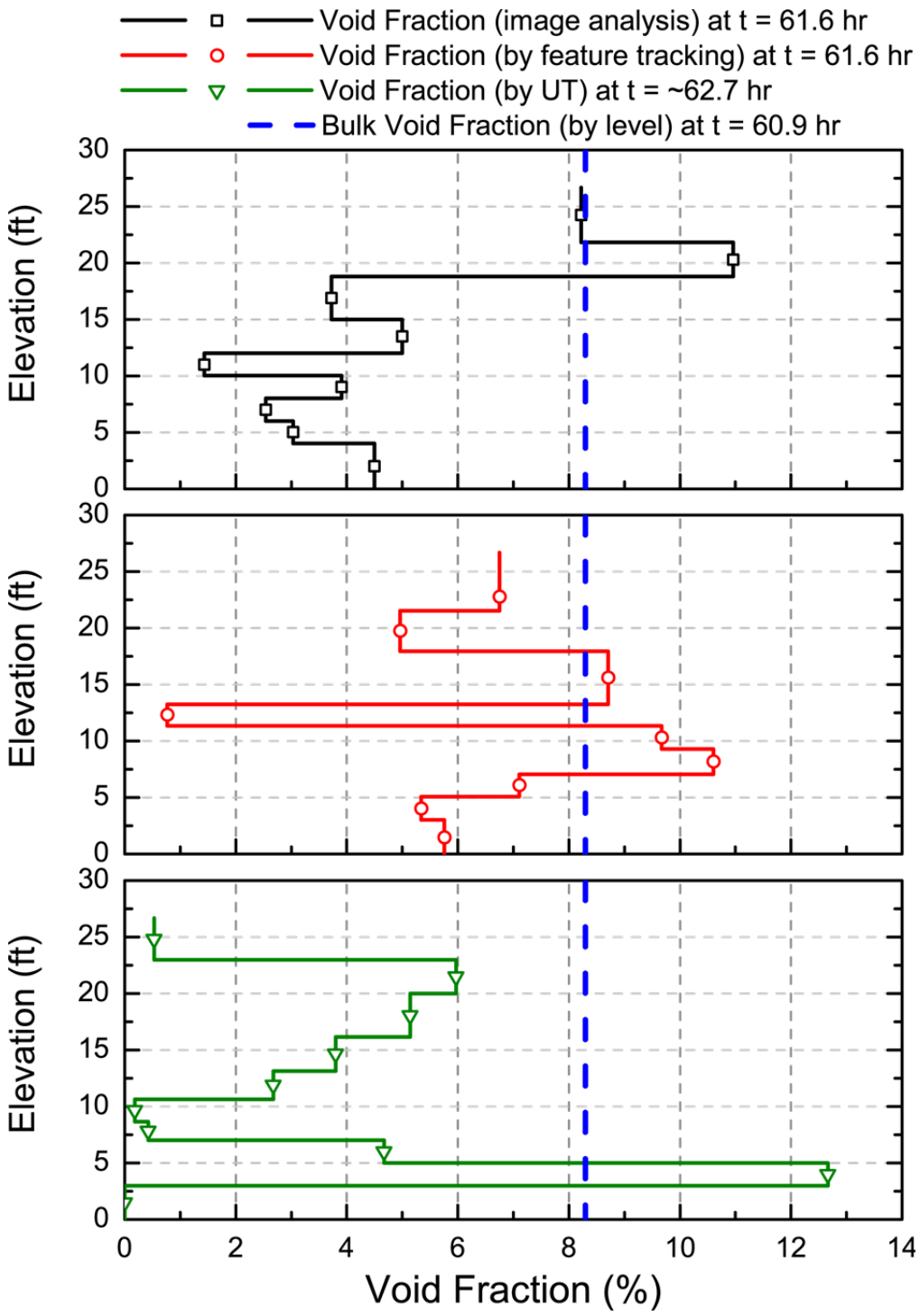

Figure 8.30. Comparison of Void Profiles for Test 1 at t ~ 61 h. This is close to the peak in bulk void, which is indicated by the vertical blue line. The void fraction profiles are shown with values plotted at the mid-point of the column elevation each calculated void represents.

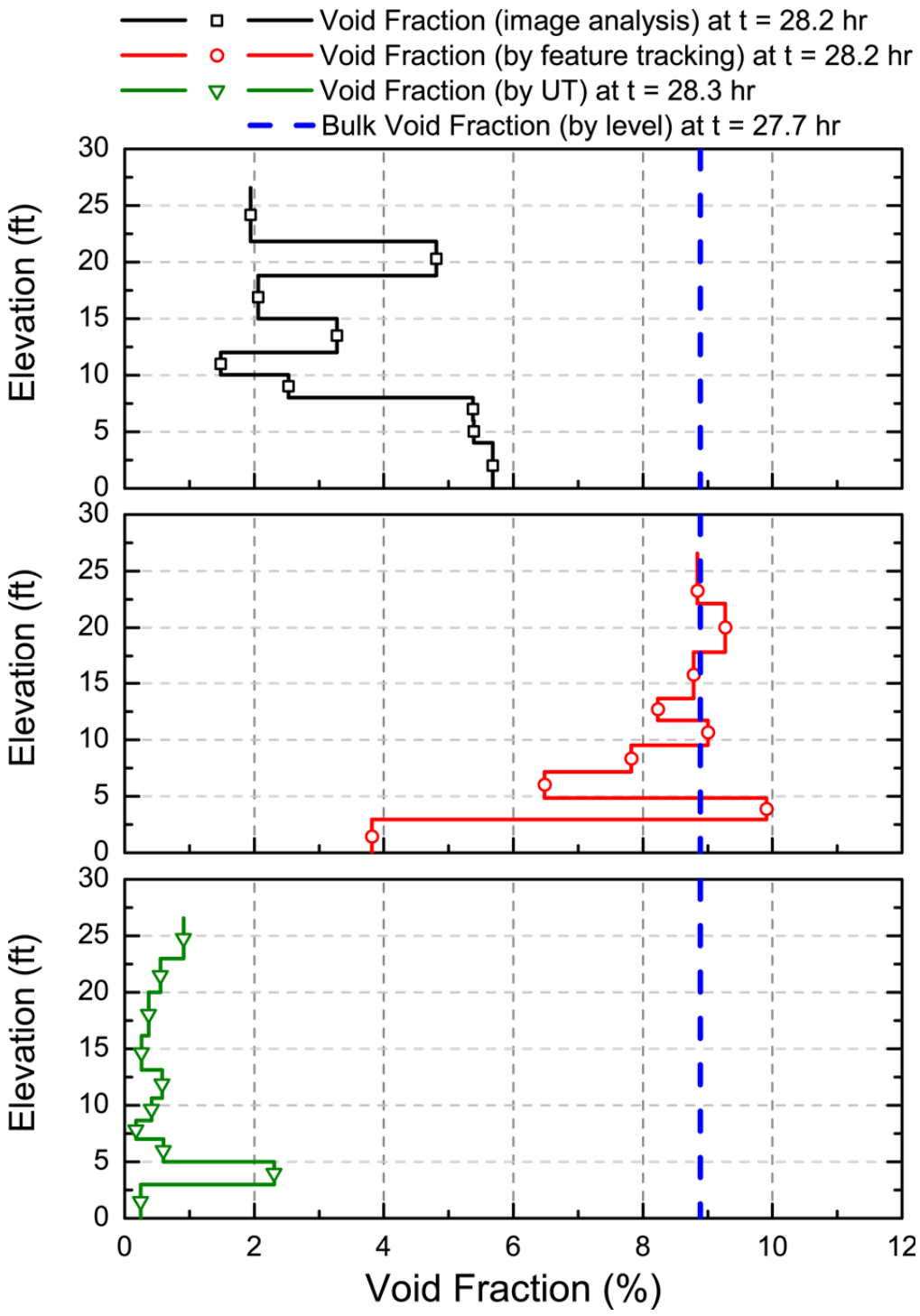

Figure 8.31. Comparison of Void Profiles for Test 2 at t ~ 28 h. This is close to the peak in bulk void, which is indicated by the vertical blue line. The void fraction profiles are shown with values plotted at the mid-point of the column elevation each calculated void represents.

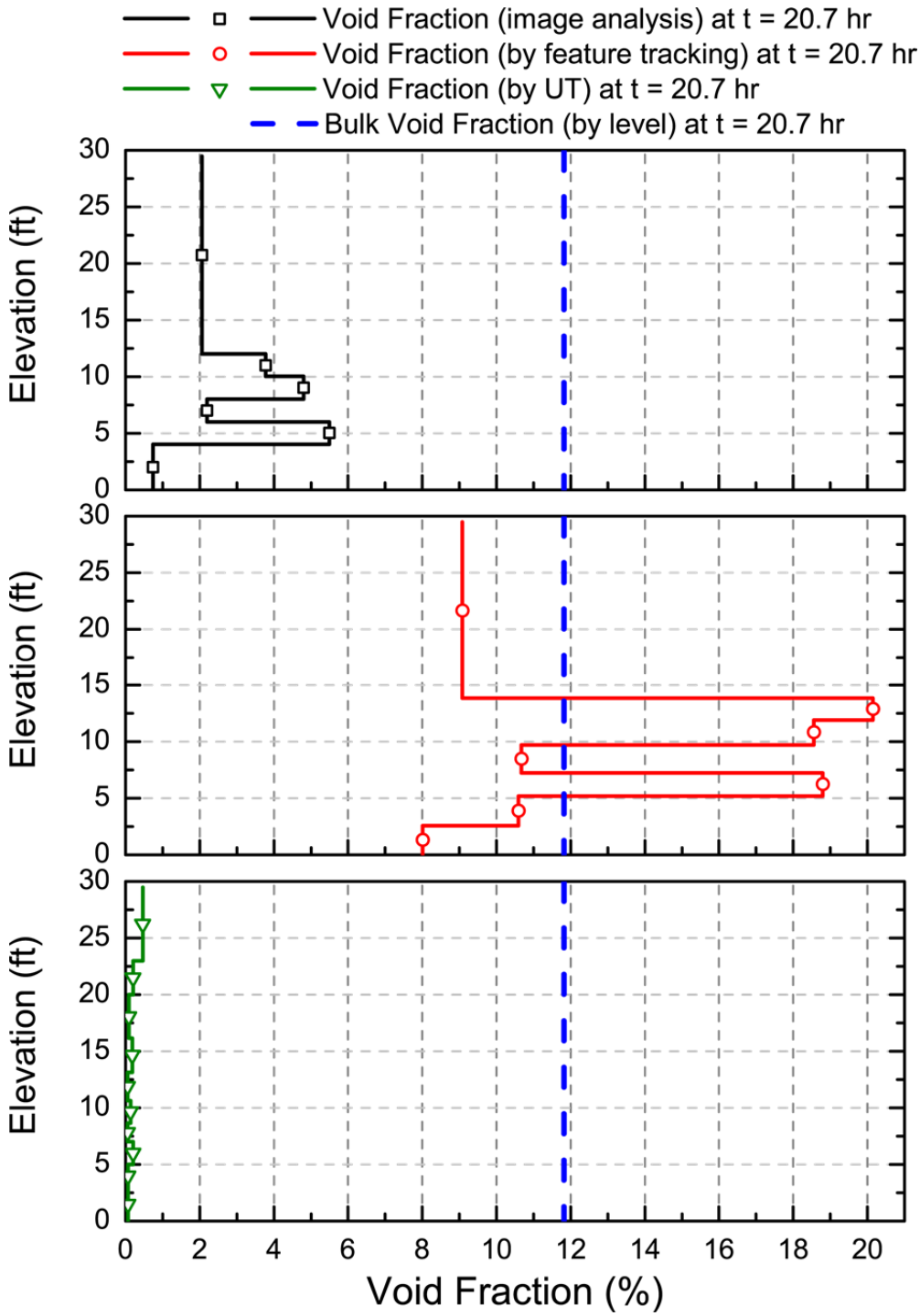

Figure 8.32. Comparison of Void Profiles for Test 3 at t ~ 21 h. This is close to the peak in bulk void, which is indicated by the vertical blue line. The void fraction profiles are shown with values plotted at the mid-point of the column elevation each calculated void represents.

The accuracy of each method used to generate void profiles was not assessed only by the visual comparison. A quantitative comparison was also performed between the bulk void measured by water level and the bulk void estimated from the profiles. The bulk void was estimated from the profiles in two ways: 1) taking a simple average (expected to be less accurate) and 2) integrating the void data with

height by assigning the data to various sections of the column. The resulting values for integrated sum are shown in Table 8.4, as well as the absolute difference between the integrated sum and the bulk void measured by water level. In this evaluation, feature tracking was substantially more accurate than the other two methods. Image analysis and ultrasonic data underestimate the bulk void by sizeable amounts, whereas the feature-tracking method is within ~1.5% (absolute) for all three tests. The test (Test 1) that shows the greatest divergence is driven mostly by the single low data point at ~12.5 ft (refer back to Figure 8.30).

Table 8.4. Comparison of Integrated Void Fractions Between Methods

		Image Analysis		Feature Tracking		Ultrasonic Measurements	
Test No.	Bulk Void Near Peak (%)	Void by Integrated Sum (%)	Bulk Void – Void by Integrated Sum (%)	Void by Integrated Sum (%)	Bulk Void – Void by Integrated Sum (%)	Void by Integrated Sum (%)	Bulk Void – Void by Integrated Sum (%)
1	8.30	5.32	2.98	6.78	1.52	3.50	4.80
2	8.89	3.53	5.36	8.10	0.79	0.61	8.27
3	11.82	2.43	9.39	11.37	0.45	0.20	11.62

In total, five methods were developed to determine void fraction profile in the tall column tests. Of the five, only three provided estimates of the void profile with elapsed time. Though some methods have more limitations than others, each method describes a void profile that does not exhibit significant increases in void fraction at the lowest elevations. The recommendation for the best estimate of the void fraction profile during the tall column tests is the data obtained by the feature-tracking method. It was the technique with the least uncertainty, as it does not suffer from the inconsistent correlation data and large variations that plague the UT approach or have the limitations of the image analysis, which performs only a two-dimensional measurement that was sensitive to changing gradients in light intensity. Ultimately, feature tracking is recommended because its component measurements, when integrated, are in good agreement with independently measured bulk void fractions in all three tall column tests. The implications of the void fraction profile data on d_{max} theory are discussed in Section 9.0.

9.0 Summary and Conclusions

Three tall column tests were conducted to challenge the predictions of d_{max} theory at full scale, using simulant depths greater than projected waste depths in DSTs. The sludge simulant in the tests was prepared to have representative shear strengths of sludge wastes in DSTs: Tests 1 and 2 with a bulk shear strength of ~600 Pa, and Test 3 ~900 Pa. In each test, the simulant was mixed, loaded into the column, and observed for several days. During the observation period, iron particles reacted to produce hydrogen gas in the simulant matrix. The gas formed bubbles that accumulated in the slurry until a peak average void fraction was reached, followed by a slow decline in void until the test ended. A post-test compression was also performed to collect additional data. Table 9.1 summarizes the major results of each test.

Table 9.1. Summary Table of Tall Column Tests

Test No.	Bulk Shear Strength (Pa)	Initial Simulant Level (in.)	Conservative Estimate of d_{max} (in.)	Initial Bulk (average) Void (%)	Peak Bulk (average) Void (%)	Final Bulk (average) Void (%)	Peak Gas Generation Rate (L/min)
1	594	320.25	221.3	2.3	8.3	7.1	4.55
2	627	318.75	226.3	1.3	9.1	7.6	7.12
3	~920[(a)]	353.5	310.8	7.2	11.8	9.4	11.90

(a) Refer to discussion in Section 7.3 for justification of this bulk shear strength.

The bulk void fractions measured in the tall column experiments are similar to values estimated for other large-scale systems, such as Hanford tanks and depots of contaminated lake mud. Best estimates of the void profile with elevation were obtained using a feature-tracking method that was in good agreement with the bulk void fraction determined by level change in the column. The calculated void profiles (see Figure 9.1) demonstrated that void fractions near the column bottom **are not** larger relative to other elevations. In fact, the lowest elevations typically had lower values, with the middle elevations having the highest values (including void fractions that were greater than the bulk void). In all tests, as Table 9.1 and Figure 9.1 show, a portion of the simulant was below the most conservative estimate of d_{max}, and the theory predicts increased gas fraction at these elevations. The void profiles determined from the tall column test data do not support the prediction.

The observed gas retention behavior in all three tests was very similar even though there were some differences in parameters between tests, such as shear strength, temperature, simulant height, loading procedure, and gas generation rate. In all three tests, more gas (in volume terms) was produced than the volume of simulant in the column. Consequently, the visual evidence collected during each test, namely that gas retention behavior in the simulant **did not** obey d_{max} predictions, was a significant finding. In all three tests, gas was transported freely from all depths in the column, even before the peak void fraction was achieved, and the void morphology was not a function of the simulant depth, i.e., the voids had a similar appearance (primarily slits and cracks) from the top of the simulant layer to the bottom.

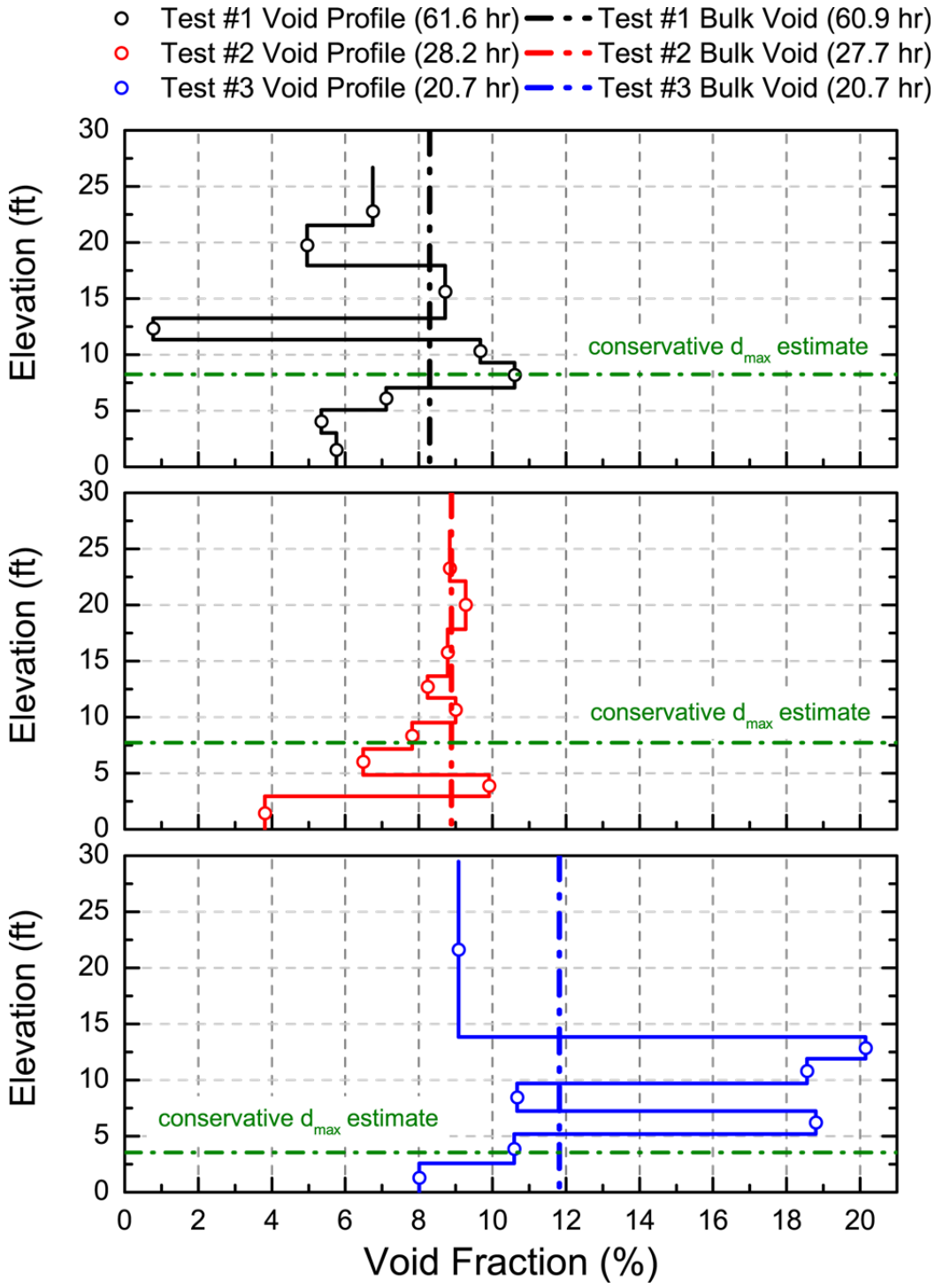

Figure 9.1. Best Estimate Void Profiles Determined by Feature Tracking for the Tall Column Tests. The bulk void fraction (determined at a similar time) and the conservative estimate of d_{max} for each test are shown for reference. The void fraction profiles are shown with values plotted at the mid-point of the column elevation each calculated void represents.

The tall column experiments call into question the validity of the d_{max} theory for predicting how a cohesive sludge simulant will retain gas as a function of depth. There were no data or observations made

that support the hypothesis that gas was retained in greater volume amounts at the lowest depths. If anything, the opposite occurred, as gas was retained in lesser volumes at the lowest depths. It does not appear that the basis for the theory—that there are long, cylindrical channels facilitating gas transport—is correct given observations made during the tall column tests.

These conclusions should take into context the limitations of the tall column testing. The majority of the data during testing was collected using the video camera system, which only sees a portion of the simulant contained in the tall column. An accurate quantitative method for determining void fraction in the column without using images collected from the camera was not employed, despite the attempted use of methods such as core sampling and ultrasonic measurements. However, data and visual observations that were collected consistently supported the conclusion that d_{max} (and the gas retention behavior it implies) did not exist in the tall column experiments. Taken together, the body of evidence implies d_{max} theory is not an appropriate predictor of gas retention behavior in sludge layers.

From the outset, the applicability of d_{max} theory to sludge waste was unclear and required experimental investigation. In this work, theoretical predictions of gas retention behavior were made based on assumed closure of slits and cracks below d_{max}. These predictions were not realized in actual testing. In test configurations representative of Hanford tank sludges, gas was readily and continuously released. The tall column tests, combined with other literature observations of gas release behavior, indicate that predictions of increased gas retention below d_{max} are inaccurate and that revision of d_{max} expectations and theory may be necessary.

Thus, application of d_{max} theory to the sludge waste tanks would likely result in inaccurate predictions of gas retention behavior. Given the data collected in the tall column experiments, the outcome of increasing waste depth in DSTs would be gas fractions at the lowest depths that are either similar to or lower than the current bulk gas fractions in the DSTs. No changes from historical trends in gas retention behavior in the waste sludge tanks are anticipated, at least up to planned retrieval depths (~310 in.).

10.0 References

Algar CK and BP Boudreau. 2009. "Transient Growth of an Isolated Bubble in Muddy, Fine-Grained Sediments." *Geochim. Cosmochim. Acta* 73:2581-2591.

Algar CK and BP Boudreau. 2010. "Stability of Bubbles in a Linear Elastic Medium: Implications for Bubble Growth in Marine Sediments." *J. Geophys. Res.* 115:F03012.

Algar CK, BP Boudreau, and MA Barry. 2011a. "Initial Rise of Bubbles in Cohesive Sediments by a Process of Viscoelastic Fracture." *J. Geophys. Res.* 116, B04207.

Algar CK, BP Boudreau, and MA Barry. 2011b. "Release of multiple bubbles from cohesive sediments." *Geophysical Research Letters* 38: L08606.

Anderson AL and LD Hampton. 1980. "Acoustics of gas-bearing sediments I: Background." *Journal of the Acoustical Society of America.* 67:1865-1889.

ASTM C1750-11. 2011. Standard Guide for Development, Verification, Validation, and Documentation of Simulated High-Level Tank Waste. ASTM International, West Conshohocken, Pennsylvania.

Barry MA, BP Boudreau, BD Johnson, and AH Reed. 2010. "First-Order Description of the Mechanical Fracture Behavior of Fine-Grained Surficial Marine Sediments during Gas Bubble Growth." *J. Geophys. Res.* 115:F04029.

Best AI, MDJ Tuffin, JK Dix, and JM Bull. 2004. "Tidal Height and Frequency of Dependence of Acoustic Velocity and Attenuation in Shallow Gassy Marine Sediments." *J. Geophys. Res*. 109, B08101.

Bontha JR, JJ Jenks, GP Morgen, TJ Peters, WA Wilcox, HE Adkins, CA Burns, MS Greenwood, PJ MacFarlan, KM Denslow, PP Schonewill, J Blanchard, and EB Baer. 2010. *Evaluation of Slurry Transfer Line Critical Velocity Measurement Instruments.* PNNL-19441 Rev. 0. Pacific Northwest National Laboratory, Richland, Washington.

Boudreau BP, CK Algar, BD Johnson, I Croudace, A Reed, Y Furukawa, KM Dorgan, PA Jumars, AS Grader, and BS Gardiner. 2005. "Bubble growth and rise in soft sediments." *Geology* 33(6): 517-520.

Boudreau BP. 2012. "The physics of bubbles in surficial, soft, cohesive sediments." *Marine and Petroleum Geology* 38: 1-18.

Bredt PR and SM Tingey. 1996. *The Effect of Dilution on the Gas Retention Behavior of Tank 241-SY-103 Waste.* PNNL-10893, Pacific Northwest National Laboratory, Richland, Washington.

Bredt PR, SM Tingey, and EH Shade. 1995. *The Effect of Dilution on the Gas Retention Behavior of Tank 241-SY-101 Waste.* PNL-10781, Pacific Northwest Laboratory, Richland, Washington.

Chhabra RP. 1993. *Bubbles, Drops, and Particles in Non-Newtonian Fluids*. CRC Press, Boca Raton, Florida.

Crosato A. 1998. "Non-Homogeneous Mud Structure at Consolidation." Report DM16. *Drainage System Behavior*. August 2005, z2313.10. Delft Hydraulics.

Duffy SM, SJ Wheeler, and JD Bennell. 1994. "Shear modulus of kaolin containing methane bubbles." *Journal of Geotechnical Engineering-ASCE* 120(5): 781-796.

Epstein M and PA Gauglitz. 2010. *An Experimental Study of the Stability of Vessel-Spanning Bubbles in Cylindrical, Annular, Obround and Conical Containers*. Fauske & Associates Report FAI/09-272, Rev.2, (April), Burr Ridge, Illinois.

Follett JR. 2014. *Cone Penetrometer Shear Strength Measurements of Sludge Waste in Tanks 241-AN-101 and 241-AN-106*. RPP-RPT-56585, Rev. 0, Washington River Protection Solutions LLC, Richland, Washington.

Gardiner BS, BP Boudreau, and BD Johnson. 2003. "Growth of Disk-Shaped Bubbles in Sediments." *Geochim. Cosmochim. Acta* 6(8):1485-1494.

Gauglitz PA, LA Mahoney, DP Mendoza, and MC Miller. 1994. *Mechanisms of Gas Bubble Retention*. PNL-10120, Pacific Northwest Laboratory, Richland, Washington.

Gauglitz PA, SD Rassat, MR Powell, RR Shah, and LA Mahoney. 1995. *Gas Bubble Retention and Its Effects on Waste Properties: Retention Mechanisms, Viscosity, and Tensile and Shear Strengths*. PNL-10740, Pacific Northwest Laboratory, Richland, Washington.

Gauglitz PA, SD Rassat, PR Bredt, JH Konynenbelt, SM Tingey, and DP Mendoza. 1996. *Mechanisms of Gas Bubble Retention and Release: Results for Hanford Waste Tanks 241-S-102 and 241-SY-103 and Single-Shell Tank Simulants*. PNNL-11298, Pacific Northwest National Laboratory, Richland, Washington.

Gauglitz PA, G Terrones, SJ Muller, MM Denn, and WR Rossen. 2001. *Mechanics of Bubbles in Sludges and Slurries: Final Report for U.S. Department of Energy*. PNNL-13748, Pacific Northwest National Laboratory, Richland, Washington.

Gauglitz PA, WC Buchmiller, JJ Jenks, J Chun, RL Russell, AJ Schmidt, and MM Mastor, Jr. 2010. *The Disruption of Vessel-Spanning Bubbles with Sloped Fins in Flat-Bottom and 2:1 Elliptical-Bottom Vessels*. PNNL-19345, Rev. 0, Pacific Northwest National Laboratory, Richland, Washington.

Gauglitz PA, WC Buchmiller, SG Probert, AT Owen, and FJ Brockman. 2012. *Strong-Sludge Gas Retention and Release Mechanisms in Clay Simulants*. PNNL-21167, Rev. 0, Pacific Northwest National Laboratory, Richland, Washington.

Jain AK and R Juanes. 2009. "Preferential Mode of Gas Invasion in Sediments: Grain-Scale Mechanistic Model of Coupled Multiphase Fluid Flow and Sediment Mechanics." *J. Geophys. Res.* 114:B08101.

Johnson BD, BP Boudreau, BS Gardiner, and R Maass. 2002. "Mechanical Response of Sediments to Bubble Growth." *Marine Geology*, 187:347-363.

Judd AG, and M Hovland. 1992. "The Evidence of Shallow Gas in Marine Sediments." *Continental Shelf Research,* 12(10):1081-1095.

Katsman R, I Ostrovsky, and Y Makovsky. 2013. "Methane Bubble Growth in Fine-Grained Aquatic Sediment: Insight from Modeling." Earth and Planetary Sci. Let. 377-378:336-346.

Kepkay PE and RC Cooke. 1978. "Velocity of Sound as a Function of Bubble Distribution in Gas-bearing Sediments." *Geophysical Research Letters.* **5**:1071-1073.

Khelifa A and PS Hill. 2006. "Models for effective density and settling velocity of flocs." *Journal of Hydraulic Research,* 44: 390-401.

Lide DR, editor. 2003. *Handbook of Chemistry and Physics.* CRC Press, New York.

Maggi F, F Mietta, and JC Winterwerp. 2007. "Effect of variable fractal dimension on the floc size distribution of suspended cohesive sediment." *Journal of Hydrology,* 343: 43-55.

Meacham JE, SJ Harrington, JR Follett, BE Wells, PA Gauglitz, PP Schonewill, MR Powell, and SD Rassat. 2014. *Gas Retention and Release from Hanford Site High Shear Strength Waste.* RPP-RPT-26836, Rev. 1 (to appear), Washington River Protection Solutions, Richland, Washington.

Mietta F. 2010. *Evolution of the floc size distribution of cohesive sediments*. PhD dissertation, Delft University of Technology, Technologiestichting STW.

NFPA 496. 2013. Standard for Purged and Pressurized Enclosures for Electrical Equipment, 2013 Edition. National Fire Protection Association, Quincy, Massachusetts.

NFPA 497. 2012. Recommended Practice for the Classification of Flammable Liquids, Gases, or Vapors and of Hazardous (Classified) Locations for Electrical Installations in Chemical Process Areas, 2012 Edition. National Fire Protection Association, Quincy, Massachusetts.

Otsu N. 1979. "A Threshold Selection Method from Gray-Level Histograms," *IEEE Transactions on Systems, Man, and Cybernetics*, 9 (1): 62-66.

Panetta PD, BJ Tucker, KM Judd, and AA Diaz. 2004. *Ultrasonic determination of gas volume fraction (proof of principle results)*. Unpublished data, Pacific Northwest National Laboratory, Richland, Washinton.

Powell MR, CM Gates, CR Hymas, MA Sprecher, and NJ Morter. 1995. *Fiscal Year 1994 1/25-Scale Sludge Mobilization Testing*. PNL-10582, Pacific Northwest Laboratory, Richland, Washington.

Powell MR, PA Gauglitz, KM Denslow, CM Fischer, DJ Heldebrant, MS Prowant, SA Sande, JM Davis, and MR Telander. 2014. *Evaluation of Gas Retention in Waste Simulants: Intermediate-Scale Column and Open-Channel Depth Tests*. PNNL-23136, DSGREP-RPT-003, Pacific Northwest National Laboratory, Richland, Washington.

Rassat SD, PA Gauglitz, PR Bredt, LA Mahoney, SV Forbes, and SM Tingey. 1997. *Mechanisms of Gas Bubble Retention and Release: Experimental Results for Hanford Waste Tanks 241-AW-101 and 241-AN-103.* PNNL-11642, Pacific Northwest National Laboratory, Richland, Washington.

Rassat SD, SM Caley, PR Bredt, PA Gauglitz, DE Rinehart, and SV Forbes. 1998. *Mechanisms of Gas Bubble Retention and Release: Experimental Results for Hanford Single Shell Waste Tanks 241-A-101, 241-S-106, and 241-U-103.* PNNL-11981, Pacific Northwest National Laboratory, Richland, Washington.

Rassat SD, PA Gauglitz, SM Caley, LA Mahoney, and DP Mendoza. 1999. *A of SY-101 Crust Gas Retention and Release Mechanisms.* PNNL-12092, Pacific Northwest National Laboratory, Richland, Washington.

Rassat SD, LM Bagaasen, LA Mahoney, RL Russell, DD Caldwell, and DP Mendoza. 2003. *Physical and Liquid Chemical Simulant Formulations for Transuranic Wastes in Hanford Single-Shell Tanks*. PNNL-14333, Pacific Northwest National Laboratory, Richland, Washington.

Rassat SD, PA Gauglitz, LA Mahoney, RP Pires, DR Rector, JA Fort, GK Boeringa, DN Tran, MR Elmore, WC Buchmiller, and ML Kimura. 2014. *Gas Release Due to Rayleigh-Taylor Instability within Sediment Layers in Hanford Double-Shell Tanks: Results of Scaled Vessel Experiments, Modeling, and Extrapolation to Full Scale*. PNNL-23060, DSGREP-RPT-002, Rev. 1, Pacific Northwest National Laboratory, Richland, WA.

Reardon EJ. 1995. "Anaerobic Corrosion of Granular Iron: Measurement and Interpretation of Hydrogen Evolution Rates." *Environ. Sci. Technol.* 26:2936-2945.

Scandella BP, C Varadharajan, HF Hemond, C Ruppel, and R Juanes. 2011. "A Conduit Dilation Model of Methane Venting from Lake Sediments." *Geophys. Res. Lett.*, 38:L06408.

Sills GC and R Gonzalez. 2001. "Consolidation of Naturally Gassy Soft Soil." *Géotechnique* 51(7): 629-639.

Sills GC and SJ Wheeler. 1992. "The Significance of Gas for Offshore Operations." *Continental Shelf Research*, 12(10):1239-1250.

Sills GC, SJ Wheeler, SD Thomas, and TN Gardner. 1991. "Behavior of Offshore Soils Containing Gas Bubbles." *Géotechnique*, 41:227-241.

Son M and T-J Hsu. 2009. "The effect of variable yield strength and variable fractal dimension on flocculation of cohesive sediment." *Water Research* 43: 3582-3592.

Stewart CW, CL Shepard, JM Alzheimer, TI Stokes, and G Terrones. 1995. *In Situ Determination of Rheological Properties and Void Fraction in Hanford Tank 241-SY-101.* PNL-10682, Pacific Northwest National Laboratory, Richland, Washington.

Stewart CW, ME Brewster, PA Gauglitz, LA Mahoney, PA Meyer, KP Recknagle, and HC Reed. 1996. *Gas Retention and Release Behavior in Hanford Single-Shell Tanks.* PNNL-11391, Pacific Northwest National Laboratory, Richland, Washington.

Uytioco EM. 2010. *BDGRE and Supernatant Limit Assessment for Enhanced Use of AN Farm for C Farm Single Shell Tank Retrieval*. RPP-RPT-44254, Rev. 1, Washington River Protection Solutions, Richland, Washington.

Van Kessel T and WGM van Kesteren. 2002. "Gas Production and Transport in Artificial Sludge Depots." *Waste Management* 22(1):19–28.

Walker DD, CL Crawford, and NE Bibler. 1994. "Radiolytic Bubble Formation and Level Changes in Simulated High-level Waste Salts and Sludges – Application to HLW Storage Tanks." In *Proceedings of Waste Management 1994*, Vol 1, pp. 393-396. February 27-March 3, 1994, Tucson, Arizona.

Wells BE, JJ Jenks, G Boeringa, NN Bauman, and AD Guzman. 2010. *Lateral Earth Pressure at Rest and Shear Modulus Measurements on Hanford Sludge Simulants*. PNNL-19829, Pacific Northwest National Laboratory, Richland, Washington.

Wheeler SJ. 1988a. "A Conceptual Model for Soils Containing Large Gas Bubbles." *Géotechnique.* 38:389-397.

Wheeler SJ. 1988b. "The Undrained Shear Strength of Soils Containing Large Gas Bubbles." *Géotechnique* 38(3): 399-413.

Wheeler SJ. 1990. "Movement of Large Gas Bubbles in Unsaturated Fine-grained Sediments." *Marine Geotechnology* 9(2):113-129.

Wheeler SJ and TN Gardner. 1989. "Elastic Moduli of Soils Containing Large Gas Bubbles." *Géotchnique.* 39:333-342.

Wheeler SJ, WK Sham, and SD Thomas. 1990. "Gas Pressure in Unsaturated Offshore Soils." *Can Geotech. J.* 27:79-89.

Wichman BGHM, GC Sills, and R Gonzalez. 2000. "Experimental Validation of a Finite Strain Theory for Gassy Mud." *Can. Geotech. J.*, 37:1227-1240.

Wilkens RH and MD Richardson. 1998. "The influence of gas bubbles on sediment acoustic properties: in situ, laboratory, and theoretical results from Eckernforde Bay, Baltic sea." *Continental Shelf Research* 18:1859-1892.

Wilson PS, AH Reed, WT Wood, and RA Roy. 2008. "The low-frequency sound speed of fluid-like gas-bearing sediments." *Journal of the Acoustical Society of America Express Letters*. 123:EL99-EL104

Winterwerp JC. 2002. "On the flocculation and settling velocity of estuarine mud." *Continental Shelf Research,* 22:1339–1360.

Winterwerp JC and WGM van Kesteren. 2004. "Introduction to the Physics of Cohesive Sediment in the Marine Environment." *Developments in Sedimentology*, Vol 56, Elsevier, New York.

Wood AB. 1955. *A Textbook of Sound*, 3rd edition, McGraw-Hill, New York, 1930.

Yarbrough RJ. 2013. *Methodology and Calculations for the Assignment of Waste Groups for the Large Underground Waste Storage Tanks at the Hanford Site*. RPP-10006, Rev. 11, Washington River Protection Solutions LLC, Richland, Washington.

Appendix A

Supplementary Tall Column Test Data

Appendix A

Supplementary Tall Column Test Data

This appendix presents supplementary data from the tall column tests that were not discussed or presented in Section 7.0 or 8.0. The appendix is broken into four sections depending on the data type. The first part tabulates data that were recorded manually during each test. The second part contains some supplementary figures from either raw or analyzed test data. The third part has the data from the post-test compression events tabulated that support the calculations of the void fraction. Finally, the fourth part presents the physical property measurements conducted on core samples taken during Test 1 and Test 2.

A.1 Test Data Sheets

This section presents the level and volume data for each test in Table A.1, Table A.2, and Table A.4. Note that the slurry level was not recorded as frequently as the water level (denoted by "--" when it was not recorded). The column with ΔV values is the difference GV2 – GV1. Pressure data, which are tabulated for Tests 2 and 3 (Table A.3 and Table A.5), are given in gauge (raw) pressures. Refer to Figure 6.3 for the locations of the pressure sensors (P1A, P2A, etc.) in the tall column. In all the tables in this section, elapsed times appended with an asterisk ("*") were collected after the post-test compression occurred.

Table A.1. Tall Column Test 1 Data: Levels and Gas Volumes

Date/Time	Elapsed Time (h)	Slurry Level (in.)	Water Level (in.)	GV1 (L)	GV2 (L)	ΔV (L)
12/29/2013 22:26	0.0	320.25	345	0	0	0
12/30/2013 00:00	1.6	--	345.375	322	349.1	27.1
12/30/2013 02:40	4.2	--	345.875	1072.5	1186.2	113.7
12/30/2013 05:30	7.1	--	346.125	1850.5	2034.8	184.3
12/30/2013 07:25	9.0	321.375	346.4375	2409.7	2657	247.3
12/30/2013 09:19	10.9	323	348.125	2937.5	3302.4	364.9
12/30/2013 11:13	12.8	324	350	3460.2	3980.1	519.9
12/30/2013 12:55	14.5	--	351.75	3937.3	4730.8	793.5
12/30/2013 14:45	16.3	324.5	353.5	4449.9	5601.9	1152
12/30/2013 16:30	18.1	327.5	354.5	4936.7	6460.2	1523.5
12/30/2013 18:34	20.1	328.5	355.625	5494.7	7523.3	2028.6
12/30/2013 20:26	22.0	--	356.5	6008.4	8480.2	2471.8
12/30/2013 22:17	23.9	329	356.75	6530	9434.5	2904.5
12/31/2013 00:25	26.0	--	356.5	7117.9	10407.7	3289.8
12/31/2013 02:45	28.3	--	358.25	7770.9	11625.5	3854.6
12/31/2013 04:33	30.1	--	358.875	8273.9	12498.7	4224.8

Date/Time	Elapsed Time (h)	Slurry Level (in.)	Water Level (in.)	GV1 (L)	GV2 (L)	ΔV (L)
12/31/2013 06:48	32.4	330	359.625	8902.9	13610.4	4707.5
12/31/2013 08:36	34.2	--	360	9419.7	14517	5097.3
12/31/2013 10:42	36.3	330.5	360.5	9987.6	15532.8	5545.2
12/31/2013 12:20	37.9	--	360.875	10436.7	16302.1	5865.4
12/31/2013 14:12	39.8	--	361.25	10946.7	17221.6	6274.9
12/31/2013 16:02	41.6	--	361.625	11446.2	18137.1	6690.9
12/31/2013 17:15	42.8	--	362	11790.1	18766.6	6976.5
12/31/2013 18:22	43.9	--	362.25	12110	19384.7	7274.7
12/31/2013 19:00	44.6	--	362.375	12292.3	19724.6	7432.3
12/31/2013 20:00	45.6	--	362.625	12570.4	20253	7682.6
12/31/2013 21:03	46.6	--	362.75	12873.1	20827.2	7954.1
12/31/2013 22:01	47.6	332.5	363	13148.5	21357	8208.5
12/31/2013 23:15	48.8	--	363.25	13509.9	22051.8	8541.9
01/01/2014 00:18	49.9	--	363.25	13804.2	22615.2	8811
01/01/2014 01:20	50.9	--	363.375	14115.1	23201.6	9086.5
01/01/2014 02:21	51.9	--	363.5	14400.8	23734.1	9333.3
01/01/2014 03:21	52.9	333.25	363.625	14684.6	24253.2	9568.6
01/01/2014 04:43	54.3	--	364	15075.3	24988.9	9913.6
01/01/2014 05:30	55.1	--	364	15284.6	25380.7	10096.1
01/01/2014 06:30	56.1	333.125	364.125	15567.9	25919.2	10351.3
01/01/2014 08:15	57.8	--	364.25	16074.4	26880.9	10806.5
01/01/2014 09:20	58.9	--	364.375	16363.4	27421.5	11058.1
01/01/2014 10:20	59.9	--	364.375	16645.7	27949.9	11304.2
01/01/2014 11:20	60.9	--	364.375	16954.9	28532.3	11577.4
01/01/2014 12:50	62.4	331	364.375	17338.5	29250	11911.5
01/01/2014 14:16	63.8	331	364.4375	17753.1	29996.9	12243.8
01/01/2014 15:13	64.8	--	364.5	18010.2	30453.8	12443.6
01/01/2014 16:14	65.8	--	364.5	18294.7	30957.2	12662.5
01/01/2014 17:16	66.8	--	364.375	18587.5	31469.7	12882.2
01/01/2014 18:42	68.3	--	364.25	18983.9	32158.4	13174.5
01/01/2014 20:00	69.6	--	364.25	19349.6	32783	13433.4
01/01/2014 21:00	70.6	327	364.125	19637.2	33271.1	13633.9
01/01/2014 22:15	71.8	--	364	19983.1	33845.6	13862.5
01/01/2014 23:05	72.7	--	364	20218.5	34233.7	14015.2
01/02/2014 00:03	73.6	--	363.875	20477.5	34658.5	14181
01/02/2014 01:00	74.6	--	363.875	20749.4	35099.2	14349.8
01/02/2014 02:38	76.2	--	363.75	21220.7	35857.6	14636.9
01/02/2014 03:38	77.2	327	363.625	21489.5	36290.4	14800.9
01/02/2014 04:31	78.1	--	363.625	21740.2	36688.6	14948.4
01/02/2014 05:30	79.1	--	363.5	22024.6	37131.6	15107

Date/Time	Elapsed Time (h)	Slurry Level (in.)	Water Level (in.)	GV1 (L)	GV2 (L)	ΔV (L)
01/02/2014 06:30	80.1	--	363.5	22300.7	37560.9	15260.2
01/02/2014 07:30	81.1	--	363.5	22591.6	38004.3	15412.7
01/02/2014 09:00	82.6	--	363.25	23017.9	38646.9	15629
01/02/2014 10:20	83.9	--	363.125	23400.4	39213.9	15813.5
01/02/2014 11:24	85.0	--	n/a	23699.6	39673.3	15973.7
01/02/2014 12:20	85.9	--	363	23960	40069	16109
01/02/2014 13:30	87.1	--	362.875	24293	n/a	n/a
01/02/2014 14:20	87.9	--	362.875	24527.6	40926.4	16398.8
01/02/2014 15:43	89.3	--	362.75	24927.6	41515.4	16587.8
01/02/2014 16:48	90.4	--	362.75	25237.8	41979.3	16741.5
01/02/2014 18:02	91.6	--	362.75	25592	42506	16914
01/02/2014 19:30	93.1	--	362.625	26023	43134	17111
01/02/2014 20:31	94.1	--	362.5	26315.1	43558.3	17243.2
01/02/2014 21:29	95.1	--	362.375	26601.7	43960.7	17359
01/02/2014 23:13	96.8	--	362.25	27098.1	44662.2	17564.1
01/03/2014 00:15	97.8	--	362.125	27403.5	45079.8	17676.3
01/03/2014 01:15	98.8	--	362	27682.6	45438.4	17755.8
01/03/2014 02:34	100.1	--	362	28075.9	45965.6	17889.7
01/03/2014 03:30	101.1	--	362	28340.8	46318.1	17977.3
01/03/2014 04:30	102.1	--	362	28622.9	46692.3	18069.4
01/03/2014 05:30	103.1	--	361.875	28924	47087.1	18163.1
01/03/2014 07:00	104.6	--	361.75	29352.6	47649.8	18297.2
01/03/2014 08:18	105.9	--	361.75	29752.6	48166.5	18413.9
01/03/2014 09:09	106.7	--	361.75	29996.5	48498.7	18502.2
01/03/2014 10:09	107.7	--	361.625	30283.8	48902.1	18618.3
01/03/2014 11:07	108.7	--	361.625	30550.3	49265.8	18715.5
01/03/2014 12:07	109.7	--	361.625	30825.6	49645.7	18820.1
01/03/2014 13:06	110.7	--	361.5	31108.9	50031.5	18922.6
01/03/2014 14:13	111.8	--	361.375	31403.1	50431.2	19028.1
01/03/2014 15:13	112.8	--	361.375	31683.4	50797.5	19114.1
01/03/2014 16:14	113.8	--	361.375	31964.8	51143.5	19178.7
01/03/2014 17:45	115.3	324	361.25	32404.2	51666.7	19262.5
01/03/2014 19:06	116.7	--	361.125	32784	52122	19338
01/03/2014 20:11	117.8	--	361.125	33091.5	52500	19408.5
01/03/2014 21:05	118.6	--	361.125	33353.3	52823.8	19470.5
01/03/2014 22:02	119.6	--	361	33621.1	53149	19527.9
01/03/2014 23:26	121.0	--	360.875	34030.7	53655.4	19624.7
01/04/2014 00:30	122.1	--	360.875	34325.9	54022.4	19696.5
01/04/2014 01:30	123.1	--	360.875	34624.5	54390.4	19765.9
01/04/2014 02:29	124.1	--	360.875	34911.7	54735.8	19824.1

Date/Time	Elapsed Time (h)	Slurry Level (in.)	Water Level (in.)	GV1 (L)	GV2 (L)	ΔV (L)
01/04/2014 03:30	125.1	--	360.75	35201.9	55089.2	19887.3
01/04/2014 04:30	126.1	--	360.75	35490	55442.3	19952.3
01/04/2014 05:30	127.1	--	360.625	35782.6	55789.5	20006.9
01/04/2014 06:12	127.8	--	360.625	35998.7	56047.7	20049
01/04/2014 08:05	129.7	--	360.625	36550	56698.3	20148.3
01/04/2014 09:08	130.7	--	360.5625	36851	57063.4	20212.4
01/04/2014 10:00	131.6	--	360.5	37098	57368.7	20270.7
01/04/2014 11:05	132.7	--	360.5	37400	57760.8	20360.8
01/04/2014 12:00	133.6	--	360.4375	37650	58088.1	20438.1
01/04/2014 13:03	134.6	--	360.4375	37940	58451.6	20511.6
01/04/2014 14:28	136.0*	--	464.75	38330	58539.9	20209.9

Table A.2. Tall Column Test 2 Data: Levels and Gas Volumes

Date/Time	Elapsed Time (h)	Slurry Level (in.)	Water Level (in.)	GV1 (L)	GV2 (L)	ΔV (L)
01/16/2014 20:46	0.0	319.75	343.25	0	0	0
01/16/2014 21:30	0.7	321.25	344.375	0	0	0
01/16/2014 22:25	1.7	323.5	347.25	0	23.1	23.1
01/16/2014 23:30	2.7	326.125	350	0	23.1	23.1
01/17/2014 00:30	3.7	331.5	354.5	0	23.1	23.1
01/17/2014 01:30	4.7	333.125	357	187.5	574.2	386.7
01/17/2014 02:30	5.7	334	358.25	446.2	1260.1	813.9
01/17/2014 03:30	6.7	335.125	359.375	709.7	1882.7	1173
01/17/2014 04:30	7.7	336	360.5	1020.4	2546.2	1525.8
01/17/2014 05:30	8.7	338	361.5	1354.3	3217.2	1862.9
01/17/2014 06:30	9.7	--	362.25	1693.8	3893.6	2199.8
01/17/2014 07:30	10.7	--	362.875	2029.5	4560.9	2531.4
01/17/2014 08:30	11.7	338.5	363.5	2352.8	5199.2	2846.4
01/17/2014 09:30	12.7	339	364	2683.3	5845.4	3162.1
01/17/2014 10:30	13.7	339.875	364.5	3000	6469.8	3469.8
01/17/2014 11:30	14.7	340	364.875	3321.5	7107.4	3785.9
01/17/2014 12:30	15.7	340.25	365.125	3644.8	7748.7	4103.9
01/17/2014 13:30	16.7	340.375	365.375	3966	8351.1	4385.1
01/17/2014 14:30	17.7	340.75	365.75	4285	8970.3	4685.3
01/17/2014 15:30	18.7	340.75	366.125	4601	9588	4987
01/17/2014 16:40	19.9	340.75	366.375	4976	10293	5317
01/17/2014 18:20	21.6	340.75	366.625	5524	11293	5769
01/17/2014 19:20	22.6	340.75	366.875	5863	11905	6042

Date/Time	Elapsed Time (h)	Slurry Level (in.)	Water Level (in.)	GV1 (L)	GV2 (L)	ΔV (L)
01/17/2014 20:30	23.7	340.75	367	6238	12574	6336
01/17/2014 21:30	24.7	340.75	367.125	6565	13159	6594
01/17/2014 22:30	25.7	340.625	367.25	6891	13740	6849
01/17/2014 23:30	26.7	340.625	367.25	7214	14320	7106
01/18/2014 00:30	27.7	339.875	367.5	7550	14927	7377
01/18/2014 01:30	28.7	339.875	367.5	7868	15497	7629
01/18/2014 02:30	29.7	339.875	367.5	8191	16063	7872
01/18/2014 03:30	30.7	339.875	367.5	8522	16636	8114
01/18/2014 04:30	31.7	339.875	367.5	8852	17206	8354
01/18/2014 05:30	32.7	339.875	367.875	9183	17767	8584
01/18/2014 06:30	33.7	339.875	367.875	9510	18001	8491
01/18/2014 07:30	34.7	339.5	367.875	9820.9	18523.6	8702.7
01/18/2014 08:30	35.7	--	367.875	10150.5	19060.4	8909.9
01/18/2014 09:30	36.7	--	367.875	10478.7	19592.1	9113.4
01/18/2014 10:30	37.7	--	367.75	10804.4	20079.1	9274.7
01/18/2014 11:30	38.7	--	367.875	11129.9	20594	9464.1
01/18/2014 12:30	39.7	--	367.875	11446.9	21116.5	9669.6
01/18/2014 13:30	40.7	--	367.875	11770	21652	9882
01/18/2014 14:30	41.7	--	368	12097.8	22187	10089.2
01/18/2014 15:30	42.7	339.5	368.125	12421.7	22708.2	10286.5
01/18/2014 16:30	43.7	--	368.125	12747	23226.5	10479.5
01/18/2014 17:30	44.7	--	368.125	13084.1	23758.8	10674.7
01/18/2014 18:42	45.9	--	368.125	13470.2	24357.7	10887.5
01/18/2014 19:33	46.8	--	368.25	13750.9	24789	11038.1
01/18/2014 20:31	47.8	--	368.25	14072.8	25289.1	11216.3
01/18/2014 21:30	48.7	--	368.125	14394.8	25776.2	11381.4
01/18/2014 22:31	49.8	--	368.125	14723.3	26281.2	11557.9
01/18/2014 23:30	50.7	--	368.125	15056.3	26769.7	11713.4
01/19/2014 00:30	51.7	--	368.125	15394	27273.9	11879.9
01/19/2014 01:30	52.7	--	367.75	15714.1	27742.1	12028
01/19/2014 02:30	53.7	--	367.625	16043.4	28222.1	12178.7
01/19/2014 03:30	54.7	--	367.5	16382.4	28716.1	12333.7
01/19/2014 04:30	55.7	--	367.375	16717.3	29196.8	12479.5
01/19/2014 05:30	56.7	--	367.375	17044.4	29663.5	12619.1
01/19/2014 06:30	57.7	--	367.375	17350.8	30097.2	12746.4
01/19/2014 07:30	58.7	--	367.25	17692.2	30577.9	12885.7
01/19/2014 08:34	59.8	--	367.25	18046.2	31067.2	13021
01/19/2014 09:31	60.8	--	367.125	18371.2	31511.5	13140.3
01/19/2014 10:30	61.7	--	367.125	18696.8	31958.9	13262.1
01/19/2014 11:30	62.7	--	367.125	19027.9	32413.6	13385.7

Date/Time	Elapsed Time (h)	Slurry Level (in.)	Water Level (in.)	GV1 (L)	GV2 (L)	ΔV (L)
01/19/2014 12:30	63.7	--	367.125	19360.2	32869.3	13509.1
01/19/2014 13:30	64.7	--	367	19693.8	33321.9	13628.1
01/19/2014 14:30	65.7	--	366.875	20022.3	33767.6	13745.3
01/19/2014 15:32	66.8	--	366.875	20380.9	34239.6	13858.7
01/19/2014 16:47	68.0	--	366.75	20791.5	34768	13976.5
01/19/2014 17:31	68.8	329	366.625	21033.7	35078.6	14044.9
01/19/2014 18:34	69.8	--	366.5	21385.4	35529.8	14144.4
01/19/2014 19:43	71.0	--	366.375	21762.6	36006.6	14244
01/19/2014 20:23	71.6	--	366.25	21986.9	36289.4	14302.5
01/19/2014 21:46	73.0	--	366.25	22454.5	36873.3	14418.8
01/19/2014 22:31	73.8	--	366.125	22709.6	37193.8	14484.2
01/19/2014 23:32	74.8	--	366.125	23070.7	37648.7	14578
01/20/2014 00:30	75.7	--	366	23383.7	38038.6	14654.9
01/20/2014 01:30	76.7	--	366.125	23714.4	38453.2	14738.8
01/20/2014 02:30	77.7	--	365.875	24052.9	38868.1	14815.2
01/20/2014 03:30	78.7	--	366	24390.9	39282.7	14891.8
01/20/2014 04:30	79.7	--	365.75	24725.7	39690.4	14964.7
01/20/2014 05:30	80.7	--	365.625	25062.4	40097.7	15035.3
01/20/2014 06:30	81.7	--	365.5	25409.3	40516.3	15107
01/20/2014 07:37	82.9	323	365.25	25783.3	40966.1	15182.8
01/20/2014 08:24	83.6	323	365.25	26047.1	41278.5	15231.4
01/20/2014 09:30	84.7	322.5	365.125	26412.7	41707.8	15295.1
01/20/2014 10:34	85.8	322	365.125	26770.7	42124.5	15353.8
01/20/2014 11:31	86.8	322	365	27089.5	42503.4	15413.9
01/20/2014 12:38	87.9	--	365	27466.9	42955.5	15488.6
01/20/2014 13:27	88.7	321.5	365	27742.8	43281	15538.2
01/20/2014 14:27	89.7	321.5	365	28083.5	43684.7	15601.2
01/20/2014 15:30	90.7	321	365	28432.1	44087.8	15655.7
01/20/2014 16:30	91.7	--	364.875	28779.9	44493	15713.1
01/20/2014 17:30	92.7	321	364.75	28967.8	44749.6	15781.8
01/20/2014 18:33	93.8	321	364.625	29131.2	44977.3	15846.1
01/20/2014 19:28	94.7	--	364.625	29268	45164.9	15896.9
01/20/2014 20:36	95.8	320.5	364.5	29439.8	45400.5	15960.7
01/20/2014 21:32	96.8	326	364.5	29583.5	45593.9	16010.4
01/20/2014 22:30	97.7	--	364.375	29731.2	45792.4	16061.2
01/20/2014 23:45	99.0	--	364.375	29934	46062.5	16128.5
01/21/2014 00:30	99.7	--	364.375	30033.1	46196.8	16163.7
01/21/2014 01:30	100.7	--	364.25	30198.6	46416.1	16217.5
01/21/2014 02:30	101.7	--	364.25	30345.8	46612.5	16266.7
01/21/2014 03:30	102.7	--	364.125	30495.8	46807.7	16311.9

Date/Time	Elapsed Time (h)	Slurry Level (in.)	Water Level (in.)	GV1 (L)	GV2 (L)	ΔV (L)
01/21/2014 04:30	103.7	--	364.125	30657.2	47018.3	16361.1
01/21/2014 05:30	104.7	--	364.125	30799.9	47203.1	16403.2
01/21/2014 06:30	105.7	--	364	30948.4	47393.9	16445.5
01/21/2014 07:30	106.7	--	363.875	31102.1	47592.8	16490.7
01/21/2014 08:30	107.7	--	363.8125	31253	47785	16532
01/21/2014 09:30	108.7	--	363.75	31430.7	47996.6	16565.9
01/21/2014 10:30	109.7	--	363.6875	31690.5	48289.9	16599.4
01/21/2014 11:35	110.8	317	363.625	31991.9	48632.8	16640.9
01/21/2014 12:50	112.1	--	363.375	32322.9	49008.4	16685.5
01/21/2014 15:14	114.5*	--	463.875	33003.3	49056.5	16053.2
01/21/2014 15:48	115.0*	--	463.875	33067.1	49116.5	16049.4
01/21/2014 16:18	115.5*	--	463.875	33185.3	49229.3	16044
01/21/2014 16:49	116.1*	--	464	33275.9	49317.5	16041.6

Table A.3. Tall Column Test 2 Data: Gauge Pressures

Elapsed Time (h)	P1A (kPa)	P1B (kPa)	P2A (kPa)	P2B (kPa)	P3A (kPa)	P3B (kPa)	P4A (kPa)	P4B (kPa)	P5 (mbar)
0.0	61.8	101.07	38.78	79.75	44.6	45.2	21.3	20.47	1015.8
0.7	76.35	101.71	46.15	79.64	47.77	46.18	24.99	21.34	1015.6
1.7	89.36	100.87	53.99	78.61	49.61	47.52	26.11	23.36	1015.2
2.7	98.7	101.26	61.62	79.04	50.94	48.56	28.37	24.78	1014.2
3.7	102.56	100.17	68.57	78.14	51.63	49.1	23.3	25.86	1013.5
4.7	103.34	99.36	75.4	78.1	51.59	48.86	29.07	25.66	1014.1
5.7	103.5	99.41	79.69	78.22	51.71	49.16	29.78	26.44	1014
6.7	103.54	99.35	82.23	78.42	51.88	49.37	30.24	26.79	1013.7
7.7	103.52	100.37	83.26	78.68	52.17	50.58	30.65	27.77	1013.6
8.7	103.37	99.49	83.42	78.68	52.38	50.85	31.05	27.84	1013.6
9.7	103.24	99.22	82.77	78.94	52.62	50.97	31.12	28.17	1013.8
10.7	103.12	98.65	82.62	78.94	52.89	51.4	31.56	28.06	1013.7
11.7	103	98.2	82.5	79.1	53	50.5	31.6	28	1014
12.7	102.85	98.1	82.17	78.75	53.1	51	31.7	28.2	1015
13.7	102.9	98.3	82.2	78.9	53.2	50.6	31.9	28.1	1014.6
14.7	102.7	97.8	82.2	77.9	53.2	50.3	31.9	28.2	1014.6
15.7	102.6	97.6	82.4	77.8	53.4	50.2	31.9	28.1	1013.7
16.7	102.7	97.4	82.5	77.4	53.7	50	32.3	28.3	1013.5
17.7	102.7	97.3	82.5	77.8	53.7	49.9	32.3	28.5	1013.3
18.7	102.4	96.5	82.77	77.3	53.72	49.7	32.42	28.4	1013
19.9	102.35	97.5	82.78	78.1	53.87	50.2	32.75	29.1	1013.5
21.6	102.06	97.9	82.7	78.9	53.96	50.6	32.84	29.8	1013.3

Elapsed Time (h)	P1A (kPa)	P1B (kPa)	P2A (kPa)	P2B (kPa)	P3A (kPa)	P3B (kPa)	P4A (kPa)	P4B (kPa)	P5 (mbar)
22.6	102.38	97.8	82.87	78.7	53.86	50.9	32.96	29.9	1013.1
23.7	102.6	98	82.95	79.1	53.89	50.9	33.15	30.3	1013.3
24.7	102.58	97.9	82.9	79	53.95	51.2	32.96	30.4	1013.5
25.7	102.36	97.8	82.85	78.4	53.92	50.6	32.9	30.3	1013.8
26.7	102.14	97.06	82.64	78.4	53.87	50.69	32.98	30.19	1013.8
27.7	102.12	96.6	82.59	77.89	53.78	50.61	32.72	30.15	1013.5
28.7	102.17	96.96	82.72	78.19	53.81	50.42	32.55	30.39	1013.5
29.7	101.89	97.12	82.99	78.79	53.82	50.84	32.65	30.75	1013.9
30.7	101.6	97.3	83.35	78.89	53.74	51	32.84	31.14	1013.7
31.7	101.6	96.94	83.51	78.86	53.79	51.01	32.9	31.16	1013.5
32.7	101.7	96.83	83.73	78.77	53.76	50.96	32.98	31.17	1013.4
33.7	101.45	99.02	83.19	79.49	54.09	51.25	33.28	31.76	1013.8
34.7	101.4	98	83.6	79.3	54	50.9	32.9	31.4	1013.9
35.7	101.2	97.5	83.8	79.3	53.8	50.7	33.1	31.2	1014.3
36.7	101.2	98.5	83.8	79.7	53.6	50.4	32.9	31.1	1014.3
37.7	101.2	98.4	83.7	79.6	54.1	50.5	32.9	31.4	1014.6
38.7	101.4	98.5	82.1	79.1	54.5	50.1	33	31.2	1013.9
39.7	101.5	98.4	82.3	79.4	54.6	50	33.1	31	1013
40.7	101.4	98	82.5	78.8	54.5	49.8	33.1	30.7	1012
41.7	101.3	97.3	82.3	79.3	54.3	49.7	33.2	30.7	1011.3
42.7	101	97.5	82.6	79	54	49.8	33.3	31.1	1011
43.7	100.6	97.7	82.5	79	53.7	49.8	33.2	30.9	1010.8
44.7	100.5	97.6	82.6	79.1	53.3	50	33.3	31	1010.7
45.9	100.3	97.8	82.3	78.8	53.5	49.9	33.2	31.2	1010.5
46.8	100.2	98.4	81.8	78.3	53.4	50.1	33.2	31.1	1010.5
47.8	100.1	98.2	80.2	77.8	53	49.7	33.1	30.8	1009.8
48.7	99.8	97.5	80.2	78.6	53	49.7	33	31.1	1010.2
49.8	99.5	97.6	80.5	78.9	52.8	49.8	33	31	1010.4
50.7	99.3	97.4	80.6	78.8	52.8	49.7	33.9	31	1009.9
51.7	99.2	96.8	80.6	78.9	52.7	49.9	32.9	31	1009.3
52.7	98.9	97.4	80.3	78.8	52.7	49.7	32.9	31.1	1008.9
53.7	98.9	97.4	80.5	79	52.6	49.7	32.9	31.3	1008.4
54.7	98.7	97.1	80.6	78.9	52.4	50	32.8	31	1008.2
55.7	98.6	97.5	80.1	78	52.1	49.9	32.8	31	1008.1
56.7	98.5	98.2	80.2	77.9	52.3	49.9	32.6	30.9	1007.9
57.7	98.3	97.8	80.2	78.4	51	49.6	32.4	30.8	1008
58.7	98.1	97.9	80.3	78.3	50.9	50	32.5	30.8	1008
59.8	98	97.6	80.6	78.6	51.4	49.9	32.5	30.9	1008.3
60.8	97.7	98.2	80.9	78.6	51.7	50.1	32.4	30.8	1009
61.7	97.6	98	81.3	78.4	51.7	49.9	32.3	30.8	1009.3

Elapsed Time (h)	P1A (kPa)	P1B (kPa)	P2A (kPa)	P2B (kPa)	P3A (kPa)	P3B (kPa)	P4A (kPa)	P4B (kPa)	P5 (mbar)
62.7	97.42	97.7	81.8	78.1	51.3	49.7	32.1	30.5	1009.3
63.7	97.2	97.7	82.2	78.9	51.3	49.4	32.1	30.5	1009.2
64.7	97.1	97.5	82.6	79.7	51	49.6	32	30.4	1009.2
65.7	96.9	97.9	83	80	50.9	49.6	32	30.4	1009
66.8	96.7	98.6	83.2	80.5	50.8	49.7	31.8	30.5	1009.8
68.0	96.5	99.1	83.4	80.3	50.5	50	31.7	30.6	1010.6
68.8	96.4	99.3	83.6	80	50.6	50.1	31.6	30.6	1011.1
69.8	96.2	98.8	84	80.4	50.4	50.2	31.6	30.7	1011.7
71.0	96	99.9	84.4	80.1	50.3	50.2	31.5	30.7	1012.8
71.6	95.9	100	84.6	80.3	50.2	50.4	31.5	30.7	1013.3
73.0	95.8	100.3	84.9	80.8	50.2	50.7	31.3	30.6	1014.5
73.8	95.7	100.8	85.1	81.2	50.1	50.7	31.3	30.7	1014.9
74.8	95.6	101.1	85.4	81.6	50	50.9	31.4	30.7	1015.3
75.7	95.5	101.8	85.7	81.8	49.9	50.4	31.3	30.6	1015.3
76.7	95.5	100.9	85.9	81.9	49.8	50.7	31.1	30.4	1015.5
77.7	95.4	100.9	86.1	80.9	49.8	50.7	31.2	30.6	1016.3
78.7	95.3	101.2	86.4	80.4	49.8	50.8	31.1	30.6	1016.7
79.7	95.2	101.1	81.4	80.7	49.7	50.6	30.8	30.5	1017.1
80.7	95.1	101.7	81.6	80.7	49.6	50.7	30.6	30.4	1017.5
81.7	95.1	102.1	81.9	80.6	49.5	51	30.8	30.5	1017.7
82.9	95	103.1	82.3	80.9	49.5	50.7	30.5	30.3	1018
83.6	95	102.5	82.6	80.7	49.4	50.8	30.7	30.5	1018.1
84.7	94.9	102.3	82.8	80.2	49.3	50.6	30.4	30.4	1018.9
85.8	94.9	102.4	83.1	80.8	49.3	50.7	30.5	30.3	1019.3
86.8	94.9	103.2	83.3	80.9	49.4	50	31.1	30.3	1018.8
87.9	94.9	98.5	83.6	80.6	49.5	50.1	31.1	30.3	1018
88.7	94.9	100.8	83.8	80.5	49.4	50.5	30.8	30.2	1017.7
89.7	94.9	102	84	80.9	49.4	50	30.4	29.7	1017.5
90.7	94.8	103	81.9	79.8	49.3	50.5	30.5	29.7	1017.6
91.7	94.8	102.7	82.1	79.9	49.3	50.6	30.9	30	1017.7
92.7	94.7	103.5	82.3	80.3	49.2	50.6	30.8	29.9	1017.8
93.8	94.6	104.3	82.6	80.2	49.2	51.5	30.8	30.2	1017.7
94.7	94.6	104.6	82.8	79.9	49.1	52.3	30.6	30.2	1017.7
95.8	94.5	104.8	83.1	79.6	48.9	53.4	30.1	29.9	1017.7
96.8	94.4	105.9	83.4	79.8	48.9	54	29.9	29.6	1017.7
97.7	94.3	106.2	83.5	79.9	48.7	53.9	30	29.6	1017.9
99.0	94.2	106.7	83.7	80	48.9	54.5	29.9	29.7	1018.1
99.7	94.2	107.3	83.9	79.8	48.9	54.5	30.2	29.9	1017.9
100.7	94.1	106.9	81	80.1	48.8	54.4	30	29.9	1017.8
101.7	94	107.7	81.3	80.1	48.7	54.6	29.6	29.6	1017.5

Elapsed Time (h)	P1A (kPa)	P1B (kPa)	P2A (kPa)	P2B (kPa)	P3A (kPa)	P3B (kPa)	P4A (kPa)	P4B (kPa)	P5 (mbar)
102.7	94	107.85	81.7	79.8	48.6	55	29.6	29.9	1017.4
103.7	93.9	107.9	82.3	79.8	48.6	54.7	29.6	29.7	1017.2
104.7	93.8	108.5	82.7	79.7	48.7	54.8	29.6	29.6	1017.1
105.7	93.6	108.6	83	80	48.6	55	30.1	30.1	1017.2
106.7	93.6	108.6	83.4	79.7	48.4	54.9	30.1	30.4	1017.1
107.7	93.5	108.6	83.6	79.5	48.4	54.6	29.6	30.2	1017.1
108.7	93.4	109.1	83.8	80.1	48.4	54.8	29.3	30	1017.5
109.7	93.3	108.9	82.7	80.4	48.5	54.6	29.7	29.5	1017.4
110.8	93.3	109.2	83	79.8	48.4	54.4	29.7	29.8	1017
112.1	93.4	109.5	83.3	79.9	48.4	53.9	29.8	29.5	1016.2
114.5*	95.3	125.9	86.2	103	59.8	74.5	50	53.6	1015.1
115.0*	96.9	126.8	87.5	103.6	63.9	74.9	53.2	53.3	1014.6
115.5*	98.8	128.3	89.2	105.1	67.6	75.5	54.9	53.3	1015
116.1*	100.7	129.9	91.1	106.7	70.7	75.8	55.9	53.2	1015.2

Table A.4. Tall Column Test 3 Data: Levels and Gas Volumes

Date/Time	Elapsed Time (h)	Slurry Level (in.)	Water Level (in.)	GV1 (L)	GV2 (L)	ΔV (L)
02/21/2014 15:20	0.0	353.5	378.125	0	0	0
02/21/2014 15:30	0.2	359.375	378.875	11.3	26.6	15.3
02/21/2014 16:00	0.7	360.5	380.75	151.2	500.3	349.1
02/21/2014 16:30	1.2	362.625	382.125	296.4	1000.1	703.7
02/21/2014 17:00	1.7	363.5	383.875	439.6	1488.8	1049.2
02/21/2014 17:30	2.2	364.875	384.75	582.4	1964.3	1381.9
02/21/2014 18:04	2.7	365.75	386.0375	750.3	2514.9	1764.6
02/21/2014 18:35	3.2	367.25	387.325	904.1	3017.3	2113.2
02/21/2014 19:02	3.7	368.125	388.875	1024.9	3419.5	2394.6
02/21/2014 19:31	4.2	369.25	389.75	1166.7	3906.3	2739.6
02/21/2014 20:01	4.7	370.25	391	1308.5	4399.9	3091.4
02/21/2014 20:30	5.2	370.625	391.0625	1431.9	4799.5	3367.6
02/21/2014 21:01	5.7	371	391.75	1586.7	5268.4	3681.7
02/21/2014 21:30	6.2	371.375	391.875	1717.7	5651.1	3933.4
02/21/2014 22:00	6.7	371.5	392.25	1891.1	6126.5	4235.4
02/21/2014 22:30	7.2	371.375	392.375	2008.9	6449.3	4440.4
02/21/2014 23:00	7.7	371.625	392.5	2151.6	6823.9	4672.3
02/22/2014 00:00	8.7	371.75	392.5	2438.3	7561.6	5123.3
02/22/2014 01:00	9.7	371.75	393.125	2721.1	8266.9	5545.8
02/22/2014 02:00	10.7	371.75	393.125	3025.4	9009.1	5983.7
02/22/2014 03:08	11.8	371.325	393.125	3355.1	9782.5	6427.4

Date/Time	Elapsed Time (h)	Slurry Level (in.)	Water Level (in.)	GV1 (L)	GV2 (L)	ΔV (L)
02/22/2014 04:08	12.8	371	393.25	3641.8	10448.1	6806.3
02/22/2014 05:00	13.7	371.125	393.375	3887.7	11018.6	7130.9
02/22/2014 06:00	14.7	371.125	393.5	4171.6	11665.4	7493.8
02/22/2014 07:01	15.7	371.25	393.75	4473	12361.5	7888.5
02/22/2014 08:00	16.7	370.5	393.875	4748	12998	8250
02/22/2014 09:00	17.7	370	394	5035	13644.3	8609.3
02/22/2014 10:00	18.7	370.25	394	5320.2	14270.7	8950.5
02/22/2014 11:00	19.7	369.75	394.125	5603	14886.5	9283.5
02/22/2014 12:00	20.7	370	394.375	5878	15476.2	9598.2
02/22/2014 13:00	21.7	369.75	394.125	6156	16061.7	9905.7
02/22/2014 14:00	22.7	369.75	394.125	6435	16641.8	10206.8
02/22/2014 15:00	23.7	369.625	394	6712	17209.1	10497.1
02/22/2014 16:00	24.7	369.375	394	6983.8	17737.9	10754.1
02/22/2014 17:00	25.7	369.375	393.875	7316.8	18361.8	11045
02/22/2014 18:00	26.7	367.25	393.875	7580	18842.9	11262.9
02/22/2014 19:00	27.7	367	393.625	7866.3	19359.8	11493.5
02/22/2014 20:00	28.7	367	393.375	8165.5	19889.8	11724.3
02/22/2014 21:00	29.7	367	393	8437	20371	11934
02/22/2014 22:00	30.7	367	392.875	8707.7	20854.5	12146.8
02/22/2014 23:00	31.7	367	392.875	9019.2	21395.1	12375.9
02/23/2014 00:01	32.7	367	392.875	9294.2	21871.4	12577.2
02/23/2014 01:07	33.8	367	392.875	9595	22368.7	12773.7
02/23/2014 02:01	34.7	367	392.75	9846.5	22796.3	12949.8
02/23/2014 03:05	35.7	367	392.5	10141.9	23284.1	13142.2
02/23/2014 04:01	36.7	367	392.5	10396.1	23701.1	13305
02/23/2014 05:00	37.7	--	392.125	10673	24141.5	13468.5
02/23/2014 06:01	38.7	--	392	10951.9	24591.3	13639.4
02/23/2014 07:00	39.7	--	391.5	11221.1	25016.9	13795.8
02/23/2014 08:00	40.7	--	391.25	11495	25435.5	13940.5
02/23/2014 09:00	41.7	366	391.125	11768	25849.7	14081.7
02/23/2014 10:00	42.7	366	391	12036	26264.6	14228.6
02/23/2014 11:00	43.7	366	390.75	12306	26684	14378
02/23/2014 12:00	44.7	365	390.5	12573	27094.3	14521.3
02/23/2014 13:00	45.7	365	390.25	12843	27513.1	14670.1
02/23/2014 14:00	46.7	364	390.25	13111	27922.1	14811.1
02/23/2014 15:00	47.7	365	390	13384	28317.9	14933.9
02/23/2014 16:00	48.7	365	389.75	13652.5	28704.1	15051.6
02/23/2014 17:00	49.7	365	389.625	13926.9	29090.1	15163.2
02/23/2014 18:00	50.7	365	389.375	14206.7	29478.8	15272.1
02/23/2014 19:00	51.7	363	389.25	14484.6	29858.7	15374.1

Date/Time	Elapsed Time (h)	Slurry Level (in.)	Water Level (in.)	GV1 (L)	GV2 (L)	ΔV (L)
02/23/2014 20:00	52.7	363	389	14769.7	30244.8	15475.1
02/23/2014 21:00	53.7	--	388.875	15045.5	30615.4	15569.9
02/23/2014 22:00	54.7	362	388.625	15333.7	30994.2	15660.5
02/23/2014 23:00	55.7	362	388.5	15602.8	31353.1	15750.3
02/24/2014 00:02	56.7	--	388.375	15891.8	31730.3	15838.5
02/24/2014 01:00	57.7	--	388.25	16166.5	32090.1	15923.6
02/24/2014 02:00	58.7	--	388	16449.7	32461.7	16012
02/24/2014 03:00	59.7	--	387.875	16722.6	32820.1	16097.5
02/24/2014 04:00	60.7	--	387.8125	16998.7	33176.1	16177.4
02/24/2014 05:00	61.7	357	387.75	17280.8	33536.5	16255.7
02/24/2014 06:00	62.7	357	387.5	17552.2	33880.1	16327.9
02/24/2014 07:00	63.7	357	387.375	17815.2	34211.5	16396.3
02/24/2014 08:00	64.7	357	387.25	18103.6	34574.4	16470.8
02/24/2014 09:08	65.8	357	387.25	18415.7	34945.5	16529.8
02/24/2014 10:00	66.7	357	387.25	18643.9	35222.3	16578.4
02/24/2014 11:00	67.7	357	387.25	18914.5	35557.4	16642.9
02/24/2014 12:05	68.7	357	387.25	19218.1	35938.7	16720.6
02/24/2014 12:30	69.2	--	391.75	n/a	n/a	n/a
02/24/2014 13:05	69.8	--	391.625	19506	36267.5	16761.5
02/24/2014 14:00	70.7	--	391.625	19758.8	36582.2	16823.4
02/24/2014 15:00	71.7	--	391.5625	20033.9	36921.8	16887.9
02/24/2014 16:00	72.7	--	391.375	20322.1	37275.3	16953.2
02/24/2014 17:00	73.7	--	391.3125	20590.8	37602.8	17012
02/24/2014 18:00	74.7	--	391.25	20875.5	37942.3	17066.8
02/24/2014 19:00	75.7	--	391.125	21155.4	38281.5	17126.1
02/24/2014 20:00	76.7	--	391.0625	21485	38680	17195
02/24/2014 21:00	77.7	--	391	21716	38955.8	17239.8
02/24/2014 22:00	78.7	--	390.875	22009.1	39307.6	17298.5
02/24/2014 23:00	79.7	--	390.75	22278.8	39630.6	17351.8
02/25/2014 00:02	80.7	--	390.75	22575.6	39978.3	17402.7
02/25/2014 01:00	81.7	--	390.625	22854.8	40304.1	17449.3
02/25/2014 02:00	82.7	--	390.625	23128.3	40622.8	17494.5
02/25/2014 03:00	83.7	--	390.5	23423.6	40969.7	17546.1
02/25/2014 04:00	84.7	--	390.5	n/a	n/a	n/a
02/25/2014 05:00	85.7	--	390.5	23967.7	41592.5	17624.8
02/25/2014 06:00	86.7	--	390.5	24249.1	41912.6	17663.5
02/25/2014 07:00	87.7	--	390.5	24507.2	42207.3	17700.1
02/25/2014 08:00	88.7	--	390.375	24807.1	42551.2	17744.1
02/25/2014 08:53	89.5	--	390.25	25056	42835.5	17779.5
02/25/2014 10:03	90.7*	--	486.75	25401.1	43013.8	17612.7

Date/Time	Elapsed Time (h)	Slurry Level (in.)	Water Level (in.)	GV1 (L)	GV2 (L)	ΔV (L)
02/25/2014 11:02	91.7*	--	486.75	25659.7	43267.6	17607.9
02/25/2014 12:00	92.7*	--	487.25	25933	43546	17613

Table A.5. Tall Column Test 3 Data: Gauge Pressures

Elapsed Time (h)	P1A (kPa)	P1B (kPa)	P2A (kPa)	P2B (kPa)	P3A (kPa)	P3B (kPa)	P4A (kPa)	P4B (kPa)	P5 (mbar)
0.0	46.33	101.66	47.42	75.26	42.66	49.38	35.36	27.80	1002.8
0.2	48.67	102.36	48.34	76.01	43.97	49.69	35.97	28.79	1002.9
0.7	56.33	102.97	51.21	77.56	47.27	50.46	37.28	29.26	1003.1
1.2	65.37	103.99	54.48	78.21	49.92	51.03	37.65	29.94	1002.8
1.7	73.57	104.38	57.47	79.47	51.82	51.24	38.13	30.91	1003
2.2	80.79	105.79	61.60	80.20	53.36	52.24	38.81	31.34	1003.1
2.7	87.70	105.63	65.59	79.73	54.74	52.95	39.30	32.16	1003.5
3.2	92.97	106.25	68.91	79.77	55.95	53.20	39.73	33.25	1003.8
3.7	96.44	105.98	71.54	79.70	56.82	53.64	40.42	33.27	1004.1
4.2	99.88	105.97	73.80	80.83	57.77	54.70	41.59	33.96	1004.2
4.7	102.60	105.36	75.51	80.73	58.56	55.16	41.78	34.16	1004.5
5.2	104.35	105.12	77.60	80.75	59.88	54.10	41.85	33.86	1004.6
5.7	105.95	105.03	79.43	80.90	59.86	55.22	41.96	34.09	1004.8
6.2	106.94	104.55	80.90	80.95	59.62	54.94	42.23	34.34	1004.8
6.7	107.95	105.12	82.79	81.13	59.86	55.00	42.46	34.84	1005.1
7.2	108.41	104.53	84.01	81.26	59.98	55.10	41.51	34.92	1004.9
7.7	108.64	104.97	85.24	81.55	60.01	55.55	42.31	34.93	1005
8.7	108.90	104.13	87.26	81.31	60.06	55.07	42.26	35.16	1005.2
9.7	108.92	104.88	89.01	81.6	60.24	55.67	41.67	35.9	1005.1
10.7	108.67	102.88	90.36	81.4	60.03	55.46	42.12	35.73	1005
11.8	108.5	104.28	90.6	81.45	59.93	55.51	41.64	36.28	1005
12.8	108.45	103.52	90.65	81.32	60.12	56.03	41.59	35.99	1004.8
13.7	108.44	104.32	90.37	81.97	60.05	56.6	41.73	36.44	1004.9
14.7	108.65	102.73	90.24	82.05	60.49	56.62	41.49	36.77	1004.9
15.7	108.98	103.51	89.89	82.16	60.43	56.91	41.32	37.13	1004.8
16.7	108.91	102.35	89.19	82.31	60.44	56.24	41.64	36.7	1004.8
17.7	108.84	103.54	88.74	82.59	60.72	56.49	41.93	37.01	1004.6
18.7	108.61	103.67	88.76	81.93	60.69	56.05	42.27	36.26	1004.5
19.7	108.27	102.74	88.86	81.36	60.73	55.86	42.36	35.56	1004.2
20.7	107.97	102.31	88.68	81.08	60.7	56.03	42.2	35.81	1003.9
21.7	107.74	101.3	88.47	80.97	60.73	55.29	42.37	35.49	1003.1
22.7	107.41	101.79	88.33	80.15	60.76	54.59	41.73	35.11	1002.5
23.7	107.15	101.31	88.14	80.12	60.69	55.21	41.96	35.53	1002

Elapsed Time (h)	P1A (kPa)	P1B (kPa)	P2A (kPa)	P2B (kPa)	P3A (kPa)	P3B (kPa)	P4A (kPa)	P4B (kPa)	P5 (mbar)
24.7	106.86	100.84	87.79	80.33	60.48	55.36	42.58	35.75	1001.9
25.7	106.52	101.55	87.66	81.1	60.49	55.94	42.21	36.48	1001.8
26.7	106.19	100.58	87.49	81.52	60.37	56.11	41.45	36.6	1002
27.7	105.77	100.83	87.19	81.32	60.27	56.18	41.65	36.81	1002
28.7	105.33	101.79	86.76	81.83	60.32	56.64	41.31	36.71	1002.1
29.7	105.07	101.6	86.86	82.2	60.23	56.18	41.2	36.89	1002.3
30.7	104.8	101.25	86.45	82.46	60.26	56.64	41.23	37	1002
31.7	104.66	100.84	86.56	82.48	60.35	56.75	41.37	37.11	1001.8
32.7	104.48	100.94	85.79	82.56	60.09	58.97	41.63	37.67	1001.5
33.8	104.55	100.3	86.02	83.5	60.45	57.25	41.93	37.64	1001.6
34.7	104.46	100.14	85.38	83.09	60.14	57.11	42.09	37.37	1001.6
35.7	104.17	99.19	84.61	83.42	60.26	57.29	40.8	37.54	1001.1
36.7	103.84	99.37	84.18	82.9	59.97	56.71	40.63	37	1001.1
37.7	103.42	99.51	84.62	83.12	59.73	57.01	40.66	37.55	1001.2
38.7	103.08	98.54	86.06	82.41	59.45	56.75	40.8	37.06	1000.9
39.7	102.75	98.38	88.42	81.72	59.03	57.15	40.94	37.43	1000.5
40.7	102.39	99.74	90.29	82.11	58.92	57.15	41.25	37.48	1000.9
41.7	102.27	98.64	92.51	83.64	59.14	57.22	41.7	37.2	1000.7
42.7	102.19	97.81	93.73	83.79	58.89	57.05	42.07	37.13	1000.4
43.7	101.94	96.98	94.48	83.12	58.46	57.15	42.29	36.54	1000.5
44.7	101.81	97.15	95.28	82.91	58.45	56.85	42.59	36.8	1000.1
45.7	101.85	97.76	95.96	83.01	58.65	56.69	42.92	36.77	999.1
46.7	101.54	96.24	92.94	82.31	58.07	56.4	42.51	36.63	998.7
47.7	101.17	96.5	92.31	83.61	58.15	56.85	43.03	36.97	998.7
48.7	100.94	96.51	92.28	84.15	57.8	56.76	42.33	36.8	998.7
49.7	100.66	96.25	92.23	83.68	57.73	56.85	42.18	36.93	999.1
50.7	100.5	97.19	91.72	83.4	57.46	57.18	42.45	37.29	999.4
51.7	100.43	96.92	92.06	83.97	57.3	57.12	42.72	37.73	999.7
52.7	100.26	97.57	91.61	83.71	57.28	57.46	42.89	37.88	1000.2
53.7	100.03	98.12	91.87	83.41	57.16	57.34	41.98	37.86	1000.9
54.7	99.84	97.89	92.18	82.58	57.14	57.83	42.15	38	1001.9
55.7	99.65	98.78	92.35	82.63	57.06	57.78	42.32	37.67	1002.6
56.7	99.56	98.23	92.39	82.59	56.97	58.01	42.43	37.87	1003.4
57.7	99.38	98.71	92.39	83.16	56.77	57.81	42.52	37.97	1004.1
58.7	99.21	98.8	91.94	84	56.57	57.93	42.53	38.03	1004.9
59.7	99.15	99.03	91.96	83.81	56.49	58.07	42.56	38.04	1005
60.7	98.95	99.76	91.73	84.54	56.44	57.91	42.56	37.91	1005.7
61.7	99	100.12	91.76	85.22	56.47	58.06	42.62	38.18	1006.3
62.7	99	100.87	91.94	88.29	56.6	57.85	42.1	37.88	1006.5
63.7	99.05	101.48	92.27	89.24	56.7	57.73	42.26	37.5	1006.6

Elapsed Time (h)	P1A (kPa)	P1B (kPa)	P2A (kPa)	P2B (kPa)	P3A (kPa)	P3B (kPa)	P4A (kPa)	P4B (kPa)	P5 (mbar)
64.7	99.05	100.65	92.15	89.44	56.76	57.93	42.16	37.05	1007
65.8	98.9	101.9	92.5	90.9	56.9	57.4	42.1	37.1	1007.2
66.7	98.9	102.4	91.9	91.7	57.2	56.8	41.7	37.4	1007.5
67.7	98.8	101.2	91.7	91.8	57	57	42	37.2	1007.4
68.7	98.6	101.8	91.2	92.2	56.6	56.7	41.7	37.3	1007.3
69.2	n/a	n/a	n/a	n/a	n/a	n/a	n/a	n/a	n/a
69.8	98.6	103.6	91.5	93.1	57.5	58.2	41.2	39.2	1007
70.7	98.8	103.9	91.8	93.8	57.5	57.7	41.6	39.4	1007.2
71.7	98.7	103.4	92.2	94.1	57.5	58.6	41.9	39.5	1007.1
72.7	98.6	103.5	92.2	94.6	57.3	58.9	42.2	39.7	1007.1
73.7	98.5	104.1	91.9	94.5	57.2	58.9	42.3	39.8	1007
74.7	98.3	104.9	92.3	96.2	57.2	58.6	42.3	39.9	1007.3
75.7	98	104.3	91.6	96.5	57.1	58.9	42	39.8	1008
76.7	97.7	104.4	91.7	97.1	56.9	58.7	41.9	39.9	1008.1
77.7	97.6	104	91.8	97.3	57	59	41.9	40	1008.7
78.7	97.5	104.3	91.8	98.3	57	58.9	41.8	40.2	1009
79.7	97.36	104.31	91.5	98.54	56.86	58.97	41.69	40.05	1009.4
80.7	97.27	105.46	91.41	100	56.98	58.96	41.7	40.02	1009.8
81.7	97.18	105.65	91.13	101.66	57.14	59.21	40.45	40.14	1010.1
82.7	97.2	105.83	90.9	102.74	57.05	58.91	40.6	40.16	1010.5
83.7	96.98	105.94	90.62	103.67	56.8	59.04	40.77	39.83	1010.5
84.7	96.81	106.43	90.44	104.33	56.61	59.13	40.88	39.98	1010.8
85.7	96.65	107.5	90.15	105.21	56.54	59.3	40.97	40.36	1011.3
86.7	96.45	107.47	90.14	107.48	56.45	59.37	41.07	40.62	1011.7
87.7	96.32	107.02	90.19	108.47	56.17	59.16	41.18	40.37	1012.1
88.7	96.14	107.32	90.15	109.65	56.09	59.07	41.3	40.72	1012.5
89.5	96.07	107.09	89.94	110.75	56.08	58.94	41.4	40.63	1012.8
90.7*	101.46	128.08	105.31	115.16	74.85	81.17	51.76	63.01	1012.9
91.7*	108.54	131.84	111.31	114.57	81.52	82.46	56.54	63.71	1012.6
92.7*	116.4	132.7	114.61	108.14	84.29	83.25	61.38	62.57	1012.1

A.2 Supplementary Figures

The following figures are supplemental data from each of the three tall column tests. There are three figures for each test: 1) the raw measurements of cumulative volume by the wet test meters GV1 (in-flow) and GV2 (out-flow); 2) the bulk void superimposed with the specific volumetric gas generation rate (L of gas/L of simulant × h); and 3) the bulk void superimposed with the specific molar gas generation rate (moles of gas/m^3 of simulant × day).

The moles of gas were estimated from the specific volumetric gas generation rate using the ideal gas law and some assumptions, e.g., the ideal gas law rearranged to solve for a molar rate

$$\dot{n}_g = \frac{P\dot{V}_g}{RT}, \tag{A.1}$$

where $\dot{n}_g$ is moles per time, P is the pressure, $\dot{V}_g$ is volume per time, R is the ideal gas constant, and T is the absolute temperature. For the purposes of the estimation, P is assumed to be atmospheric and T is a representative temperature measured by T5 and T6 during testing (typically around 0 °C). The specific volumetric gas generation rate can then be modified as given in the expression below

$$\frac{\dot{V}_g\left(\frac{P}{RT}\right)}{V_s} = \frac{\dot{n}_g}{V_s} \tag{A.2}$$

where V_s is the initial slurry volume. Unit conversions required to convert between quantities were performed but are not shown in these expressions.

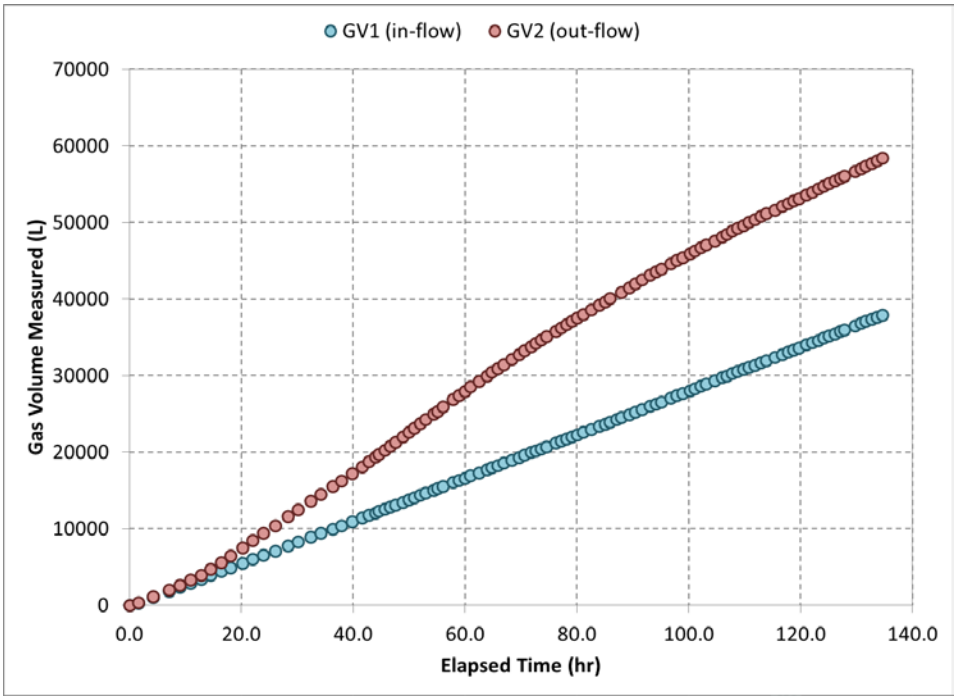

Figure A.1. Cumulative Gas Volumes Measured During Test 1: GV1 (in-flow) and GV2 (out-flow)

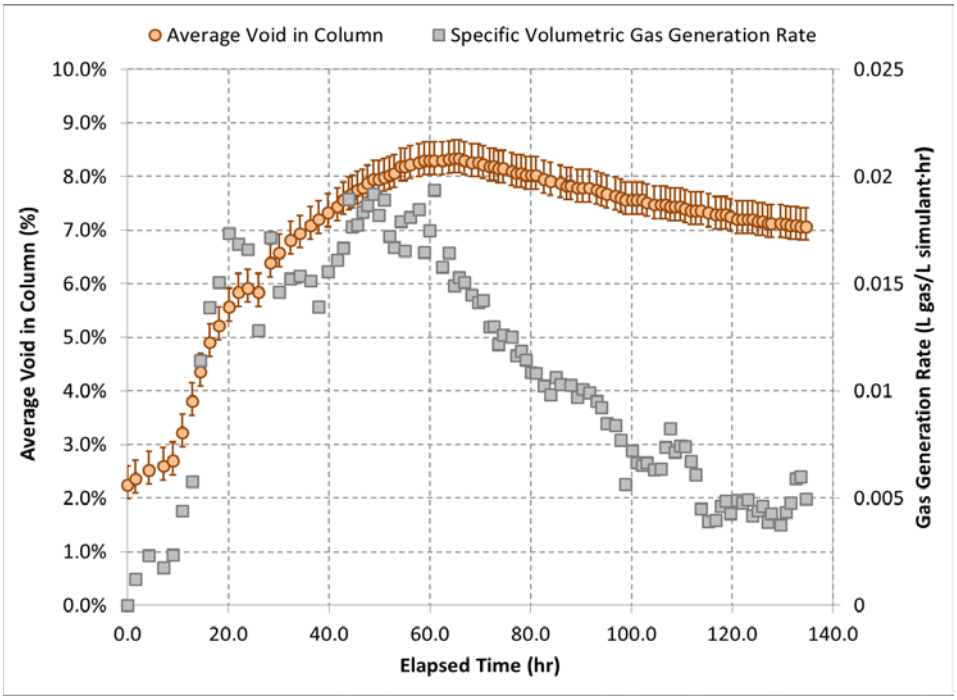

Figure A.2. Bulk (Average) Void (left axis) and Specific Volumetric Gas Generation Rate (right axis) in Tall Column Test 1

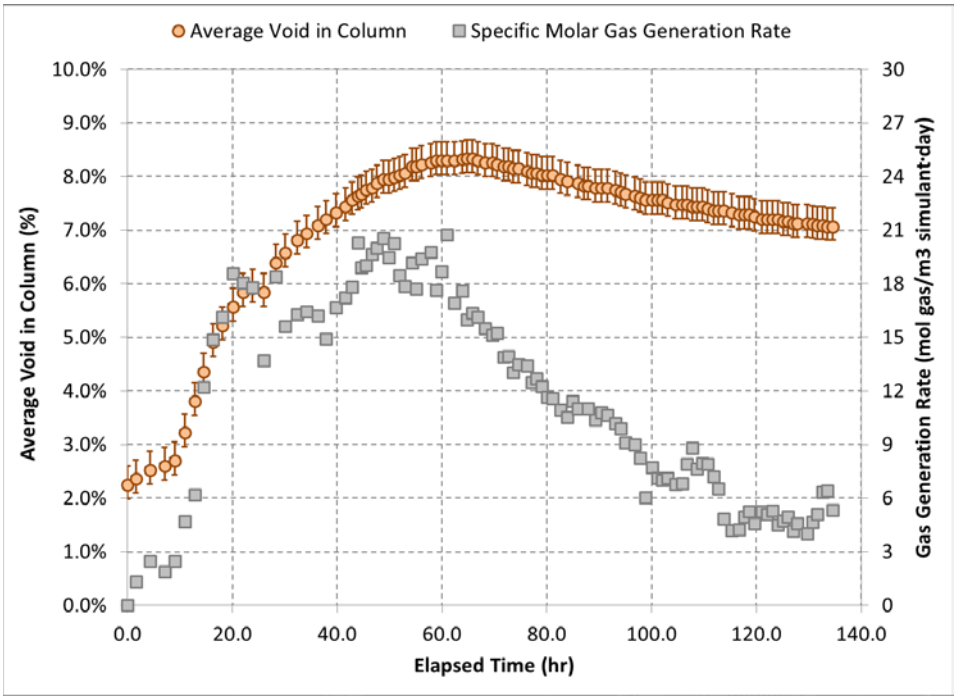

Figure A.3. Bulk (Average) Void (left axis) and Specific Molar Gas Generation Rate (right axis) in Tall Column Test 1

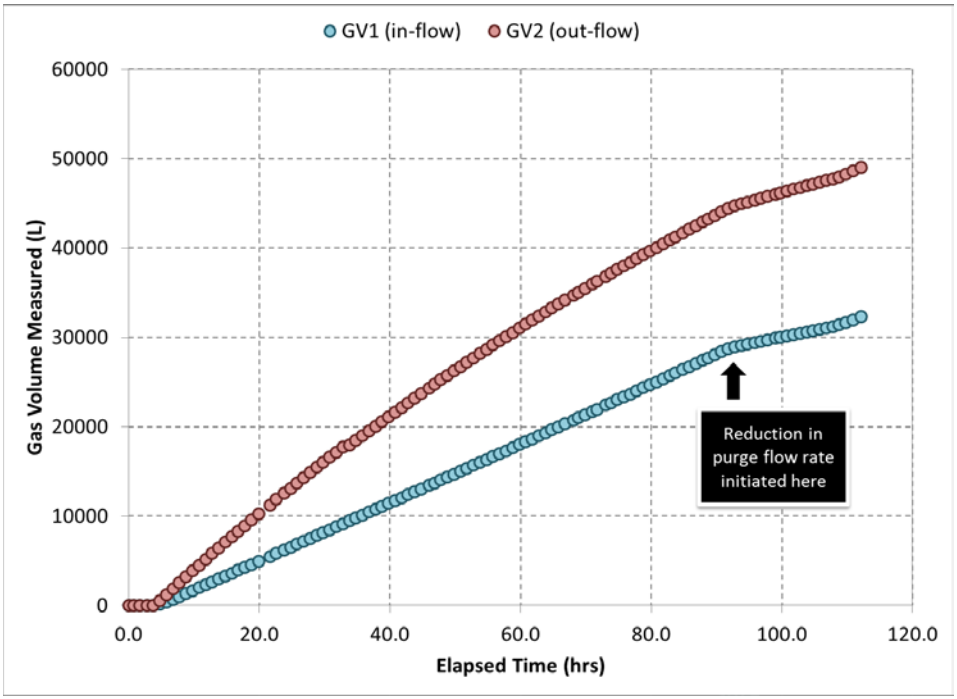

Figure A.4. Cumulative Gas Volumes Measured During Test 2: GV1 (in-flow) and GV2 (out-flow)

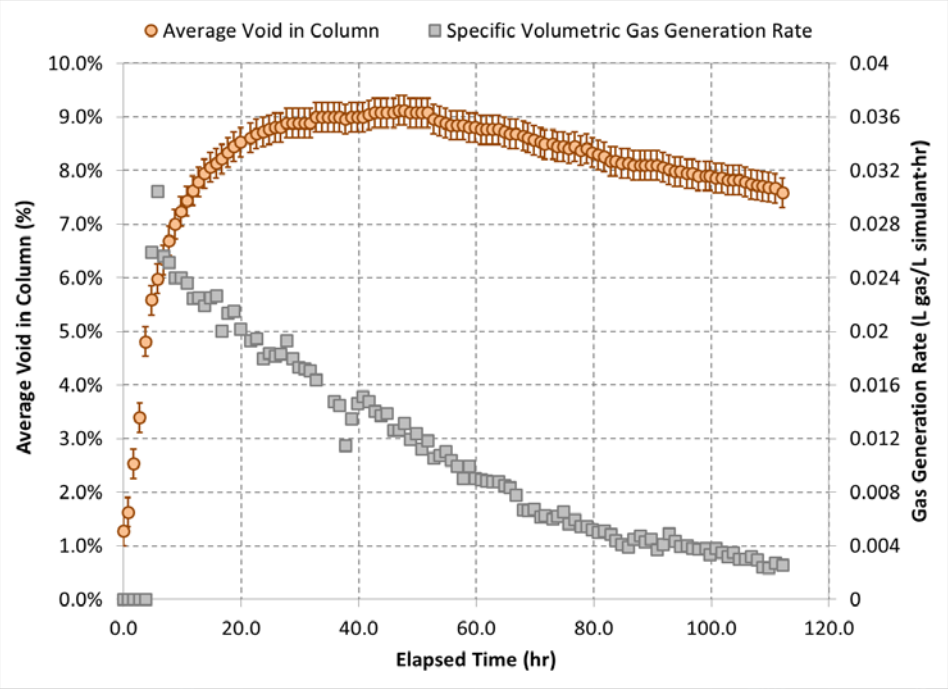

Figure A.5. Bulk (Average) Void (left axis) and Specific Volumetric Gas Generation Rate (right axis) in Tall Column Test 2

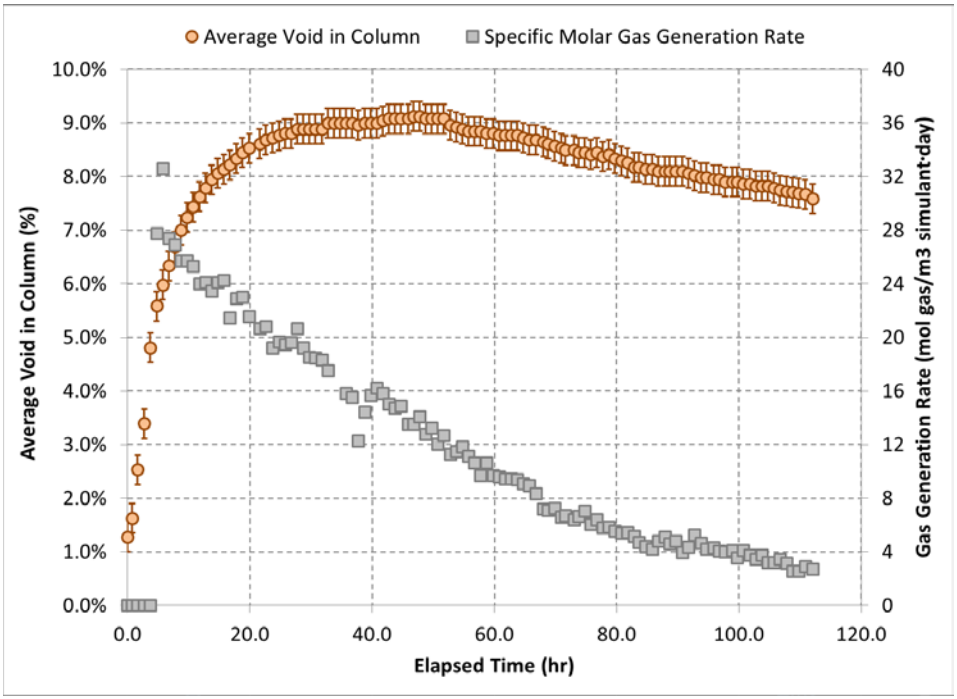

Figure A.6. Bulk (Average) Void (left axis) and Specific Molar Gas Generation Rate (right axis) in Tall Column Test 2

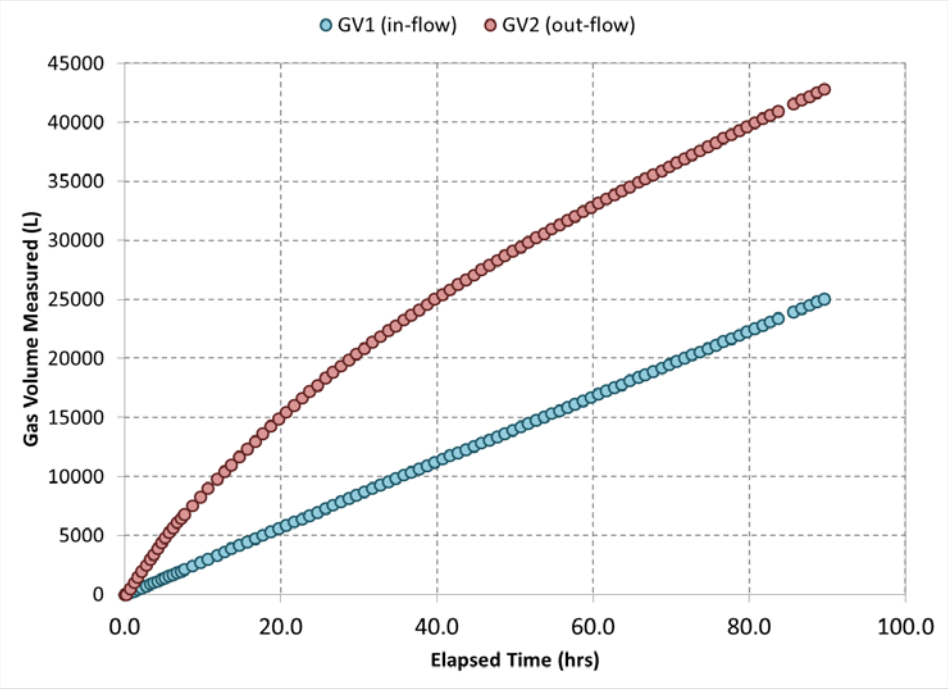

Figure A.7. Cumulative Gas Volumes Measured During Test 3: GV1 (in-flow) and GV2 (out-flow)

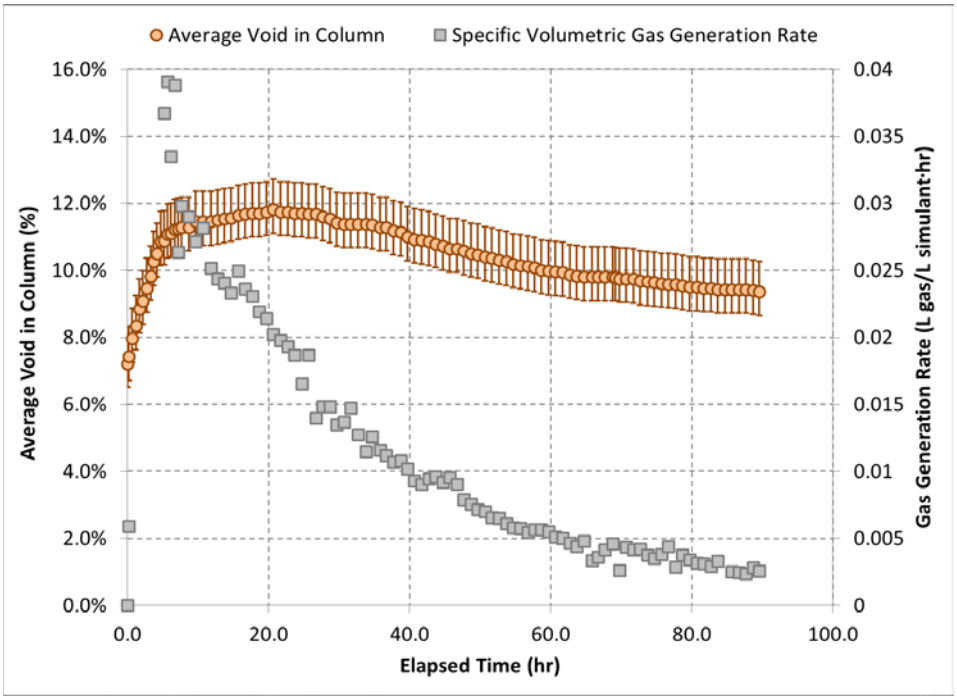

Figure A.8. Bulk (Average) Void (left axis) and Specific Volumetric Gas Generation Rate (right axis) in Tall Column Test 3

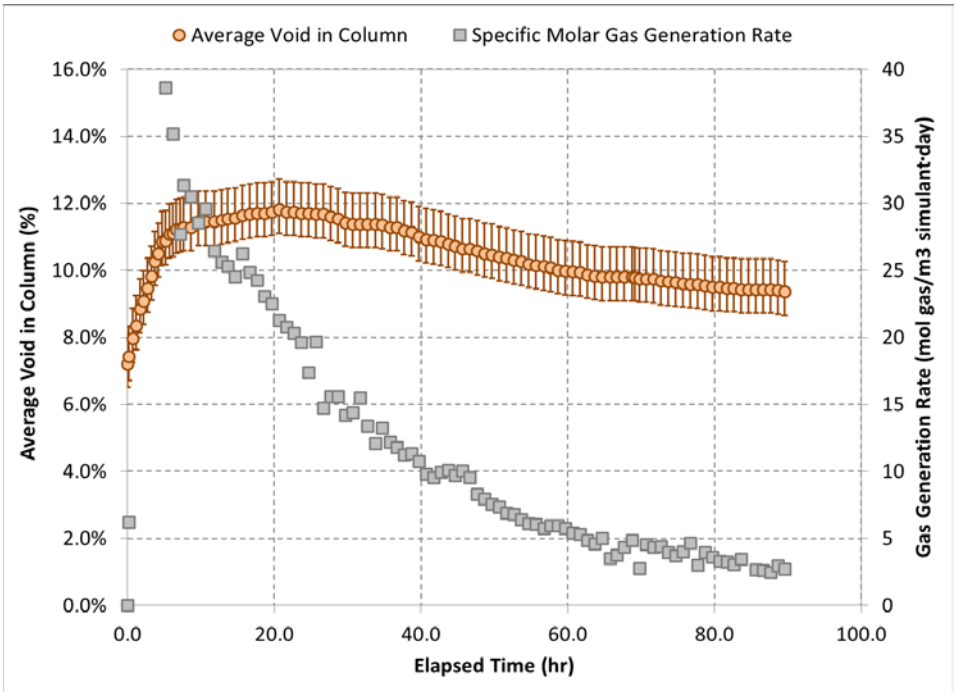

Figure A.9. Bulk (Average) Void (left axis) and Specific Molar Gas Generation Rate (right axis) in Tall Column Test 3

A.3 Post-Test Compression Data

In Table A.6, the post-test compression data recorded during each of the three tall column tests are presented. The table does not include any assumptions or analysis of the data to calculate the bulk void fraction.

Table A.6. Post-Test Compression Data for All Three Tall Column Tests

Quantity	Test 1	Test 2	Test 3
Water level before addition	360.44 in.	363.38 in.	390.25 in.
Maximum[(a)] slurry level (assuming no consolidation)	335.69 in.	338.88 in.	365.63 in.
Best estimate[(b)] of slurry level (using rover camera)	324 in.	317 in.	357 in.
Temperature of water added	5.5 °C	7.5 °C	6.4 °C
Mass of water added	10,440 lb	10,120 lb	9,940 lb
Water level after addition	464.75 in.	463.88 in.	486.75 in.
Water volume added	4736 L	4591 L	4509 L
Level change implied by volume	107.63 in.	104.34 in.	102.48 in.
Level change observed	104.31in.	100.50 in.	96.50 in.
Change in level caused by compression of gas in the slurry	3.32 in.	3.84 in.	5.98 in.

(a) Estimated by assuming that the original water layer added at the start of the test was the same height at the end of the test.

(b) Highly uncertain estimate, as the slurry level is almost indistinguishable at the end of the test.

During the post-test compression events in Test 2 and Test 3, pressure data were collected for approximately 24 hours after the addition of the water layer. In Table A.7 and Table A.8, the gauge pressures for each pressure transducer (refer to Figure 6.2 for the locations of the transducers) are presented as a function of the elapsed time for Test 2 and Test 3, respectively. The elapsed time is referenced to the start of water addition, meaning the water addition in the post-test compression began at an elapsed time of t = 0 h. These data are also shown graphically in Figure A.10 (Test 2) and Figure A.11 (Test 3).

Using the known amount of water added from Table A.6, the expected increase in pressure can be calculated. For both Tests 2 and 3, the water addition was performed in approximately 0.25 h and the expected increase in pressure is ~26 kPa. The expected pressure response is compared to the measured pressure response in Figure A.12 (Test 2) and Figure A.13 (Test 3). The pressure data in these figures have been normalized by the average pressures (both total and pore pressures) before the addition of water, and thus are changes in pressure from these baseline values. The pressure change data are compared to the change in pressure that was expected over a time period when the water addition occurred. In general, the measured changes in total pressure lag slightly in their response to the applied pressure (the water addition) and do not achieve the expected pressure change value of ~26 kPa. The total pressures fall short of the expected pressure by approximately 1 to 10 kPa; the pore pressure transducers have a long response time compared to the time-scale of the water addition and thus cannot be as easily compared.

Table A.7. Transient Pressure Data (Gauge) Collected During Test 2 Post-Test Compression

Elapsed Time (h)	P1A (kPa)	P1B (kPa)	P2A (kPa)	P2B (kPa)	P3A (kPa)	P3B (kPa)	P4A (kPa)	P4B (kPa)	P5 (mbar)
-2.77	93.32	109.13	83.1	79.78	48.41	54.55	29.98	29.7	1016.7
-2.60	93.33	109.41	83.14	79.9	48.39	54.57	29.4	29.49	1016.6
-2.44	93.35	109.3	83.18	80.01	48.98	54.22	29.3	29.47	1016.4
-2.27	93.36	109.89	83.23	80.18	48.41	54.1	29.64	29.03	1016.3
-2.10	93.35	109.12	83.26	79.97	48.41	54.15	29.66	29.3	1016.3
-2.02	93.37	109.47	83.29	80.07	48.42	54.27	29.72	29.4	1016.3
-1.85	93.36	109.9	83.3	80.03	48.4	54.11	29.67	29.5	1016.2
-1.60	93.39	109.08	83.4	79.67	48.38	54.08	29.43	29.07	1015.9
-1.44	93.38	109.41	83.48	79.72	48.34	54.06	29.39	29.12	1015.9
-1.27	93.37	108.95	82.77	79.92	48.29	54.3	29.22	29.29	1016
-1.10	93.37	109.28	82.82	79.4	48.26	54.32	29.24	29.1	1015.7
-0.94	93.38	109.07	82.87	79.42	48.21	54.09	28.98	29.13	1015.7
-0.77	93.37	109.86	82.9	79.48	48.18	54.25	28.87	29.07	1015.5
-0.60	93.36	108.88	82.94	79.32	48.14	54.39	28.92	29.06	1015.3
-0.44	93.36	108.91	83	79.31	48.13	54.21	29.11	28.67	1015.3
-0.27	93.33	108.83	83.01	79.19	48.07	53.98	29.2	28.9	1015.4
-0.10	93.34	108.43	83.06	79.39	48.03	54.29	29.24	28.86	1015.2
-0.02	93.33	109.18	83.08	79.27	48.02	54.09	29.28	28.91	1015.2
0.06	93.36	110.95	83.1	82.97	48.05	56.39	30.58	33.93	1015.3
0.15	93.48	116.92	83.16	91.15	48.68	63.16	32.3	42.05	1015.4
0.23	93.73	123.52	83.45	99.25	51.56	70.67	40.61	50.23	1015.6
0.31	94.03	125.92	85.09	102.84	55.36	74.26	45.58	53.72	1015.7
0.40	94.39	125.81	85.43	102.68	56.74	74.17	47	53.52	1015.5
0.48	94.66	125.7	85.68	102.61	57.84	74.06	48.18	53.39	1015.3
0.56	94.97	125.78	85.93	102.84	58.81	74.54	49.07	53.95	1015.2
0.65	95.27	125.88	86.17	102.95	59.71	74.44	49.95	53.65	1015.1
0.73	95.59	126.01	86.42	103.08	60.58	74.52	50.71	53.53	1014.8
0.81	95.91	126.16	86.68	103.16	61.44	74.62	51.41	53.41	1014.6
0.90	96.24	126.33	86.94	103.24	62.24	74.73	52.03	53.33	1014.5
0.98	96.59	126.51	87.21	103.38	63	74.83	52.59	53.3	1014.5
1.06	96.85	126.73	87.47	103.53	63.79	74.92	53.06	53.27	1014.5
1.15	97.16	126.95	87.74	103.7	64.43	74.98	53.48	53.22	1014.7
1.23	97.48	127.21	88.04	103.93	65.1	75.1	53.89	53.33	1014.7
1.31	97.78	127.45	88.38	104.21	65.74	75.2	54.13	53.31	1014.8
1.40	98.1	127.71	88.61	104.45	66.35	75.29	54.43	53.27	1014.8
1.48	98.42	127.98	88.9	104.72	66.93	75.37	54.64	53.25	1014.9
1.56	98.72	128.24	89.18	105	67.48	75.44	54.86	53.35	1015
1.73	99.32	128.77	89.75	105.61	68.53	75.59	55.23	53.12	1015.1

Elapsed Time (h)	P1A (kPa)	P1B (kPa)	P2A (kPa)	P2B (kPa)	P3A (kPa)	P3B (kPa)	P4A (kPa)	P4B (kPa)	P5 (mbar)
1.90	99.95	129.28	90.36	106.15	69.53	75.72	55.58	53.09	1015.2
2.06	100.57	129.76	90.96	106.56	70.46	75.77	55.83	53.1	1015.2
2.23	101.22	130.4	91.59	106.95	71.33	75.77	56.03	53.28	1015.2
2.40	101.88	130.76	92.23	107.23	72.13	75.62	56.2	53.64	1015.3
2.56	102.58	130.89	92.85	107.19	72.9	75.39	56.33	53.4	1015.2
2.73	103.26	130.86	93.46	107.08	73.61	75.19	56.49	53.52	1015.2
2.98	104.34	130.6	94.34	107.19	74.51	74.9	56.58	53.76	1015.1
3.23	105.42	129.92	95.19	107.22	75.22	74.76	56.67	53.76	1014.9
3.48	106.5	128.9	95.88	107.36	75.8	74.79	56.72	54.4	1014.5
3.73	107.47	128.27	96.52	107.24	76.34	74.82	56.77	54.15	1014.5
3.98	108.4	128.08	97.18	107.28	76.81	74.88	56.72	54.19	1014.4
4.23	109.32	127.95	98.46	107.81	77.2	76.27	56.81	54.2	1014.3
4.48	110.22	127.68	99.7	107.8	77.51	76	56.86	54.18	1014.2
4.73	111.05	127.36	100.79	107.89	77.86	75.88	56.92	54.28	1014.4
4.98	111.86	127.36	101.88	108.13	78.08	75.8	56.94	54.26	1014.4
5.23	112.68	127.1	102.73	108.05	78.26	75.79	57	54.37	1014.5
5.73	114.22	127.17	104.41	107.99	78.46	75.91	57.02	54.5	1014.4
6.23	115.7	127.06	105.84	107.8	78.6	76.11	57.04	54.56	1014.5
6.73	117.04	126.76	107.06	107.88	78.88	76.16	56.98	54.63	1014.6
7.23	118.11	127.04	108.07	107.7	78.76	76.27	57.02	54.49	1014.6
7.73	119.11	127.12	108.89	107.68	78.77	76.51	57.13	54.78	1014.5
8.23	120.12	127.46	109.63	107.37	78.81	76.59	57.14	54.89	1014.2
8.73	121	127.46	110.07	107.19	78.82	76.78	57.04	54.88	1014
9.23	121.71	127.78	110.3	107.22	78.84	76.8	57.14	55.03	1013.7
10.23	122.81	127.94	110.42	106.99	78.84	76.73	57.17	55.01	1013.3
11.23	123.7	128	110.26	106.55	78.78	76.58	57.27	55	1012.8
12.23	124.27	127.6	109.95	106.19	78.66	76.62	57.13	55.02	1013.2
13.23	124.57	127.1	109.37	105.62	78.42	76.16	56.8	54.89	1013.3
14.23	124.61	126.86	108.56	105.35	77.73	75.84	56.76	54.99	1013.8
15.23	124.47	126.55	105.15	104.75	77.37	75.43	56.71	55.06	1013.9
16.23	124.1	126.6	103.84	104.23	76.89	75.65	56.86	55.38	1013.9
17.23	123.85	127.31	104.11	104.9	76.55	76.32	57.35	56.06	1013.8
18.23	123.5	126.69	104.28	103.52	76.08	75.36	55.94	54.86	1014
19.23	122.88	126.29	104.66	102.82	75.46	75.12	56.11	54.89	1014.2
20.23	122.4	125.93	105.07	103.24	75.02	75.17	55.46	54.6	1014.2
21.23	120.94	122.68	105.23	102.78	69.84	72.84	51.67	50.99	1014
23.23	116.52	124.5	103.38	106.59	70.8	73.92	52.37	52.78	1013.6

Table A.8. Transient Pressure Data (Gauge) Collected During Test 3 Post-Test Compression

Elapsed Time (h)	P1A (kPa)	P1B (kPa)	P2A (kPa)	P2B (kPa)	P3A (kPa)	P3B (kPa)	P4A (kPa)	P4B (kPa)	P5 (mbar)
-2.95	96.4	106.74	90.18	107.28	56.56	59.52	41.11	40.59	1011.8
-2.70	96.38	107.13	90.23	107.89	56.47	59.3	41.14	40.75	1012
-2.45	96.36	106.82	90.26	107.97	56.29	59.15	41.16	40.03	1012
-2.20	96.32	107.01	90.2	108.27	56.18	59.16	41.19	40.43	1012.1
-1.95	96.27	107.59	90.25	108.95	56.12	59.16	41.21	40.58	1012.3
-1.70	96.2	107.2	90.13	108.65	56.14	59.17	41.24	40.47	1012.3
-1.45	96.16	107.22	90.08	109.88	56.14	59.26	41.27	40.66	1012.3
-1.20	96.19	107.56	90.15	109.72	56.09	59.04	41.31	40.84	1012.5
-0.95	96.16	107.89	90.21	110.11	56.16	58.97	41.39	40.82	1012.5
-0.70	96.12	107.66	90.2	110.32	56.27	59.18	41.36	40.68	1012.7
-0.45	96.12	107.27	90.2	110.42	56.23	59.06	41.4	40.46	1012.7
-0.20	96.05	107.48	89.94	110.4	56.1	58.96	41.41	40.63	1012.8
-0.12	96.05	107.75	89.95	111.17	56.14	58.89	41.41	40.8	1012.9
-0.04	96.04	107.42	89.93	110.89	56.13	59	41.39	40.77	1012.8
0.05	96.03	107.26	89.75	110.68	56.13	58.8	41.18	40.8	1012.9
0.13	96.15	112.9	89.84	110.14	57.44	66.47	41.48	48.18	1012.8
0.21	96.6	120.66	90.56	111.85	59.12	74.28	42.01	55.91	1012.8
0.30	97.22	127.72	92.83	115.64	62.79	81.38	47.78	63.55	1012.8
0.38	97.87	127.27	95.73	115.34	66.67	80.99	48.65	63.2	1012.9
0.46	98.47	127.08	97.92	115.16	68.33	80.88	49.22	62.89	1012.9
0.55	99.02	127.12	99.84	115.09	69.78	80.88	49.68	62.81	1012.9
0.63	99.58	127.26	101.45	115.09	71.08	80.94	50.17	62.9	1012.9
0.71	100.12	127.45	102.78	115.1	72.3	80.99	50.62	62.91	1012.9
0.80	100.68	127.67	103.91	115.09	73.41	81.03	51.07	62.93	1012.8
0.96	101.8	128.25	105.76	115.17	75.28	81.21	51.96	63.04	1012.9
1.13	102.94	128.86	107.2	115.19	76.88	81.38	52.79	63.12	1012.9
1.30	104.1	129.47	108.31	115.17	78.22	81.55	53.59	63.17	1012.8
1.46	105.36	130.23	109.34	115.18	79.4	81.85	54.42	63.37	1012.7
1.63	106.57	130.9	110.15	115.08	80.33	82.05	55.18	63.48	1012.7
1.80	107.83	131.48	110.9	114.81	81.11	82.27	56	63.62	1012.7
2.05	109.72	132.33	111.94	114.1	82.08	82.69	57.31	63.74	1012.6
2.30	111.76	133.06	112.94	112.77	82.86	83.11	58.68	63.62	1012.4
2.55	114.07	133.99	114.04	110.74	83.54	83.4	59.82	63.3	1012.3
2.80	115.99	132.99	114.54	108.57	84.15	83.36	61.11	62.72	1012.2
3.30	119.06	132.25	115.49	107.27	85.17	83.76	63.14	61.64	1011.9
3.80	121.72	131.77	115.96	106.93	85.79	84.23	64.42	61.64	1011.6
4.30	124.01	131.53	116.06	108.61	86.17	84.1	65.08	63.05	1011.2
4.80	125.95	131.35	116.22	107.7	86.43	84.34	65.47	63.04	1010.8

Elapsed Time (h)	P1A (kPa)	P1B (kPa)	P2A (kPa)	P2B (kPa)	P3A (kPa)	P3B (kPa)	P4A (kPa)	P4B (kPa)	P5 (mbar)
5.30	127.6	131.21	116.37	107.92	86.55	84.33	65.65	62.87	1010.7
5.80	129.07	131.32	116.57	107.98	86.71	84.5	65.78	62.55	1010.5
6.30	130.34	131.61	116.8	108.23	86.85	84.41	65.98	62.57	1010.2
6.80	131.41	131.8	116.98	108.61	86.93	84.53	65.85	62.55	1009.8
7.80	133.07	132.33	117.14	109.13	87.17	84.79	66.06	62.69	1009.5
8.80	134.22	132.56	117.22	109.43	87.33	84.74	66.2	62.96	1009.3
9.80	134.94	132.54	117.19	109.79	87.41	85.26	66.24	63.44	1009.2
10.80	135.4	132.86	117.18	110.6	87.58	85.52	66.34	63.59	1009.1
11.80	135.55	132.44	117.15	110.72	87.47	85.38	66.32	63.78	1009
12.80	135.46	132.34	117	110.51	87.34	85.25	66.45	63.92	1008.8
13.80	135.23	131.37	116.86	110.36	87.04	85.26	66.52	64.04	1008.5
14.80	134.86	131.31	116.51	110.2	86.85	85.14	66.54	64.29	1008.2
15.80	134.36	130.79	116.09	110.46	86.94	85.31	66.49	64.11	1008
16.80	133.85	131.2	114.86	110.66	86.91	85.44	66.47	63.97	1007.5
17.80	133.25	130.8	114.06	110.08	86.72	85.28	66.35	63.82	1007
18.80	132.49	130.52	113.86	109.98	86.36	85.27	66.02	63.99	1006.8
19.80	131.76	130.69	113.51	111.23	86.88	85.07	65.91	63.78	1006.9
20.80	131.02	130.79	113.18	111	85.49	84.82	65.72	63.22	1006.4
21.80	130.28	131.19	112.67	112.19	85.44	84.92	65.61	64.08	1005.9
22.80	129.58	130.89	112.11	112.57	85.55	84.56	65.65	63.32	1006
23.80	128.94	131.02	111.48	112.24	84.79	83.93	65.13	62.69	1005.9

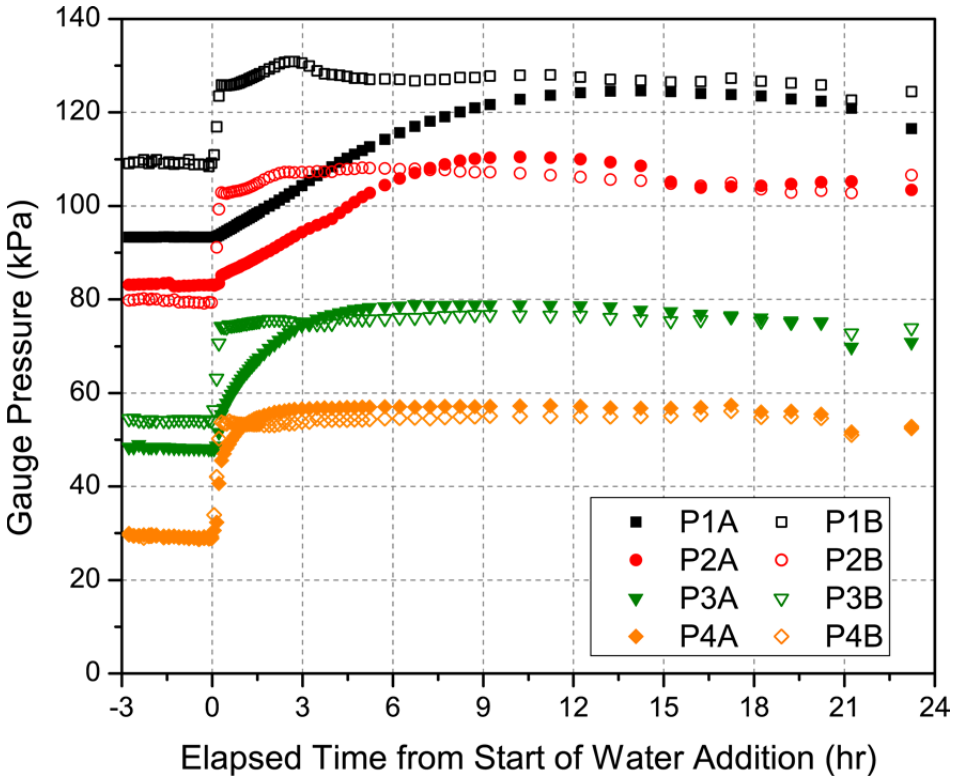

Figure A.10. Transient Pressure (Gauge) Measured During Post-Test Compression Event in Test 2

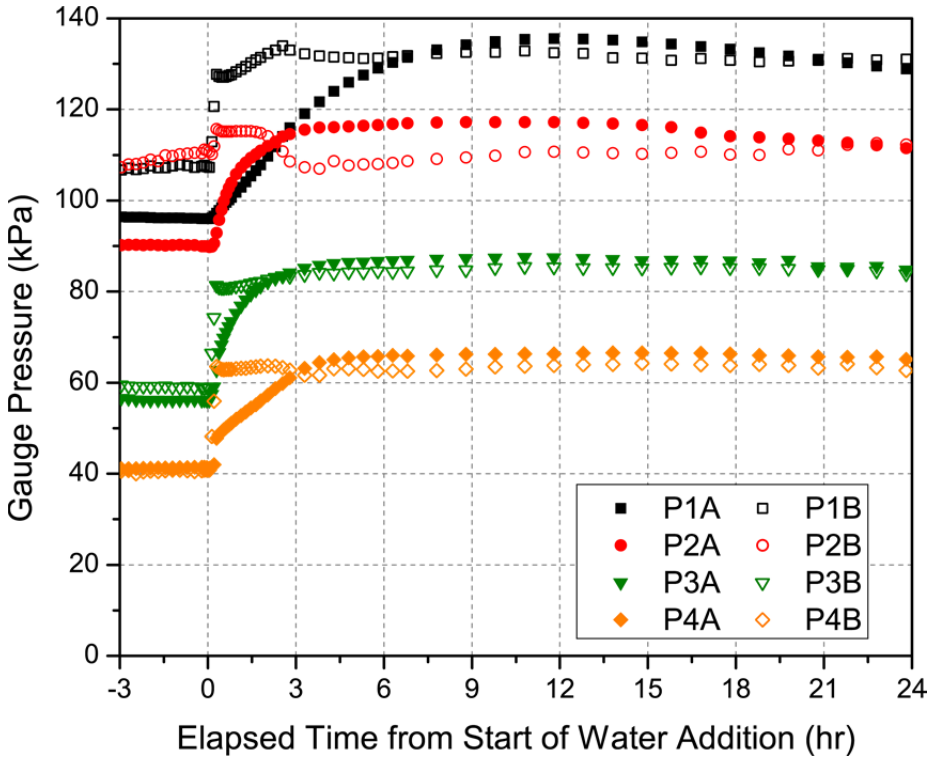

Figure A.11. Transient Pressure (Gauge) Measured During Post-Test Compression Event in Test 3

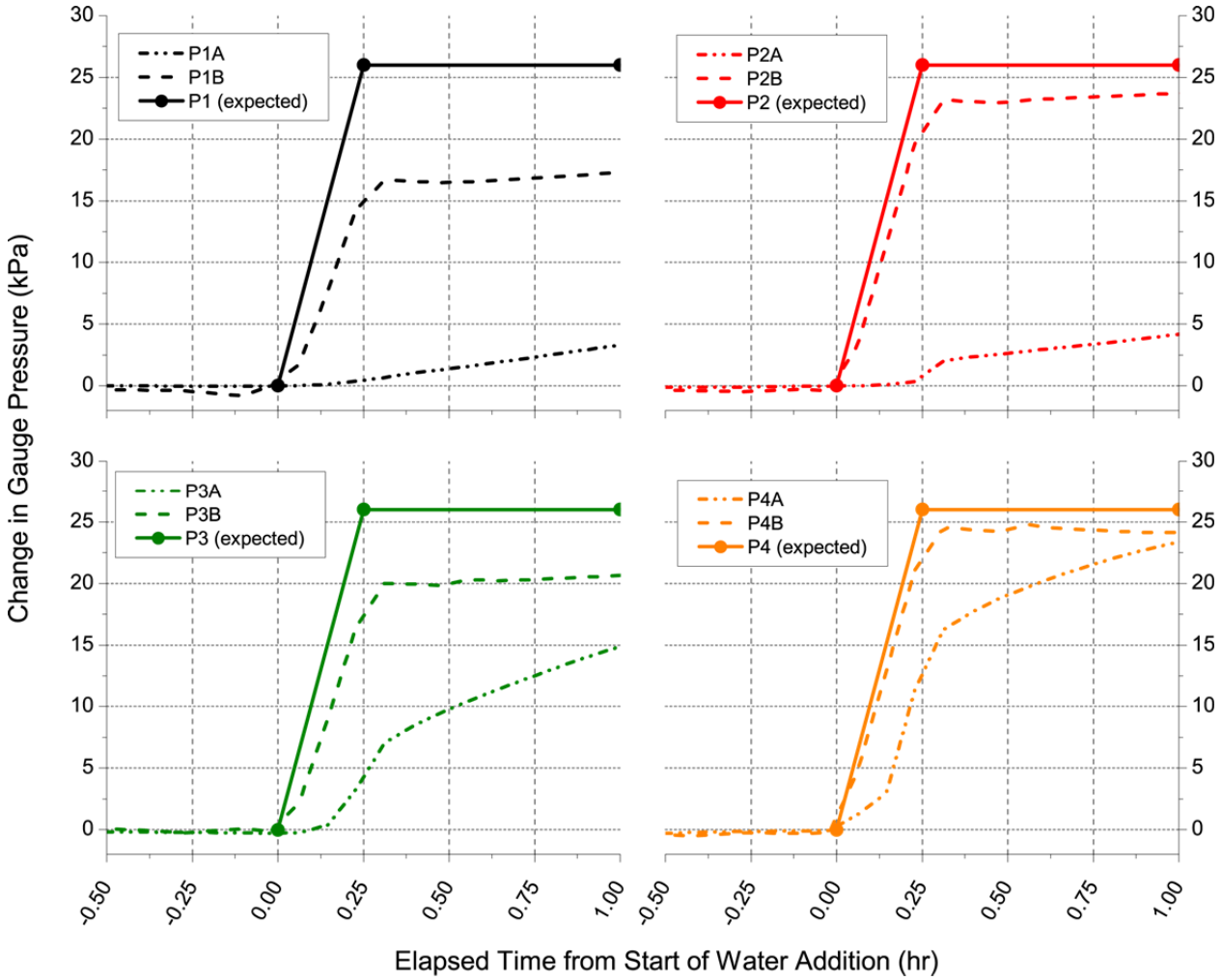

Figure A.12. Change in Total Pressure (dash-dotted lines) and Pore Pressure (dashed lines) Measured During Post-Test Compression Event in Test 2 Compared to Expected Change in Pressure (solid lines with filled circles)

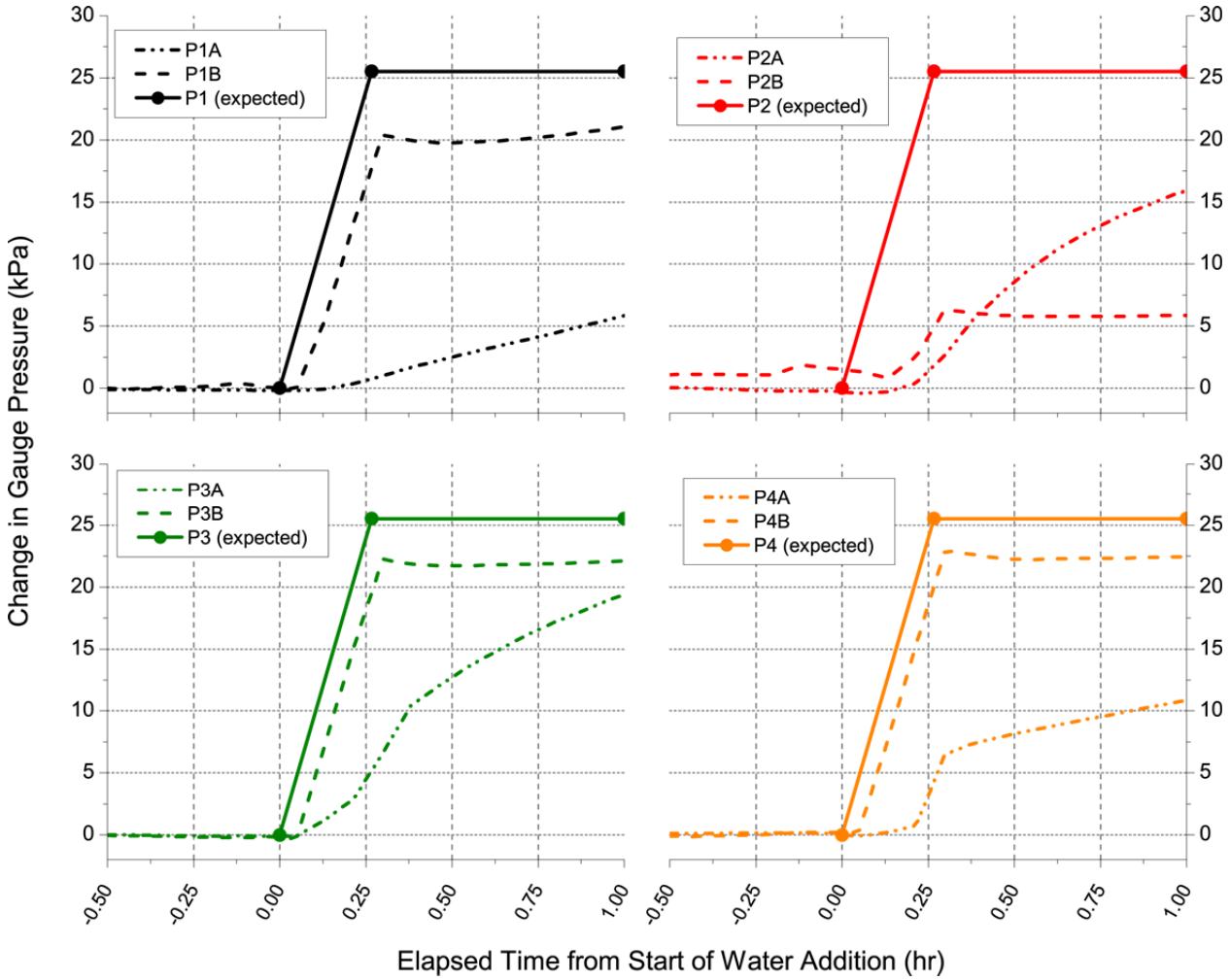

Figure A.13. Change in Total Pressure (dash-dotted lines) and Pore Pressure (dashed lines) Measured During Post-Test Compression Event in Test 3 Compared to Expected Change in Pressure (solid lines with filled circles)

A.4 Physical Property Data

Physical property data from core samples collected during Test 1 and Test2 are presented in Table A.9 and Table A.10. The sample identification numbers correspond to the samples described in Appendix B, since they were analyzed for moisture content (% TS) and shear strength after they were extracted from the core sample coring tube. Refer to Section 6.1.2 for the locations of the sample ports (the second part of the sample number) on the tall column.

Table A.9. Total Solids and Shear Strength Data for Core Samples Taken During Test 1

	Core Sample IDs	TS%	Shear Strength, As-Received (Pa) - Run 1	Shear Strength, As-Received (Pa) - Run 2	Average Shear Strength, As-Received (Pa)	Shear Strength, Post-Agitation (Pa) - Run 1	Shear Strength, Post-Agitation (Pa) - Run 2	Average Shear Strength, Post-Agitation (Pa)
Samples taken near the start of Test 1	Test1-S1A	54.590	564.3	480.4	522.4	355.6	359.1	357.4
	Test1-S2A	53.547	359.1	406.9	383.0	321.8	309.0	315.4
	Test1-S3A	53.103	356.8	396.4	376.6	328.8	327.6	328.2
	Test1-S4A	54.961	403.4	397.6	400.5	420.9	408.1	414.5
	Test1-S5A	54.354	372.0	339.3	355.7	377.8	380.1	379.0
Samples taken near the end of Test 1	Test1-S1C	53.492	452.4	441.9	447.2	337.0	347.5	342.3
	Test1-S2C	53.529	454.7	473.4	464.1	355.6	376.6	366.1
	Test1-S3C	54.263	941.0	808.0	874.5	446.6	459.4	453.0
	Test1-S4C	56.826	958.5	960.8	959.7	677.4	691.4	684.4
	Test1-S5C	56.599	749.7	1000.0	874.9	679.8	692.6	686.2

Table A.10. Total Solids and Shear Strength Data for Core Samples Taken During Test 2

	Core Sample IDs	TS%	Shear Strength, As-Received (Pa) - Run 1	Shear Strength, As-Received (Pa) - Run 2	Average Shear Strength, As-Received (Pa)	Shear Strength, Post-Agitation (Pa) - Run 1	Shear Strength, Post-Agitation (Pa) - Run 2	Average Shear Strength, Post-Agitation (Pa)
Samples taken near the start of Test 2	Test2-S1B	51.835	537.5	542.2	539.9	292.7	290.3	291.5
	Test2-S2A	52.876	497.9	501.4	499.7	295.0	300.8	297.9
	Test2-S3A[(a)]	n/a	n/a	n/a	n/a	n/a	n/a	n/a
	Test2-S4A	52.829	535.2	503.7	519.5	291.5	291.5	291.5
	Test2-S5A	52.833	473.4	552.7	513.1	297.3	298.5	297.9
Samples taken near the end of Test 2	Test2-S1C	52.540	385.9	373.1	379.5	309.0	318.3	313.7
	Test2-S2C	52.890	345.1	360.3	352.7	312.5	342.8	327.7
	Test2-S3C	53.164	387.1	382.4	384.8	314.8	313.7	314.3
	Test2-S4C	53.441	405.8	358.0	381.9	358.0	351.0	354.5
	Test2-S5C	52.935	367.3	360.3	363.8	318.3	317.2	317.8
	Test2-S1A-2	53.111	510.7	455.9	483.3	361.5	362.6	362.1
	Test2-S2B-2	53.023	392.9	341.6	367.3	337.0	337.0	337.0
	Test2-S3B	54.635	529.4	478.1	503.8	441.9	434.9	438.4
	Test2-S4B	54.097	559.7	527.0	543.4	406.9	413.9	410.4
	Test2-S5B	54.259	499.0	499.0	499.0	406.9	398.8	402.9

(a) The core sample was attempted but the sampler failed – no simulant was available to analyze.

Appendix B

Core Sampling Method for Determining Void Fraction

Appendix B

Core Sampling Method for Determining Void Fraction

During Tests 1 and 2, core samples of the clay were taken from the tall column and the gas void fraction was measured. This method locally disturbs the simulant and has fewer advantages than the ultrasonic or level measurement methods. As such, sampling was used as a backup measurement and was deployed at a few vertical locations at the most critical times (i.e., start and end of a test). This section discusses the core sampler design, methodology, performance checks, and results obtained from the samples taken during Tests 1 and 2.

B.1 Sampling Technique

A related method of measuring retained gas fractions in bubbly materials was previously developed and deployed for making in situ measurements in Hanford DSTs (Stewart et al. 1995, 1996). This method used a purpose-built sampling device capable of being deployed in the tank riser, pushing through a water-lanced hole in the hard crust layer, rotating 90° to become horizontal, lowering to multiple depths, opening and closing the sampling chamber, pressurizing the sample at the tank sampling location, measuring temperature and pressure, and releasing the sample when moving to the next sampling location. Development of the purpose-built void fraction instrument was a substantial financial and schedule commitment.

The Stewart et al. (1995, 1996) approach as originally designed cannot be applied to the present testing because it will substantially disturb the slurry column or provide a pathway for vertical gas release. Also, such a sampler could interfere with the ultrasonic and level measurements. Therefore, in the present testing, sampling was planned to occur horizontally through ball valve flanges that have been positioned at strategic elevations on the tall column. The ball valves have a significantly smaller diameter than the in-riser sampling method of Stewart et al. (1995, 1996) and therefore constrained equipment design and sample collection methods. While Stewart et al. (1995, 1996) pressurized the sample chamber at the sampling location inside the tank, the current project personnel felt pressurization inside the tall column slurry would create excessive risk of leaking gas inadvertently increasing the void fraction and other experimental difficulties. Therefore, a long, slender sampling device was designed to fit into the tall column test stand and the sampler was transported to APEL for gas void fraction determination. In addition, multiple sampling devices were fabricated to minimize the delay between sampling events due to the time required to collect a sample, transport it to the APEL test stand, measure the gas void fraction, clean the sampler, and transport the sampler back to the test stand.

Each sampling device, schematically shown in Figure B.1, consists of the following major components: 1) sample coring tube, 2) plunger to facilitate capture and discharge of the sample into and out of the sampler, 3) drive mechanism to insert and remove the sample coring tube and plunger from the tall column, and 4) ball valve assemblies to mate with the tall column and isolate the collected sample for transportation. The sampler also has a port (not shown in Figure B.1) for pressurizing the sample for void fraction determination. Finally, the sampler includes a pressure transducer to measure the sampler pressure prior to void fraction determination.

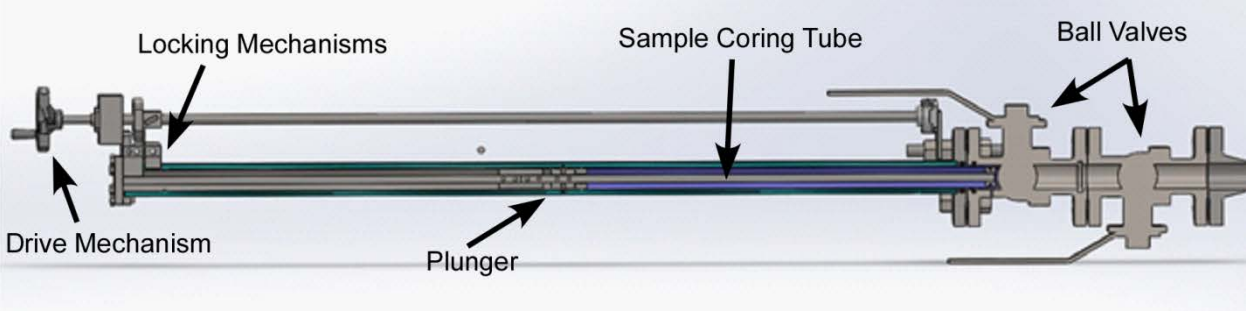

Figure B.1. Sampling Device Used in Tall Column Testing

B.2 Sample Collection Approach

The sampling process involved mating the sampling device to the tall column via the ball valve connection points prior to collecting a slurry sample at each specific location. Once mated, the main column and sample ball valves were opened and the sample coring tube and plunger assembly was moved to a point just inside the inner wall of the tall column. Then the plunger position was locked and the sample coring tube was extended about 24 inches farther into the tall column. This process filled the coring tube with slurry without pressurizing or depressurizing the sample. Once filled, the plunger was disengaged and then fixed relative to the sample coring tube. Both plunger and sample coring tube were then retracted and the main column and sampler valves were closed. At this point, the sample in the sampler should be at the same pressure as the slurry in the tall column at the location where the sample was collected. The sampling device was detached and transported to APEL for pressurization and sample removal for analysis of physical properties.

B.3 Sample Void Fraction Determination

The gas void fraction in the sample collected was determined by connecting the sampler to a reference gas bottle of known volume, pressure, and temperature. The volume and pressure of this reference gas volume and the volume of the sample contained in the core sampler were similar to those used with the void fraction instrument (Stewart et al. 1995, 1996). Figure B.2 schematically shows the test setup used for determining the gas void fraction of thee slurry sample taken in the sampler. The test setup consisted of a reference bottle with temperature and pressure sensors, N_2 gas cylinder (not shown in Figure B.2) to charge to reference bottle, a small connecting line, and valves (V1 and V2) to isolate the reference bottle from the sampler. The reference gas bottle was first pressurized to 500 ±5 psi with N_2 and allowed to stabilize in both temperature and pressure. After stabilization, the line connecting the sample bottle to the sampler was pressurized by opening valve V1 and keeping valve V2 closed. After stabilization in both temperature and pressure, the gas in the reference bottle was exposed to the gas in the sampler by opening the valve V2. At each stage, the pressure and temperature of the reference bottle were recorded along with the pressure in the sampler. This information and the known volume of the reference bottle and empty sampler were used to compute the volume of gas in the sampler and hence the void fraction as discussed in the next section.

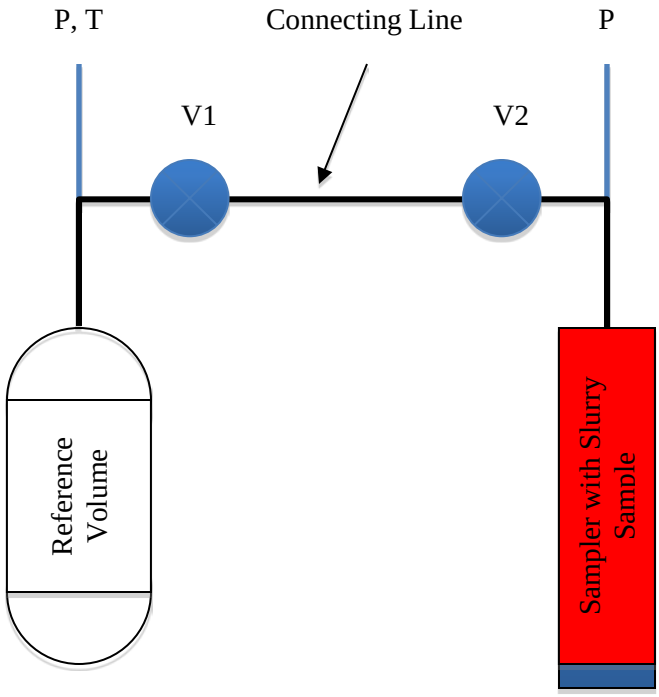

Figure B.2. Apparatus for Gas Void Fraction Determination

B.4 Analysis Methodology

The analysis method was similar to the approach used by Stewart et al (1995, 1996). The gas void fraction was calculated from the known volume of the reference chamber, and the measured pressure and temperatures measured before (initial state) and after (final state) the reference volume and sampler are permitted to communicate with one another.

The gas void fraction measurements were carried out using ultra high purity grade nitrogen gas. Two important factors, which differentiate an ideal gas from a real gas, are the compressibility factor and the residual volume. Ideal gases will have a compressibility factor equal 1.0 and a residual volume equal to zero. Nitrogen gas, at conditions around room temperature (~300 K) and pressures ≤ 500 psi that were considered for void fraction measurements, is far away from its critical point and has a compressibility factor close to 1.0. Also, nitrogen at room temperature is close to its Boyle temperature (332 K) and thus has residual volume near to zero in the pressure ranges considered. Because of the aforementioned reasons, pure nitrogen essentially behaves as an ideal gas under the temperature and pressure conditions of void fraction measurements. Nevertheless, the void fraction estimations were performed using both ideal and real gas laws to quantify resulting uncertainty.

As illustrated in Figure B.2, the sampler with slurry during gas void fraction measurements (or with water during sampler volume uncertainty estimation tests) is connected to the reference bottle of a known volume via a small connecting line. The reference bottle volume is estimated by a gravimetric method as described in Section B.5.1. The connecting line and sampler volumes are determined using the reference

bottle containing pressurized nitrogen gas at a measured pressure (~500 psi) and temperature (~23 °C). The derivations of the equations used for determining the sampler void fractions are presented below.

B.4.1 Nomenclature

Table B.1 lists the variables and constants used in equations presented in Sections B.4.2 and B.4.3.

Table B.1. Nomenclature of Variables and Constants

Variable	Definition
P	Pressure (psi or atm)
T	Temperature (K)
V	Volume (mL or liters)
n	Number of moles
ν	Molar volume (liters/gmole)
R	Universal Gas Constant
A_0, a, B_0, b, c	Constants of the Beattie-Bridgeman Equation of State
P_1, V_1, T_1	Initial conditions of the pressurized reference bottle
P_c, V_c, T_c	Initial conditions of the un-pressurized connecting line
P_2, V_2, T_2	Final conditions of the pressurized reference bottle and connecting line
P_3, V_3, T_3	Final conditions of the pressurized reference bottle, connecting line, and sampler

B.4.2 Volume Estimation Using Ideal Gas Law

The inital state of gas (pressurised) in the reference bottle is given by

$$P_1V_1 = n_1RT_1 \qquad (B.1)$$

The initial state of gas in the connecting line before opening the valve V1 shown in Figure B.2 is given by, $P_CV_C = n_CRT_C$ $(B.2a)$

The state of gas in the connecting line after opening the valve V1 is given by

$$P_2\left(V_1+V_C\right) = \left(n_1+n_C\right)RT_2 \qquad (B.2b)$$

$$\text{or } P_2V_2 = n_2RT_2 \qquad (B.2c)$$

$$\textit{where } V_2 = V_1+V_C \textit{ and } n_2 = n_1+n_C$$

The initial state of gas in the sampler before opening the valve V2 shown in Figure B.2 is given by $P_SV_S = n_SRT_S$ $(B.3a)$

The state of gas in the sampler after opening the valve V2 is given by

$$P_3\left(V_1+V_C+V_S\right) = \left(n_1+n_C+n_S\right)RT_2 \qquad (B.3b)$$

$$\text{or } P_3\left(V_2+V_S\right) = \left(n_2+n_S\right)RT_3 \quad \text{or} \quad P_3V_3 = n_3RT_3 \qquad (B.3c)$$

Substituting Equations (B.1) and (B.2a) into (B.2b) and by using the known reference volume V_1, the connecting line volume V_C could be determined as follows

$$P_2\left(V_1+V_C\right)=\left(\frac{P_1V_1}{RT_1}+\frac{P_CV_C}{RT_C}\right)RT_2 \qquad (B.4a)$$

$$V_C\left(P_2-\frac{P_CT_2}{T_C}\right)=-V_1\left(P_2-\frac{P_1T_2}{T_1}\right) \qquad (B.4b)$$

$$V_C=-V_1\times\frac{\left(P_2-\frac{P_1T_2}{T_1}\right)}{\left(P_2-\frac{P_CT_2}{T_C}\right)}=-V_1\times\frac{\left(1-\frac{P_1T_2}{P_2T_1}\right)}{\left(1-\frac{P_CT_2}{P_2T_C}\right)}=-V_1\times\frac{\left(1-\frac{\nu_2}{\nu_1}\right)}{\left(1-\frac{\nu_2}{\nu_C}\right)} \qquad (B.4c)$$

where $V_2=V_1+V_C$ (B.4d)

Similarly, by substituting Equations (B.2c) and (B.3a) into (B.3c) and using the connecting line volume V_C caclulated above, sampler volume V_S is determined.

$$V_S=-V_2\times\frac{\left(P_3-\frac{P_2T_3}{T_2}\right)}{\left(P_3-\frac{P_ST_3}{T_S}\right)}=-V_2\times\frac{\left(1-\frac{P_2T_3}{P_3T_2}\right)}{\left(1-\frac{P_ST_3}{P_3T_S}\right)}=-V_2\times\frac{\left(1-\frac{\nu_3}{\nu_2}\right)}{\left(1-\frac{\nu_3}{\nu_S}\right)} \qquad (B.5)$$

B.4.3 Volume Estimation using Real Gas Law

The Beattie-Bridgemen emperical equation of state for a real gas is given by (Van Wylen and Sonntag, 1967)

$$P=\frac{RT}{\nu}+\frac{\beta}{\nu^2}+\frac{\gamma}{\nu^3}+\frac{\delta}{\nu^4} \qquad (B.6a)$$

where,

$$\beta=B_0RT-A_0-cR/T^2 \qquad (B.6b)$$

$$\gamma=-B_0bRT+A_0a-B_0cR/T^2 \qquad (B.6c)$$

$$\delta=B_0bcR/T^2 \qquad (B.6d)$$

Since this is a 4th order equation, Newton-Raphson numerical technique was used in the following derivation to solve this equation.

The inital state of gas (pressurized) in the reference bottle that could be solved for molar volume ν_1 is

$$P_1 = \frac{RT_1}{\nu_1} + \frac{\beta_1}{\nu_1^2} + \frac{\gamma_1}{\nu_1^3} + \frac{\delta_1}{\nu_1^4} \quad \text{where} \quad \nu_1 = \frac{V_1}{n_1} \tag{B.7}$$

The state of gas in the connecting line before and after opening valve V1 shown in Figure B.2 could be described by the following equations which are solved for molar volume ν_c and ν_2

$$P_c = \frac{RT_c}{\nu_c} + \frac{\beta_c}{\nu_c^2} + \frac{\gamma_c}{\nu_c^3} + \frac{\delta_c}{\nu_c^4} \quad \text{where } \nu_c = \frac{V_C}{n_C} \tag{B.8a}$$

$$P_2 = \frac{RT_2}{\nu_2} + \frac{\beta_2}{\nu_2^2} + \frac{\gamma_2}{\nu_2^3} + \frac{\delta_2}{\nu_2^4} \quad \text{where } \nu_2 = \frac{V_C + V_1}{n_C + n_1} = \frac{V_2}{n_2} \tag{B.8b}$$

The state of gas in the sampler before and after opening the valve V2 shown in Figure B.2 could be represented by the following equations which are solved for molar volume ν_s and ν_3

$$P_s = \frac{RT_s}{\nu_s} + \frac{\beta_s}{\nu_s^2} + \frac{\gamma_s}{\nu_s^3} + \frac{\delta_s}{\nu_s^4} \quad \text{where } \nu_s = \frac{V_S}{n_S} \tag{B.9a}$$

$$P_3 = \frac{RT_3}{\nu_3} + \frac{\beta_3}{\nu_3^2} + \frac{\gamma_3}{\nu_3^3} + \frac{\delta_3}{\nu_3^4} \quad \text{where } \nu_3 = \frac{V_S + V_C + V_1}{n_S + n_C + n_1} = \frac{V_S + V_2}{n_S + n_2} \tag{B.9b}$$

by substituting Equations (B.7) and (B.8a) in equation (B.8b), the connecting line volume V_C is determined with the following equation

$$\nu_2 = \frac{V_C + V_1}{\left(\frac{V_C}{\nu_C} + \frac{V_1}{\nu_1}\right)} \Rightarrow V_C = -V_1 \times \frac{\left(1 - \frac{\nu_2}{\nu_1}\right)}{\left(1 - \frac{\nu_2}{\nu_C}\right)} \tag{B.10}$$

Similarly, by substituting Equations (B.8b) and (B.9a) into equation (B.9b), and using the connecting line volume V_C calculated above, the sampler volume V_S is determined as shown below

$$V_S = -V_2 \times \frac{\left(1 - \frac{\nu_3}{\nu_2}\right)}{\left(1 - \frac{\nu_3}{\nu_S}\right)} \tag{B.11}$$

B.5 Sampler Qualification

Before using the samplers to determine gas void fractions in the tall column tests, the volume of the reference gas bottle and the sampler needed to be measured. In addition, the uncertainty of the sampler to accurately measure the gas void fraction needed to be established. The following sections discuss how these various tasks were accomplished.

B.5.1 Reference Gas Bottle Volume

The reference gas bottle volume was determined gravimetrically by measuring the empty weight of the bottle and filling the gas bottle with deionized water (DI) of measured density and determining the weight again. Based on triplicate measurements, the volume of the reference bottle was 492.15 ± 0.11 mL.

B.5.2 Sampler Volume

Once the reference gas bottle volume was determined, the sampler volume was determined by adding a known amount of DI water to the sampler and following the sampler void fraction determination approach discussed in Section B.3 and the analysis methodology in Section B.4. Adding the volume of the added water to the measured void volume, the total volume of the sampler was calculated. Five samplers were fabricated for use during the tall column tests, and their measured volumes as determined by the application of the ideal gas law (Equations B.1 through B.5) and the real gas law (Equations B.6 through B.11) are listed in Table B.2. Also listed in Table B.2 are the volumes estimated by the gravimetric method, which included completely filling the sampler with water and subtracting the weights before and after filling.

Table B.2. Sampler IDs and Measured Volumes

	Estimated Internal Volume (mL)			
ID #	Ideal Gas Law	Real Gas Law	Gravimetric Method	Notes
1	539.42	539.53	520.68	--
2	579.46	579.73	Not Performed	--
3	538.71	538.72	525.43	--
4	624.27	624.68	527.89	Sampler was not recommended for use
5	Sampler leaked	Sampler leaked	Not Performed	Sampler was not recommended for use

The volumes of the samplers listed in Table B.2 under the columns “Ideal Gas Law” and “Real Gas Law” were determined after adding water to create a ~10% to 20% void volume in the samplers. The value of ~10% to 20% void was chosen because it minimized the impact of stainless steel expansion on the measured sampler volume, and this void fraction falls within the void fraction range of 0% to 25% anticipated during the tall column tests. A couple of key points can be inferred from the data in Table B.2. First, differences in sampler volumes determined by the real gas and ideal gas approaches are minimal. Therefore, the ideal gas approach was chosen for use because of the simplicity of the solved equations. In addition, the volumes of Samplers 1 and 3 determined by the gravimetric approach were 13 to 15 mL smaller than their corresponding volumes determined using the pressurization approach. These differences are attributed to expansion of stainless steel under pressure and difficulties in completely filling the sampler with water. With Sampler 4, on the other hand, the differences were on the order of ~ 97 mL. This difference was attributed to gas leaking into the globe valve cavity as noted from observations of gas discharge from Sampler 4 when the globe valve was opened after the sampler was depressurized. Sampler 5 had a significant leak issue. Therefore, Samplers 4 and 5 were not recommended for use in the tall column tests.

B.5.3 Sampler Performance Checks

Once the reference gas bottle and sampler volumes were determined, a performance check of the samplers was conducted by adding known amounts of DI water to the sampler to manipulate the gas void fraction in the sampler and determine the void fraction using the approaches described in Sections B.3 and B.4 These void fractions (reported as %) are compared to the estimated void fractions from the amount of DI water added and the sampler volume determined in SectionB.5.2. Table B.3 shows the measured uncertainties in the void fractions for Samplers 1, 2, and 3.

Table B.3. Performance Check Data (Measured versus Actual Void Fraction, in %) for Samplers 1, 2, and 3

Measured	Actual	Difference	Measured	Actual	Difference	Measured	Actual	Difference
Sampler 1			Sampler 2			Sampler 3		
40.96	41.68	-0.72	45.73	47.95	-2.22	41.17	41.98	-0.81
26.84	27.27	-0.43	31.45	34.83	-3.38	26.95	27.51	-0.56
16.52	16.68	-0.16	25.00	25.94	-0.94	16.37	16.72	-0.35
12.30	12.30	0.00	21.38	21.38	0.00	9.92	9.92	0.00
7.58	7.36	0.22	17.13	16.66	0.47	4.88	3.26	1.63

The void fraction data reported in Table B.3 show that the maximum absolute error in the gas void fractions was observed with Sampler 2. The errors with Samplers 1, 2, and 3 were all <1% except for Sampler 3 at low void fraction. Based on the data presented in Table B.3, Samplers 1, 2, and 3 were recommended for use during testing; however, only Samplers 1 and 3 were used.

B.6 Results

During the tall column Tests 1 and 2, initial and final samples were collected for void fraction measurement. These samples were transported to the APEL highbay, where the gas void fraction measurements were done. As soon as the samplers were received at APEL, they were checked to ensure that they were properly labeled and that all sample valves were properly closed. Once the samplers were accepted at APEL, they were quickly connected to the reference bottle, which was usually pressurized ahead of time and allowed to equilibrate. Upon connecting the sampler to the reference bottle, the gas void fraction was measured using the approach described in Section B.3. After void fraction measurement, the sampler was depressurized and the slurry sample was extruded from the sampler for temperature measurement and rheology characterization. The sampler was cleaned and prepared for reuse.

Table B.4 lists the gas void fractions measured from the initial and final samples collected during tall column Test 1 and Test 2.

Table B.4. Gas Void Fractions Measured from the Initial and Final Samples Taken During Test 1 and Test 2

Date	Sample ID	Sampler Used	%VF Ideal
TEST-1 Initial Samples			
12/30/13	TEST1-S1A	1	4.4
12/30/13	TEST1-S2A	3	21.7
12/30/13	TEST1-S3A	1	11.7
12/31/13	TEST1-S4A	1	15.2
12/31/13	TEST1-S5A	3	17.0
TEST-1 Final Samples			
1/4/14	TEST1-S1C	3	16.8
1/4/04	TEST1-S2C	1	18.5
1/4/13	TEST1-S3C	3	12.4
1/4/14	TEST1-S4C	3	9.8
1/4/04	TEST1-S5C	1	13.5
TEST-2 Initial Samples			
1/17/14	TEST2-S2A	1	18.49
1/17/14	TEST2-S4A	1	18.99
1/17/14	TEST2-S1B	1	15.08
1/17/14	TEST2-S5A	1	12.85
TEST-2 Final Samples			
1/20/14	TEST2-S1C	1	12.83
1/20/14	TEST2-S2C	1	18.90
1/20/14	TEST2-S3C	1	18.79
1/21/14	TEST2-S4C	1	12.86
1/21/14	TEST2-S5C	1	13.51

B.7 Discussion

As discussed in Section 6.0, the samples IDs with the designation -S1*, -S2*, -S3*, -S4*, and -S5* correspond to elevations of 3, 6.75, 11, 17, and 20.5 feet, respectively. The elevations were measured from the bottom plate of the tall column. The data in Table B.4 show no obvious trends in the measured gas void fractions with sample elevation for both the initial and final samples taken during the tests. In addition, some of the initial samples had gas void fractions on the order of 20%. Finally and most importantly, the gas void fraction data determined from the sampling approach are significantly greater (10% to 15%) than the void fractions determined using the level approach (see Section 8.0). The reasons for such significantly large differences in gas void fraction results between the sampling method and the level method is puzzling given that 1) the performance check data for the samplers were <1% of the actual void fractions and 2) the pressure drop when the samplers were exposed to the charged reference gas bottle was significant. The latter (i.e., the measured pressure drop) indicates that there were significant voids within the samples collected. This was also confirmed by the presence of pockets of gas when the slurry sample was extruded from the sampler. Therefore, it is speculated that the mechanism by which the core sampler was introduced into the highly viscous and very high yield strength material used during testing resulted in a slower rate of slurry entering the sampler compared with the rate at which the sampler was inserted into the tall column. The faster movement of the sampler coring tube relative to the slurry could have compacted the slurry rather than performing uniform coring and maintaining larger voids.

Another explanation for the differences in the sampler- and level-based void fraction data is the possibility of air trapped in the sampler when it is mated with the flange on the tall column. The sampler was designed to bleed off the air trapped between the flanges through the valve used to connect with the pressurization chamber (V2 in Figure B.2). Every time the sampler was mated to the tall column and the ball valves were opened to expose the tank contents to the sampler, the operator would briefly open valve V1 to let the air escape as the fluid from the column entered the sampler. The valve (V1) was then closed and sampling proceeded as described in Section B.2. Despite the precaution taken by the sampling crew to eliminate this issue, gas may still have been left inside the valves and trapped with the sample when the coring tube was moved forward.

B.8 References

Stewart CW, CL Shepard, JM Alzheimer, TI Stokes, and G Terrones. 1995. *In Situ Determination of Rheological Properties and Void Fraction in Hanford Tank 241-SY-101*. PNL-10682, Pacific Northwest Laboratory, Richland, Washington.

Stewart CW, JM Alzheimer, ME Brewster, G Chen, RE Mendoza, HC Reid, CL Shepard, and G Terrones. 1996. *In Situ Rheology and Gas Volume in Hanford Double-Shell Waste Tanks.* PNNL-11296, Pacific Northwest National Laboratory, Richland, Washington.

Van Wylen G J and R E Sonntag. 1967. Fundamentals of Classical Thermodynamics, 4th Edition, John Wiley and Sons, New York, NY.

Appendix C

Supplementary Ultrasonic Information

Appendix C

Supplementary Ultrasonic Information

The ultrasonic sensors were used in the tall column testing to estimate the gas void fraction. The sensors were deployed on the exterior of the tall column at ten different elevations. Before ultrasonic transducers could be employed, they required some method development. The development process started from the principle of detecting gas volume fraction by measuring changes in ultrasonic attenuation and prepared it for field measurements. Though some of the method is described in Section 4.3.3, additional details are provided in this appendix. This section discusses the ultrasonic correlation development performed in the laboratory at PNNL (Section C.1.1), the configuration and collection of data during tall column testing (Section C.1.2), data from the correlation testing (Section C.2), and presents some supplementary ultrasonic data. The supplementary data presented in Section C.3 provides information that assists in interpretation of the results shown in Section 8.3.

C.1 Ultrasonic Measurement Description

C.1.1 Laboratory Testing for Attenuation-to-GVF-Correlation Development

Laboratory testing was performed to develop a mathematical correlation between ultrasonic attenuation and gas void fraction (GVF) for the 500 and 1000 Pa kaolin test slurries. Correlation-development laboratory testing was performed in a test vessel that represented a cross-diameter horizontal swath of the tall column. The purpose of using this geometry in lieu of a pipe segment with a full cross-section was to reduce the required simulant volume. The interior end-to-end length of the test vessel was 60 in. to mimic the inner diameter of the tall column. Two 3/8-in.-thick carbon steel walls with curvatures made to match that of the tall column were located at both ends of the test vessel. An acrylic base, two parallel acrylic side walls, and stabilization bars bridging the tops of the acrylic side walls completed the test vessel. A drawing of the test section is provided in Figure C.1.

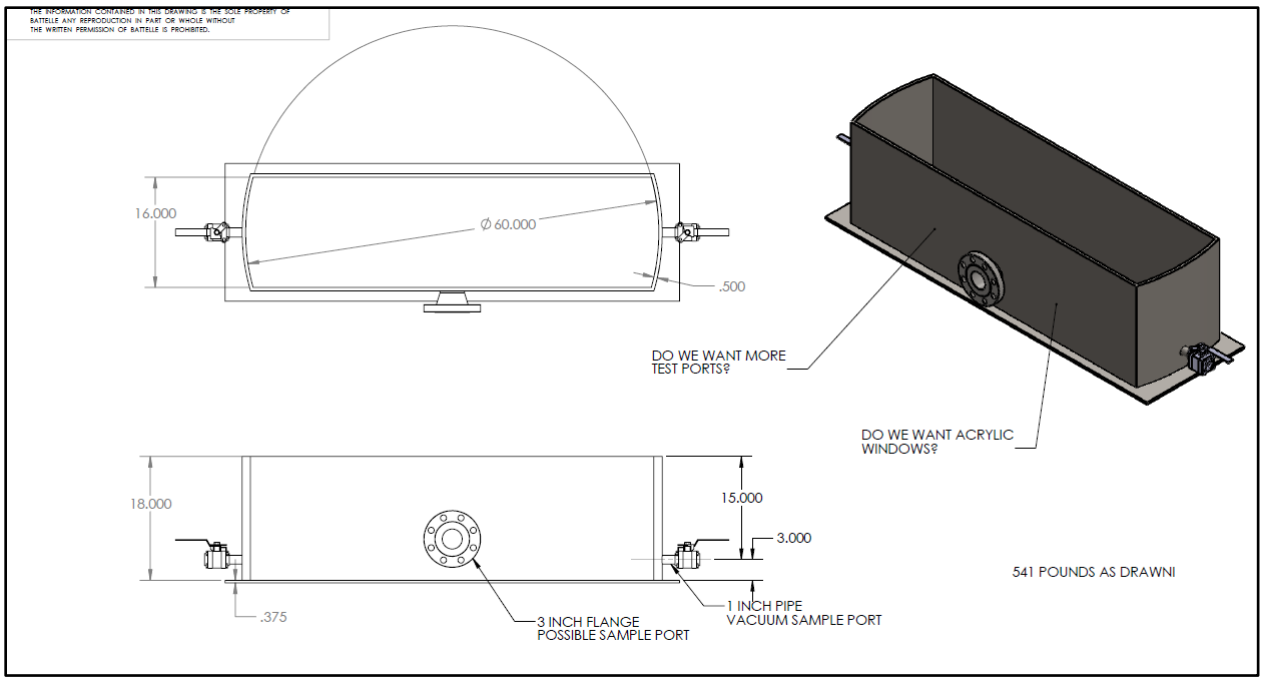

Figure C.1. Drawing of the Test Vessel Used for Ultrasonic Correlation Testing (dimensions shown are in inches)

Four vertically aligned measuring tapes that spanned the height of the test vessel were adhered to each acrylic side wall to measure kaolin and water levels during testing. The test vessel was filled to approximately 12 in. with the kaolin simulant at the start of a test. Approximately 1 in. of water was added to the top of the kaolin layer. The top of the test vessel was not sealed due to the potentially large volume of hydrogen gas that could evolve during testing. Instead, plastic wrap was placed on the stabilization bars along the top of the test vessel to reduce the degree of water evaporation. Water was added to the test vessel as needed during the course of a test to replace water lost to evaporation. Water was added until a target mass was reached (the test cell was placed on a floor scale), which was consistent throughout each test.

The GVF generated by the oxidation of dispersed zero valent iron particles in the kaolin slurry was quantified by measuring changes in the level of the water layer placed above the kaolin layer. These level measurements were made using the four rulers affixed to each acrylic side wall of the test vessel. The water level measurements were used to generate the reference “true state” gas void fraction of the kaolin slurry, which was assumed to be evenly distributed in the test section. The bulk GVF data were half the data required for the mathematical correlation between GVF and ultrasonic attenuation.

Ultrasonic measurements were performed immediately after the water and kaolin slurry level measurements were performed to facilitate the correlation of the true state GVF with an ultrasonic response as accurately as possible. Ultrasonic measurements were performed with two identical 250 kHz Olympus model V1012 ultrasonic transducers positioned 180 degrees apart at the same elevation on the outside of the carbon steel walls of the test vessel. Photographs of the transducers are shown in Figure C.2.

Figure C.2. Photographs of the Transducer Diameter (left) and Length (right)

The transducers operated in through-transmission mode, which entails one transducer transmitting an ultrasonic pulse that traverses across the test cell and is received by the opposite transducer. The transducers were held in position on the test vessel by magnetic fixtures that were aligned using a rigid frame. The magnetic fixtures remained in place during the course of testing to reduce errors associated with manually positioning and coupling the transducers by operators. Photographs of the test vessel, magnetic transducer fixtures, and transducer fixture alignment tool during transducer installation are shown in Figure C.3.

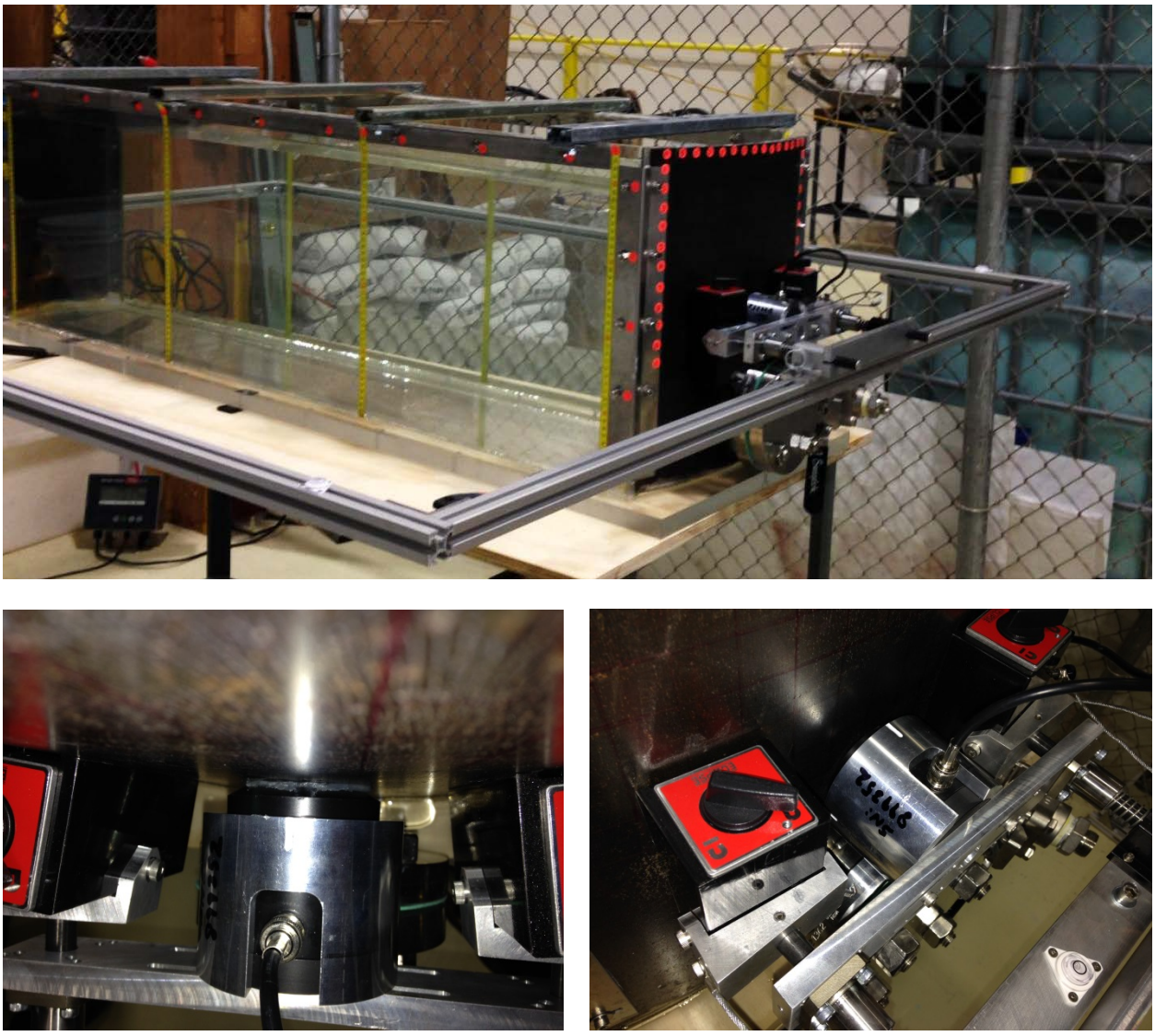

Figure C.3. Clockwise from the top: A Photograph of the Acoustic Test Vessel During Alignment of the Magnetic Transducer Fixtures Using the Square Transducer Fixture Alignment Tool; a Photograph of a Transducer Installed in the Magnetic Transducer Fixture; and a Transducer Coupled to the End of the Test Vessel**.**

Ultrasonic measurements were performed with the transducers positioned approximately 7 in. above the base of the test vessel. Ultrasonic pulses were generated by an Olympus 5058PR ultrasonic pulser-receiver unit. The same unit was used to amplify and filter the received pulse. The ultrasonic signals from the pulser-receiver were digitized, displayed, and saved to a LeCroy waveRunner 64Xi digital oscilloscope. A photograph of the test vessel with the data acquisition equipment is shown in Figure C.4.

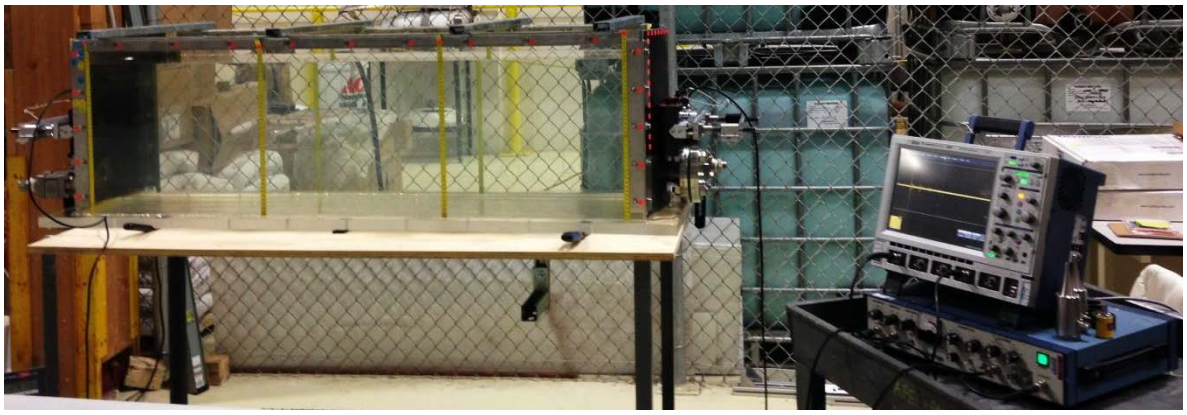

Figure C.4. Photograph of the Test Vessel and Data Acquisition Equipment Used During Correlation Development Tests

A set of data that included water and kaolin level measurements and ultrasonic waveforms was typically collected at 30- to 60-minute intervals during each correlation test. Level measurements were made using the eight rulers on the acrylic side walls of the test vessel to an accuracy of ±1 mm. Three replicate ultrasonic signals were collected after the level measurements. Approximately 10 minutes were required to collect level measurements and 3 to 5 minutes were required to collect the ultrasonic waveforms. Therefore, there was an unavoidable time lag between level measurements and ultrasonic measurements for each set of data collected during a measurement interval. Time-based disharmony between the water level and ultrasonic data has little impact when gas evolves slowly in the test vessel; however, it has a significant impact when gas evolves rapidly.

The amplitudes of the three ultrasonic signals for each measurement interval were collected and averaged. Ultrasonic attenuation was calculated for each measurement interval in time relative to the gas-free sludge simulant. Attenuation is expressed in units of decibels (dB) using Equation C.1:

$$\text{Attenuation (dB)} = 20 \log_{10} \frac{A_1}{A_2} \tag{C.1}$$

where A_1 denotes the amplitude of the signal through the gas-free kaolin and A_2 denotes the amplitude of the signal through gassy kaolin. The attenuation data were subsequently time-correlated with the GVF values that were calculated from the water level measurements made immediately before the ultrasonic measurements. The time-correlated data were plotted as attenuation versus GVF. A correlation equation to relate attenuation to GVF was calculated using a polynomial fit. The results of the ultrasonic correlation test data are presented in Section C.2.1.

C.1.2 Tall Column Testing for Ultrasonic Measurement of GVF

The purpose of performing ultrasonic measurements on the tall column was to determine if high GVFs existed in the lower elevations of the column during testing. Ultrasonic transducers were installed at elevations of 24 feet and below. Kaolin simulant was loaded to elevations above 24 feet during tall column testing (27 feet during Tests 1 and 2 and 29.5 feet during Test 3); however, ultrasonic data were not collected for these higher elevations.

Forty ultrasonic transducers having the same specifications as those used for the laboratory correlation development tests were installed on the tall column using the magnetic transducer fixtures. Two transducer pairs were installed at each of the ten different elevations selected for ultrasonic measurements along the tall column, which were 2, 4, 6, 8, 9.3, 12, 14.3, 18, 22, and 24 feet from the column base. Transducers were positioned 60, 120, 240, and 300 degrees relative to the camera column at each elevation. Each transducer pair positioned 180 degrees apart circumferentially at a given elevation was used to perform through-transmission measurements, each transducer alternately operating as a transmitter and receiver to test measurement reciprocity. The transducers were connected to the data acquisition equipment inside the control trailer via 100-foot-long, 50-ohm, coaxial BNC cables rated for outdoor use. Photographs of the transducers installed on the tall column are shown in Figure C.5.

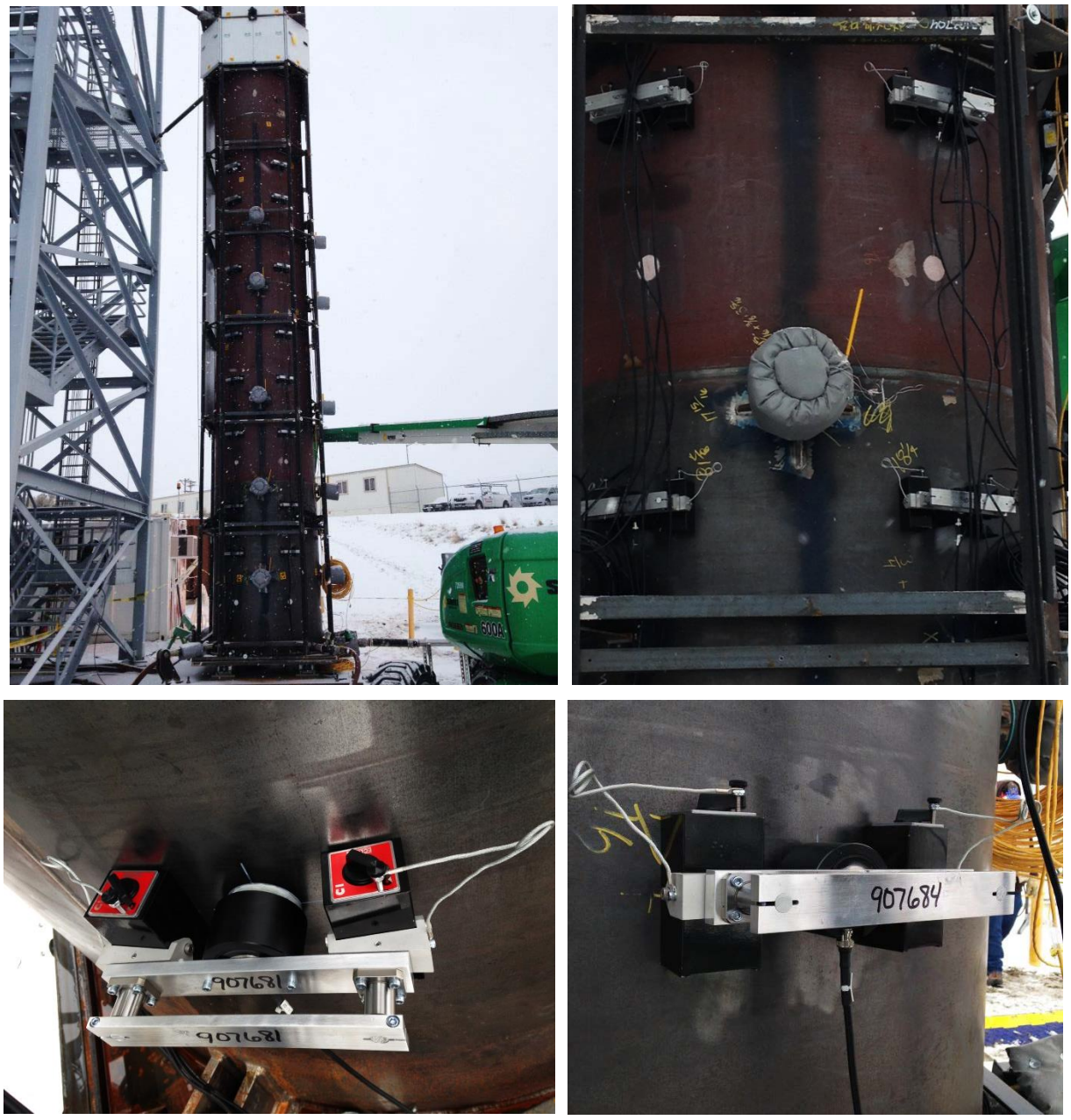

Figure C.5. Clockwise from the top: A Photograph of the Tall Column After Transducer Installation and Before Installation of the Insulation Panels; a Close-up Photograph of Four Transducers Installed on the Tall Column; a Top-down View of a Transducer in a Magnetic Fixture on the Tall Column; and a Backside View of a Magnetic Fixture Holding a Transducer on the Tall Column

The positions and serial numbers of the transducers installed on the tall column and their corresponding cable labels are provided in Table C.1 for reference. No transducers were installed above the 24 ft elevation on the tall column.

Table C.1. Ultrasonic Sensor Locations and Identification

Elevation of Transducer	Angular Location of Transducer Relative to Camera Column	Transducer ID (on UT cable at column)	Transducer ID (on UT cable in control trailer)	Transducer Serial Number
2 ft	60°	LVL1-60°	1-X1	907686
2 ft	120°	LVL1-120°	2-X1	907689
2 ft	240°	LVL1-240°	3-X1	907684
2 ft	300°	LVL1-300°	4-X1	907681
4 ft	60°	LVL2-60°	1-X2	907899
4 ft	120°	LVL2-120°	2-X2	907888
4 ft	240°	LVL2-240°	3-X2	907881
4 ft	300°	LVL2-300°	4-X2	907894
6 ft	60°	LVL3-60°	1-X3	907897
6 ft	120°	LVL3-120°	2-X3	907882
6 ft	240°	LVL3-240°	3-X3	907895
6- ft	300°	LVL3-300°	4-X3	907898
8 ft	60°	LVL4-60°	1-X4	907679
8 ft	120°	LVL4-120°	2-X4	907677
8 ft	240°	LVL4-240°	3-X4	907673
8 ft	300°	LVL4-300°	4-X4	907672
9.33 ft	60°	LVL5-60°	1-X5	907886
9.33 ft	120°	LVL5-120°	2-X5	907893
9.33 ft	240°	LVL5-240°	3-X5	899759
9.33 ft	300°	LVL5-300°	4-X5	907884
12 ft	60°	LVL6-60°	1-X6	907678
12 ft	120°	LVL6-120°	2-X6	907671
12 ft	240°	LVL6-240°	3-X6	907683
12 ft	300°	LVL6-300°	4-X6	907676
14.33 ft	60°	LVL7-60°	1-X7	907887
14.33 ft	120°	LVL7-120°	2-X7	907889
14.33 ft	240°	LVL7-240°	3-X7	907896
14.33 ft	300°	LVL7-300°	4-X7	907891
18 ft	60°	LVL8-60°	1-X8	907690
18 ft	120°	LVL8-120°	2-X8	907685
18 ft	240°	LVL8-240°	3-X8	907680
18 ft	300°	LVL8-300°	4-X8	907688
22 ft	60°	LVL9-60°	1-X9	907885
22 ft	120°	LVL9-120°	2-X9	907880
22 ft	240°	LVL9-240°	3-X9	907890
22 ft	300°	LVL9-300°	4-X9	907892
24 ft	60°	LVL10-60°	1-X10	907682
24 ft	120°	LVL10-120°	2-X10	907687
24 ft	240°	LVL10-240°	3-X10	907675
24 ft	300°	LVL10-300°	4-X10	907674

Test 1 – 500 Pa

Ultrasonic measurements were performed approximately once every four hours during tall column Test 1 using the same pulser-receiver and oscilloscope used during the laboratory correlation tests. Transducer cables for each transducer pair were manually connected to the pulser-receiver unit during a measurement. Waveforms were stored on the digital oscilloscope using a file naming convention that related each data file with transducer position, elevation, and duty (transmitter). The ultrasonic waveforms were analyzed to obtain the signal amplitudes and to analyze for attenuation. The attenuation data from the tall column test and the correlation equation generated from the 500 Pa ultrasonic correlation tests were used to calculate GVF for the tall column Test 1. The results of the ultrasonically determined GVF data are presented in Section 8.3 as GVF versus time and column height versus GVF.

Test 2 – 500 Pa

Ultrasonic measurements were performed once every 15 minutes during tall column Test 2 using an automated ultrasonic transducer data acquisition system (UT-DAS). The UT-DAS was an assembly of data acquisition hardware that was interfaced with the ultrasonic pulser-receiver and the forty ultrasonic transducers on the tall column. Data acquisition with the UT-DAS was controlled via the BubbleSense 1.0 software developed, verified, and validated to automatically perform the following tasks:

1. automate transducer pairing,
2. collect a user-specified quantity of waveforms per transducer pair,
3. display waveforms,
4. automate transducer pair sequencing,
5. save waveform data, and
6. initiate data acquisitions at time periods specified by the user.

A photograph of the UT-DAS is provided in Figure C.6. The core UT-DAS components included a Dell T7600 computer that housed a GaGe CSE4424 digitizer card, and a National Instruments PXI-1042 expansion chassis that housed four Pickering model 40-332-001 matrix switch cards. The UT-DAS was interfaced with the Olympus 5058PR ultrasonic pulser-receiver unit via two adapter/interface boxes and forty 250 kHz Olympus model V1012 ultrasonic transducers via forty 100-foot-long coaxial cables that extended between the tall column and the control trailer. A connection diagram for the core UT-DAS components and the ultrasonic equipment with which the UT-DAS is interfaced is provided in Figure C.7. The user interfaced with the UT-DAS via the BubbleSense software, a monitor, keyboard, and mouse. Data storage and transfer was facilitated by 4 TB 2big Quadra USB3 LaCie external hard drives.

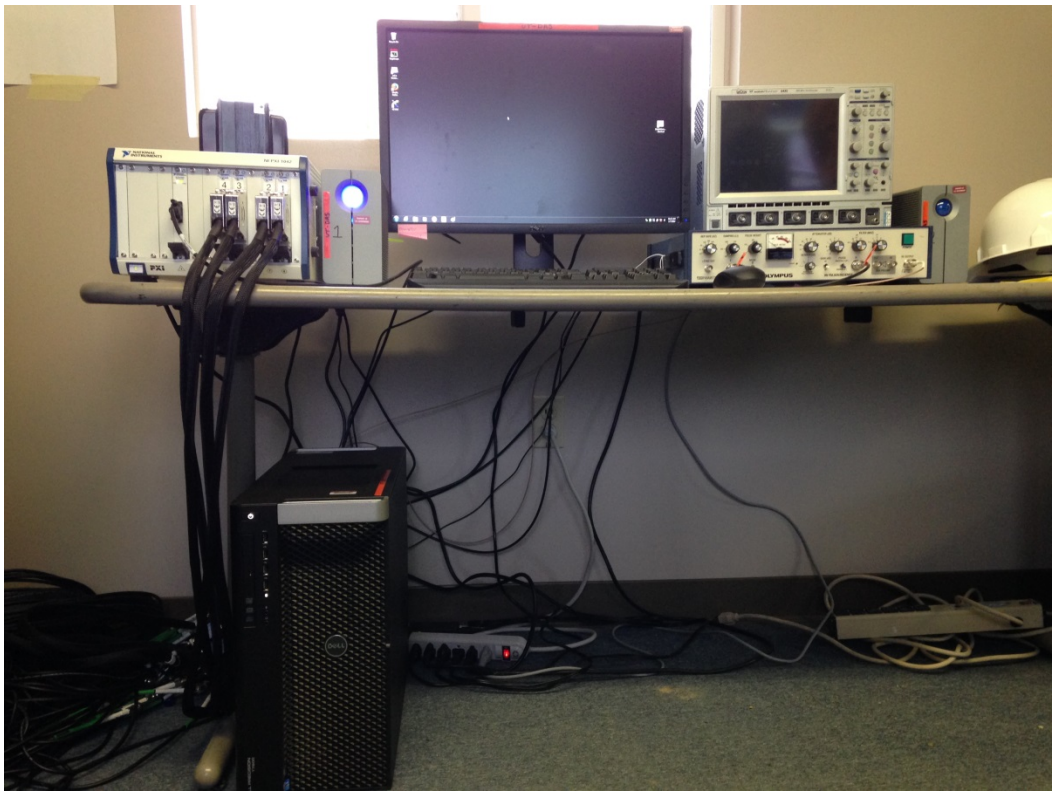

Figure C.6. Photograph of the UT-DAS

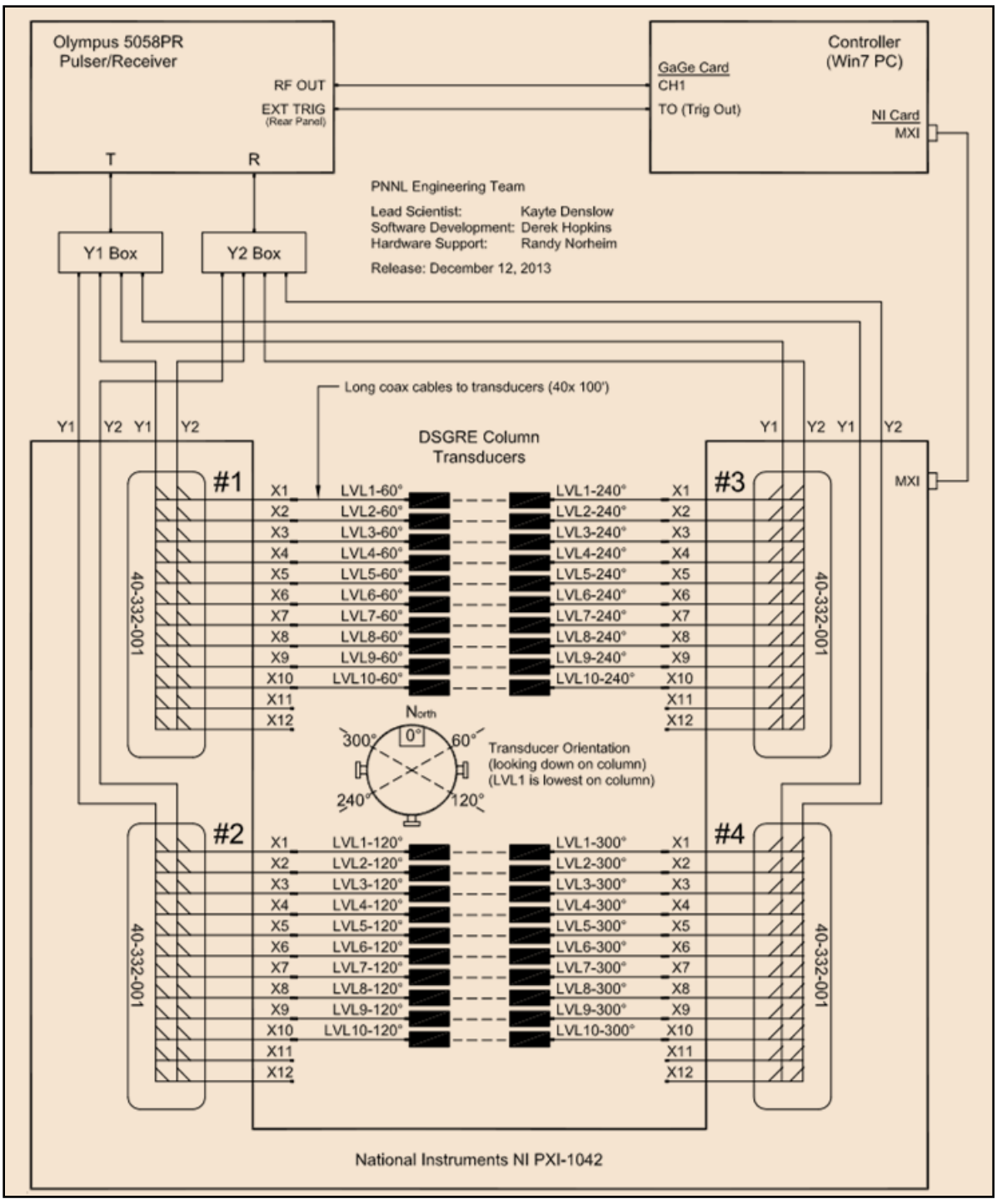

Figure C.7. Illustration of Wiring Diagram for the UT-DAS

The ultrasonic waveforms collected during tall column Test 2 were analyzed to obtain the signal amplitudes and to analyze for attenuation. The attenuation data from the tall column test and the correlation equation generated from the 500 Pa ultrasonic correlation tests were used to calculate GVF for the tall column Test 2. The results of the ultrasonically determined GVF data are presented in Section 8.3 as GVF versus time and column height versus GVF.

Test 3 – 1000 Pa

Ultrasonic measurements were performed once every 15 minutes during tall column Test 3 using the UT-DAS. The ultrasonic waveforms collected during tall column Test 3 were analyzed to obtain the signal amplitudes and to analyze for attenuation. The attenuation data from the tall column test and the correlation equation generated from the 1000 Pa ultrasonic correlation tests were used to calculate GVF for the tall column Test 3. The results of the ultrasonically determined GVF data are presented in Section 8.3 as GVF versus time and column height versus GVF.

C.2 Retained Gas Fraction Profile from Measurements of Ultrasonic Attenuation

C.2.1 Correlation Tests

Two ultrasonic attenuation-to-GVF correlation tests were conducted as described in Section C.1.1. One correlation test was performed for each shear strength. The correlation tests will be referred to as the 500 Pa correlation test and the 1000 Pa correlation test. The results from the 500 Pa correlation test showed, as expected, increasing attenuation with increasing GVF as shown in Figure C.9. However, closer inspection of the data plot in the time range of 135 to 145 hours reveals an apparent lag between the time attenuation increases and the time the bulk average GVF of the test vessel increases. The attenuation remains essentially constant during 135 to 145 hours while the bulk average GVF increased from 4% to 10% GVF. As a result, the time-correlated attenuation-vs.-GVF data plot has a slope of nearly zero in the range of 4% to 10% GVF, as shown in Figure C.10.

The slope of a polynomial fit to the 500 Pa attenuation-vs.-GVF correlation data increases with increasing GVF up to approximately 2% GVF, whereupon the slope changes to nearly zero between 2% and 10% GVF. The slope becomes steep once more between 10% and 15% GVF.

The variable slopes in the attenuation-vs.-void fraction 500 Pa correlation data mean the correlation can only be used to reliably quantify GVF from 0% to 2% GVF and 10% to 15% GVF and determine if GVF is “between 2% and 10% GVF” for tall column tests with 500 Pa kaolin (Test 1 and Test 2). For example, an attenuation value of 3 to 5 dB corresponds to a GVF range of 2% and 10% GVF. Rather than using the 500 Pa attenuation-to-GVF correlation to quantify GVF with high resolution and accuracy, it can be used to determine if there are large differences in GVF along the tall column for Test 1 and Test 2 by determining if GVF at each elevation is “below 2%” and “above 10%.”

The attenuation-vs.-void fraction 500 Pa correlation data does not demonstrate sensitivity to void between 2% and 10% GVF; however, it does suggest that attenuation data can discern void between 10% and 15% GVF. Disharmony between the data plot in Figure C.10 could be attributed to the following:

- Unavoidable time lag between water level measurements and ultrasonic measurements for a given measurement increment. Approximately 10 minutes are required to collect level measurements for the eight test vessel rulers. An additional 3 to 5 minutes are required to save the ultrasonic data. Time-based disharmony between the water level and ultrasonic data has little impact when gas retention changes slowly in the test vessel; however, it has a significant impact when gas retention changes rapidly.

- The uneven distribution of gas in the test vessel. The approach of using a correlation equation to relate attenuation to GVF relies heavily on good agreement between the bulk average GVF and the GVF of the kaolin in the sound field. The sound field volume is a fraction of the test vessel volume. A correlation test example where the GVF did not appear to be even throughout the test vessel was during the 500 Pa test at 4% GVF. See Figure C.8.
- General measurement uncertainty. Additional correlation tests would allow for an improved understanding of uncertainty related to attenuation measurements and bulk average GVF measurements.

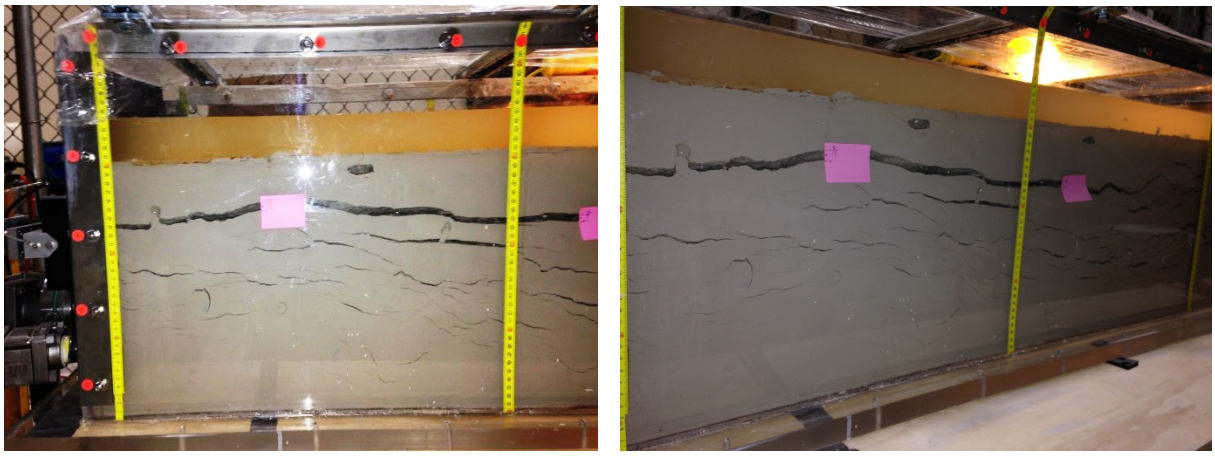

Figure C.8. Photographs of the Gas Distribution in the Test Vessel at 4% GVF During the 500 Pa Correlation Test

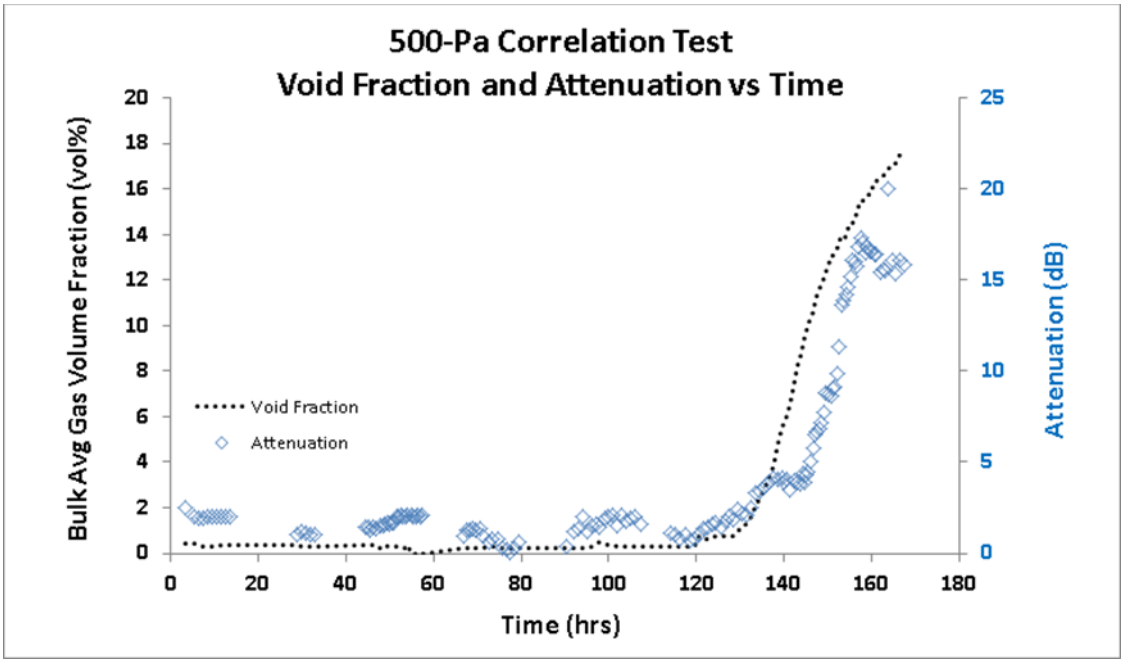

Figure C.9. 500 Pa Correlation Test: Ultrasonic Attenuation and GVF vs. Time

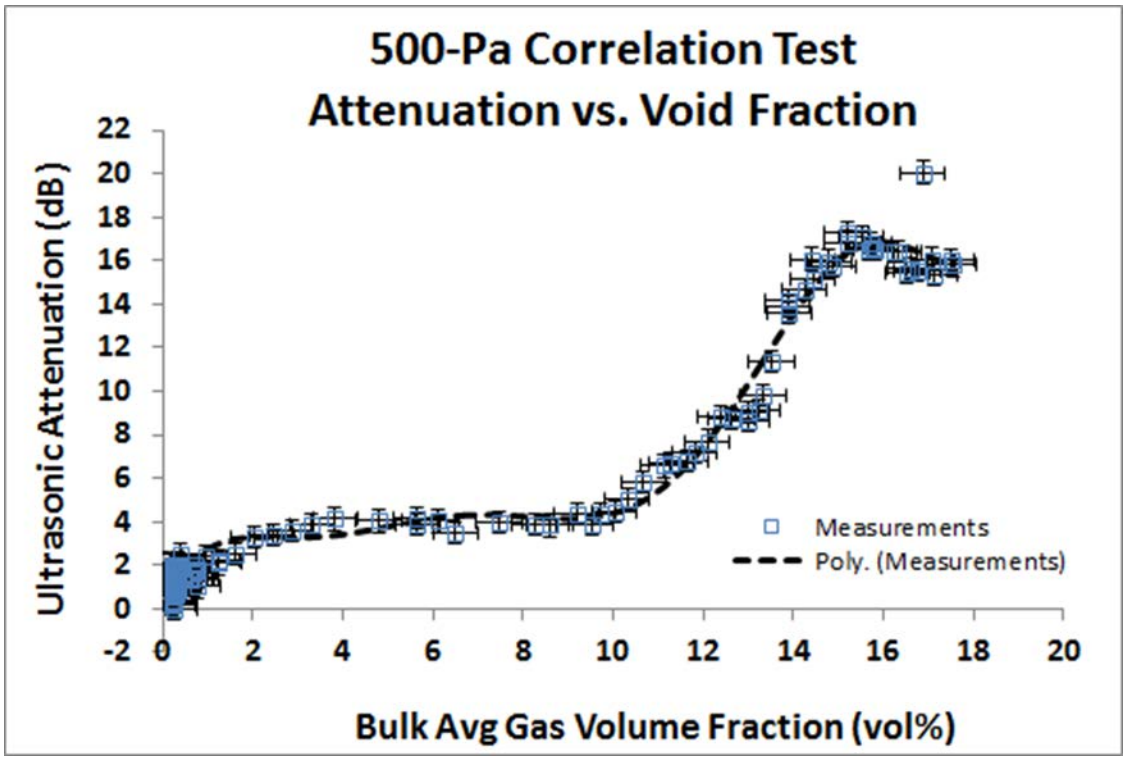

Figure C.10. 500 Pa Correlation Test: Time-correlated Attenuation vs. GVF

The results from the 1000 Pa correlation test also showed increasing attenuation with increasing GVF as shown in Figure C.11. The attenuation-vs.-void fraction 1000 Pa correlation plot has a steady slope, as shown in Figure C.12, and can be used to discern between different GVFs.

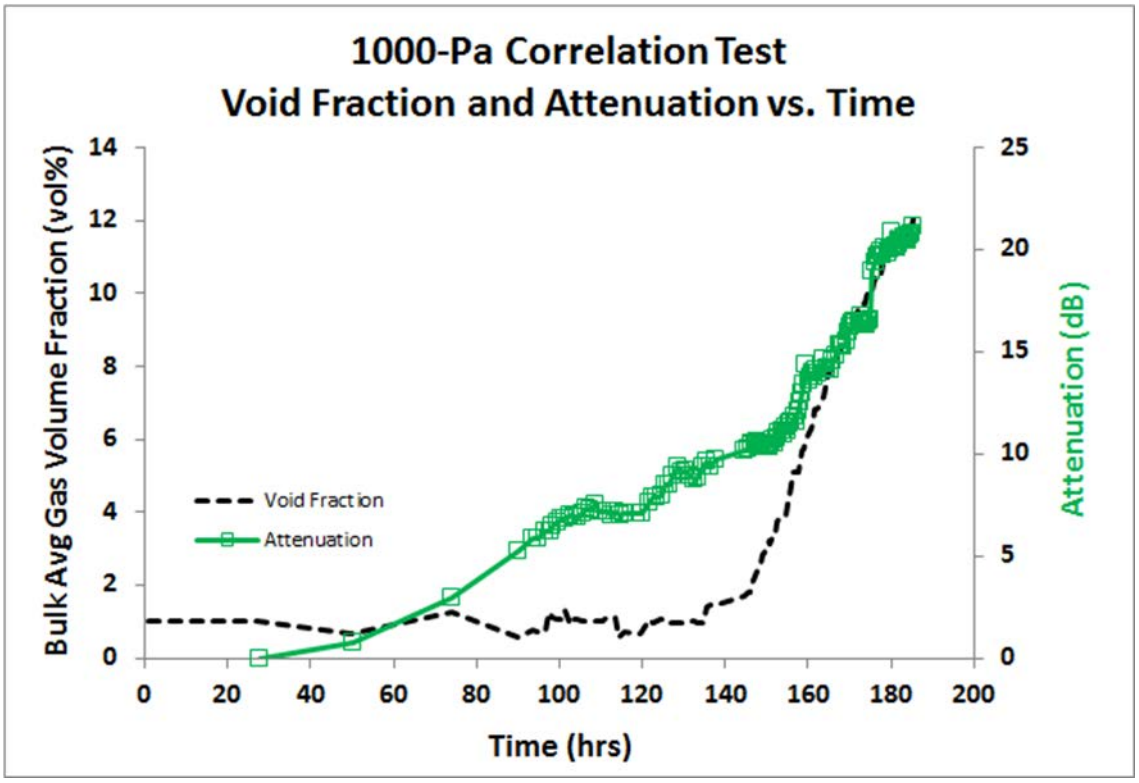

Figure C.11. 1000 Pa Correlation Test: Ultrasonic Attenuation and GVF vs. Time

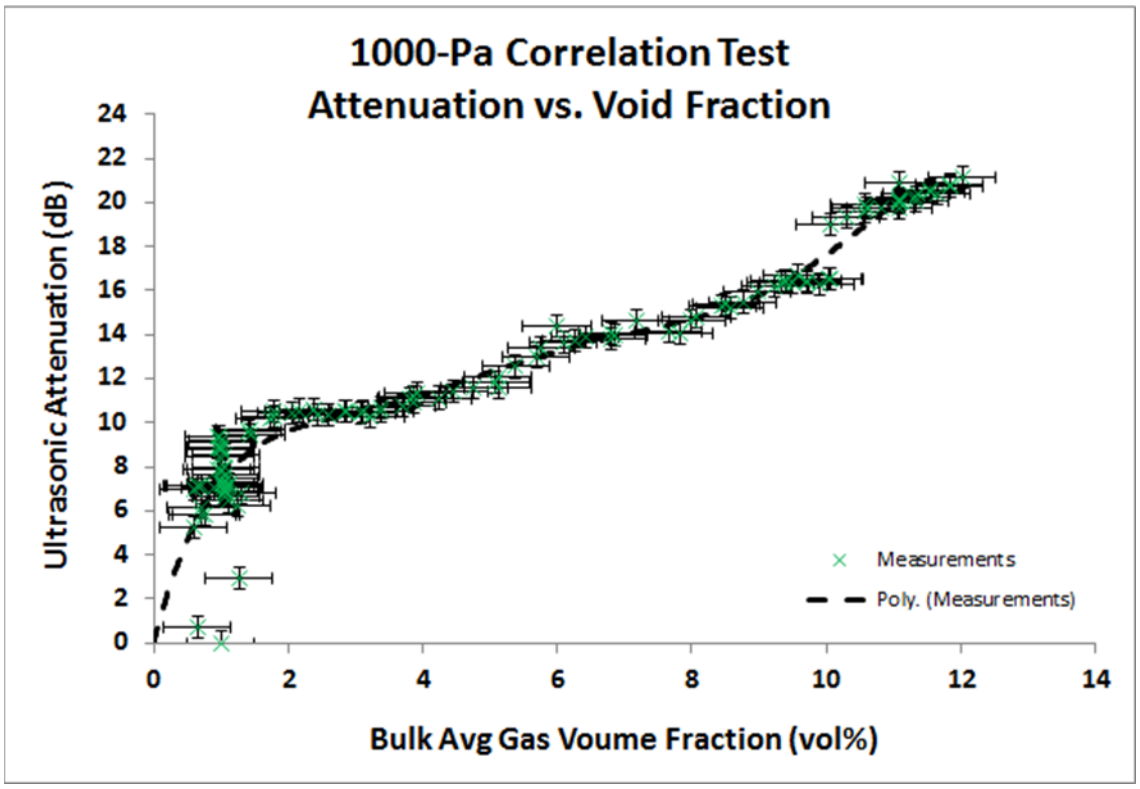

Figure C.12. 1000 Pa Correlation Test: Time-correlated Attenuation vs. GVF

C.3 Supplementary Test Result Figures

The following figures are supplemental gas void fraction data from the ultrasonic sensors for each of the three tall column tests. For these figures, the GVF results from the two transducer pairs at each height, or sensor level, were averaged and plotted against elapsed time. These results highlight some of the variability in the ultrasonic measurements and, accordingly, the uncertainty in the GVF data from this method. One notable feature in the results, particularly from Tests 1 and 2, is the variability in the GVF as a function of time. The expected behavior for the tall column tests was a gradual increase in GVF with time, similar to what was measured in the acoustic test cell for the correlation tests (see, for example, the relatively smooth increase in attenuation with time in Figure C.9 and Figure C.11). One example of unexpected variability is the results for the 22 and 24 ft elevations for Test 2 shown in Figure C.14. Between 60 and 110 hours for these two elevations, the GVF shifts upward and downward over periods spanning about 10 hours. A second example of variability is that the measured GVF did not start at a low value at the beginning of a test and then increase over time, as expected, but often started at an elevated value, then decreased initially and subsequently increased during the tests. Figure C.14 shows this behavior at all of the elevations for Test 2. Overall, the details of the GVF variation with time show more variability than was seen in the laboratory acoustic cell tests and the cause of the variability in the tall column tests has not been determined.

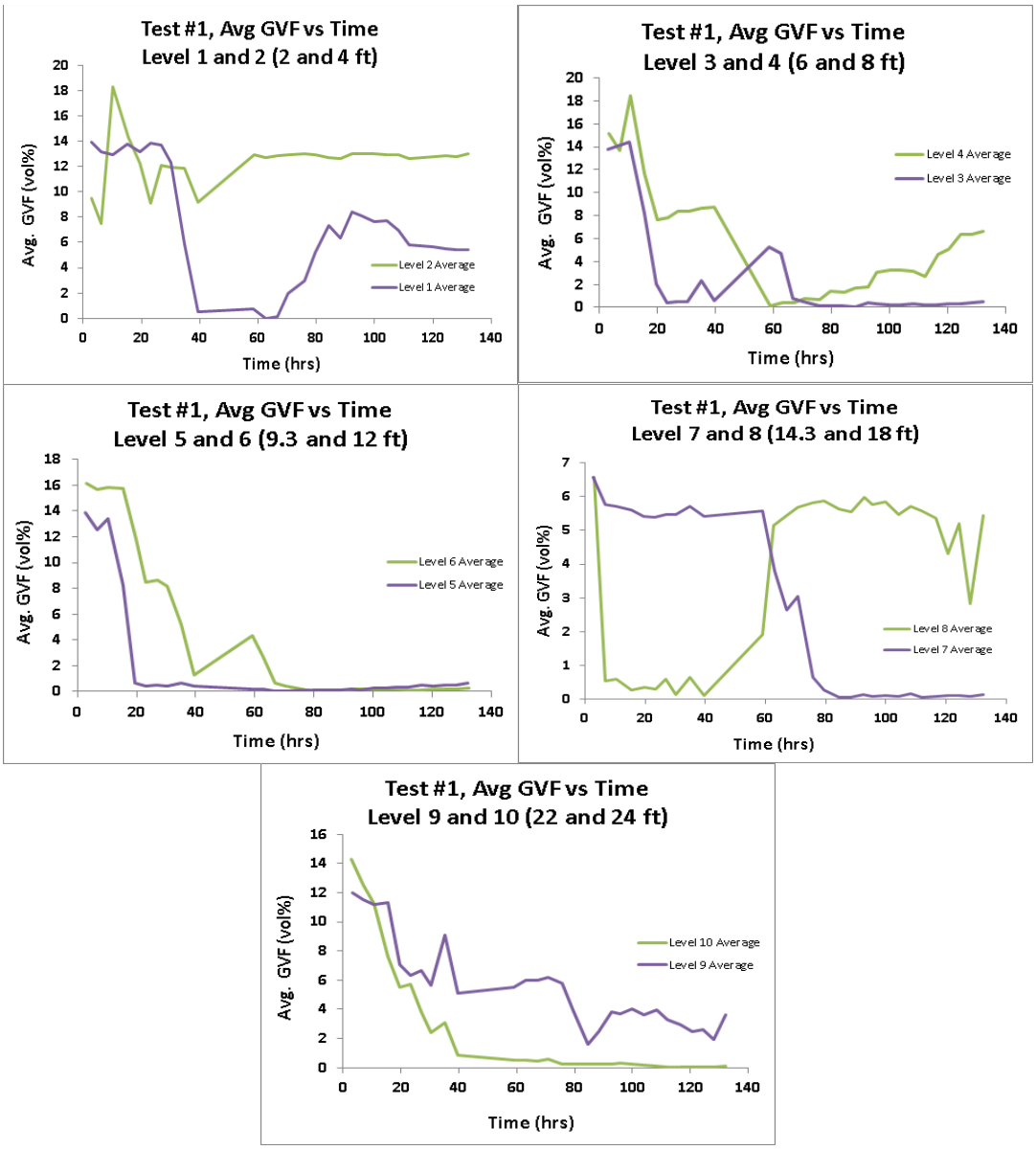

Figure C.13. Gas Void Fraction (average of both transducer pairs at each level) as a Function of Time for Test 1

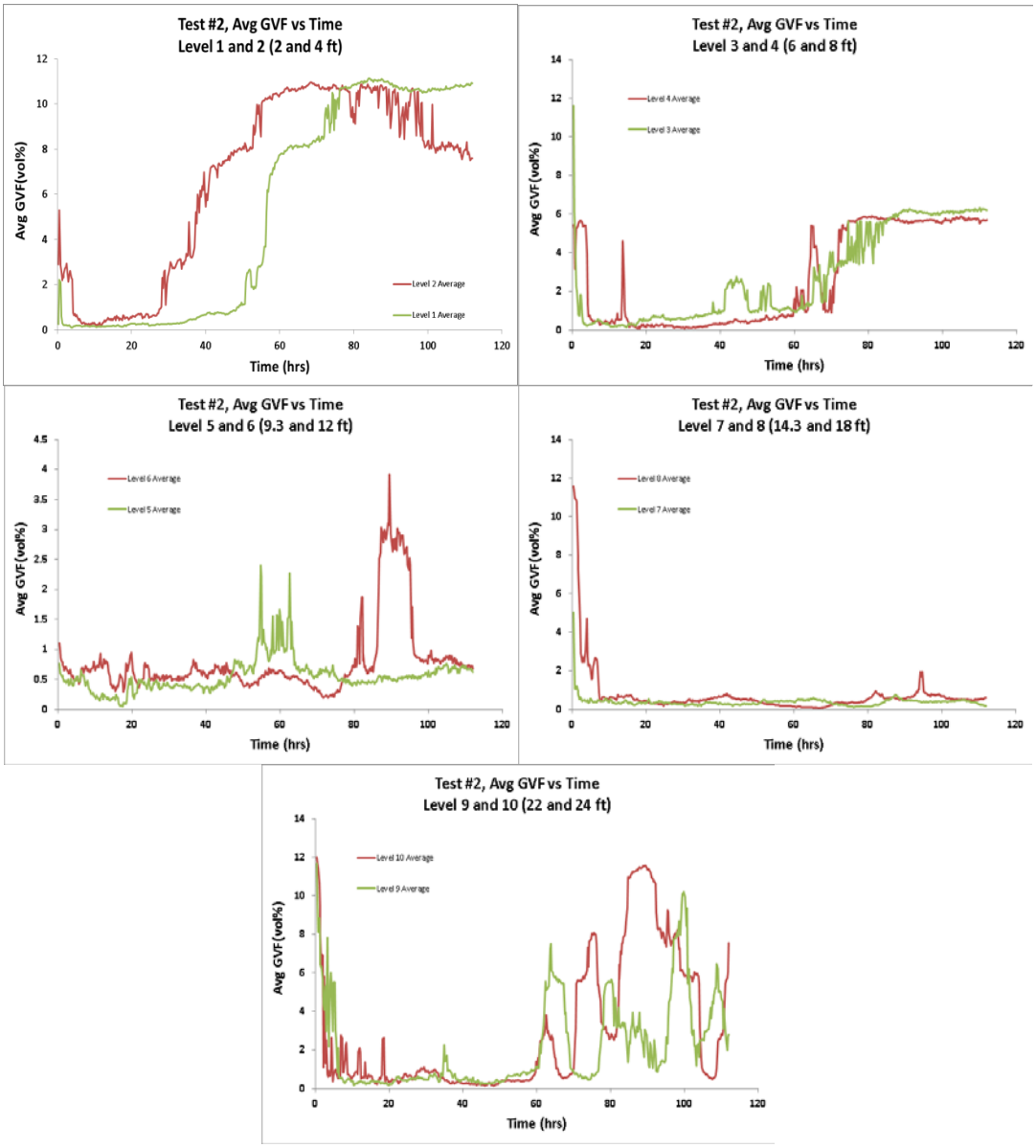

Figure C.14. Gas Void Fraction (average of both transducer pairs at each level) as a Function of Time for Test 2

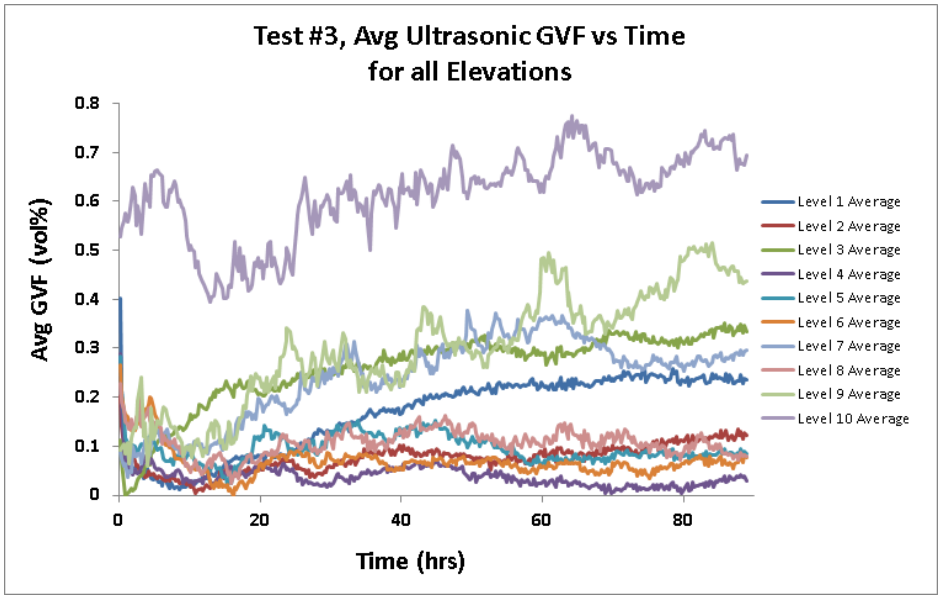

Figure C.15. Gas Void Fraction (average of both transducer pairs at each level) as a Function of Time for Test 3

Distribution

No. of Copies

OFFSITE

1 M Epstein
Fauske and Associates, LLC
1118 3rd Street, #308
Santa Monica, CA 90403

1 G Terrones
Applied Physics Division (X-4)
MS: T086
Los Alamos National Laboratory
Los Alamos, NM 87545

2 Savannah River National Laboratory
Savannah River Site
Aiken, SC 29808
C Nash
B Wilmarth

1 RD Holtz
Civil & Environmental Engineering
University of Washington
201 More Hall, Box 352700
Seattle, WA 98195-2700

No. of Copies

ONSITE

9 **Washington River Protection Solutions**

WB Barton	S7-90
WE Bryan	H3-20
R Calmus	H8-04
JM Grigsby	S7-90
NW Kirch	R2-58
DB Little	R2-58
JE Meacham	R2-58
TL Sams	R2-52
DB Smet	G5-58

28 **Pacific Northwest National Laboratory**

GK Boeringa	K7-15
JR Bontha	P7-25
RC Daniel	P7-22
KM Denslow	K5-26
LS Fifield	K2-12
PA Gauglitz (10)	K7-15
DJ Heldebrant	K2-44
NK Karri	J4-55
LA Mahoney	K7-15
MR Powell	K6-24
SD Rassat	K6-28
SA Sande	K6-01
PP Schonewill (3)	P7-25
RW Shimskey	P7-27
DN Tran	K6-24
BE Wells	K7-15
Project Records	

Pacific Northwest
NATIONAL LABORATORY

Proudly Operated by Battelle *Since 1965*

U.S. DEPARTMENT OF
ENERGY

902 Battelle Boulevard
P.O. Box 999
Richland, WA 99352
1-888-375-PNNL (7665)
www.pnnl.gov